

Classical and quantum investigations
of four-dimensional maps
with a mixed phase space

Dissertation
zur Erlangung des wissenschaftlichen Grades
Doctor rerum naturalium

vorgelegt von

Martin Richter
geboren am 01.07.1982 in Leipzig

Institut für Theoretische Physik
Fachrichtung Physik
Fakultät für Mathematik und Naturwissenschaften
Technische Universität Dresden
2012

Eingereicht am 12. April 2012

1. Gutachter: Prof. Dr. Roland Ketzmerick
2. Gutachter: Prof. Dr. Srihari Keshavamurthy

Verteidigt am 5. Juli 2012

Abstract

Systems with more than two degrees of freedom are of fundamental importance for the understanding of problems ranging from celestial mechanics to molecules. Due to the dimensionality the classical phase-space structure of such systems is more difficult to understand than for systems with two or fewer degrees of freedom. This thesis aims for a better insight into the classical as well as the quantum mechanics of 4D mappings representing driven systems with two degrees of freedom. In order to analyze such systems, we introduce 3D sections through the 4D phase space which reveal the regular and chaotic structures. We introduce these concepts by means of three example mappings of increasing complexity. After a classical analysis the systems are investigated quantum mechanically. We focus especially on two important aspects: First, we address quantum mechanical consequences of the classical Arnold web and demonstrate how quantum mechanics can resolve this web in the semi-classical limit. Second, we investigate the quantum mechanical tunneling couplings between regular and chaotic regions in phase space. We determine regular-to-chaotic tunneling rates numerically and extend the fictitious integrable system approach to higher dimensions for their prediction. Finally, we study resonance-assisted tunneling in 4D maps.

Kurzfassung

Für das Verständnis einer Vielzahl von Problemen von der Himmelsmechanik bis hin zur Beschreibung von Molekülen spielen Systeme mit mehr als zwei Freiheitsgraden eine entscheidende Rolle. Aufgrund der Dimensionalität gestaltet sich ein Verständnis dieser Systeme jedoch deutlich schwieriger als bei Systemen mit zwei oder weniger Freiheitsgraden. Die vorliegende Arbeit soll zum besseren Verständnis der klassischen und quantenmechanischen Eigenschaften getriebener Systeme mit zwei Freiheitsgraden beitragen. Hierzu werden dreidimensionale Schnitte durch den Phasenraum von 4D Abbildungen betrachtet. Anhand dreier Beispiele, deren Phasenräume zunehmend kompliziert sind, werden diese 3D Schnitte vorgestellt und untersucht. In einer sich anschließenden quantenmechanischen Untersuchung gehen wir auf zwei wichtige Aspekte ein. Zum einen untersuchen wir die quantenmechanischen Signaturen des klassischen „Arnold Webs“. Es wird darauf eingegangen, wie die Quantenmechanik dieses Netz im semiklassischen Limes auflösen kann. Darüberhinaus widmen wir uns dem wichtigen Aspekt quantenmechanischer Kopplungen klassisch getrennter Phasenraumgebiete anhand der Untersuchung dynamischer Tunnelraten. Für diese wenden wir sowohl den in der Literatur bekannten „fictitious integrable system approach“ als auch die Theorie des resonanz-unterstützten Tunnelns auf 4D Abbildungen an.

Contents

Contents	v
1. Introduction	1
2. 2D mappings	5
2.1. Hamiltonian systems with 1.5 degrees of freedom	5
2.2. The 2D standard map	6
3. Classical dynamics of higher dimensional systems	11
3.1. Coupled standard maps as paradigmatic example	12
3.2. Near-integrable systems	15
3.2.1. Analytical description of multidimensional, near-integrable systems	15
3.2.2. Pendulum approximation	18
3.2.3. Normal forms	24
3.2.4. Arnold diffusion and Arnold web	24
3.3. Numerical tools for the analysis of regular and chaotic motion	26
3.3.1. Frequency analysis	26
3.3.2. Fast Lyapunov indicator	31
3.3.3. Phase-space sections	33
3.4. Systems with regular dynamics and a large chaotic sea	35
3.4.1. Designed maps: Map with linear regular region, \mathcal{P}_{llu}	36
3.4.2. Designed maps: Islands with resonances, \mathcal{P}_{nnc}	46
3.4.3. Generic maps: Coupled standard maps, \mathcal{P}_{csm}	63
4. Quantum Mechanics	75
4.1. Quantization of Classical Maps	77
4.2. Eigenstates of the time evolution operator U	79
4.2.1. Eigenstates of \mathcal{P}_{llu}	80
4.2.2. Eigenstates of \mathcal{P}_{nnc}	84
4.2.3. Eigenstates of \mathcal{P}_{csm}	87
4.3. Quantum signatures of the stochastic layer	89
4.3.1. Eigenstates resolving the stochastic layer	90
4.3.2. Wave-packet dynamics into the stochastic layer	94

4.4.	Dynamical tunneling rates	98
4.4.1.	Numerical calculation of dynamical tunneling rates	99
4.4.2.	Direct regular-to-chaotic tunneling rates γ^d of \mathcal{P}_{llu}	101
4.4.3.	Prediction of γ^d using the fictitious integrable system approach	103
4.4.4.	Dynamical tunneling rates of \mathcal{P}_{nnc}	105
4.4.5.	Interlude: Theory of resonance assisted tunneling (RAT)	106
4.4.6.	Prediction of tunneling rates for \mathcal{P}_{nnc} , RAT	111
4.4.7.	Dynamical tunneling rates of \mathcal{P}_{csm}	120
5.	Summary and outlook	123
Appendix		125
A.	Potential of the designed map	125
B.	Quantum-number assignment-algorithm	128
C.	Alternate paths due to alternate resonances in the description of RAT	131
D.	Alternate resonances in the description of RAT leading to different tunneling rates	133
E.	Tunneling rates of map with nonlinear resonances but uncoupled regular region	133
F.	Interpolation of quasienergies	135
G.	2D Poincaré map for the pendulum approximation	137
H.	RAT prediction broken down to single paths	139
I.	Linearization of the pendulum approximation	140
J.	Iterative diagonalization schemes for the semiclassical limit	143
List of figures		148
Bibliography		163

1. Introduction

Probably one of the most beautiful physical findings concerning dynamical systems is the statement of the KAM theorem by Kolmogorov [1], Arnold [2], and Moser [3]. It is the answer to the long standing question of classical mechanics about the fate of integrable Hamiltonian systems under a weak perturbation. The KAM theorem's beauty stems from the fundamental insight that initial conditions in phase space are not the relevant quantities to decide about the behavior under the perturbation. Far more important are the frequencies of the bounded regular motion. Whenever these frequencies are not sufficiently irrational, the motion will fundamentally change and take place on completely different topological objects compared to the unperturbed case. A further part of the beauty of the theorem is given by its tremendous generality. The answer to the question, whether under perturbation a domain in phase space will undergo a drastic change, only assumes very weak and general prerequisites.

Especially the number of degrees of freedom f of a given Hamiltonian system does not play any role for the KAM theorem [4]. Therefore, it is indispensable when investigating systems with two or fewer degrees of freedom as well as systems with many degrees of freedom. But why should one distinguish between systems with $f \leq 2$ and $f > 2$ in the first place? The first answer might be a very practical one: In systems with $f \leq 2$ it is possible to reduce the dynamics to a 2D phase space by using Poincaré surfaces of section. Hence, it is possible to look at the phase space in total. This is an aspect which may sound obvious but it is of vital importance when analyzing the dynamics of generic systems revealing regular motion, nonlinear resonances, and chaotic dynamics [5]. Especially the consequences arising from the coexistence of the different types of motion are very interesting, such as the overlap of resonances and the onset of global chaotic motion in 2D systems [6, 7].

The possibility of visualizing the phase space is quite fundamental to understand the physical concepts behind Hamiltonian systems, such as atom-optics billiards [8, 9] or mesoscopic transport in 2D electron gases [10, 11]. However, one can only rarely reduce physical questions to a 2D phase space. The vast majority of problems ranging from investigations of the solar system [12–16] over solid state physics and ballistic transport [17, 18] to the understanding of molecules [19–21] has a higher dimensional phase space.

The possibility of reducing a system with $f \leq 2$ to a 2D phase space is a very practical difference in comparison to systems with $f > 2$. There is a much more fundamental difference given by the fact that for $f \leq 2$ regular motion creates an impenetrable barrier for chaotic motion. This is due to the fact that regular motion takes place on 1D lines inside the 2D phase space. Hence, these lines separate their inside from their outside and no trajectories are allowed to cross them.

In 1964 Arnold was the first to proof that a specific system with $f = 2.5$, i. e. a system with two

degrees of freedom and an additional time-periodic external driving, exhibits a global instability [22]. He proved that orbits starting in the vicinity of an arbitrary torus are able to get arbitrarily close to any other torus in phase space [23] not matter how small the perturbation of the integrable system is. Later this web of pathways connecting the vicinities of all regular tori was called *Arnold web* and drew attention to it ever since [6, 16, 24–46].

In the first part of this thesis we introduce and discuss how the phase space can be visualized for higher dimensional systems. In order to set notations and introduce the reader to the concepts of a mixed phase space we give a brief introduction on 2D mappings in chapter 2 where the importance of the visualization of the whole phase space is obvious. Afterwards we introduce systems with more than two degrees of freedom and their classical description in chapter 3. This introduction will be accompanied by the theoretical basics necessary for the understanding of higher dimensional systems as well as by numerical methods, including the determination of the frequencies of the regular motion which are fundamentally important to the above KAM theorem. After introducing the basics we furthermore present three example systems which are chosen such that their classical phase space ranges from clean and simple to generic. These example systems are analyzed and we present several possibilities of their visualization trying to follow the case of 2D maps as closely as possible.

Quantum mechanically a first and very important observation is that the different types of classical dynamics entail different types of eigenstates, namely regular and chaotic states. This was found by Percival in 1973 when he was investigating quantum mechanical energy levels of mixed systems [47]. However, the real picture is more complicated than the classification of eigenstates into regular and chaotic states. The full picture depends on the properties of the system and on the scale up to which quantum mechanics can resolve classical phase space structures. In chapter 4 we therefore study the eigenstates of the example systems introduced in chapter 3 in order to see if and how they obey the classification into regular and chaotic eigenstates.

Apart from this classification of eigenstates the crucial difference between systems with $f \leq 2$ and $f > 2$, the existence of the Arnold web, raises the urgent question whether this difference is also visible in quantum mechanics. The Arnold web and its influence on quantum mechanics has already been the subject of several investigations [48–53], including works on nonlinear Schrödinger equations [54, 55]. In this thesis we want to approach this fundamental question from two different starting points. First we search for eigenstates which are supported on the main chaotic sea and on the tiny stochastic layers at the same time. Then we consider the time evolution of quantum mechanical wave packets started in the chaotic domain. We demonstrate how the wave packets enter into the Arnold web and look at the scaling of the penetration in the semiclassical limit.

While the slow Arnold diffusion is a classical phenomenon with consequences on quantum mechanics, there are other classically forbidden transport processes which only occur quantum mechanically. The commonly known example is the tunneling process in systems with one degree of freedom, where two regions in position space are divided by a potential barrier. This barrier creates two classically independent regions in phase space which are quantum mechanically connected by tunneling. A more general class of tunneling phenomena called *dynamical tunneling* was introduced by Davis and

Heller [56] in 1981. They study couplings between different regions in the phase space for molecules where there are no simple potential barriers, yet different disconnected regions in phase space exist. Quantum mechanically these regions are coupled by tunneling processes, for example between different regular domains or between regular and chaotic regions.

The fact that the majority of physical systems has a mixed phase space makes dynamical tunneling of particular importance. Prominent examples cover classically forbidden processes in atoms and molecules [56–64], optical or microwave resonators [65–69], and mesoscopic systems [11, 70]. A key property to the understanding of the coupling between different phase-space regions are the dynamical tunneling rates γ . They describe the quantum decay of an initial state placed in one particular phase-space region into another classically disconnected domain. These rates have been the subject of various investigations for systems with $f \leq 2$, e. g. 2D maps [71–79], billiards systems [68, 76], measurements on optical or microwave cavities [67, 80–82], or transport processes in 2D electron systems [11, 70].

In chapter 4 we present numerically determined tunneling rates for the model systems introduced in chapter 3. Furthermore, we extend the fictitious-integrable-system approach [78], which was introduced for systems with $f \leq 2$ [81, 82], to higher dimensional systems. This approach allows to predict tunneling rates which are caused by direct couplings between the regular and chaotic regions. The resulting prediction of the numerical rates are in very good agreement.

However, the direct coupling described by the fictitious integrable system approach is not the only important coupling mechanism between different regions in phase space. The coupling might be significantly enhanced by very effective transitions via intermediate states. A very important non-direct coupling mechanism relevant for regular-to-regular and regular-to-chaotic tunneling processes is linked to classical nonlinear resonances in phase space. These resonances induce very effective couplings between certain regular states and the corresponding effects are called *resonance-assisted tunneling* (RAT) by Brodier, Schlagheck, and Ullmo [83, 84]. Due to the ubiquity of nonlinear resonances in generic systems this type of tunneling coupling is very important. Also for our model systems resonance-assisted tunneling is relevant. In chapter 4 we numerically determine tunneling rates, present a first application of the theory of resonance assisted tunneling to higher dimensions and thereby obtain a qualitative understanding of the tunneling rates.

2. 2D mappings

Understanding the interplay between regular and chaotic dynamics in classical systems is a very challenging and interesting subject. This subject is most naturally accompanied by the likewise challenging and interesting question of how quantum mechanical systems are effected by this classical interplay. All this is addressed in this thesis for systems with more than two degrees of freedom. However, some of the properties are present in lower dimensional systems. In order to give an introduction into the necessary fundamentals we would like to start with a discussion based on systems with one and a half degrees of freedom – a notation which will be explained also on the following pages.

2.1. Hamiltonian systems with 1.5 degrees of freedom

The simplest class of dynamical systems in classical mechanics is given by systems with one degree of freedom. This means that the phase space of the system is spanned by just one position q and one momentum p . The corresponding Hamiltonian function $H(p, q)$ governs the dynamics according to Hamilton's equation of motion

$$\begin{aligned}\dot{p}(t) &= -\frac{\partial H}{\partial q}(p(t), q(t)) \\ \dot{q}(t) &= \frac{\partial H}{\partial p}(p(t), q(t))\end{aligned}\tag{2.1}$$

and does not explicitly depend on time. For such systems the value of the Hamiltonian is always a conserved quantity for every solution of equation (2.1). This implies that such systems exhibit integrable motion, i.e. there are as many conserved quantities as degrees of freedom [85].

In order to introduce the possibility of chaotic dynamics it is necessary to destroy the conserved quantity given by the Hamiltonian. This is achieved by adding an explicit time dependence to H which is often called an *external driving* of the system. It is now necessary to describe the system in an extended phase space spanned by q , p , and the time t . While strictly speaking the system still has one degree of freedom this setup is said to have one and a half degrees of freedom ($f = 1.5$) as the relevant phase space has three dimensions.

Among all possible time dependencies one of the most important ones is the periodic driving [6, page 275]. This form of the driving has the advantage that the solution of equation (2.1) can be reduced to integer multiples of the external driving period which we set to unity in this thesis. This choice $t_n = t_0 + n$ reduces the continuous solution of the equations of motion to a mapping \mathcal{P} connecting

the values of position and momentum at time t_n to their values at time t_{n+1} according to

$$\begin{pmatrix} p_n \\ q_n \end{pmatrix} \mapsto \mathcal{P} \begin{pmatrix} p_n \\ q_n \end{pmatrix} = \begin{pmatrix} p_{n+1} \\ q_{n+1} \end{pmatrix} \quad (2.2)$$

where \mathcal{P} is given by the solution of equation (2.1) over one period of the driving.

In order to ease the calculation of such a mapping, a common choice for the time dependence is given by so-called *kicked systems* exhibiting most of the generic features of Hamiltonian systems. There the Hamiltonian function has the special form

$$H(p, q, t) = T(p) + V(q) \sum_{n \in \mathbb{Z}} \delta(t - n). \quad (2.3)$$

In other words H is separated in a kinetic energy T depending on the momentum and a potential energy V depending on the position only. Furthermore, the latter potential is switched on periodically by a Dirac-comb given by an infinite sum of δ functions. For such systems the mapping from equation (2.2) can be given explicitly. If the phase space variables are considered at times after the kicks $t_n = t_0 + n$ in the limit $t_0 \rightarrow 0$, then the mapping reads

$$\begin{pmatrix} p_{n+1} \\ q_{n+1} \end{pmatrix} = \mathcal{P} \begin{pmatrix} p_n \\ q_n \end{pmatrix} = \begin{pmatrix} p_n - \frac{dV}{dq}(q_{n+1}) \\ q_n + \frac{dT}{dp}(p_n) \end{pmatrix}. \quad (2.4)$$

This reduction is called a *stroboscopic Poincaré* section. The choice of T and V now determine the mapping completely. In order to introduce various definitions and concepts needed in the description of Hamiltonian systems, we use a concrete model in the next section.

2.2. The 2D standard map

One of the most prominent choices for the potential and kinetic energy in the kicked Hamiltonian from equation (2.3) is the standard map. It is given by

$$H(p, q, t) = \frac{p^2}{2} + \frac{K}{4\pi^2} \cos(2\pi q) \sum_{n \in \mathbb{Z}} \delta(t - n), \quad (2.5)$$

such that the resulting mapping according to equation (2.4) reads

$$\begin{aligned} p_{n+1} &= p_n + \frac{K}{2\pi} \sin(2\pi(q_n + p_n)) \\ q_{n+1} &= q_n + p_n, \end{aligned} \quad (2.6)$$

see references [86, page 122f.] and [6, page 310]. The form of the functional dependence on the phase space variables p and q allows us to introduce periodic boundary conditions such that we arrive at

$$\begin{aligned} p_{n+1} &= p_n + \frac{K}{2\pi} \sin(2\pi(q_n + p_n)) + 1/2 \pmod{1} - 1/2 \\ q_{n+1} &= q_n + p_n \pmod{1}. \end{aligned} \quad (2.7)$$

The modulo on the momentum is chosen such that $p \in [-1/2, 1/2)$. The position covers the range $q \in [0, 1)$.

Depending on the parameter K the standard map yields different phase-space portraits. They can be visualized by plotting the iterates of the mapping in a (p, q) coordinate system. This is done in figure 2.1. Starting with $K = 0$ in figure 2.1(a) the Hamiltonian is independent of q and hence the momentum is a conserved quantity for all initial conditions. We find integrable motion and (q, p) are

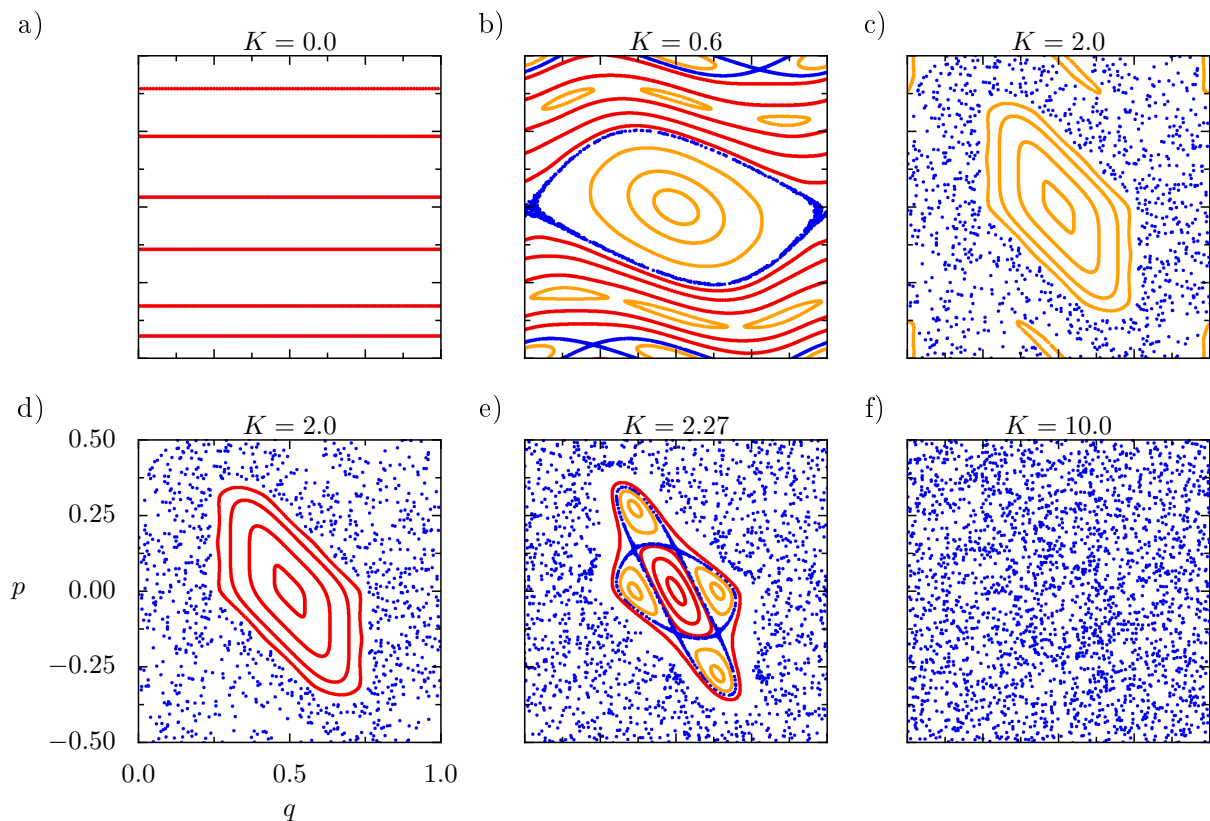


Figure 2.1.: Phase-space portraits of the 2D standard map for several values of the parameter K . In the upper panel regular tori of the standard map are shown in red and resonantly broken tori are shown in orange. In the lower panel regular orbits of the main island are shown in red and resonantly broken tori therein are shown in orange. Chaotic orbits are shown in blue. In figure (a) the integrable case $K = 0$ is depicted. Figure (b) corresponds to $K = 0.6$. Some tori are broken up. Further increasing the parameter to $K = 2$ leads to the resonance being surrounded by a large chaotic sea in figure (c). In the lower panel this island can be seen as a near-integrable system on its own, see figure (d). Increasing K further introduces resonantly broken tori into it, as can be seen in figure (e). Further increasing K leaves no visible islands anymore, figure (f).

action–angle variables. This is also reflected in the mapping where $p_{n+1} = p_n$. Hence, for every initial condition the motion takes place on a 1D curve given by a straight line at constant p . The position q changes with frequency $\omega = \frac{\partial H}{\partial p} = p$ independently of q . As the positional parameter on this 1D curve is periodic, the parameter is called an *angle* and the 1D curve is referred to as a 1D *torus*. Note that the frequency is chosen such that it covers the range $\omega \in [0, 1)$ rather than $[0, 2\pi)$.

Until the middle of the 20th century it was an open question what would happen to these tori if the system undergoes a small perturbation. The Kolmogorov–Arnold–Moser theorem [1–3], or KAM theorem for short, first formulated in 1954, addresses exactly this question. If K is increased slightly from zero, the KAM theorem guarantees that the majority of the tori survive the perturbation. The criterion whether a torus survives is based on the frequency ω with which the angle proceeds along the torus. If it is sufficiently far away from any rational number, then the torus will stay topologically the same but only get slightly deformed by a small perturbation. This can be seen in figure 2.1(b) where the red lines are still 1D curves spanning the whole q range of the phase space from the left to the right.

The tori which break up change their topology. They no longer traverse the whole q range but break up into chains of elliptical resonance zones. This is guaranteed by the Poincaré–Birkhoff theorem [87]. These zones are shown in orange in figure 2.1(b). Within them reside periodic orbits of period r which originate from a torus with a rational frequency $\omega = s/r$. Such rational frequencies are said to fulfill a *resonance condition* of the form

$$r \cdot \omega = s, \tag{2.8}$$

where the choice of $\omega \in [0, 1)$ and the period of the driving being unity has been used. The corresponding regions in phase space shown in orange are called *nonlinear resonances*.

The central periodic orbit is called *elliptic*, because orbits in its neighborhood are confined to ellipses [88]. In between these nonlinear resonances we find hyperbolic fixed points [88], e.g. $(q, p) = (0, 0)$ in figure 2.1(b), where nearby orbits separate exponentially fast in time. Their dynamics are called chaotic.

Further increasing K leads to the resonance being surrounded by a large chaotic sea in figure 2.1(c). Beyond a critical value of $K \approx 0.97$ no tori of the original system are left [7]. Hence, no red orbits are shown in figure 2.1(c). However, the central island can be seen as a near-integrable system on its own. Therefore the regular orbits in figure 2.1(d) are shown in red to readopt the color code for regular motion of figure 2.1(a). Increasing K further introduces resonantly broken tori into it, as can be seen in figure 2.1(e). It is important to note that outside of the four orange islands there is again a regular torus marked in red. As a consequence the chaotic motion confined in the thin layer in between the nonlinear resonance is not connected to the outside chaotic sea. The red torus between the thin layer and the sea acts as a barrier for the dynamics. Further increasing K destroys also the main island in the center and leaves no visible regular regions.

Figure 2.1 shows a scenario of increasing chaoticity and self-similarity in phase space. This is not only visible in 2D maps of periodically driven systems with one and a half degree of freedom.

Also autonomous systems with two degrees of freedom can be reduced to 2D maps employing the conservation of energy, see appendix G for an example. Furthermore, the cascade of tori breaking up into stable and unstable periodic orbits is also observed for higher dimensional systems. There a greater variety of effects is possible due to the increased number of degrees of freedom. This will be covered in the next chapter accompanied by necessary definitions and examples.

3. Classical dynamics of higher dimensional systems

The introduction presenting the 2D standard map in section 2.2 emphasized clearly that a visualization of a system's phase space is a great help in understanding it. This is feasible and very common for systems with up to two degrees of freedom [6, 7, 10, 82]. However, this complete visualization is only possible for 2D mappings and systems which can be reduced to such mappings. As already mentioned these systems are special in the sense that regular tori divide the classical phase space as absolute barriers. This is fundamentally different in higher dimensional systems with more than two degrees of freedom. The smallest number of dimensions necessary to see this, is given by 4D mappings. Systems with two and a half as well as systems with three degrees of freedom can be reduced to such mappings. In these systems the motion takes place inside a 4D phase space or on a 5D energy shell. The dimensionality of the tori of regular motion is given by the number of degrees of freedom, two or three, respectively. In both cases the regular tori are of codimension two and hence are missing two directions compared to the full phase space. Therefore they are no longer barriers to chaotic motion [6, 89].

The fact that chaotic motion is no longer bounded makes higher dimensional systems fundamentally different from the example of chapter 2. In 1964 Arnold was the first to provide a proof for an example system which shows this unboundedness of chaotic orbits [22]. The main difference to 2D maps is that the perturbation strength does not need to be above a certain critical threshold in order to have chaotic motion with arbitrarily large values of the position and momenta [6, 7]. Later the term *Arnold web* was introduced in order to describe the very complicated structures in phase space along which the chaotic motion takes place [89].

For systems with more than two degrees of freedom the very fertile approach of visualizing the whole phase space is not possible. Therefore usually projections of orbits are used [12, 14, 90] in order to obtain an impression of the phase space. Besides this also sections through the phase space of 4D maps are possible [91, 92].

In this chapter we introduce 4D mappings and their classical phase space. Thereby our aim is to provide insights which follow the enormously helpful pictures from the 2D mappings in figure 2.1 as closely as possible. In order to do so we first present approaches and tools from the literature. As this literature is mostly concerned with near-integrable systems we first concentrate on such systems in section 3.1 and introduce the analytical insight known for them in section 3.2. In section 3.3 we present common tools to gain understanding of classical phase-space structures. Contrary to the direct visualizations of orbits they are of more indirect nature. These methods can be divided into two

classes. One is the usage of initially nearby orbits which leads to Lyapunov-exponent type quantities. The other one regards classical orbits as time series and analyzes them by determining important frequencies contained in the signal.

In section 3.4 we introduce 4D systems which are no longer near-integrable but yield *mixed-type dynamics*. By this we mean systems with a regular island embedded in a large chaotic sea just like the 2D standard map in figure 2.1(e). For these systems we introduce various phase-space sections and projections in order to provide insight into their phase spaces on a level as close as possible to the insight figure 2.1 provided for the 2D standard map.

3.1. Coupled standard maps as paradigmatic example

In order to introduce notations and algorithms in the following sections, we will use coupled standard maps as our favorite example. This system is widely used for the analysis of higher dimensional systems. It was introduced by Froeschlé and Scheidecker [93] who adjudge it to Arnold. The model we use here is given by two standard maps coupled with a sine term according to

$$\begin{aligned}
 p'_1 &= p_1 + \frac{K_1}{2\pi} \sin(2\pi q'_1) + \frac{\xi_{12}}{2\pi} \sin(2\pi(q'_1 + q'_2)) + 1/2 \pmod{1 - 1/2} \\
 p'_2 &= p_2 + \frac{K_2}{2\pi} \sin(2\pi q'_2) + \frac{\xi_{12}}{2\pi} \sin(2\pi(q'_1 + q'_2)) + 1/2 \pmod{1 - 1/2} \\
 q'_1 &= q_1 + p_1 \pmod{1} \\
 q'_2 &= q_2 + p_2 \pmod{1}.
 \end{aligned} \tag{3.1}$$

The phase space is spanned by two momentum variables p_1, p_2 and two position variables q_1, q_2 . The positions q_j are restricted to $[0, 1)$ via the modulus operation. The momenta are restricted to $[-1/2, 1/2)$ such that the whole phase space has a volume of $V_{\text{phase space}} = 1$. This choice also implies that the used quantities are dimensionless. A real physical system governed by equation (3.1) would yield a certain area in position and momentum space. The physical momenta and positions then must be changed such that the rescaled phase-space volume equals one. In the above model the parameter ξ_{12} controls the coupling between the degrees of freedom. For $K_1 = K_2 = \xi_{12} = 0$ the coordinates p_j, q_j form action–angle variables for the integrable dynamics.

This system was already investigated by Froeschlé and Scheidecker [93, 94] with respect to the eigenvalues of the tangent mapping and in reference [26] in order to determine the number of so-called *isolating integrals of motion*. These are integrals of motion whose corresponding manifolds of constant value do not lie pathologically dense [95, page 1298]. Reference [26] thereby confirms the so-called Froeschlé conjecture [96] that in an f -degrees-of-freedom system there are either zero or f isolating integrals of motion. This covers conserved quantities which are given by observables over the whole phase space. It therefore does not contradict the existence of tori of dimension less than f [97–100]. Other investigations of equation (3.1) cover the sticking of chaotic orbits at resonantly broken tori and the corresponding diffusion processes [35, 37, 101].

Stability of fixed points in 4D maps Just like the 2D standard map the coupled standard maps also yield fixed points and periodic orbits. A main part of understanding from classical phase-space structures emerges from the analysis of these periodic points and their different behavior under parameter changes [87]. A characteristic feature of periodic orbits \mathbf{u}_p of period p is their stability making a statement about the behavior of orbits started in the vicinity of \mathbf{u}_p . It is important to remark that this Lyapunov-stability coincides with the so called *spectral stability* in almost every case [85, 102]. The latter is determined by the linearization $D\mathcal{P}^p$ of the p -fold map according to the position of the eigenvalues in \mathbb{C}^{2f} . In 2D maps it is possible to reduce this information to one real quantity which is given by the trace $t = \text{tr}\{D\mathcal{P}^p\}$. It allows to determine which of the possible stabilities of elliptic, parabolic, or hyperbolic behavior is present depending on the value the trace being $|t| < 2$, $t = 2$, or $|t| > 2$, respectively.

A similar criterion can be given for symplectic maps of arbitrary dimension $2f$. The different stability cases can be described by solving the reduced characteristic polynomial of the linearized mapping [89]. This links the quantities $\text{tr}\{D\mathcal{P}^p\}$, $\text{tr}\{(D\mathcal{P}^p)^2\}$, \dots , $\text{tr}\{(D\mathcal{P}^p)^f\}$ to the eigenvalues. It was done for continuous Hamiltonian systems [103] and for symplectic mappings [102]. Due to the larger number of eigenvalues more different kinds of stability of periodic points are possible. For 4D maps they are *elliptic–elliptic* (EE), *elliptic–hyperbolic* (EH), *hyperbolic–hyperbolic* (HH), and *complex unstable* (CU). Furthermore, the hyperbolic cases can be divided into hyperbolic and *inverse hyperbolic* like in 2D maps. At the edges of regions of different stability periodic orbits might bifurcate under changes of the map parameters and change from one stability type to another one. The crossing into the CU domain is called Krein collision, see [102]. Besides this, all bifurcations from 2D maps like tangent bifurcations and period-doublings may also occur. The quantities used to discriminate between the different kinds of stability are shown in figure 3.1.

One reason for the importance of periodic orbits is that their presence structures the classical phase space. This is due to the fact that periodic orbits are equipped with invariant manifolds. These manifolds are able to dominate the phase space for example by introducing barriers or partial barriers to chaotic motion [21].

Center manifolds of elliptic degrees of freedom An important difference between 4D and 2D maps is the presence of center manifolds. In general all eigenvectors of the linearized mapping $D\mathcal{P}$ can be used to construct 1D lines or higher dimensional planes through the phase space which are invariant under the linearized dynamics. In 2D maps this is used to construct the invariant stable and unstable manifold of hyperbolic fixed points [85]. The two eigenvectors belonging to an elliptic fixed point are complex conjugated to one another. If their real and the imaginary part is used, then they also span a 2D plane which is invariant under the linearized dynamics. In 2D maps this plane is the phase space itself and therefore not much information is contained in these eigenvectors.

In 4D maps the two complex conjugated eigenvectors of each degree of freedom can be used to construct a 2D plane in phase space. This plane is tangential to an invariant manifold, called the *center manifold*. While for purely hyperbolic fixed points the theorem of Hartman–Grobman assures that the

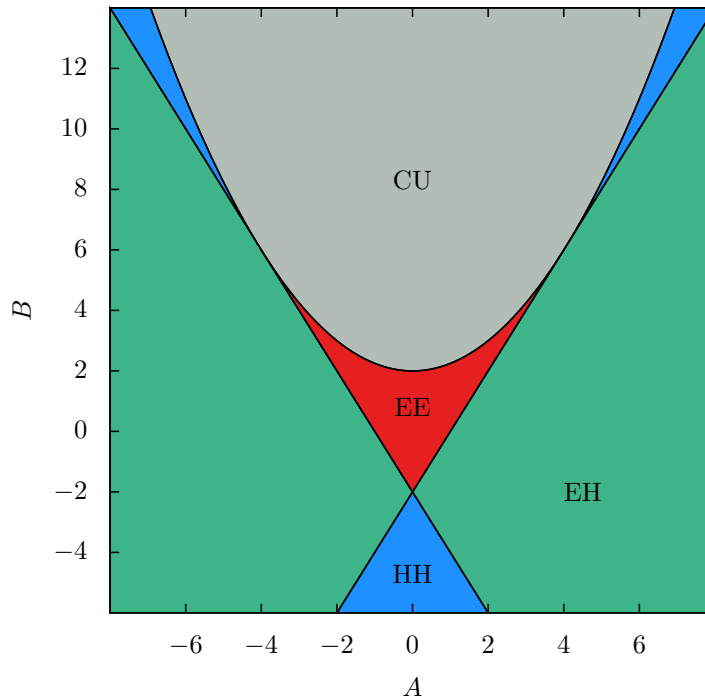


Figure 3.1.: Stability ranges of fixed points expressed by the coefficients A and B of the characteristic polynomial of $D\mathcal{P}$, namely $A = \text{tr}\{D\mathcal{P}\}$ and $2B = (\text{tr}\{D\mathcal{P}\})^2 - \text{tr}\{(D\mathcal{P})^2\}$. Different stabilities are reflected by different colors. This diagram is based on the work of Howard and MacKay [102].

linearized dynamics is topologically conjugated to the full system this is not true for elliptic degrees of freedom. However, the motion belonging to the elliptic degrees of freedom can be separated from the hyperbolic ones and reduces to a lower dimensional system [104, page 94]. This restriction to a lower dimensional manifold which is invariant under the dynamics can be carried out numerically [105]. It is done using a polynomial expansion of the invariant center manifold and yields a 2D mapping thereon. For EE-type fixed points there are two 2D center manifolds intersecting each other at the fixed point. For EH-type fixed points the stable and unstable manifolds of the hyperbolic degree of freedom attach a stable and an unstable manifold to the center manifold. These objects are three-dimensional and can therefore be responsible for trapping mechanisms in 4D mappings. In general such *normally hyperbolic invariant manifolds* (NHIMs) can be used to calculate reaction rates of classical as well as quantum systems [21, 106]. The 2D planes which are invariant under the dynamics are used later to choose suitable sections through the 4D phase space in order to visualize the phase space in the vicinity of periodic orbits in section 3.3.3.

Having introduced the very general notations of stability and center manifolds we start the analysis of 4D mappings by reviewing properties known for higher dimensional systems and numerical tools used in the literature. For this purpose coupled standard maps are very suitable. Due to their parameters they allow to examine systems which are close to integrable (small K_i , ξ_{12}) or which yield a predominantly regular region close to the center of phase space embedded in a large region of chaotic motion, so-called mixed systems ($1.5 \lesssim K_i \leq 4$ and $\xi_{12} \lesssim 1$). As the majority of the literature deals with the near-integrable case we will concentrate on this first.

3.2. Near-integrable systems

A great part of the understanding of mixed systems originates from near-integrable systems. The starting point are action–angle coordinates given by $I_1, I_2, \dots, I_f, \theta_1, \theta_2, \dots, \theta_f$ and a Hamiltonian H_{reg} depending nonlinearly on the actions only

$$H_{\text{reg}}(\mathbf{I}) \quad \text{with} \quad \det \left(\frac{\partial^2 H_{\text{reg}}}{\partial I_i \partial I_j} \right) \neq 0. \quad (3.2)$$

Usually the actions are defined as positive real numbers and the angles are periodic over the interval $[0, 2\pi)$ [89]. The solution of Hamilton’s equations of motion are

$$I_j(t) = I_j(0) \quad (3.3)$$

$$\theta_j(t) = \frac{\partial H_{\text{reg}}}{\partial I_j}(\mathbf{I}(0)) \cdot t + \theta_j(0) =: \omega_j(\mathbf{I}) \cdot t + \theta_j(0) \quad (3.4)$$

in which the angles are evolving linearly in time with the frequencies ω_j given by the first derivative of the Hamiltonian. This system is now perturbed by adding a further contribution to the Hamiltonian which is assumed to be very small. Its smallness is then used to provide several approximations of the perturbed system in terms of properties of the unperturbed one. Among possible methods are classical perturbation theory or – if the Hamiltonian is of a special form – the calculation of adiabatic invariants [89]. The latter will be especially helpful when describing the vicinity of nonlinear resonances in section 3.2.2. Besides an analytical treatment it is also possible and necessary to use numerical tools for an analysis of the classical phase space. In this section we will introduce the analytical description and numerical tools available in the literature.

3.2.1. Analytical description of multidimensional, near-integrable systems

Starting from an integrable Hamiltonian in action–angle coordinates which we will call H_{reg} we add a perturbation to it which makes it non-integrable. We assume that this perturbation is periodic in time with period $2\pi/\Omega$ and periodic in the angles such that it can be written as a Fourier series

$$H_\varepsilon(\mathbf{I}, \boldsymbol{\theta}, t) = H_{\text{reg}}(\mathbf{I}) + \varepsilon V(\mathbf{I}, \boldsymbol{\theta}, t) = H_{\text{reg}}(\mathbf{I}) + \varepsilon \sum_{\mathbf{m}, n} V^{\mathbf{m}, n}(\mathbf{I}) e^{i(\mathbf{m}\boldsymbol{\theta} - n\Omega t)}. \quad (3.5)$$

The KAM theorem ensures that tori of the unperturbed system will survive the perturbation and just get deformed if their frequency (3.4) is sufficiently irrational. This is the case if the frequency vector $\boldsymbol{\omega}$ is Diophantine which means it must fulfill

$$|\mathbf{m}\boldsymbol{\omega} - n\Omega| > \frac{\mathcal{K}(\boldsymbol{\omega}, \Omega)}{(\|\mathbf{m}\|_1 + |n|)^{f+2}} \quad \forall n \in \mathbb{Z}, \mathbf{m} \in \mathbb{Z}^f \quad \text{with} \quad \|\mathbf{m}\|_1 + |n| \neq 0 \quad (3.6)$$

where we used the norm $\|\mathbf{m}\|_1 := \sum_j |m_j|$ and introduced the function \mathcal{K} . The latter is independent of \mathbf{m} and n [4, page 266]. Its concrete shape is not of importance here. Apart from this there are

regions in phase space where this relation is violated and it is not guaranteed for the associated tori to survive. They rather change their topology completely. In the following we will concentrate on such tori starting with a vector of actions \mathbf{I}_{res} for which the frequencies of the unperturbed system

$$\boldsymbol{\omega}_{\text{res}} := \boldsymbol{\omega}(\mathbf{I}_{\text{res}}) = \partial H_{\text{reg}} / \partial \mathbf{I}(\mathbf{I}_{\text{res}}) \quad (3.7)$$

fulfill k resonance conditions with the external frequency Ω

$$\mathbf{r}^i \boldsymbol{\omega}_{\text{res}} - s^i \Omega = 0, \quad i = 1, \dots, k \quad (3.8)$$

where again $s^i \in \mathbb{Z}$ and the vector $\mathbf{r}^i \in \mathbb{Z}^f$. In the following introduction we keep Ω and f arbitrary. Afterwards we consider $f = 2$ and $T = 1$ for describing 4D mappings. This leads to an external driving frequency of $\Omega = 2\pi$.

Resonance structures in 4D maps While for 2D maps the Poincaré–Birkhoff theorem tells what happens to tori which fulfill a resonance condition [87] there is no direct generalization of this theorem to more degrees of freedom. Nevertheless, one differentiates four types of phase-space structures for 4D maps [100, 107]. Starting from a completely integrable Hamiltonian the winding number $\boldsymbol{\omega}(\mathbf{I})$ of a torus given by initial conditions $(\mathbf{I}, \boldsymbol{\varphi})$ can fall into one of the four cases shown in figure 3.2. The first row gives the name of the different classifications. The second row represents the resonance

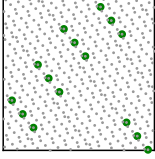
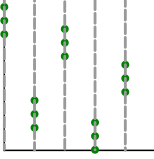
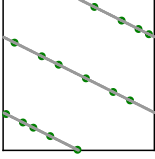
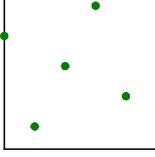
	(i)	(ii)	(iii)	(iv)
classification	non-resonant $k = 0$	single-uncoupled resonance $k = 1$	single-coupled resonance $k = 1$	double resonance $k = 2$
resonance condition $\mathbf{r}\boldsymbol{\omega} = s\Omega$	none	one with $\mathbf{r} = (r, 0)^T$ or $\mathbf{r} = (0, r)^T$	one with $\mathbf{r} = (r_1, r_2)^T$	two with $\mathbf{r}^1 \nparallel \mathbf{r}^2$
an orbit on the 2D torus	 θ_2 θ_1	 θ_2 θ_1	 θ_2 θ_1	 θ_2 θ_1
result after perturbation	deformed torus if (3.6) fulfilled	2 times: r 1D lines filled densely	2 times: one 1D lines filled densely	has periodicity $p = \det(\mathbf{r}^1 \mathbf{r}^2) $ 4 periodic orbits

Figure 3.2.: Overview of resonance structures in 4D maps based on [107]. In the row of resonance conditions the quantities are $\mathbf{r} \in \mathbb{Z}^2$, $s \in \mathbb{Z}$ such that r_x, r_y, s are coprime. In columns (ii) and (iii) there exists only one such (\mathbf{r}, s) apart from a multiplication with -1 . The last row illustrates which structures might appear in phase space.

conditions fulfilled on the torus. The third row shows symbolic pictures of the motion on this torus. The last row of this table gives an insight into what structures might be found in the 4D phase space of near-integrable maps. This is covered in section 3.2.2. The same objects will later re-occur for mixed systems within the regular region embedded in a large chaotic sea in section 3.4.

Column (i) addresses non-resonant tori. After switching on a small perturbation they will still be tori with the original topology according to the KAM theorem. These 2D objects are still densely traversed by orbits starting upon them.

In column (iv) the original torus fulfills two independent resonance conditions $\mathbf{r}^1, \mathbf{r}^2$. It follows from this that it also fulfills infinitely many resonance conditions given by all possible integer linear combinations $\boldsymbol{\rho} := \alpha\mathbf{r}^1 + \beta\mathbf{r}^2$ and $\sigma := \alpha s^1 + \beta s^2$

$$\boldsymbol{\rho}\boldsymbol{\omega}_{\text{res}} - \sigma\boldsymbol{\Omega} = 0. \quad (3.9)$$

This leads to the definition of the so-called *resonance module* [108]. It is the sublattice of \mathbb{Z}^f given by

$$\mathcal{L}(\boldsymbol{\omega}_{\text{res}}, \boldsymbol{\Omega}) := \left\{ \boldsymbol{\rho} \in \mathbb{Z}^f, \boldsymbol{\rho} \neq \mathbf{0} : \exists \sigma \in \mathbb{Z} \text{ such that } \boldsymbol{\rho}\boldsymbol{\omega}_{\text{res}} - \sigma\boldsymbol{\Omega} = \mathbf{0} \right\} \subset \mathbb{Z}^f \quad (3.10)$$

where in our case $f = 2$. The number of independent vectors in \mathcal{L} defines the *rank of the resonance*. The rank of the double resonant case is therefore two. It is the resonance with the largest possible rank for the case of 4D maps. All orbits starting on this torus are periodic. Therefore, column (iv) corresponds to resonant tori of 2D maps which are also given by a family of periodic orbits. The resonance module \mathcal{L} allows to define the order of the resonance. According to Meiss the order of the resonance is the $\|\cdot\|_1$ norm of the smallest nonzero vector in \mathcal{L} [108]

$$\text{ord}(\mathcal{L}) = \min_{\mathbf{r} \in \mathcal{L}} \{\|\mathbf{r}\|_1\}. \quad (3.11)$$

This generalizes the notion of the resonance order to higher than rank-1 resonances where it is just given by $\text{ord}(\mathcal{L}) = \|\mathbf{r}\|_1$.

Under a perturbation all what remains of a double resonant torus are four periodic orbits. Their period p is defined by \mathcal{L} in the following way. In order to calculate p it is necessary to take two “minimal” representatives $\mathbf{r}^1, \mathbf{r}^2$ from \mathcal{L} . By this we mean that these form a basis in \mathcal{L} as \mathbb{Z} -module space. In other words all elements in \mathcal{L} can be written as integer linear combinations of $\mathbf{r}^1, \mathbf{r}^2$. With these vectors we can write the period as

$$p = \left| \det \left(\mathbf{r}^1 \middle| \mathbf{r}^2 \right) \right|. \quad (3.12)$$

If instead of a basis of \mathcal{L} two arbitrary vectors $\alpha_1\mathbf{r}^1 + \beta_1\mathbf{r}^2, \alpha_2\mathbf{r}^1 + \beta_2\mathbf{r}^2$ are used, equation (3.12) would be larger by a factor $|\alpha_1\beta_2 - \alpha_2\beta_1|$. Later we will use this as a test whether the chosen set of resonance vectors is a suitable basis for \mathcal{L} . In this sense the above “minimal” means that the vectors of the basis span a parallelogram of minimal area. We will comment on a possibly insufficient choice in appendix C.

The remnants of a double-resonant torus after a perturbation will be detectable in phase space by a search for periodic orbits. The types of these periodic points are either [107]

one elliptic–elliptic (EE), one hyperbolic–hyperbolic (HH), and two elliptic–hyperbolic (EH) ones
or

two complex unstable (CU) and two elliptic–hyperbolic (EH) ones.

All other points of the unperturbed torus in (iv) change their topology. This is described in section 3.2.2 where the vicinity of such a torus is analyzed.

The vicinity of a torus which fulfills only a single resonance condition is different from the double-resonance case. Cases (ii) and (iii) address these types which do not occur in 2D maps. After a small perturbation both yield one elliptic object and one hyperbolic object. In (ii) these objects are given by r disjoint 1D lines each. In (iii) these objects are just one 1D line each. Although the torus does not survive the perturbation, it does not break into periodic points. Opposite to the double-resonant case these structures are not detectable by a search for periodic orbits. Depending on the resonance condition the fundamental object at the center of the resonance is either one or r 1D lines. If an orbit is started on them, then it will fill these 1D objects densely. Therefore, they can be found in the phase space by searching for 1D invariant objects or regular tori which degenerate to 1D curves [109].

3.2.2. Pendulum approximation

While the analysis of section 3.2.1 on resonance structures only tells something about a single torus, we would now like to concentrate on the vicinity of such a resonantly broken torus. This is done by introducing coordinates close to the resonant torus. The new action \mathbf{J} are chosen such that they express local deviation from the resonant torus. We first introduce a canonical transformation given by the generating function [6, 83]

$$F(\mathbf{J}, \boldsymbol{\theta}, t) = \mathbf{J}(\underline{\boldsymbol{\mu}}\boldsymbol{\theta} - \boldsymbol{\nu}\Omega t) + \mathbf{I}_{\text{res}}\boldsymbol{\theta} \quad (3.13)$$

with a $f \times f$ matrix $\underline{\boldsymbol{\mu}}$ and a vector $\boldsymbol{\nu} \in \mathbb{R}^f$ which have to be chosen appropriately later. From the generating function (3.13) the transformation and their inverse are

$$\begin{aligned} \boldsymbol{\psi} &= (\underline{\boldsymbol{\mu}}\boldsymbol{\theta} - \boldsymbol{\nu}\Omega t) & \boldsymbol{\theta} &= \underline{\boldsymbol{\mu}}^{-1}(\boldsymbol{\psi} + \boldsymbol{\nu}\Omega t) \\ \mathbf{I} &= \mathbf{J}\underline{\boldsymbol{\mu}} + \mathbf{I}_{\text{res}} & \mathbf{J} &= (\mathbf{I} - \mathbf{I}_{\text{res}})\underline{\boldsymbol{\mu}}^{-1}. \end{aligned} \quad (3.14)$$

The generating function (3.13) must be chosen such that the old angles θ_i in equation (3.14) are given by an integer linear combination of the new angles ψ_j in order to keep the periodicity of the Hamiltonian (3.5) intact. This is achieved by using an integer matrix $\mathbf{R} \in \mathbb{Z}^{f \times f}$ and setting

$$\underline{\boldsymbol{\mu}} = \frac{1}{r}\mathbf{R}^T \quad (3.15)$$

where we defined $r := \det(\mathbf{R})$. With equation (3.15) the inverse of $\underline{\boldsymbol{\mu}}$ in equation (3.14) becomes $\underline{\boldsymbol{\mu}}^{-1} = \text{adj}(\mathbf{R}^T) \in \mathbb{Z}^{f \times f}$.

With the transformation from equation (3.14) the new Hamiltonian reads

$$K_\varepsilon(\mathbf{J}, \boldsymbol{\psi}, t) = H_{\text{reg}}(\mathbf{I}_{\text{res}} + \mathbf{J}\underline{\boldsymbol{\mu}}) - \mathbf{J}\boldsymbol{\nu}\Omega + \varepsilon V_{\text{res}}(\mathbf{J}, \boldsymbol{\psi}, t). \quad (3.16)$$

Here the abbreviation for the potential in the new coordinates in the vicinity to the resonance has been introduced as

$$V_{\text{res}}(\mathbf{J}, \boldsymbol{\psi}, t) := V(\mathbf{I}_{\text{res}} + \mathbf{J}\underline{\boldsymbol{\mu}}, \underline{\boldsymbol{\mu}}^{-1}(\boldsymbol{\psi} + \boldsymbol{\nu}\Omega t), t) \quad (3.17)$$

$$= \sum_{\mathbf{m}, n} \underbrace{V^{\mathbf{m}, n}(\mathbf{I}_{\text{res}} + \mathbf{J}\underline{\boldsymbol{\mu}})}_{=: V_{\text{res}}^{\mathbf{m}, n}(\mathbf{J})} e^{i(\mathbf{m}\underline{\boldsymbol{\mu}}^{-1}\boldsymbol{\psi} - \Omega(n - \mathbf{m}\underline{\boldsymbol{\mu}}^{-1}\boldsymbol{\nu})t)}. \quad (3.18)$$

It is important to realize that we can choose $\underline{\boldsymbol{\mu}}$ and $\boldsymbol{\nu}$ such that the first k new angles evolve much more slowly than the remaining $f - k$ ones. We can then average over time and the fast degrees of freedom in order to obtain a Hamiltonian approximating the vicinity of the resonance. To see this difference in the time scales, the regular part H_{reg} is expanded up to second order in the new actions. With the matrix of second derivatives of H_{reg} ,

$$\mathcal{H}_{ij} = \frac{\partial^2 H_{\text{reg}}}{\partial I_i \partial I_j}(\mathbf{I}_{\text{res}}), \quad (3.19)$$

and the resonant frequency defined in equation (3.7) the Hamiltonian reads

$$K_\varepsilon(\mathbf{J}, \boldsymbol{\psi}, t) = H_{\text{reg}}(\mathbf{I}_{\text{res}}) + \mathbf{J}(\underline{\boldsymbol{\mu}}\boldsymbol{\omega}_{\text{res}} - \boldsymbol{\nu}\Omega) + \frac{1}{2}\mathbf{J}^T \underline{\boldsymbol{\mu}} \cdot \mathcal{H} \cdot \underline{\boldsymbol{\mu}}^T \mathbf{J} \\ + \varepsilon \sum_{\mathbf{m}, n} V_{\text{res}}^{\mathbf{m}, n}(\mathbf{J}) e^{i(\mathbf{m}\underline{\boldsymbol{\mu}}^{-1}\boldsymbol{\psi} - \Omega(n - \mathbf{m}\underline{\boldsymbol{\mu}}^{-1}\boldsymbol{\nu})t)}. \quad (3.20)$$

It yields the equation of motion for the angles

$$\dot{\psi}_i = \mu_{ij}\omega_{\text{res}j} - \nu_i\Omega + \mathcal{O}(\varepsilon, \mathbf{J}) \quad (3.21)$$

where $\mathcal{O}(\varepsilon, \mathbf{J})$ covers all terms of the order ε , J_k and higher.

For initial conditions close to the resonance $J_i = 0$ and small perturbation strengths ε this will give the separation of time scales provided $\underline{\boldsymbol{\mu}}$ and $\boldsymbol{\nu}$ are chosen appropriately. If there are k independent resonance conditions (3.8), then the matrix \mathbf{R} from equation (3.15) can be built up from integers in the following way. The first k rows are set to be the \mathbf{r}^i . The remaining rows must now be chosen such that $\det(\mathbf{R}) \neq 0$. We call these integer vectors $\mathbf{r}^{k+1} \dots \mathbf{r}^f$ and get

$$\mathbf{R} := \left(\mathbf{r}^1 \mid \dots \mid \mathbf{r}^k \mid \mathbf{r}^{k+1} \mid \dots \mid \mathbf{r}^f \right). \quad (3.22)$$

The additional \mathbf{r}^{k+1} to \mathbf{r}^f are chosen mutually perpendicular and perpendicular to the first $\mathbf{r}^1, \dots, \mathbf{r}^k$.

Furthermore, all \mathbf{r}^i must be chosen such that

$$r = \det(\underline{\mathbf{R}}) \rightarrow \min. \quad (3.23)$$

In order to achieve this, it might be necessary to use a possible freedom in the choice of the resonance vectors (3.8). The minimality of r corresponds to the one mentioned on page 17 for the period (3.12) for the case $k = f$. Equation (3.23) ensures that the first k columns of $\underline{\mathbf{R}}$ span the resonance module \mathcal{L} with integer coefficients, i. e.

$$\mathbf{m} \in \mathcal{L} \Rightarrow \exists! \mathbf{l} \in \mathbb{Z}^k : \mathbf{m} = \sum_{i=1}^k l_i \mathbf{r}^i. \quad (3.24)$$

The vector $\boldsymbol{\nu}$ is set to

$$\boldsymbol{\nu} = \begin{cases} s^i/r & i = 1, \dots, k \\ 0 & \text{else.} \end{cases} \quad (3.25)$$

From equation (3.21) it follows that

$$\dot{\psi}_i = \frac{1}{r} (\mathbf{r}^i \boldsymbol{\omega}_{\text{res}} - r \nu_i \Omega) + \mathcal{O}(\varepsilon, \mathbf{J}) \quad (3.26)$$

and therefore up to first order in ε and \mathbf{J}

$$\begin{aligned} \dot{\psi}_i &\approx 0 & \text{for } i = 1, \dots, k \\ \dot{\psi}_i &\approx \frac{1}{r} \mathbf{r}^i \boldsymbol{\omega}_{\text{res}} & \text{for } i = k+1, \dots, f \end{aligned} \quad (3.27)$$

such that the first k degrees of freedom are indeed slowly varying. The remaining $f - k$ degrees of freedom vary much faster because $\mathbf{r}^i \boldsymbol{\omega}_{\text{res}} \neq 0$. If this expression would be zero, the corresponding \mathbf{r}^i would fulfill a resonance condition with $s^i = 0$ and had to be put into the set of resonance vectors at the very beginning. The difference between fast and slow angles suggests to split the vector $\boldsymbol{\psi}$ into

$$\boldsymbol{\psi}_{\text{slow}} := (\psi_{\text{slow},1}, \dots, \psi_{\text{slow},k})^T := (\psi_1, \dots, \psi_k)^T \quad (3.28)$$

$$\boldsymbol{\psi}_{\text{fast}} := (\psi_{\text{fast},1}, \dots, \psi_{\text{fast},f-k})^T := (\psi_{k+1}, \dots, \psi_f)^T \quad (3.29)$$

which will simplify later notation by setting $V(\mathbf{J}, \boldsymbol{\psi}, t) \equiv V(\mathbf{J}, \boldsymbol{\psi}_{\text{slow}}, \boldsymbol{\psi}_{\text{fast}}, t)$.

Although we follow Chirikov [6] here, he uses a slightly different choice for the matrix $\underline{\boldsymbol{\mu}}$ and differentiates between two possibilities [6, p. 281]. He attributes the choice (3.22) to Ford although he does not explicitly state that the remaining rows might best be filled up with integers only. If $\boldsymbol{\omega}_{\text{res}}$ is not a linear combination of the first $\mathbf{r}^1, \dots, \mathbf{r}^k$, then Chirikov prefers the so-called *orthogonal metric*. This means that the $k+1$ -th row is set to a vector parallel to $\boldsymbol{\omega}_{\text{res}}$ and the remaining rows are just set perpendicular to $\boldsymbol{\omega}_{\text{res}}$ and all preceding \mathbf{r}^i . This choice is advantageous for the examination of Arnold diffusion. We will not use it here.

With the above choice (3.22) of $\underline{\mu}$ the Hamiltonian (3.16) can be further simplified by means of an adiabatic approximation which uses the separation of time scales. This is done analogously to references [84, 89] but extended to more than just one fast action [110]. The average is performed by using a close-to-identity canonical transformation generated by

$$G(\bar{\mathbf{J}}, \boldsymbol{\psi}, t) = \bar{\mathbf{J}}\boldsymbol{\psi} + \varepsilon G_1(\bar{\mathbf{J}}, \boldsymbol{\psi}, t) + \varepsilon^2 G_2(\bar{\mathbf{J}}, \boldsymbol{\psi}, t) + \dots \quad (3.30)$$

introducing new coordinates $\bar{\mathbf{J}}, \bar{\boldsymbol{\psi}}$. This yields the transformation up to first order in ε

$$\bar{\boldsymbol{\psi}} = \boldsymbol{\psi} + \varepsilon \frac{\partial G_1}{\partial \bar{\mathbf{J}}}(\bar{\mathbf{J}}, \boldsymbol{\psi}) + \mathcal{O}(\varepsilon^2) \quad \text{and} \quad \mathbf{J} = \bar{\mathbf{J}} + \varepsilon \frac{\partial G_1}{\partial \boldsymbol{\psi}}(\bar{\mathbf{J}}, \bar{\boldsymbol{\psi}}) + \mathcal{O}(\varepsilon^2) \quad (3.31)$$

together with the inverse

$$\boldsymbol{\psi} = \bar{\boldsymbol{\psi}} - \varepsilon \frac{\partial G_1}{\partial \bar{\mathbf{J}}}(\bar{\mathbf{J}}, \bar{\boldsymbol{\psi}}) + \mathcal{O}(\varepsilon^2) \quad \text{and} \quad \bar{\mathbf{J}} = \mathbf{J} - \varepsilon \frac{\partial G_1}{\partial \boldsymbol{\psi}}(\mathbf{J}, \boldsymbol{\psi}) + \mathcal{O}(\varepsilon^2). \quad (3.32)$$

Again with the matrix of second derivatives \mathcal{H} from equation (3.19) the quadratic approximation of equation (3.20) reads in the new coordinates

$$\begin{aligned} \bar{K}_\varepsilon(\bar{\mathbf{J}}, \bar{\boldsymbol{\psi}}, t) &= H_{\text{reg}}(\mathbf{I}_{\text{res}}) + \left(\bar{\mathbf{J}} + \varepsilon \frac{\partial G_1}{\partial \boldsymbol{\psi}}(\bar{\mathbf{J}}, \bar{\boldsymbol{\psi}}) \right) (\underline{\mu}\boldsymbol{\omega}_{\text{res}} - \boldsymbol{\nu}\Omega) \\ &\quad + \frac{1}{2} \left(\bar{\mathbf{J}} + \varepsilon \frac{\partial G_1}{\partial \boldsymbol{\psi}}(\bar{\mathbf{J}}, \bar{\boldsymbol{\psi}}) \right)^T \underline{\mu} \cdot \mathcal{H} \cdot \underline{\mu}^T \left(\bar{\mathbf{J}} + \varepsilon \frac{\partial G_1}{\partial \boldsymbol{\psi}}(\bar{\mathbf{J}}, \bar{\boldsymbol{\psi}}) \right) \\ &\quad + \varepsilon V_{\text{res}}(\bar{\mathbf{J}}, \bar{\boldsymbol{\psi}}, t) + \varepsilon \frac{\partial G_1}{\partial t}(\bar{\mathbf{J}}, \bar{\boldsymbol{\psi}}, t) + \mathcal{O}(\varepsilon^2, J^3) \end{aligned} \quad (3.33)$$

$$\begin{aligned} &= H_{\text{reg}}(\mathbf{I}_{\text{res}}) + \left(\bar{\mathbf{J}} + \varepsilon \frac{\partial G_1}{\partial \boldsymbol{\psi}}(\bar{\mathbf{J}}, \bar{\boldsymbol{\psi}}) \right) (\underline{\mu}\boldsymbol{\omega}_{\text{res}} - \boldsymbol{\nu}\Omega) + \frac{1}{2} \bar{\mathbf{J}}^T \underline{\mu} \cdot \mathcal{H} \cdot \underline{\mu}^T \bar{\mathbf{J}} \\ &\quad + \varepsilon V_{\text{res}}(\bar{\mathbf{J}}, \bar{\boldsymbol{\psi}}, t) + \varepsilon \frac{\partial G_1}{\partial t}(\bar{\mathbf{J}}, \bar{\boldsymbol{\psi}}, t) + \mathcal{O}(\varepsilon^2, \varepsilon J, J^3) \end{aligned} \quad (3.34)$$

where in the last step also terms of the order $\varepsilon \cdot \bar{\mathbf{J}}$ are neglected. On the contrary, terms of the order $\bar{\mathbf{J}}^2$ are taken into account. It is important to note that due to the choice of $\underline{\mu}$ and $\boldsymbol{\nu}$ the term

$$\bar{\mathbf{J}} (\underline{\mu}\boldsymbol{\omega}_{\text{res}} - \boldsymbol{\nu}\Omega) = \sum_{i=k+1}^f \sum_{j=1}^f \bar{J}_i \mu_{i,j} \omega_{\text{res},j} = \sum_{i=1}^{f-k} \bar{J}_{\text{fast},i} \frac{1}{r} \mathbf{r}^{k+i} \boldsymbol{\omega}_{\text{res}} \quad (3.35)$$

includes only $\mathbf{r}^{k+1} \dots \mathbf{r}^f$ and reduces to contributions by the fast actions $\bar{\mathbf{J}}_{\text{fast}}$. The same holds for

$$\varepsilon \frac{\partial G_1}{\partial \boldsymbol{\psi}}(\bar{\mathbf{J}}, \bar{\boldsymbol{\psi}}) (\underline{\mu}\boldsymbol{\omega}_{\text{res}} - \boldsymbol{\nu}\Omega) = \sum_{i=1}^{f-k} \varepsilon \frac{\partial G_1}{\partial \psi_{\text{fast},i}}(\bar{\mathbf{J}}, \bar{\boldsymbol{\psi}}) \frac{1}{r} \mathbf{r}^{k+i} \boldsymbol{\omega}_{\text{res}}. \quad (3.36)$$

The transformation G_1 has to be chosen such that the resulting Hamiltonian neither depends on the time t nor on the fast angles $\bar{\boldsymbol{\psi}}_{\text{fast}}$. In order to achieve this, a new potential is introduced. It is the old potential V_{res} averaged with respect to time over one period of the driving and with respect to

the fast angles specified in equation (3.27) over $[0, 2\pi)$. It reads

$$\langle V_{\text{res}} \rangle(\mathbf{J}, \boldsymbol{\psi}_{\text{slow}}) := \frac{1}{(2\pi)^{f-k} T} \int_0^T dt \int_0^{2\pi} d\psi_{\text{fast},1} \dots \int_0^{2\pi} d\psi_{\text{fast},f-k} V_{\text{res}}(\mathbf{J}, \boldsymbol{\psi}, t) \quad (3.37)$$

$$= \frac{1}{(2\pi)^{f-k} T} \sum_{\mathbf{m}, n} V_{\text{res}}^{\mathbf{m}, n}(\mathbf{J}) \int_0^T dt \int_0^{2\pi} d\psi_{k+1} \dots \int_0^{2\pi} d\psi_f e^{i(\mathbf{m}\underline{\boldsymbol{\mu}}^{-1}\boldsymbol{\psi} - \Omega(n - \mathbf{m}\underline{\boldsymbol{\mu}}^{-1}\boldsymbol{\nu})t)}. \quad (3.38)$$

The choice of this average guarantees that the new potential only depends on the slow angles and describes the phase space in the vicinity of the resonance most appropriately. With $\underline{\boldsymbol{\mu}}$ from equation (3.22) the averaged potential simplifies further as the integrals over the fast angles yield Kronecker symbols. At this point it is important that $\underline{\boldsymbol{\mu}}$ was chosen in equation (3.15) such that its inverse is an integer matrix. If we set this integer matrix $\underline{\mathbf{S}} := \underline{\boldsymbol{\mu}}^{-1}$, we obtain from the integrals over $\psi_{\text{fast},i}$

$$\frac{1}{(2\pi)^{f-k}} \int_0^{2\pi} d\psi_{k+1} \dots \int_0^{2\pi} d\psi_f e^{i\mathbf{m}\underline{\mathbf{S}}\boldsymbol{\psi}} = e^{i\mathbf{m}\underline{\mathbf{S}}\boldsymbol{\psi}_{\text{slow}}} \prod_{j=k+1}^f \delta_{\sum_i m_i s_{ij}, 0} = e^{i\mathbf{m}\underline{\mathbf{S}}\boldsymbol{\psi}_{\text{slow}}} \prod_{j=k+1}^f \delta_{(\underline{\mathbf{S}}^T \mathbf{m})_j, 0} \quad (3.39)$$

where in the product $\underline{\mathbf{S}}\boldsymbol{\psi}_{\text{slow}}$ the vector $\boldsymbol{\psi}_{\text{slow}}$ is thought to be filled up with zeros. Equation (3.39) tells that only those Fourier components \mathbf{m} contribute for which the $f-k$ last elements of the vector $\underline{\mathbf{S}}^T \mathbf{m}$ are all zero. This is fulfilled for all vectors of the resonance module \mathcal{L} due to the orthogonality of $\mathbf{r}^{k+1}, \dots, \mathbf{r}^f$ on \mathcal{L} . Furthermore, the right choice of the vectors in $\underline{\boldsymbol{\mu}}$, equation (3.23), asserts that all integer vectors $\mathbf{m} \in \mathbb{Z}^f$ fulfilling equation (3.39) are given by an integer linear combination of the first k columns of $\underline{\mathbf{R}}$. Therefore the sum over \mathbf{m} in the Fourier series can be expressed by a sum over the elements of \mathcal{L} using equation (3.24). With the abbreviation $\underline{\mathbf{R}}_{\text{slow}}$ for the first k columns of $\underline{\mathbf{R}}$ we can replace an arbitrary sum over the Fourier components according to

$$\sum_{\mathbf{m} \in \mathbb{Z}^f} f(\mathbf{m}) \prod_{j=k+1}^f \delta_{(\underline{\mathbf{S}}^T \mathbf{m})_j, 0} = \sum_{\mathbf{l}_{\text{slow}} \in \mathbb{Z}^k} f(\underline{\mathbf{R}}_{\text{slow}} \mathbf{l}_{\text{slow}}) \quad (3.40)$$

and obtain with

$$\mathbf{m}\underline{\boldsymbol{\mu}}^{-1}\boldsymbol{\nu} \equiv \mathbf{m}^T \underline{\boldsymbol{\mu}}^{-1}\boldsymbol{\nu} = (\text{adj}(\underline{\mathbf{R}})\mathbf{m})^T \boldsymbol{\nu} = r \boldsymbol{\nu}_{\text{slow}} \mathbf{l}_{\text{slow}} \quad (3.41)$$

for the averaged potential (3.25)

$$\langle V_{\text{res}} \rangle(\mathbf{J}, \boldsymbol{\psi}_{\text{slow}}) = \frac{1}{T} \sum_{\mathbf{l}_{\text{slow}} \in \mathbb{Z}^k} \sum_{n \in \mathbb{Z}} V_{\text{res}}^{\underline{\mathbf{R}}_{\text{slow}} \mathbf{l}_{\text{slow}}, n}(\mathbf{J}) e^{i(\underline{\mathbf{R}}_{\text{slow}} \mathbf{l}_{\text{slow}})^T \underline{\mathbf{S}} \boldsymbol{\psi}_{\text{slow}}} \int_0^T dt e^{-i(\Omega(n - \mathbf{s}_{\text{slow}} \mathbf{l}_{\text{slow}})t)} \quad (3.42)$$

$$= \sum_{\mathbf{l}_{\text{slow}} \in \mathbb{Z}^k} V_{\text{res}}^{\underline{\mathbf{R}}_{\text{slow}} \mathbf{l}_{\text{slow}}, \mathbf{s}_{\text{slow}} \mathbf{l}_{\text{slow}}}(\mathbf{J}) e^{i r \mathbf{l}_{\text{slow}} \boldsymbol{\psi}_{\text{slow}}}. \quad (3.43)$$

The generating function G is used to remove all fast degrees of freedom from the Hamiltonian (3.34).

In order to achieve this, the time dependent potential, the term $\frac{\partial G_1}{\partial t}$, and the expression (3.36) will be replaced by $\langle V_{\text{res}} \rangle$. In order to achieve this replacement, G_1 has to fulfill

$$\sum_{i=k+1}^f \left(\frac{\varepsilon}{r} \mathbf{r}^i \boldsymbol{\omega}_{\text{res}} \right) \frac{\partial G_1}{\partial \psi_i}(\bar{\mathbf{J}}, \bar{\boldsymbol{\psi}}, t) - \varepsilon \frac{\partial G_1}{\partial t}(\bar{\mathbf{J}}, \bar{\boldsymbol{\psi}}, t) = \varepsilon (\langle V_{\text{res}} \rangle(\mathbf{J}, \boldsymbol{\psi}_{\text{slow}}) - V_{\text{res}}(\bar{\mathbf{J}}, \bar{\boldsymbol{\psi}}, t)) \quad (3.44)$$

where equation (3.35) has been used in the sum at the right hand side. In order to get G_1 it is useful to expand it into a Fourier series. As the concrete shape of G_1 does not provide further insight, we omit it here.

After the averaging over time and the fast angles the Hamiltonian reads

$$\bar{K}_\varepsilon(\bar{\mathbf{J}}, \bar{\boldsymbol{\psi}}, t) = H_{\text{reg}}(\mathbf{I}_{\text{res}}) + \sum_{i=1}^{f-k} \bar{J}_{\text{fast},i} \frac{1}{r} \mathbf{r}^{k+i} \boldsymbol{\omega}_{\text{res}} + \frac{1}{2} \bar{\mathbf{J}}^T \underline{\boldsymbol{\mu}} \cdot \underline{\boldsymbol{\mathcal{H}}} \cdot \underline{\boldsymbol{\mu}}^T \bar{\mathbf{J}} + \varepsilon \langle V_{\text{res}} \rangle(\mathbf{J}, \boldsymbol{\psi}_{\text{slow}}) \quad (3.45)$$

$$\approx H_{\text{reg}}(\mathbf{I}_{\text{res}} + \mathbf{J} \underline{\boldsymbol{\mu}}) + \varepsilon \langle V_{\text{res}} \rangle(\mathbf{J}, \boldsymbol{\psi}_{\text{slow}}). \quad (3.46)$$

In case of just one resonance \mathbf{r}^1, s^1 the resonance approximation is given by

$$\bar{K}_\varepsilon(\bar{\mathbf{J}}, \bar{\boldsymbol{\psi}}, t) = H_{\text{reg}}(\mathbf{I}_{\text{res}} + \mathbf{J} \underline{\boldsymbol{\mu}}) + \varepsilon \sum_{\alpha \in \mathbb{Z} \setminus \{0\}} \tilde{V}_{\text{res}}^{\alpha \mathbf{r}^1, \alpha s^1}(\bar{\mathbf{J}}) \cdot \cos(r \alpha \psi_1) \quad (3.47)$$

which is exactly the expression known from 2D maps ($f = 1$) embedded in a higher dimensional phase space [6, page 282]. In the case of 4D maps there might also be two resonance conditions fulfilled. Then the phase space in the vicinity of the destroyed torus is described by

$$\bar{K}_\varepsilon(\bar{\mathbf{J}}, \bar{\boldsymbol{\psi}}, t) = H_{\text{reg}}(\mathbf{I}_{\text{res}} + \mathbf{J} \underline{\boldsymbol{\mu}}) + \varepsilon \sum_{\alpha, \beta \in \mathbb{Z} \setminus \{0\}} \tilde{V}_{\text{res}}^{\alpha \mathbf{r}^1 + \beta \mathbf{r}^2, \alpha s^1 + \beta s^2}(\bar{\mathbf{J}}) \cdot \cos r(\alpha \psi_1 + \beta \psi_2). \quad (3.48)$$

Although this Hamiltonian is time-independent, it is not integrable. This significantly complicates the description. Note that in equation (3.47) and equation (3.48) real Fourier coefficients have been introduced.

The last step is to transform the Hamiltonian (3.46) back to the original coordinates. Now we omit the time t from the transformation (3.14) and use

$$\bar{\boldsymbol{\psi}} = \underline{\boldsymbol{\mu}} \boldsymbol{\theta} \quad \bar{\mathbf{J}} = (\mathbf{I} - \mathbf{I}_{\text{res}}) \underline{\boldsymbol{\mu}}^{-1} \quad (3.49)$$

which yields the Hamiltonian

$$H(\mathbf{I}, \boldsymbol{\theta}) = H_{\text{reg}}(I) + \varepsilon \sum_{\boldsymbol{\alpha} \in \mathbb{Z}^k} V^{\alpha_1 \mathbf{r}^1 + \dots + \alpha_k \mathbf{r}^k, \alpha_1 s^1 + \dots + \alpha_k s^k}(\mathbf{I}) e^{i(\alpha_1 \mathbf{r}^1 + \dots + \alpha_k \mathbf{r}^k) \boldsymbol{\theta}} \quad (3.50)$$

approximating the vicinity of the resonance in phase space. The most important fact about this averaged Hamiltonian is that it does not depend on time and that only certain Fourier modes are present, namely the ones given by linear combinations of the resonance vectors $\mathbf{r}^1, \dots, \mathbf{r}^k$. Especially

for 4D mappings it is possible to derive a 2D Poincaré map for this conservative Hamiltonian in a straight forward manner. This is outlined in appendix G for an example choice of Fourier coefficients.

3.2.3. Normal forms

Another possibility to obtain Hamiltonians describing resonant motion is given by normal form analysis which is a very useful tool to gain insight into the phase-space structure of systems with more than two degrees of freedom. The different topologies of resonantly broken tori is presented in figure 3.2 on page 16. This difference is also visible from a normal form analysis by distinguishing resonant, single resonant, and double resonant normal forms [100, 107, 111–113]. Just like the above pendulum approximation also the normal forms of double resonant tori do not yield an integrable approximation for the vicinity of the resonance [107]. The use of normal forms is not covered in this thesis.

3.2.4. Arnold diffusion and Arnold web

In this work we consider systems for which the number of degrees of freedom is too high to let the regular tori separate different phase-space regions. Therefore, in these systems chaotic motion is not longer confined by regular tori. If these systems are near-integrable, then the majority of tori will still be existing due to the KAM theorem. As they are surrounded by resonantly broken tori and their stochastic layers [6], these thin regions of chaotic motion form an interconnected web of chaoticity. In 1964 Arnold was the first one to show by means of an example system that chaotic orbits will be able to slowly meander from the vicinity of an arbitrary torus into an arbitrary close vicinity of another torus [22, 23]. Therefore, this web is called *Arnold web*. The proof of its existence is based on several steps. First, he proves that the torus is a so-called whiskered torus. This is a torus which has stable and unstable manifold attached to it along which it is possible to get into the vicinity of another torus. Then such tori are used to built up transition chains connecting initial and final torus [23]. The literature distinguishes between the so-called *Arnold diffusion* and the *Arnold mechanism*. The latter term refers to the mechanism described by Arnold in terms of so-called whiskered tori and transition chains. This mechanism does not need to be a unique one [114]. The term Arnold diffusion more generally describes the global instability of near-integrable systems. As the latter takes place by means of a slow drift along resonances, it is called diffusion although the process itself is deterministic. Moreover, the term diffusion is slightly confusing as it is unclear whether the process can be modeled by a diffusion process with a diffusion coefficient D or if it is e.g. sub-diffusive due to trapping mechanisms.

The lowest dimensional case where Arnold diffusion is possible is given by periodically driven systems with two degrees of freedom or equivalently by autonomous system with three degrees of freedom as already mentioned on page 11. Both kinds of systems can be reduced to 4D maps by using either a stroboscopic Poincaré section or by an ordinary Poincaré section on the energy shell. Due to their dimensionality these $f = 2.5$ and $f = 3$ cases provide an Arnold web. However, in this case the web is special with respect to the diffusion as it will take place along a 1D direction [6, page 353] and – provided that it is a diffusion process – is describable using a scalar diffusion coefficient.

Higher dimensional problems with more than three degrees of freedom yield a diffusion tensor and various directions in which the Arnold diffusion proceeds. Following Chirikov we will call these regions *stochastic layers*. The notion of stochasticity raises from the fact that the orbits seem to perform a stochastic process although the dynamics are completely deterministic of course. The narrowness of these regions in near-integrable systems gives rise to call them layers. This term will allow us later to distinguish between these layers and a large chaotic sea surrounding a generic regular region with interwoven channels of the Arnold web, see section 3.4.2.

Following Chirikov [6] the Arnold diffusion can in principle be estimated from the pendulum approximation presented in section 3.2.2. The dynamics in the web of chaoticity is dominated by a fast motion in the vicinity of rank-1 resonances. This fast motion is also present in 2D maps where orbits move around the elliptic regions of resonantly broken tori very fast. In the context of higher dimensional maps it is called *motion across the resonance layer*. Contrary to this fast motion there is a motion along the direction of the resonance condition (3.8) in whose vicinity the motion takes place. Here we have $k = 1$ as it is a rank-1 resonance. This slow component of the chaotic motion which gives rise to the Arnold diffusion is called *motion along the resonance layer*.

The minimal example model of Arnold diffusion must yield a so-called three-frequency Hamiltonian [6, page 352]. Instead of starting with the general Hamiltonian from equation (3.5) where all Fourier components are present the Hamiltonian is set up with the minimum amount of necessary contributions. In order to provide the necessary resonance structure the minimal example model reads

$$H_\varepsilon(\mathbf{I}, \boldsymbol{\theta}, t) = H_{\text{reg}}(\mathbf{I}) + \varepsilon (V^{\text{mG}} \cos(\mathbf{m}_G \boldsymbol{\theta}) + V^{\text{mL}} \cos(\mathbf{m}_L \boldsymbol{\theta}) + V^{\text{mD}} \cos(\mathbf{m}_D \boldsymbol{\theta})). \quad (3.51)$$

The three resonances are called *guiding*, *layer*, and *driving resonance*, respectively. Which is which is thereby not ultimately defined from the very beginning. Rather a comparison of these resonances at a certain point in phase space gives rise to call one resonance the layer and another the guiding resonance, for example. Especially when following a trajectory the role of the resonances can switch [6, page 352]. At each step the resonance along which the slow diffusion takes place is called the guiding resonance, or *actual* resonance by Chirikov. If this would be the only resonance, then the motion would be integrable, compare equation (3.47). In order to introduce a small stochastic layer around this guiding resonance we need another potential term. This is the layer resonance and it does not need to be very strong. In a generic system it even does not need to be present explicitly as all the overtones of the perturbation will create the stochastic layer anyway. While the dominant resonance will be the one along which a chaotic orbit diffuses, the strength of the next-to-dominant resonance will be responsible for the velocity of the diffusion and hence be called the driving resonance, or *virtual-resonance* by Chirikov [6, page 352].

Although this three-frequency model can be used to predict the rate of Arnold diffusion [6, 35, 89] it does not need to be valid for generic systems. There the number of present and also dominant resonances might exceed three [37]. Apart from this drawback we cannot use the three-frequency model in section 3.4 as we focus on mixed systems where a regular region is embedded in a large chaotic component in phase space. In order to apply the diffusion-coefficient calculation according

to the above references, it would first be necessary to find a fictitious integrable system whose weak perturbation yields the coupled standard maps from our setup.

3.3. Numerical tools for the analysis of regular and chaotic motion

In order to be able to analyze dynamical systems, there are several tools which provide insight into the nature of the dynamics. Most of them are introduced using near-integrable systems such as the coupled standard maps for moderate K values and small coupling between the degrees of freedom. In this way it is often easier to understand how these tools work and how they allow to distinguish between regular and chaotic dynamics. The numerical methods can be divided into methods based on time-series analysis and methods based on Lyapunov exponent calculations. In this thesis we use one of each types of methods, namely the analysis of fundamental frequencies and the fast Lyapunov indicator. Beside these two there are other measures. Among them are finite-time Lyapunov-exponents like the Lyapunov characteristic exponents (LCE) [115, 116], the smaller and the general alignment index (SALI, GALI) [117–119], helicity or twist angles [120–122], or the mean exponential growth factor of nearby orbits (MEGNO) [123, 124].

3.3.1. Frequency analysis

The determination of frequencies belongs to the class of methods based on time-series analysis. It is carried out on single classical orbits interpreted as a time series. Note that in the following we use the rotation number defined in $[0, 1)$ rather than the frequency in $[0, 2\pi)$. In order to be consistent with the literature, we denote this rotation number also by the symbol ω .

Aim of the frequency analysis The KAM theorem assures that in a near-integrable system certain tori survive the non-integrable perturbation. The question arises which frequencies are the ones with which the regular motion evolves along these invariant tori. This knowledge is helpful within three respects. First, these frequencies can be used to approximate the dynamics of the regular region and extend it across stochastic layers [125]. Second, the distribution of frequencies can be used to determine very small regions of resonantly broken tori [13, 126]. This is especially important for understanding the global structure of higher dimensional phase spaces because nonlinear resonances are given in algebraic relations between the frequencies and can be checked easily. Third, it is possible to calculate time-frequency decompositions of orbits in order to see which frequencies are important at a given time. This is especially relevant when chaotic orbits are considered which get close to the regular region. Such orbits may get trapped in the vicinity of regular structures and then mimic their behavior. The frequency analysis thus allows to see at which regular tori a chaotic orbit gets trapped for a finite time span [127–131]. These three aspects make the frequency analysis a valuable tool. Besides celestial mechanics and molecular dynamics frequency analysis is also used in the examination of particle accelerator dynamics [132].

Realizations of the frequency analysis The simplest way of calculating these frequencies is using lifts, i.e. using mappings without applying any modulo operations [46, 101, 108]. This however is restricted to cases where the corresponding lift map is known. Other methods are based on wavelet transforms [129, 130, 133, 134] and are especially useful when examining the trapping of chaotic orbits in high-dimensional phase spaces. The frequency analysis used here is based on the work of Laskar [36, 128, 135] which belongs to the class of windowed Fourier transform methods which were already used before by Martens, Davis, and Ezra to examine the energy transport in molecules [127]. While Laskar used numerical minimization in order to determine the fundamental frequency of a signal, there is a much faster way using an interpolation formula given by Bartolini, Bazzani, Giovannozzi, Scandale, and Todesco [136]. This is numerically much simpler and yields the same result.

When systems are considered where there is more than just one relevant frequency then a choice has to be made how to extract the f frequencies from the $2f$ dimensional orbits. For near-integrable systems one uses the conjugate coordinate pairs (q_t^j, p_t^j) of all degrees of freedom $j = 1, \dots, f$. From these one defines a complex time signal $z_t^j = q_t^j - ip_t^j$ which is then analyzed. Hence one gets f frequencies ω . While Laskar [36] uses these z_t^j in order to calculate the windowed Fourier transform, Vela-Arevalo and Wiggins [129] use these z_t^j to calculate wavelet transforms using a Morlet–Grossman mother wavelet.

It is important to note that all of these methods have the following fundamental drawback. They all have to split the original $2f$ dimensional signal given by the orbit into f complex signals in order to get f frequencies. However all degrees of freedom and hence all signals z_t^j contain information about all frequencies. The splitting of the original orbit into the separate degrees of freedom might therefore result in spurious resonance conditions. This is especially the case for systems not being near-integrable, see section 3.4.2. We face the problem when using Laskar’s method. There the most important frequency of degree of freedom $j = 1$ is of course also present in the signal given by the second degree of freedom $j = 2$. It might even be that the contribution of ω_1 is more prominent in z_t^2 than the frequency ω_2 we are interested in. This also holds for all harmonics of both fundamental frequencies such that even $2 \cdot \omega_1$ might be more important than ω_2 in z_t^2 . Therefore blindly taking the two most important frequencies might result in erroneous output. Instead of (ω_1, ω_2) we might end up with $(\omega_1, 2 \cdot \omega_1)$ giving rise to a spurious $-2 : 1 : 0$ resonance.

In this thesis these spurious resonances can be detected by analyzing whether they are part of the image of the frequency map \mathcal{F} of the unperturbed system or not. If they lie apart, then they are spurious and can be neglected, see again section 3.4.2 for an example. Another possible solution is to calculate not only the most important frequency of $z_t^{j=1}$ and $z_t^{j=2}$ but the k most important ones [109]. Then we can choose the two most important frequencies from these $f \times k$ ones such that they are non-resonant and still maximally present in all z_t^j . While this is used in reference [109] to analyze chaotic orbits being trapped at regular tori, it might also be used to calculate the frequency map. This however excludes resonantly broken tori from the examination. A likewise problem exists when trying to calculate the actions of tori from trajectories [137] which is also impossible when the torus under consideration is broken up by the perturbation.

Using a wavelet transformation [129] instead of Laskar's method does not solve this problem per se but it eases the detection of the fundamental frequencies. This is because it allows to plot an image of all frequency contributions at a time. Thus, having determined the most important frequency all the harmonics of this frequency can be skipped when searching for the second frequency. Typically all degrees of freedom contain information about all frequencies. Therefore, all frequencies are contained in a single wavelet transform for example determined from the signal z_t^1 . The wavelet transforms are discussed in this section.

An application of the analysis of the fundamental frequencies to coupled standard maps in the near-integrable case was done by Laskar [36]. It is mainly based on analyzing the image of the frequency map

$$\mathcal{F}(\mathbf{p}, \mathbf{q}) = \boldsymbol{\omega}(\mathbf{p}, \mathbf{q}) \in [0, 1)^f. \quad (3.52)$$

It links initial conditions (\mathbf{p}, \mathbf{q}) of an integrable system to the frequency vector $\boldsymbol{\omega}$ of the torus the motion takes place on. For action–angle coordinates this map is given by the derivative of the Hamiltonian with respect to the action coordinate but it might also be defined for non-symplectic systems [108]. In order to calculate the image of the frequency map \mathcal{F} numerically, one considers a set of initial conditions placed on a set of lines, i. e. a grid with a much higher resolution in one direction. As the above mapping is continuous, the image of this grid will be a deformed set of lines. Apart from this continuous change the image will look very regular. If the above mapping is calculated for a near-integrable system, then the regularity of this map will be destroyed due to the breaking up of resonant tori. The topological change in phase space is conveyed to the frequency plane. From the non-regularity of the latter the resonance conditions can be read off.

To emphasize the procedure, we calculate the frequency map for the weakly-coupled standard maps from equation (3.1). Therein the parameter ξ_{12} is responsible for the coupling between both degrees of freedom. If it is slowly increased more and more resonances will be visible. Especially *coupling resonances* will appear, i. e. resonances with $s = 0$ in equation (3.8). The corresponding transition for increasing ξ_{12} and therefore decreasing regularity of the image of the frequency map \mathcal{F} is shown in figure 3.3.

Typically the width of the resonance lines in the frequency plane is inversely proportional to the magnitude of the integers necessary to describe the resonance condition [6, page 279]. This follows from the equation for the Diophantine frequency vectors (3.6). This is visible in figure 3.3 for the single-uncoupled resonances in figure (a). The largest resonances are $6 : 0 : 1$ and $0 : 6 : 1$ which correspond to $\omega_i = 1/6$. The next but largest are $7 : 0 : 1$ and $0 : 7 : 1$. They are indeed thinner, see the dashed lines in figure (a) as well as their surrounding. Whenever a resonance condition is fulfilled, all initial conditions lying in the resonance zone described by the pendulum approximation in section 3.2.2 will give rise to the same frequency, namely the one fulfilling the resonance condition of the broken torus. This is due to the fact that the algorithm determines the most important ω_i of the motion. By adopting to the same frequencies certain tori are missing such that there appear gaps in the image of the frequency map \mathcal{F} from (3.52). These gaps are visible as bright areas in figure 3.3.

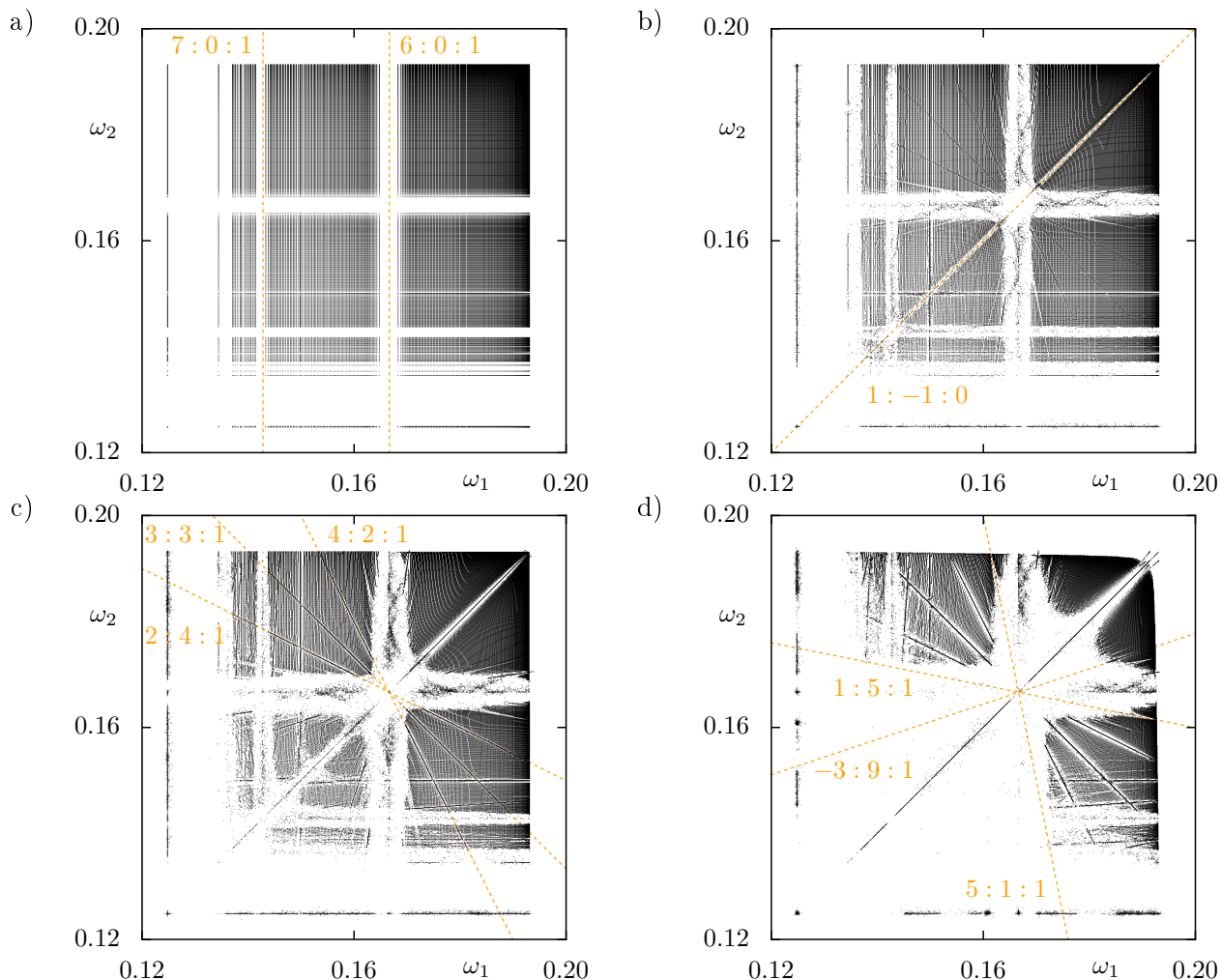


Figure 3.3.: Image of the frequency map for coupled standard maps. The parameters are set to $K_1 = K_2 = 1.3$ and $\xi_{12} = 0, 10^{-4}, 10^{-3}$ and 10^{-2} for figures (a) to (d), respectively. Already the uncoupled case contains resonances but they are of the single-uncoupled type, see column (ii) in figure 3.2. The most important ones are shown by straight dashed lines for the first degree of freedom. By introducing a coupling also slanting resonances appear in figure (b). They represent tori fulfilling single-coupled resonance condition, see column (iii) in figure 3.2. Some of these lines are again shown by straight dashed lines. Intersections of resonance lines are images of the frequency map for tori which fulfill two resonance conditions and hence are double resonant, see column (iv) in figure 3.2. With increasing coupling, figures (b) to (d), an increasing number of resonances is visible. All these resonances are present already in figure (b) but get more and more pronounced. With increasing coupling ξ_{12} and therefore increasing perturbation the image of the frequency map \mathcal{F} gets more and more distorted. Although the values of the parameters are taken from [36], the definition of the coupled standard maps in (3.1) differ by a factor two within the sine of the coupling term.

Laskar calls these structures more generally a non-regularity of the frequency map. Their shape gives rise to the resonance structure of the system.

However, not all widths of all resonances scale with the denominator of equation (3.6) in figure 3.3. A very prominent example is the $1 : -1 : 0$ coupling resonance in figures 3.3(b) to (d). The reason for this lies in the fact that the 2D grid of initial conditions used for calculating the image of \mathcal{F} from (3.52) crossed the resonance structure not at its widest point but more at a small hyperbolic region, see references [108, page 5] and [138].

Wavelet transforms

In near-integrable systems it is possible to perform an analysis of the fundamental frequencies also for chaotic orbits. Using windowed Fourier transforms or wavelet transforms allows to calculate which are the most important frequencies in the motion of a chaotic orbit at a given time. As these orbits wander around in the stochastic layers of resonantly broken tori they will yield frequencies comparable to the ones of the resonance they stick to [36, 41, 42, 101, 129, 130, 133]. Once the frequency map is known it is possible to plot chaotic orbits into it. These frequencies thereby allow to conclude what kind of motion the chaotic orbit performs while it is stucked to a resonance.

The wavelet transform we use is taken from reference [129]. For a given orbit $(p_k^1, p_k^2, q_k^1, q_k^2)$ of length N it is given by setting

$$z_k^1 = q_k^1 - ip_k^1 \quad \text{for } k = 0, \dots, N \quad (3.53)$$

and calculating

$$L_\psi z^1(a, t) = \frac{1}{\sqrt{a}} \sum_{k=0}^N z_k^1 \cdot \psi^* \left(\frac{k-t}{a} \right). \quad (3.54)$$

Therein ψ is given by the so-called Morlet–Grossman wavelet [139, page 157]

$$\psi(t) = \frac{1}{\sigma\sqrt{2\pi}} e^{2\pi i \kappa t} e^{-t^2/2\sigma^2}. \quad (3.55)$$

The quantity a in (3.54) is called *scale*. For the mother wavelet (3.55) it is inverse proportional to the frequency ω [129]

$$a = \frac{1}{2} \left(\kappa + \sqrt{\kappa^2 + \frac{1}{2\pi^2\sigma^2}} \right) \frac{1}{\omega}. \quad (3.56)$$

Apart from the simple $a(\omega)$ relation the Morlet–Grossman mother wavelet has the further advantage that it can be computed very efficiently. The decay of the Gaussian can be used to restrict the sum (3.54) to a small range of integers.

Some example wavelets of orbits from the coupled standard maps from figure 3.3(c) are shown in figure 3.4. The chosen initial conditions are such that they cover different kinds of dynamical

behavior. Figures (a) and (b) show a chaotic orbit which was started in the chaotic sea of the second degree of freedom. Although this orbit is chaotic, its chaoticity is visible only in the wavelet calculated from the second degree of freedom. For the other one it is even possible to determine the most important frequency according to Laskar. This is denoted by the arrows. During the first quarter of the time evolution a trapping occurs as can nicely be seen in figures (a) and (b). The frequency $-\omega_1$ is marked at $1 - \omega_1$ due to the frequencies being restricted to $[0, 1)$. Figures (c) and (d) show the wavelet transform of an orbit started at a point which would lie in the chaotic sea of both maps if they were uncoupled. The wavelets from both degrees of freedom yield a very similar picture. Figures (e) and (f) belong to an orbit from the EE-type surrounding of a period-6 orbit embedded in the main regular region in the center of phase space. As it is not exactly the fixed point only one of the most dominant frequencies is $1/6$ as denoted by the arrows. Figures (g) and (h) show the wavelet for an orbit from the main regular region at the center of phase space. The two frequencies are $\omega_1 = 0.18816383$ and $\omega_2 = 0.19300918$. They do not fulfill a resonance condition. They only approximately fulfill $11\omega_1 + 10\omega_2 = 3.99989396337$. Figures (i) and (j) show again an orbit from the regular region but its initial condition is chosen to be further away from the center than the period-6 orbit from figure (e) and figure (f). We could therefore call it to be outside of the period-6 rank-2 resonance. This has to be taken cum grano salis as the resonance cannot be used to define an inside and outside in phase space.

3.3.2. Fast Lyapunov indicator

In order to easily distinguish between regular and chaotic orbits, we will use the Fast Lyapunov indicator FLI. It was introduced by Froeschlé and Lega [140] and further investigated in references [43, 45, 141–145]. Given a mapping \mathcal{P} this quantity allows to distinguish between chaotic, regular, and resonantly broken behavior. It is defined as

$$F(\mathbf{u}(0), \mathbf{v}(0), t_{\max}) = \log \|\mathbf{v}(t_{\max})\| \quad (3.57)$$

where the vector \mathbf{v} is a vector propagated by the tangent mapping. In order to calculate it, the mapping \mathcal{P} and its linearization $D\mathcal{P}$ are used. First, an initial condition is chosen for the tangential vector $\mathbf{v}(0)$. In all calculations for 4D maps in this thesis it is set to $\mathbf{v}(0) := (1, 1, \frac{1}{2}(\sqrt{5} - 1), 1)$ which is taken from reference [141]. With this and an initial condition $\mathbf{u}(0) = (p_1, p_2, q_1, q_2)$ the so-called variational equations

$$\mathbf{u}(t+1) = \mathcal{P}(\mathbf{u}(t)) \quad (3.58)$$

$$\mathbf{v}(t+1) = D\mathcal{P}(\mathbf{u}(t)) \cdot \mathbf{v}(t) \quad (3.59)$$

can be solved iteratively and yield the quantities necessary to calculate (3.57). The FLI calculation is also possible for time-continuous systems where (3.58) and (3.59) are replaced by a set of differential equations such that both components (\mathbf{u}, \mathbf{v}) are solved simultaneously.

According to the authors of reference [141] the above definition fluctuates very strongly especially

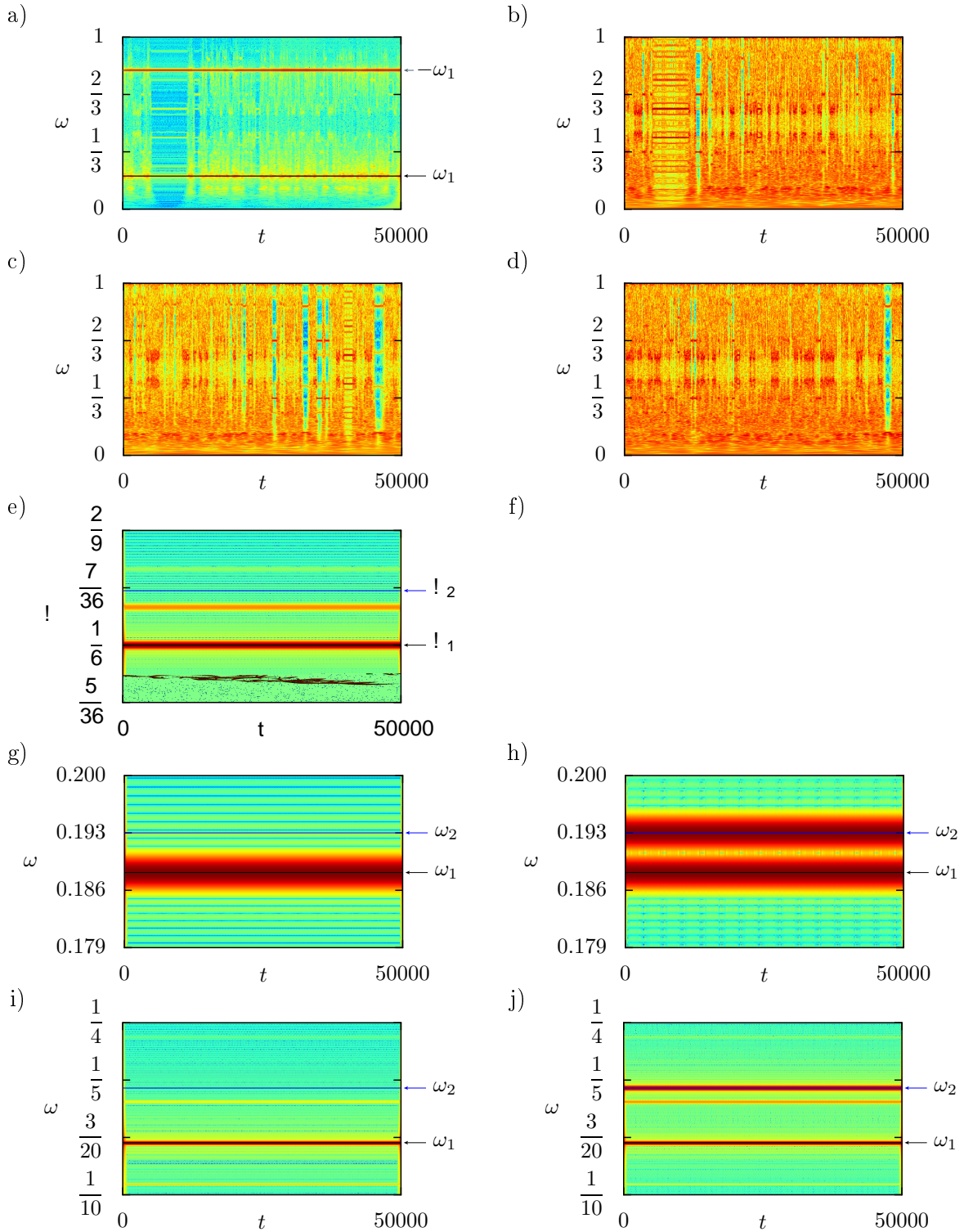


Figure 3.4.: Wavelet representations for different orbits of the coupled standard maps in the weak-coupling case. The parameters are as in figure 3.3. The different orbits cover chaotic and regular motion as well as resonantly broken tori and chaotic motion whose chaoticity is only visible in one degree of freedom, see text. The arrows denote the fundamental frequencies assigned to these orbits by Laskar's method. All plots show the logarithm of the squared wavelet $\log |L_\psi|^2$ and range from blue (low values) to red (high values).

for chaotic motion. It is therefore better to calculate a time-averaged value given by

$$\text{FLI}(\mathbf{u}(0), \mathbf{v}(0), t_{\max}) := \frac{1}{N_{\text{average}}} \sum_{k=t_{\max}-N_{\text{average}}+1}^{t_{\max}} F(\mathbf{u}(0), \mathbf{v}(0), k) \quad (3.60)$$

which will be used in this thesis. Besides the initial vector $\mathbf{v}(0)$ also the maximum iteration count or integration time t_{\max} have to be specified. With these parameters the FLI can be calculated over the whole phase space and yields a map

$$(p_1, p_2, q_1, q_2) \mapsto \text{FLI}(p_1, p_2, q_1, q_2). \quad (3.61)$$

Besides a classification of initial conditions into regular and chaotic equation (3.61) can be used to filter initial conditions such that chaotic orbits are not considered in the frequency plots above, see figure 3.3. They can also be used to estimate the volume of the region in phase space, see section 3.4.1 on page 43. Furthermore they allow to approximate the extent of this region projected onto certain coordinate planes which will be important for the quantum mechanical calculation of regular-to-chaotic tunneling rates, see section 4.4 on page 101.

3.3.3. Phase-space sections

In order to directly visualize the 4D phase space, there are two possibilities. One is to use projections onto a three-dimensional section. The not-shown direction might then be visualized by using a colormap [92, 146]. This is only useful if one orbit is displayed. It is less useful if a whole regular domain should be visualized as then different orbits will overlap within the 3D section. Apart from 3D projections many authors visualize the 4D phase space in terms of various 2D projections of orbits, like for example in references [12, 14, 90].

On the other hand one can use surfaces of section through the 4D phase space. One possibility is to use double sections [140, 147], another one to use really three-dimensional sections. We will mainly use the latter ones as they yield more insight into the overall phase-space structure. As the subject of interest is a mapping, the iterates will typically never return exactly into the section of interest. Therefore, we will introduce a small parameter ε and take points into account whose maximal distance to the section is less than ε . In the most simple case the sections are given by fixing one of the coordinates p_1, p_2, q_1 , or q_2 and only consider points of classical orbits if their component in this coordinate comes ε close to this value. Therefore, the objects we visualize are not sections of zero width but rather slabs through the phase space of a certain but very small extent 2ε . In this thesis we will mostly consider the sections $|p_i| < \varepsilon$ with $i = 1$ or $i = 2$ and $\varepsilon = 10^{-5}$ if not stated otherwise. While this choice of sections through the phase space is quite obvious it might become inappropriate in systems being far from integrable. If nonlinear resonances are considered, locally more appropriate choices are possible.

Skew phase-space sections containing invariant eigenspaces

One way of choosing a locally appropriate phase-space section is given by the eigenvectors of the linearized map around an elliptic–elliptic fixed point. In case of a periodic point of period p the linearization of the p -fold map has to be taken into account. The center manifold theorem assures the existence of an invariant center manifold in the neighborhood of an elliptic fixed point [104, page 94], see also section 3.1. Its dimension is twice the number of the elliptic degrees of freedom. At the fixed point it is tangential to the eigenspace spanned by the real and imaginary part of one of the eigenvectors. Although the eigenspace is only invariant under the linearized dynamics, it can be used to specify a more appropriate section for the nonlinear problem. The general 3D linear section through the 4D phase space is given by the hyperplane

$$\mathbf{u} \cdot \mathbf{n} = D \quad (3.62)$$

where D is the distance of the hyperplane to the origin, \mathbf{u} is the vector of momenta and positions in phase space. The vector \mathbf{n} is the normal to the section. The parameters D and \mathbf{n} have to be chosen such that the section contains the periodic point under consideration and that it contains one 2D eigenspace of the linearization. This can be achieved as follows starting from the linearization of the given map or its p -fold iteration, respectively: Assume that two eigenvectors $\boldsymbol{\xi}_1$ and $\boldsymbol{\xi}_2$ belong to an elliptic degree of freedom and are complex conjugates of one another. Then the real space spanned by real and imaginary part of the first vector

$$\mathbf{v}_1 := \operatorname{Re} \boldsymbol{\xi}_1 \quad \text{and} \quad \mathbf{v}_2 := \operatorname{Im} \boldsymbol{\xi}_1 \quad (3.63)$$

is invariant under the linearized dynamics. We now start from a vector \mathbf{n} which does not lie in the span of \mathbf{v}_1 and \mathbf{v}_2 . This can for example be done by choosing a third eigenvector of the linearized map. Then we orthogonalize \mathbf{v}_2 with respect to \mathbf{v}_1 and then \mathbf{n} with respect to the both of them by using a Gram-Schmidt algorithm. We then set

$$D = \mathbf{n} \cdot \mathbf{u}_p \quad (3.64)$$

where \mathbf{u}_p is the fixed point or periodic point, respectively.

Once the condition (3.64) on the iterates is known, points inside or close to the section can be selected by checking $|\mathbf{n} \cdot \mathbf{u} - D| < \varepsilon$. These points then have to be described by coordinates in the section. Starting from 4D polar coordinates for the unit vector \mathbf{n} perpendicular to the section

$$\mathbf{n} = \begin{pmatrix} \sin \chi \sin \vartheta \cos \varphi \\ \sin \chi \sin \vartheta \sin \varphi \\ \sin \chi \cos \vartheta \\ \cos \chi \end{pmatrix} \quad (3.65)$$

the coordinate system used for this description is spanned by the unit vectors \mathbf{n} and

$$\mathbf{e}_\varphi = \begin{pmatrix} -\sin \varphi \\ \cos \varphi \\ 0 \\ 0 \end{pmatrix} \quad \mathbf{e}_\vartheta = \begin{pmatrix} \cos \vartheta \cos \varphi \\ \cos \vartheta \sin \varphi \\ -\sin \vartheta \\ 0 \end{pmatrix} \quad \mathbf{e}_\chi = \begin{pmatrix} \cos \chi \sin \vartheta \cos \varphi \\ \cos \chi \sin \vartheta \sin \varphi \\ \cos \chi \cos \vartheta \\ -\sin \chi \end{pmatrix} \quad (3.66)$$

which form a right handed coordinate system if used in that order. This can be checked by calculating the determinant of the matrix spanned by the unit vectors, $\det(\mathbf{n}|\mathbf{e}_\varphi|\mathbf{e}_\vartheta|\mathbf{e}_\chi) = 1$. This orthogonal basis is used to span the 3D section (3.62) by using the vectors from equation (3.66)¹

The coordinates $(u_x, u_y, u_z) \in \mathbb{R}^3$ of a point inside this section are given by

$$u_x = \mathbf{u} \cdot \mathbf{e}_\varphi \quad u_y = \mathbf{u} \cdot \mathbf{e}_\vartheta \quad u_z = \mathbf{u} \cdot \mathbf{e}_\chi \quad (3.67)$$

and can be used for plotting into a 3D coordinate system. The coordinate corresponding to the unit vector \mathbf{n} is constant in this section as we have $\mathbf{u} \cdot \mathbf{n} = D$.

It is important to note that there is a subtlety for these skew sections. For each section given by \mathbf{n} and D there exist an $\tilde{\mathbf{n}} := -\mathbf{n}$ and a $\tilde{D} = -D$. This second choice gives rise to the same condition in (3.62). Nevertheless the angles which are deduced from \mathbf{n} and $\tilde{\mathbf{n}}$ in (3.65) yield different sets of unit vectors in (3.66). Although this is the same section in phase space, the coordinates inside the section differ.

The above description also holds for elliptic–hyperbolic fixed points. Furthermore, skew sections can be used in cases of rank-1 resonances. There no periodic orbit exist as mentioned in columns (ii) and (iii) of figure 3.2. However, it is possible to choose one point of the 1D torus and take its tangential at this point to use it for the definition of the section according to (3.62).

3.4. Systems with regular dynamics and a large chaotic sea

The previous section considers near-integrable systems. They have the advantage of providing coordinates which are still close to the actions of the unperturbed system as long as no low-order resonance conditions are fulfilled. Therefore, it is possible to determine approximately conserved quantities from the initial action variables. We now want to focus on systems in a different regime of perturbation, namely so-called mixed systems which yield a comparably small regular region embedded in a much larger chaotic sea. Such setups are for example encountered in the classical phase space of driven helium atoms [19, 149, 150].

The theoretical advantage of such systems is the possibility to incorporate knowledge from completely regular and completely chaotic systems. Both are limiting cases for which different aspects are known and predictable [85, 89]. This is of particular importance when considering quantum mechanical properties of systems with a mixed phase space in chapter 4 where a division of the system into the

¹ Note that the choice (3.65) slightly differs from the general definition of hyperspherical coordinates [148] where the angles are introduced with respect to another direction using $\mathbf{n} = (\cos \chi, \sin \chi \cos \vartheta, \sin \chi \sin \vartheta \cos \varphi, \sin \chi \sin \vartheta \sin \varphi)^T$.

two extreme cases of regular and chaotic dynamics will provide further insight. This further justifies to investigate such systems classically. The drawback is that in contrast to the near-integrable regime much less can be predicted globally for these systems in terms of classical perturbation theory.

The regular region of a generic system embedded in the chaotic sea is never completely integrable. It rather is near-integrable and can therefore be seen as the result of a perturbation of an unknown fictitious integrable system just like in section 3.2. If this fictitious system would be known to high accuracy and if it would be possible to determine its action and angle variables, then the regular part could be treated like the near-integrable examples of the previous section. This, however, is not part of this thesis.

In this section we introduce a designed system whose phase space is given by a regular region yielding purely linear and hence integrable dynamics. The surrounding chaotic domain is chosen such that it does not contain further regular regions and has a very narrow transition towards the regular subsystem. Afterwards, nonlinear resonances are introduced to the system. The frequency map analysis introduced in section 3.3.1 is used to monitor which resonances occur. We conclude with the generic case of coupled standard maps which yield complicated phase-space structures between regular and chaotic motion.

3.4.1. Designed maps: Map with linear regular region, \mathcal{P}_{lin}

A generic dynamical system such as the coupled standard maps introduced in section 3.1 shows a very complicated phase-space structure. This fact is caused by the self similar structure of the phase space. Regular regions are surrounded by regular regions of smaller volume given by all types of elliptic behavior listed in section 3.2.1. These regions of smaller volume are surrounded by their own regular sub-structures again giving rise to a complicated hierarchy of regular regions. Already in 2D maps tiny layers of chaotic motion exist in between these regular zones. In systems with more than two degrees of freedom this chaotic motion belongs to one and only one connected chaotic component which is usually called the Arnold web in the near-integrable case. Such a phase space is much too complicated to serve as a good starting point for our investigations especially of quantum systems as done in chapter 4.

Hence, the aim is to design a map with a clean phase-space structure. This means three things: First, the map should yield a purely regular region without chaotic layers interwoven into it, see section 3.2.4. Second, the chaotic region should not contain regular regions down to arbitrary small sizes. Third, the transition region in between regular and chaotic dynamics should be very sharp. The last point is already implied by the second one though. In order to create such a map we proceed similar to the case of 2D maps [78, 138, 151–153]. Our starting point is a general symplectic mapping derived from a kicked Hamiltonian system analogous to the case of 2D maps (2.3). While the kinetic energy is given by

$$T(\mathbf{p}) = \frac{1}{2}\mathbf{p}^2 \tag{3.68}$$

the potential energy is defined piecewise as will be described in the following. In order to obtain a resonance-free island we start with a regular region with linear dynamics which we call *linear regular region*. Such a regular island is constructed using a quadratic potential

$$V_{\text{quadratic}}(\mathbf{q}) = \frac{r_1}{2}q_1^2 + \frac{r_2}{2}q_2^2, \quad (3.69)$$

where r_1 and r_2 are real parameters. In order to introduce chaotic dynamics we truncate this potential at a certain value Q and change its definition beyond this border according to

$$V(q_1, q_2) = \begin{cases} V_{\text{quadratic}}(q_1, q_2), & V_{\text{quadratic}}(q_1, q_2) \leq Q^2 \\ Q^2 + g(q_1, q_2), & \text{otherwise.} \end{cases} \quad (3.70)$$

The definition of the outside-part g of the potential is quite rich in detail and is therefore given in appendix A. A contour plot of this potential is shown in figure 3.5. Let us again emphasize that the most important part of this potential is not the function g but the harmonic interior. This part gives rise to linear and therefore regular and resonance-free dynamics. The remaining part is chosen such that it yields a continuous and periodic function $V(q_1, q_2)$. Its parameters are adjusted to obtain chaotic dynamics. They are given by

$$r_1 = 1.51, r_2 = 1.8, Q = 0.22, a = -0.3, b = -0.27, K = 0.47, n = 6, \text{ and, } m = 7 \quad (3.71)$$

and define the mapping \mathcal{P}_{llu} used throughout this thesis where the letters **llu** stand for **linear, linear, uncoupled** and describe the motion of the degrees of freedom at the center. In the next paragraphs we will show that it indeed has a regular region as desired.

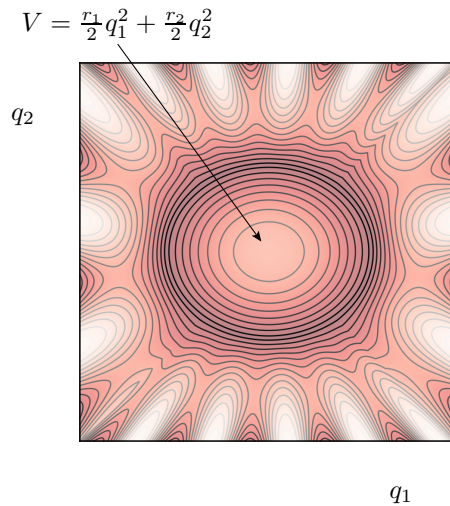


Figure 3.5.: Contour plot of the potential energy of the designed map. Bright regions represent small, red regions represent large values. The interior is given by the quadratic potential of equation (3.69) as indicated by the arrow. From the center the potential increases up to the ellipsis defined by equation (3.70) and then decreases towards the boundary of the position space. The parameter values used for this plot are given in equation (3.71)

Phase space of the designed map with linear regular region

Our aim is to gain insight into the phase-space structure of the map \mathcal{P}_{llu} . As the phase space is four-dimensional it cannot be visualized completely, as typically done for 2D maps. In order to obtain a representation of the regular region embedded in the chaotic sea, we will focus on sections through the 4D phase space. Contrary to 2D double sections introduced by Froéschle [140, 147] for single orbits we will look at 3D sections through the 4D phase space.

To calculate the 3D section a set of initial conditions is chosen and the corresponding orbits are calculated until there are enough points satisfying the section condition

$$|p_2| < \varepsilon. \quad (3.72)$$

This needs large computational effort in order to obtain enough points inside a reasonably small slab of $\varepsilon = 10^{-5}$. The main reason is that the vast majority of the calculated iterates does not lie in the section and cannot be used for the plot. The result of this calculation is shown in figure 3.6.

The linearity of the regular region allows to explain the typical picture of a section through the 4D phase space. Let us consider an initial condition inside the section $p_2 = 0$ which further fulfills $q_2 = 0$. The variables of the first degree of freedom are chosen close to the center of phase space in order to assure that we obtain a regular orbit. As both maps are decoupled in the regular region, the trajectory stays at $p_2 = q_2 = 0$ and hence lies completely inside the chosen section. Its shape is given by the linear map of the first degree of freedom only. Therefore, it will be a one dimensional curve given by the ellipsis at $q_2 = 0$ marked by the arrow in figure 3.6. If we choose an initial condition with $q_2 \neq 0$ but still close enough to the center, then the orbit will be the direct product of the ellipses shown in the figure and a likewise ellipsis in the second degree of freedom (q_2, p_2) . The section condition $p_2 = 0$ reduces this ellipsis to two points in q_2 . At these two values of q_2 we see the complete ellipsis of the first degree of freedom. This is the main reason why everything appears twice in the 3D sections. If we add more initial conditions to the plot, we obtain more and more pairs of ellipses. These are shown in red in figure 3.6. Initial conditions further towards the border of phase space yield chaotic motion shown in blue.

It is important to note that a general regular region will not yield decoupled degrees of freedom with respect to the section condition $p_2 = 0$. This can be mimicked for \mathcal{P}_{llu} by using a section specified not solely in one degree of freedom. To show the influence of a nonzero angle between the section and the decoupled degrees of freedom, figure 3.7 shows sections through the phase space which are artificially set to a skew angle α defined by $|\cos(\alpha)p_2 - \sin(\alpha)p_1| = 0$. This angle α thus allows to interpolate between the sections given by $p_1 = 0$ and $p_2 = 0$. For a generalization of the section conditions to skew sections see section 3.3.3. This will be important when considering regular regions of the coupled standard map in section 3.4.3. There the degrees of freedom are not decoupled anymore. From figure 3.7 we will later be able to deduce that some of the effects visible in straight sections of generic maps are just due to an inappropriate choice of the section.

Note that the linearity of the regular region of \mathcal{P}_{llu} can be used to compute the sections in figure 3.7

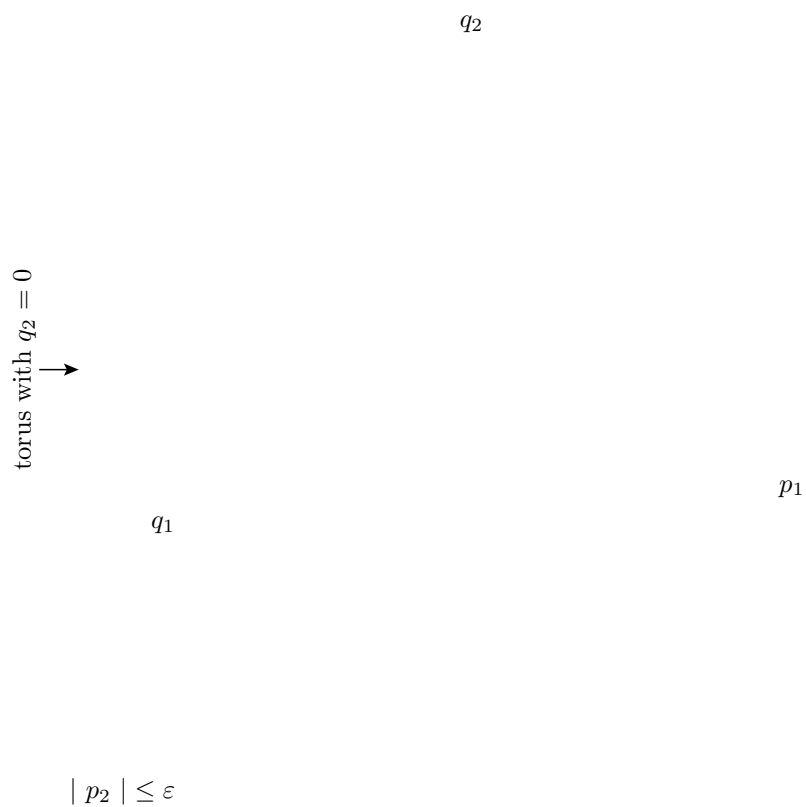


Figure 3.6.: Section through the 4D phase space of the designed map \mathcal{P}_{lu} . Shown in red are regular orbits, shown in blue are chaotic orbits. The arrow indicates the torus with an initial condition $q_2 = 0$. Due to its special initial condition it is only a 1D torus contained completely in the shown 3D section. The center of this figure corresponds to $(q_1, p_1, q_2) = (0, 0, 0)$.

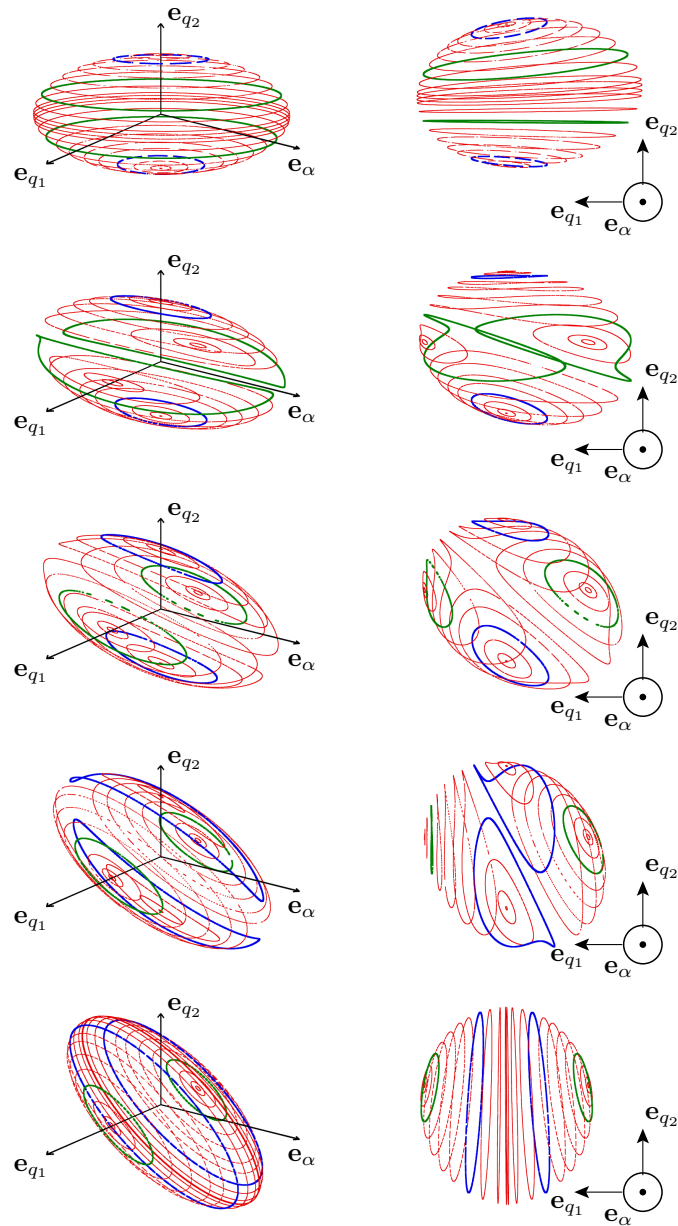


Figure 3.7.: Skew phase-space sections for \mathcal{P}_{11u} . The sections are chosen to be $|\cos(\alpha)p_2 - \sin(\alpha)p_1| = 0$ with $\alpha = 0, \frac{1}{8}\pi, \frac{1}{4}\pi, \frac{3}{8}\pi, \frac{1}{2}\pi$ from top to bottom. The direction of the axis denoted by α is $\mathbf{e}_\alpha = \cos(\alpha)\mathbf{e}_{p_1} + \sin(\alpha)\mathbf{e}_{p_2}$. The right hand side displays the same as the left hand side from a different point of view, namely along the \mathbf{e}_α -axis. Two orbits are depicted in different colors (green and blue) in order to improve the visibility of the geometry and serve as a guide to the eye.

efficiently using the solution to the equations of motion for linear 2D maps [152]. This solution allows to parametrize the position and momentum $(q_i(t_i), p_i(t_i))$ on a torus for each degree of freedom $i = 1, 2$ with two real parameters $t_i \in \mathbb{R}$. This leads to a parametrization of the 2D torus by two parameters. The points within the section can then be calculated numerically by a root search. For the purpose of visualization it is sufficient to use a routine for calculating contour lines of two dimensional data arrays [154]. This procedure is much less time consuming than iterating orbits numerically.

FLI values

Besides the orbits themselves we calculate the FLI introduced in section 3.3.2. In order to be able to interpret the values of this indicator, a 4D grid is placed over the phase space and the FLI is calculated on this grid. From the histogram of FLI values shown in figure 3.8 different kinds of orbits can be attributed to ranges of FLI values. This can then be used to define a colormap which represents the different kinds of dynamics adequately and is plotted in the background of the histogram. Red is assigned to the peak at low values as it originates from regular motion. Blue is assigned to all values larger than 10 and represents chaotic motion. In order to reduce computation time, the FLI calculation is aborted if the FLI goes above 450 such that all the chaotic orbit with $\text{FLI} \geq 450$ belong to just one bin.

This colormap is also used in figure 3.9 to display the FLI values on a 2D plane in the first degree of freedom (q_1, p_1) and via a surface of constant value for the FLI calculated on the whole 3D section. These plots allow a clear visualization of the regular domain inside the 3D section. The advantage of the FLI calculation versus the direct calculation of orbits is that it is much faster. This is due

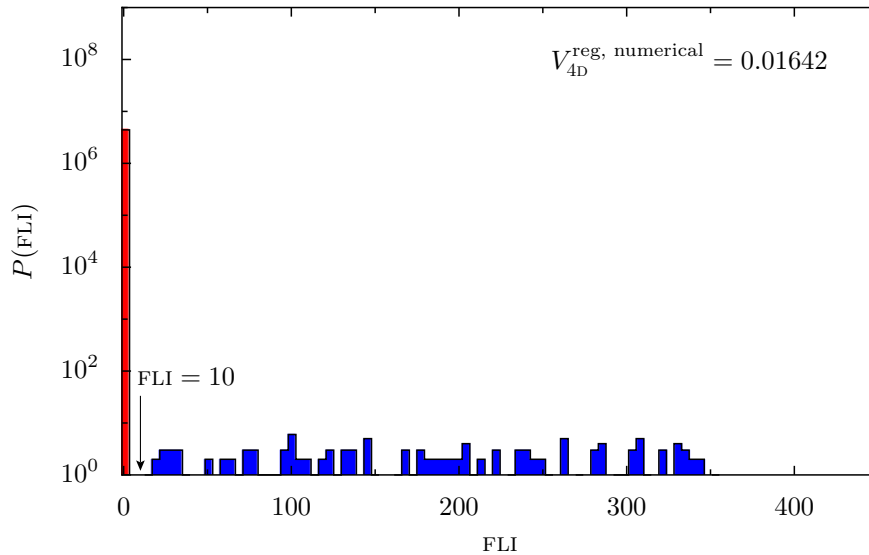


Figure 3.8.: Histogram of FLI values for \mathcal{P}_{llu} . The abscissa shows the FLI values on a linear scale while the ordinate shows the absolute number of FLI values on a logarithmic scale. The colormap in the background is chosen such that it matches the corresponding features in the FLI histogram. The arrow indicates where the orbit type changes from regular (red) to chaotic (blue). The grid of initial conditions is $128 \times 128 \times 128 \times 128$ and the number of iterations for the FLI calculation is 4000.

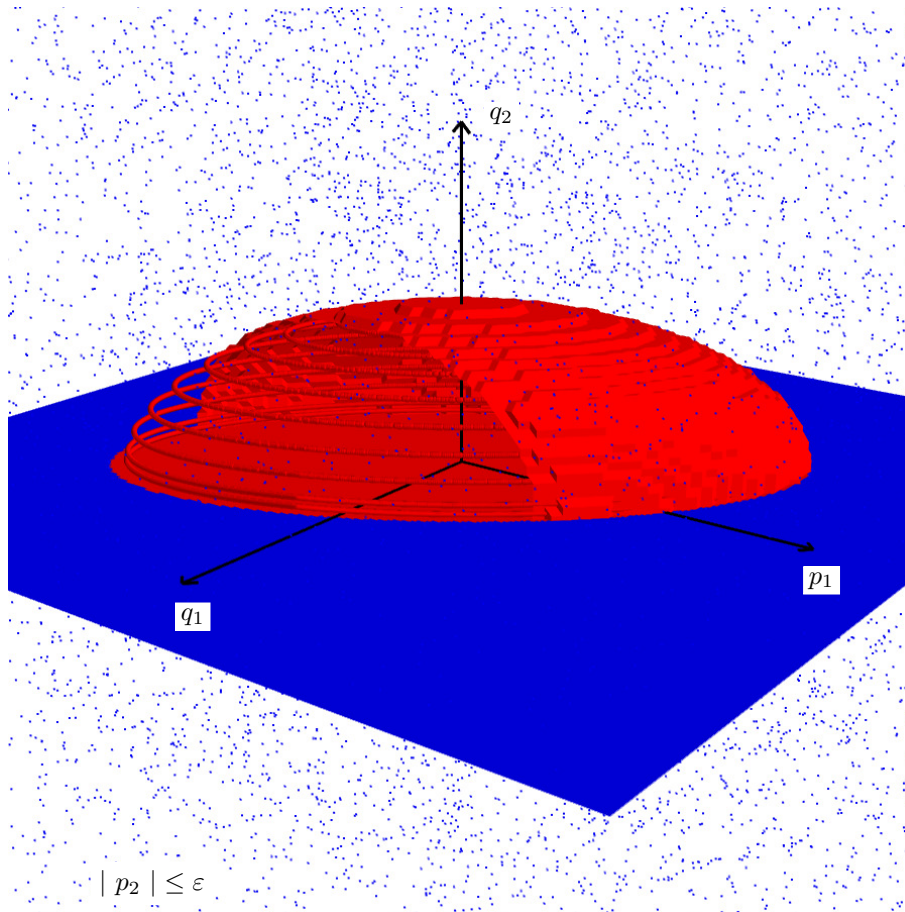


Figure 3.9.: Section of the designed map \mathcal{P}_{lu} including FLI values. The FLI is visualized on the (q_1, p_1) plane and by a surface of constant value inside the 3D section. For better visibility these isosurface is cut towards the spectator. The orbits in this phase-space section are calculated using $\varepsilon = 10^{-5}$.

to the fact that the length of the orbits in the FLI calculation is much smaller than it is necessary for the direct visualization of orbits inside the section. The number of iterations is reduced from approximately 10^9 for a slab of width $\varepsilon = 10^{-5}$ to 4000 iterations per initial condition in the FLI calculation.

Estimating the size of the regular region

With the histogram in figure 3.8 it is also possible to estimate the size of the regular phase-space volume. This estimate is only correct up to the resolution of the initial conditions used for the FLI calculation. Therefore it does not account for the fractal structure. If all initial conditions with $\text{FLI} \leq 10$ are considered regular, then from the above histogram the size of the regular region is estimated to

$$V_{4\text{D}}^{\text{reg, numerical}} = \frac{\#\{\text{initial conditions with } \text{FLI} \leq 10\}}{128^4} = \frac{4,407,331}{268,435,456} = 0.01642 \quad (3.73)$$

where the total phase-space volume equals unity. In this respect the 3D section shown in figure 3.9 is misleading as the size of the regular region shown there is intuitively overestimated.

For the case of purely linear motion inside the regular region it is also possible to determine the 4D volume of the regular region analytically. In order to do so, we first consider the 2D case. Starting point is a general linear map \mathcal{P} with no periodic boundary conditions. According to reference [152] we write this map as

$$\begin{pmatrix} q' \\ p' \end{pmatrix} = \mathcal{P} \begin{pmatrix} q \\ p \end{pmatrix} = \begin{pmatrix} \mathcal{P}_{11}q + \mathcal{P}_{12}p \\ \mathcal{P}_{21}q + \mathcal{P}_{22}p \end{pmatrix}. \quad (3.74)$$

Note that in this case $\mathcal{P} = D\mathcal{P}$. As long as the fixed point at the origin is elliptic, $|\frac{1}{2}\text{tr}(\mathcal{P})| < 1$, it is possible to write down an autonomous Hamiltonian with one degree of freedom whose curves of constant energy interpolate the orbits of the mapping. It is given by [152]

$$H(p, q) = \alpha (\mathcal{P}_{12}p^2 + (\mathcal{P}_{11} - \mathcal{P}_{22})qp - \mathcal{P}_{21}q^2) \quad \text{with} \quad \alpha = \frac{\arccos(\frac{1}{2}\text{tr}(\mathcal{P}))}{\sqrt{4 - \text{tr}(\mathcal{P})^2}}. \quad (3.75)$$

The constant prefactor α in this expression is necessary to yield a time-continuous system whose solutions have the same frequencies along the tori as the kicked system it interpolates (3.74). This Hamiltonian can be used to give the functional dependence of $p(q)$ for a given initial condition. It reads [152]

$$p_{\pm}^*(q) = \frac{\mathcal{P}_{22} - \mathcal{P}_{11}}{2\mathcal{P}_{12}}q \pm \frac{\sqrt{4 - \text{tr}(\mathcal{P})^2}}{2\mathcal{P}_{12}} \sqrt{\frac{4\mathcal{P}_{12}H(p_0, q_0)}{\alpha(4 - \text{tr}(\mathcal{P})^2)} - q^2} \quad (3.76)$$

from which the maximum deflection q_{\max} of the torus can be read off to be

$$q_{\max}^2 = \frac{4\mathcal{P}_{12}H(p_0, q_0)}{\alpha(4 - \text{tr}(\mathcal{P})^2)}. \quad (3.77)$$

For a 2D map the volume of the regular region is then given by

$$V_{2\text{D}}^{\text{reg}} = \int_{-q_{\max}}^{q_{\max}} dq (p_+^*(q) - p_-^*(q)) = \frac{\sqrt{4 - \text{tr}(\mathcal{P})^2}}{\mathcal{P}_{12}} \int_{-q_{\max}}^{q_{\max}} dq \sqrt{q_{\max}^2 - q^2} \quad (3.78)$$

$$= \frac{\pi}{2} \frac{\sqrt{4 - \text{tr}(\mathcal{P})^2}}{\mathcal{P}_{12}} q_{\max}^2, \quad (3.79)$$

where the maximum deflection q_{\max} specifies the extent of the island in position space by means of the largest position value of the outermost torus of the island. It is given as an external parameter to the map and determines the limits of the linear region. However, equation (3.78) for $V_{2\text{D}}$ is only valid if q_{\max} is really the delimiting parameter for the regular region. It does not account for possible bonds in the p direction which reduce the island size further, for example by reaching the boundary of phase space or by reaching p values where the definition of the kinetic energy differs from the linear definition on which equation (3.75) is based upon.

Equation (3.77) can now be used to determine the volume of the regular region of the 4D map given by the designed potential (3.69). Together with a kinetic energy of $T(\mathbf{p}) = \mathbf{p}^2/2$ this yields two uncoupled linear maps $\mathcal{P}^j, j = 1, 2$. According to equation (2.4) they are given by

$$\begin{pmatrix} \mathcal{P}_{11}^j & \mathcal{P}_{12}^j \\ \mathcal{P}_{21}^j & \mathcal{P}_{22}^j \end{pmatrix} = \begin{pmatrix} 1 & 1 \\ -r_j & 1 - r_j \end{pmatrix} \quad \text{and therefore} \quad 4 - \text{tr}(\mathcal{P}^j)^2 = 4r_j - r_j^2. \quad (3.80)$$

A given initial condition leads to a certain maximal deflection $q_{1,\max}$ in the first and $q_{2,\max}$ in the second degree of freedom. The corresponding orbit is regular only if these two maximal deflections do not leave the region where the potential is quadratic. With $\Gamma = [-\frac{1}{2}, \frac{1}{2}] \times [-\frac{1}{2}, \frac{1}{2}] \times [-\frac{1}{2}, \frac{1}{2}] \times [-\frac{1}{2}, \frac{1}{2}]$ being the whole phase space, we have

$$V_{4\text{D}}^{\text{reg}} = \int_{\Gamma} dp_1 dq_1 dp_2 dq_2 \Theta \left(Q^2 - \left(\frac{r_1}{2} q_{1,\max} (q_1, p_1)^2 + \frac{r_2}{2} q_{2,\max} (q_2, p_2)^2 \right) \right) \quad (3.81)$$

$$= \int_{\Gamma} dp_1 dq_1 dp_2 dq_2 \Theta \left(Q^2 - \frac{2p_1^2 + 2r_1 p_1 q_1 + 2r_1 q_1^2}{4 - r_1} - \frac{2p_2^2 + 2r_2 p_2 q_2 + 2r_2 q_2^2}{4 - r_2} \right). \quad (3.82)$$

Here the parameter Q is again the quantity defining the extent of the regular region in equation (3.70). This integral can be solved by diagonalizing the quadratic form in the Heaviside function. It consists

of two terms which can be written using $f(x) := Q^2 - \frac{x}{4-r_i}$ as

$$\text{d}p\text{d}qf(2p^2 + 2rpq + 2rq^2) = \text{d}p\text{d}qf\left(\begin{pmatrix} q \\ p \end{pmatrix}^T \begin{pmatrix} 2r & r \\ r & 2 \end{pmatrix} \begin{pmatrix} q \\ p \end{pmatrix}\right) = \text{d}p\text{d}qf\left(\begin{pmatrix} q \\ p \end{pmatrix}^T \underline{\mathcal{H}} \begin{pmatrix} q \\ p \end{pmatrix}\right) \quad (3.83)$$

$$= \text{d}\tilde{p}\text{d}\tilde{q} |\det \underline{\mathcal{V}}| f(\lambda_1 \tilde{q}^2 + \lambda_2 \tilde{p}^2) \quad (3.84)$$

$$= \text{d}\phi\text{d}\rho \frac{|\det \underline{\mathcal{V}}|}{\sqrt{\det \underline{\mathcal{H}}}} \rho f(\rho^2) \quad (3.85)$$

where $\lambda_{1,2}$ are the eigenvalues of the matrix $\underline{\mathcal{H}}$ defined in equation (3.83) and $\underline{\mathcal{V}}$ is the matrix of eigenvectors of $\underline{\mathcal{H}}$. As $\underline{\mathcal{H}}$ is symmetric, $\underline{\mathcal{V}}$ is orthogonal and $|\det(\underline{\mathcal{V}})| = 1$. In the last step (3.85) polar coordinates are introduced. Inserting equation (3.85) into equation (3.82) we obtain

$$V_{4\text{D}}^{\text{reg}} = \frac{2\pi}{\sqrt{\det \underline{\mathcal{H}}_1}} \frac{2\pi}{\sqrt{\det \underline{\mathcal{H}}_2}} \int_0^\infty \text{d}\rho_1 \rho_1 \int_0^\infty \text{d}\rho_2 \rho_2 \Theta\left(Q^2 - \frac{1}{4-r_1} \rho_1^2 - \frac{1}{4-r_2} \rho_2^2\right) \quad (3.86)$$

$$= \frac{2\pi}{\sqrt{\det \underline{\mathcal{H}}_1}} \frac{2\pi}{\sqrt{\det \underline{\mathcal{H}}_2}} \int_0^{\sqrt{4-r_1}Q} \text{d}\rho_1 \rho_1 \int_0^{\sqrt{4-r_2}\sqrt{Q^2 - \frac{1}{4-r_1}\rho_1^2}} \text{d}\rho_2 \rho_2. \quad (3.87)$$

In the first step we increase the region of integration from the compact phase space (a 4D cube) to \mathbb{R}^4 . This is possible as the Heaviside function is zero outside the original phase-space volume. With equation (3.87) the final result for the volume of the regular region reads

$$V_{4\text{D}} = \frac{1}{2} \frac{2\pi}{\sqrt{\det \underline{\mathcal{H}}_1}} \frac{2\pi(4-r_2)}{\sqrt{\det \underline{\mathcal{H}}_2}} \int_0^{\sqrt{4-r_1}Q} \text{d}\rho_1 \rho_1 \left(Q^2 - \frac{1}{4-r_1} \rho_1^2\right) \quad (3.88)$$

$$= \frac{1}{8} \cdot \frac{2\pi(4-r_1)Q^2}{\sqrt{\det \underline{\mathcal{H}}_1}} \cdot \frac{2\pi(4-r_2)Q^2}{\sqrt{\det \underline{\mathcal{H}}_2}} \quad (3.89)$$

$$= \frac{\pi^2}{2} \sqrt{\frac{4-r_1}{r_1}} \sqrt{\frac{4-r_2}{r_2}} Q^4. \quad (3.90)$$

For the parameters $r_1 = 1.51, r_2 = 1.8, Q = 0.22$ from figure 3.5 this formula yields $V_{4\text{D}}^{\text{reg}} = 0.01641$ compared to $V_{4\text{D}}^{\text{reg, numerical}} = 0.01642$ from equation (3.73). Hence, very good agreement with the analytical result is found using the FLI as a numerical estimate of the phase-space volume.

3.4.2. Designed maps: Islands with resonances, \mathcal{P}_{nnc}

In order to understand the generic case of the coupled standard maps, it is necessary to include nonlinear resonances into our designed system. We achieve this by changing the definition (3.70) to

$$V(q_1, q_2) = \begin{cases} V_{\text{quadratic}}(q_1, q_2) + \frac{R_1}{3}q_1^3 + \frac{R_2}{3}q_2^3 + R_{12}q_1q_2^2, & V_{\text{quadratic}}(q_1, q_2) \leq Q^2 \\ Q^2 + g(q_1, q_2), & \text{otherwise} \end{cases} \quad (3.91)$$

with the new parameters R_1 , R_2 , and R_{12} . In this expression the quadratic part is given by equation (3.69) plus higher order terms in q_1 and q_2 . Note that this potential is discontinuous. In order to make it continuous, the expression for the ellipsis in equation (3.70) would have to be replaced by the polar representation $r(\varphi)$ of the equipotential line of the polynomial potential including the higher order terms from equation (3.91). However, this representation is not known analytically. Another possibility is to smooth the potential using a Gaussian as it was done for 2D maps [138, 152]. However, we decided to use the discontinuous potential in order to keep the computation time in a reasonable limit. This is especially important for the very time consuming calculations necessary to calculate the 3D sections.

Frequency analysis

The new potential in equation (3.91) can be tuned by changing the parameters R_1 and R_2 as well as R_{12} . The parameters R_1 and R_2 introduce nonlinearities to the separate degrees of freedom. The third parameter R_{12} introduces a coupling between the two degrees of freedom. These nonlinearities in the potential introduce nonlinear resonances in phase space, as described in section 3.2. For 2D maps these resonances can be observed directly in phase space. This is not possible for 4D maps, at least not to the same extent. In order to see which resonances are introduced, it is useful to look at the frequency map analysis, see section 3.3.1. This is done for various parameter changes in figure 3.10.

For the linear-uncoupled case with $R_1 = R_2 = R_{12} = 0$ the frequencies of the two 2D maps can be calculated analytically [152, equation (3.16)]. They are given by

$$\omega_i = \frac{1}{2\pi} \arccos\left(1 - \frac{r_j}{2}\right) \quad (3.92)$$

and therefore

$$(\omega_1, \omega_2) = (0.2106, 0.2341). \quad (3.93)$$

The corresponding point is marked by a red circle in figure 3.10(a). If only the first degree of freedom is made nonlinear, $R_1 = 3.0$, then only the frequency ω_1 will yield resonances as depicted in figure 3.10(b). The dashed line marks the $\omega_1 = 1/5$ resonance. The second degree of freedom still yields a constant value $\omega_2 = 0.2341$. The points scattered around the line at $\omega_2 = 0.2341$ are due to chaotic orbits which were not filtered away by the criterion $\text{FLI} < 2$, see page 33. If both degrees of freedom

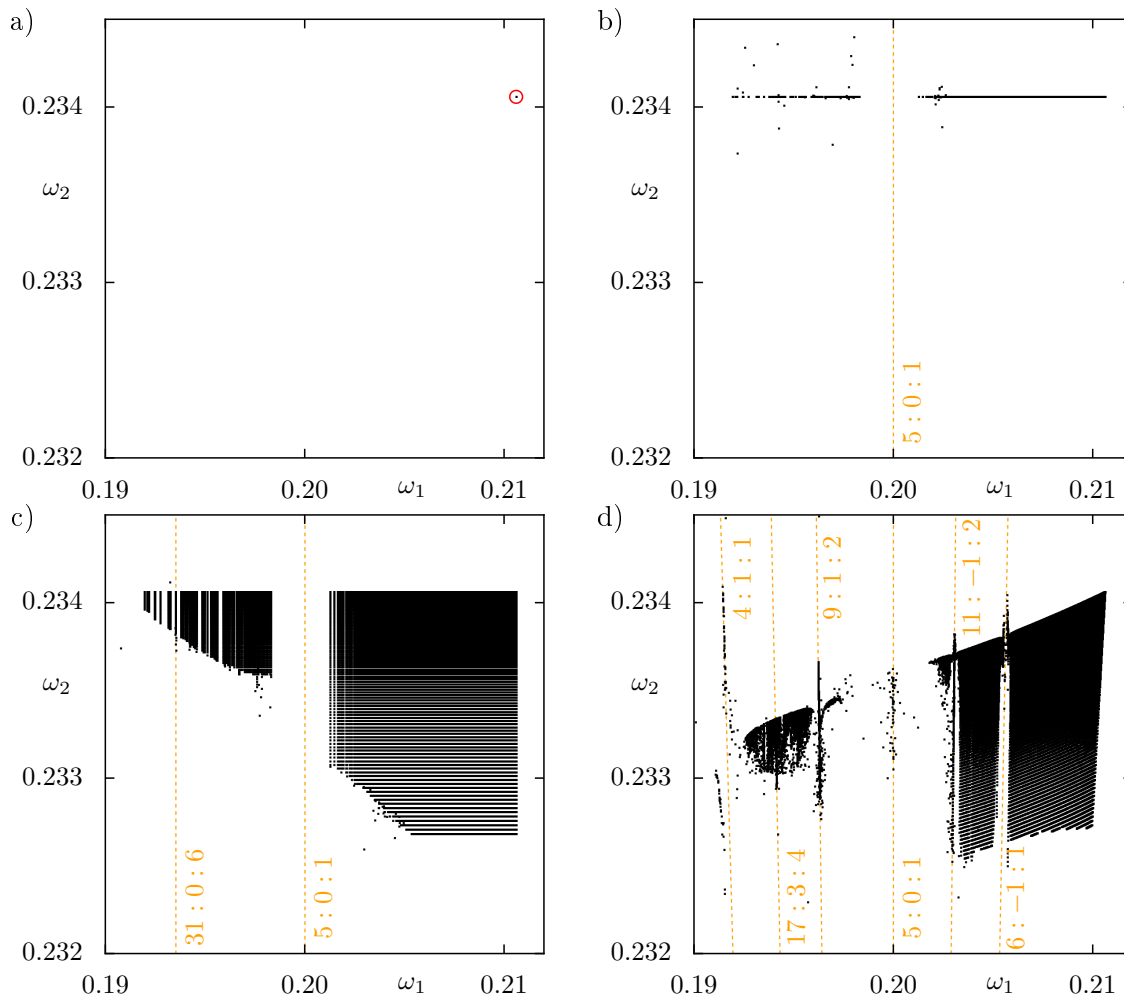


Figure 3.10.: Image of the frequency map for several different parameters R_1, R_2 , and R_{12} of the designed map (3.91). The initial conditions are placed at $p_1 = p_2 = 0$ and $q_1 \in (0, 0.13)$, $q_2 \in (0, 0.13)$. The grid of initial conditions in q_1 has 1200 points, the one in q_2 has 120 point. Figure (a) shows the linear map \mathcal{P}_{lin} , where $R_1 = R_2 = R_{12} = 0$. The frequency pair $(\omega_1, \omega_2) = (0.2106, 0.2341)$ is marked by a circle as a guide to the eye. Figure (b) shows $R_1 = 3.0, R_2 = 0.0$. Figure (c) shows $R_1 = 3.0, R_2 = 1.2$ where both degrees of freedom yield a whole range of frequencies. However there are no resonances visible in ω_2 . Figure (d) shows $R_1 = 3.0, R_2 = 1.2$ and $R_{12} = 0.3$ which define the map \mathcal{P}_{nnc} . This system also yields coupling resonances as it is typical for generic systems, see also figure 3.3.

are perturbed in an uncoupled way, $R_1 = 3.0, R_2 = 1.2$ but $R_{12} = 0$, then the image of \mathcal{F} covers a 2D region in the ω_1 - ω_2 -plane. The parameters of the second degree of freedom, $r_2 = 1.8$ and $R_2 = 1.2$, are chosen such that the resulting map covers only a small range of frequencies ω_2 , see figure 3.10(c). This ensures that there are no low-order single-uncoupled resonances in the second degree of freedom. However, due to the fact that more points are visible in the plot, further resonances in the first degree of freedom get visible. They are already present in figure 3.10(b).

By inserting a coupling between both degrees of freedom, $R_{12} = 0.3$, we generate coupling resonances. These are visible in figure 3.10(d) where again slanting resonances through the image of \mathcal{F} appear, compare figure 3.3. This final parameter set $r_1 = 1.51, R_1 = 3.0, r_2 = 1.8, R_2 = 1.2$, and $R_{12} = 0.3$ defines the map \mathcal{P}_{nnc} , where the letters **nnc** stand for **nonlinear, nonlinear, coupled** and describe the motion of the degrees of freedom at the center. The most prominently visible resonances are $5 : 0 : 1$ and $6 : -1 : 1$. Also visible in figure 3.10(d) is the different resolution in q_1 and q_2 for the grid of initial conditions, see section 3.3.1. This is the reason why the image appears to consist of nearly horizontal lines especially in the lower right part of the image of the frequency map \mathcal{F} . All slanting resonances shown by the dashed lines in figure 3.10(d) intersect at $(\omega_1, \omega_2) = (1/5, 1/5)$. According to section 3.2.1 the main resonance structure in phase space is therefore given by a period-5 orbit, see later in figure 3.11. However, in contrast to the coupled standard maps in figure 3.3 on page 29 the point of intersection of all shown resonance lines does not lie in the direct product of the frequency images of the uncoupled maps, shown in figure 3.10(c). This is due to the choice of the parameters R_1, R_2 , and R_{12} . The uncoupled maps cover very distinct ranges of frequencies, namely approximately $\omega_1 \in [0.19, 0.21]$ and $\omega_2 \in [0.2325, 0.2340]$ as can be seen in figure 3.10(c). Therefore, the point $(1/5, 1/5)$ is also not part of the image of the final nonlinear system in figure 3.10(d) and the main $1 : -1 : 0$ -coupling resonance known from the coupled standard maps example is not part of the image of \mathcal{F} .

We have to mention that the $1 : -1 : 0$ resonance occurs in the numerical data as a spurious resonance. This is due to the fact that the first degree of freedom (q_1, p_1) as well as the second one (q_2, p_2) yield a periodic signal with $\omega_i = 1/5$ such that obviously $1 \cdot \omega_1 - 1 \cdot \omega_2 = 0$ is fulfilled. This is one of the spurious resonances addressed in section 3.3.1.

Besides the single-coupled resonance-lines like $4 : 1 : 1$ or $6 : -1 : 1$ in figure 3.10(d) there is the single-uncoupled $5 : 0 : 1$ resonance which occurs due to the nonlinearity of the first degree of freedom alone. As basis of the resonance module we will use the resonances

$$5 : 0 : 1 \quad \text{and} \quad 6 : -1 : 1 \tag{3.94}$$

because they are suitable for building a basis of the resonance module \mathcal{L} from equation (3.10) as they yield the right period according to equation (3.12). We will comment on this choice in section 4.4.4 when discussing resonance-assisted tunneling. According to equation (3.11) the order of this rank-2 resonance is two. This is because $\mathbf{r} = (1, -1)$ is the smallest resonance in the corresponding resonance module $\mathcal{L}(\boldsymbol{\omega} = (1/5, 1/5))$. Note that this is the order of the rank-2 resonance. This resonance is the single point $(1/5, 1/5)$ given by both resonances in equation (3.94). The order of the rank-1 resonances $5 : 0 : 1$ and $6 : -1 : 1$ separately is six and eight, respectively.

Now that we have introduced nonlinear resonances we can have a look at the section through the 4D phase space. This is shown in figure 3.11 from two different perspectives. Shown in red are again regular tori around the central EE-type fixed point at $(p_1, p_2, q_1, q_2) = (0, 0, 0, 0)$. Embedded in this regular domain are orbits shown in orange. They belong to the broken tori of the rank-2 resonance around the period-5 orbit. Contrary to the fixed point at the center, none of the iterates of the periodic orbit is part of the section. The five p_2 values are only close to zero. Due to this closeness it is meaningful to plot their projection into this section. In between the EE-type periodic orbits \mathbf{u}_p there is also an EH-type period-5 orbit. This corresponds exactly to the general observation from section 3.2.1. The EE-type and EH-type periodic orbits are shown in red and mint, respectively, corresponding to the colors in figure 3.1.

The period-5 orbit trivially has the winding numbers $\boldsymbol{\omega} = (1/5, 1/5)$ and thereby fulfills all of the above resonance conditions (3.94). This is not the case for the uncoupled system figure 3.10(c) where we find a 5 : 1 resonance in the first degree of freedom but none in the second. Hence, the motion in the first degree of freedom is a period-5 orbit but for most initial conditions the second degree of freedom fills a 1D torus densely. This resembles the case (ii) in figure 3.2.

The EE-type periodic orbit resides at the center of the elliptic regions shown in orange. The EH-type periodic orbit lies in between. It is surrounded by a chaotic orbit shown in blue. Initial conditions placed there yield orbits which are chaotic but stay a very long time in this narrow stochastic layer. If iterated long enough, they will escape the resonance zone and enter the large chaotic sea. In

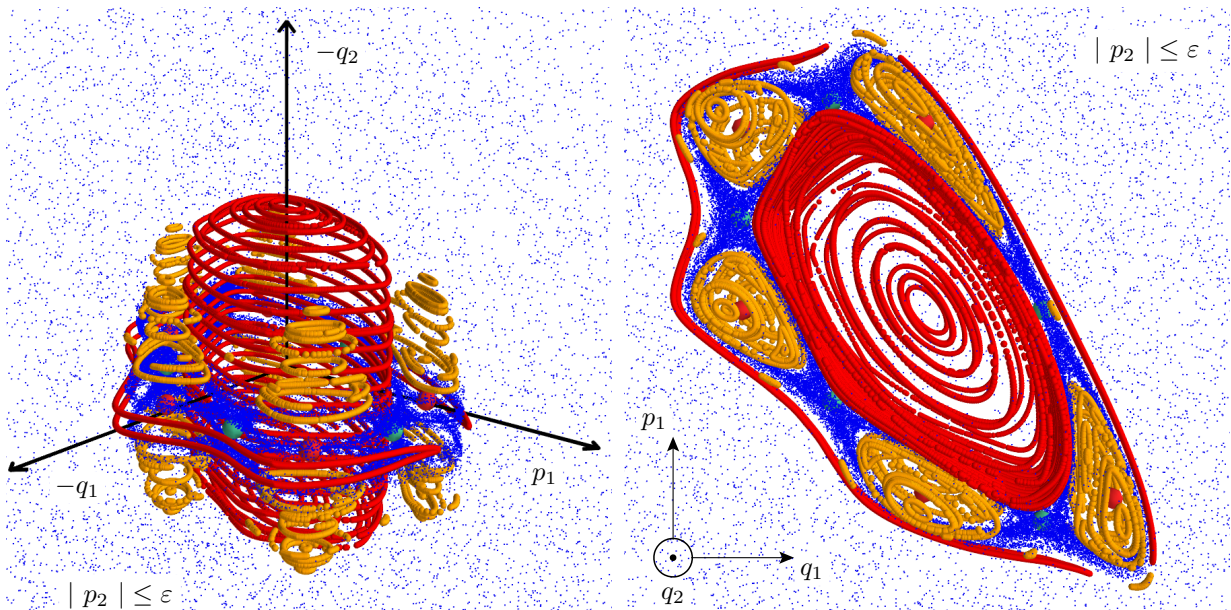


Figure 3.11.: Section through the 4D phase space of the designed map \mathcal{P}_{nnc} . The left and the right picture show the same data but differ in the spectator's perspective. Due to the nonlinear terms in equation (3.91) the regular region contains a large resonance structure depicted in orange. At the center of the orange objects there is an elliptic–elliptic period-5 orbit shown by red spheres. The blue orbit in between the resonance structure is a chaotic orbit which has not yet entered the chaotic sea. The axes in the left hand side plot are centered at $(0, 0, 0)$. On the right hand side the axes are shifted for clarity.

section 3.4.2 we will also discuss the other way around where chaotic orbits approach this zone from the outside and get trapped at regular structures.

FLI values and volume of the regular and stochastic region

A FLI calculation performed similar to the designed map with linear regular region, see page 41, shows that there is not only a regular and a fully chaotic component but also a stochastic region. The corresponding histogram is shown in figure 3.12. The volume of the regular region is estimated to be

$$V_{4D}^{\text{reg, numerical}} = \frac{\#\{\text{initial conditions with FLI} \leq 15\}}{128^4} = \frac{2,525,893}{268,435,456} = 0.00941 \quad (3.95)$$

and the volume of the stochastic region is

$$V_{4D}^{\text{stochastic, numerical}} = \frac{\#\{\text{initial conditions with FLI} \in (15, 100]\}}{128^4} = \frac{296,093}{268,435,456} = 0.00110. \quad (3.96)$$

These quantities are used later to estimate the number of quantum eigenstates living on these phase space regions, see section 4.2.2.

The FLI histogram can be used to colorize the FLI values in the 3D sections appropriately to reveal the extent of regular and chaotic regions. Apart from the distinction between regular and chaotic motion it is also possible to detect resonantly broken motion and regions of only weak chaoticity [140]. A phase-space section including FLI values is shown in figure 3.13. The extent of the EE-type period-5

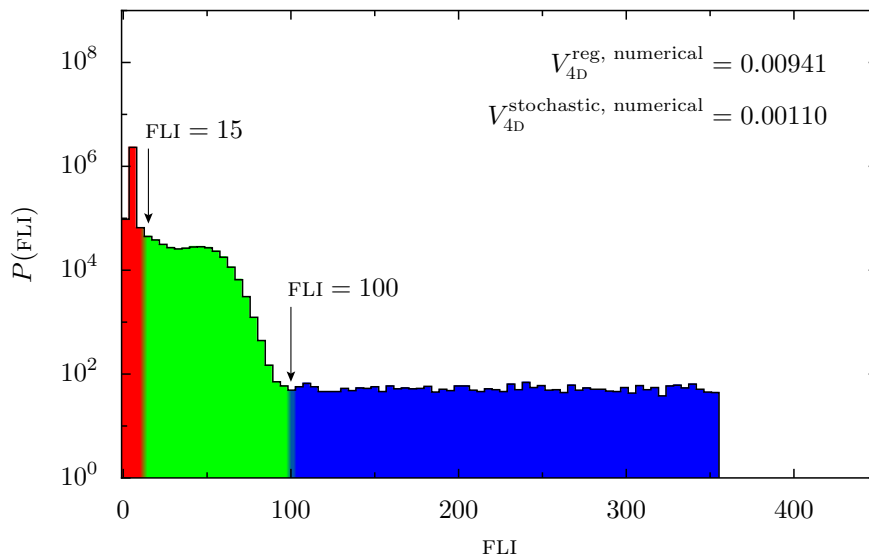


Figure 3.12.: Histogram of FLI values calculated for \mathcal{P}_{nnc} . The abscissa shows the FLI values on a linear scale while the ordinate shows the absolute number of FLI values on a logarithmic scale. Contrary to \mathcal{P}_{lu} there exists a stochastic region (green) in the phase space of \mathcal{P}_{nnc} . The grid of initial conditions is $128 \times 128 \times 128 \times 128$. The FLI calculation was aborted if the FLI went above 450 such that all chaotic orbits beyond $\text{FLI} = 450$ belong to just one bin.

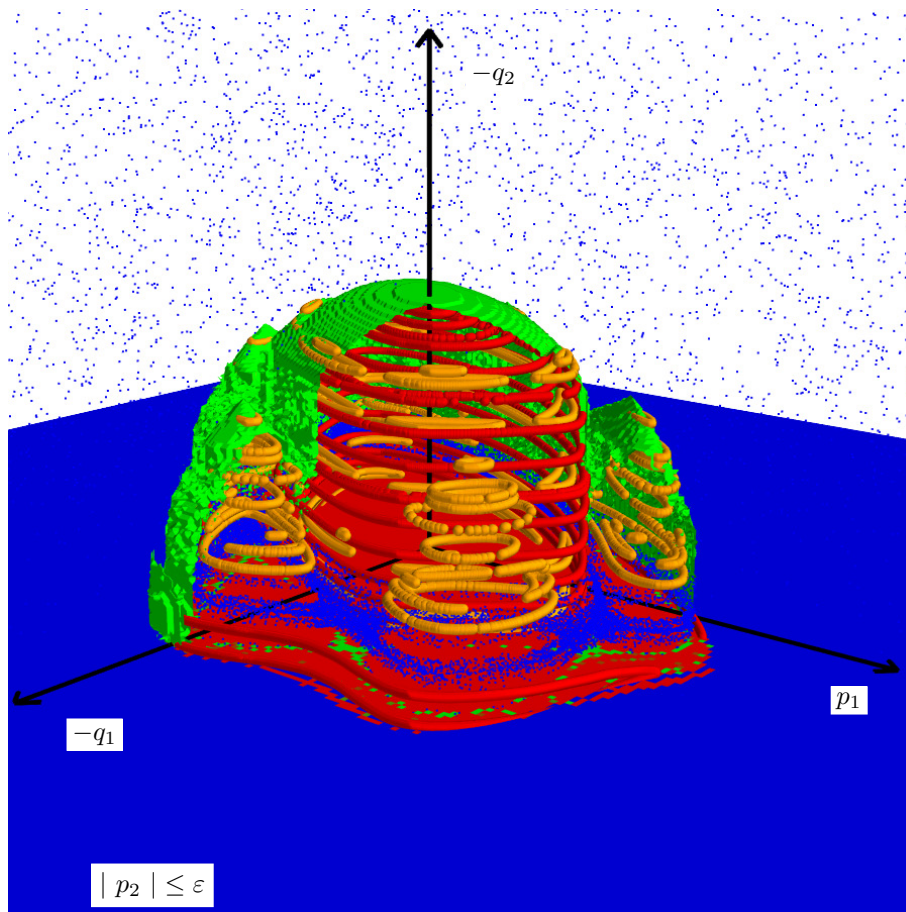


Figure 3.13.: Section through the 4D phase space of the designed map \mathcal{P}_{nnc} . The displayed orbits are the same as in figure 3.11. Additionally FLI values are visualized in the (q_1, p_1) plane and by a surface of a constant FLI value (green). The constant value of this isosurface is chosen such that it shows the border between stochastic (green) and chaotic (blue) region. The isosurface is cut towards the spectator for better visibility.

resonance zone is now visible in this plot. This is achieved by choosing the surface of constant FLI values to be at $\text{FLI} = 100$. According to figure 3.12 this is between stochastic (green) and chaotic (blue) FLI values, hence the surface is shown in green in figure 3.13.

Frequency analysis for rank-2 resonance

As the rank-2 resonance from equation (3.94) gives rise to a periodic orbit, it is possible to investigate this resonance separately by means of the frequency map analysis from section 3.4.2. In order to do so, the 5-fold map is evaluated in the vicinity of one of the EE-type zones depicted in orange in figures 3.11 and 3.13 and the corresponding frequencies are called ω'_j in order to distinguish them from the frequencies of the 1-fold map ω_j . The resonance itself yields further substructures which can be investigated using the frequency map \mathcal{F} , see figure 3.14. Note that it is not important in which section the 2D grid of initial conditions is chosen. A 2D grid in the (q_1, q_2) -plane is suited as well as a grid in the coordinate system given by a skew section. Both choices intersect enough tori to give a complete image of the frequency map. The outcome of the frequency map analysis does not depend sensitively on the concrete choice of the plane of initial conditions. This is an advantage opposed to the use of phase-space sections which rely on a most appropriate choice of the section.

The analysis shows that the considered subsystem of the rank-2 EE-type period-5 orbit is again near-integrable. It yields two rank-1 resonances, namely the $3 : 1 : 3$ and the $4 : 1 : 4$ resonance, as indicated in the figure. Their order is seven and nine, respectively. They intersect on the frequency plane at $(\omega'_1, \omega'_2) = (1, 0)$ which is equivalent to $(0, 0)$ as the frequencies are defined on $\omega'_j \in [0, 1)$, see page 26. This intersection is again not part of the image of \mathcal{F} . The rank-2 resonance induced by the intersection has order two. Its period is one in terms of the 5-fold map used for the frequency analysis. It therefore corresponds to the period-5 orbit \mathbf{u}_p at the center of the resonance zone. Furthermore,

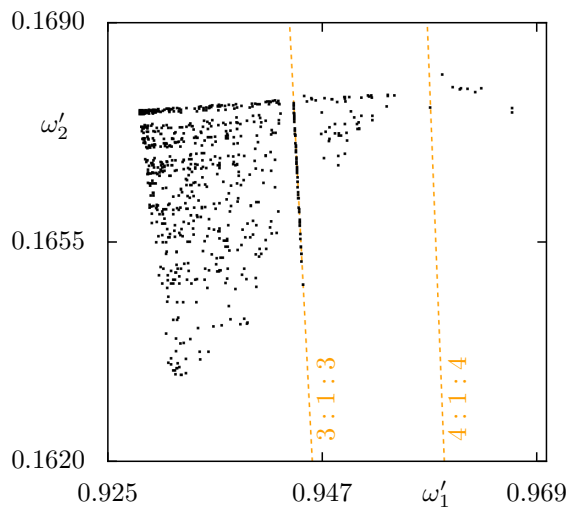


Figure 3.14.: Image of the frequency map \mathcal{F} for the main rank-2 EE-type period-5 resonance of the designed map \mathcal{P}_{unc} . Again there are several resonances visible. This time the 5-fold map is used to calculate the sequence of points from which the frequencies are determined. The initial conditions were placed around the point $(p_1, p_2, q_1, q_2) = (0.17113955, 0.00258983, -0.17379745, -0.00650123)$ for which the phase-space sections are shown later in figure 3.18 to figure 3.21.

the range of ω'_2 values in figure 3.14 is just given by the values of ω_2 along the $5 : 0 : 1$ resonance line in figure 3.10(d). They are related via the period $p = 5$ of the fixed point according to

$$\omega'_2 = 5 \cdot \omega_2 \pmod{1}. \quad (3.97)$$

For another example with a period-4 resonance see the discussion of figure 3.27.

Phase-space sections at different positions p_1 and p_2

In order to see the whole phase space, it is necessary to shift the 3D section through the phase space. This is done by choosing $p_2 = p_2^i$ for several p_2^i which is shown in figure 3.15. This is comparable to the double sections introduced by Froéschle [140, 147] for single orbits. Another choice for a phase-space section is given by choosing a fixed p_1 such that the section contains the second degree of freedom completely. The corresponding orbits are shown in figure 3.16. Here the resonance zones are not visible inside the same section but appear at different values of p_1 , cf. figure 3.15. By shifting p_1 this section also shows that there are no resonances with the external driving in the second degree of freedom, which we already noticed in figure 3.10, where the frequency map \mathcal{F} shows no irregularities in ω_2 . Due to the weak coupling such resonances would appear as island structures on the (p_2, q_2) -planes and would also be visible in the FLI planes.

Using color to provide the 4th coordinate

The varying section conditions through the 4D phase space in figures 3.15 and 3.16 allow to visualize several orbits at a time. If only one orbit is considered, then it is possible to use a projection onto the 3D section and encode the fourth coordinate by a color scale as is done for example in reference [91]. The authors call this dyeing of orbits accompanied with a 3D plotting “the method of color and rotation”. It is further used to analyze galactic potentials [92, 146].

The advantage of such projections is that we can read of the minimal and maximal extent of an orbit in the three directions of the 3D plots. This is possible as now all points of the orbit are shown in contrast to the above section through the phase space. Furthermore, it is possible to distinguish whether an orbit runs on a torus given by one connected component or if it visits several separated objects successively. This is an information which cannot be deduced from the 3D phase-space sections directly. It unveils if the resonantly broken tori were subject to a rank-1 or rank-2 resonance condition [107, 108, page R4301], cf. section 3.2.1.

Figure 3.17 shows a selection of orbits of different types from \mathcal{P}_{nnc} . As depicted by the color bar in figure 3.17(a), the colormap ranges from blue over green to red. The maximal values covered by the orbits are $|p_2| = 0.17$. Figure 3.17(a) shows an orbit inside the main regular island. It appears as one connected torus. The torus in figure 3.17(b) is of the same topology but lies further away from the center than the rank-2 resonance surrounding the period-5 orbit. In 2D maps the orbit in figure 3.17(b) would be said to lie outside the resonance zone. This is imprecise here as the resonance zone does not divide the phase space into an inside and an outside part. Figure 3.17(c) shows an

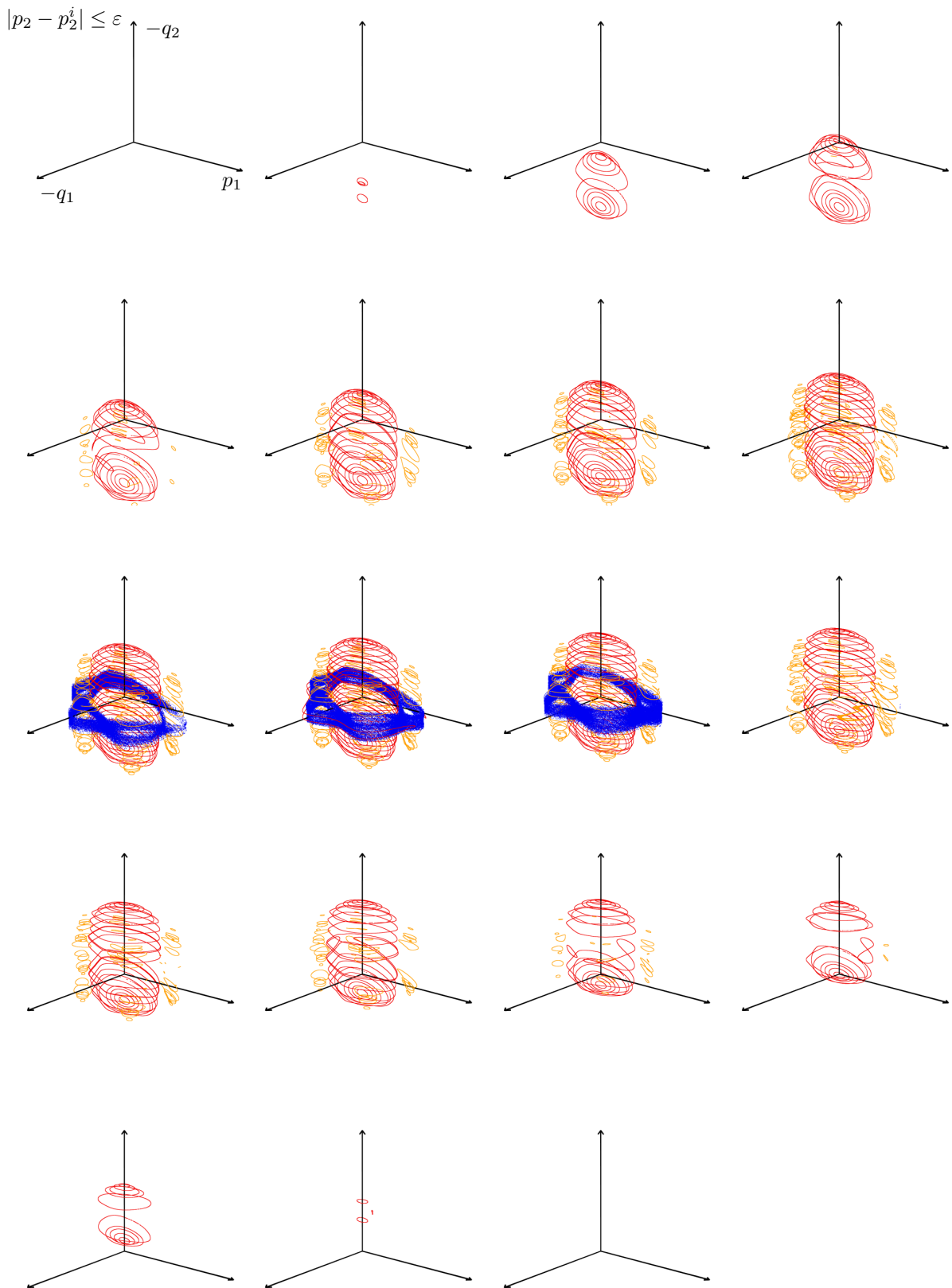


Figure 3.15.: Sections through the 4D phase space of \mathcal{P}_{nnc} at various positions $p_2 = p_2^i$ with $p_2^i = -0.315 + 0.035 \cdot i = -0.315, -0.28, \dots, 0.315$ for $i = 0, 1, \dots, 18$. As both degrees of freedom are only weakly coupled inside the regular domain, the resonance zones and the main island just change in size. Sections with p_2^i close to the phase-space boundary at $|p_2^i| = 0.5$ (not shown) yield chaotic orbits only.

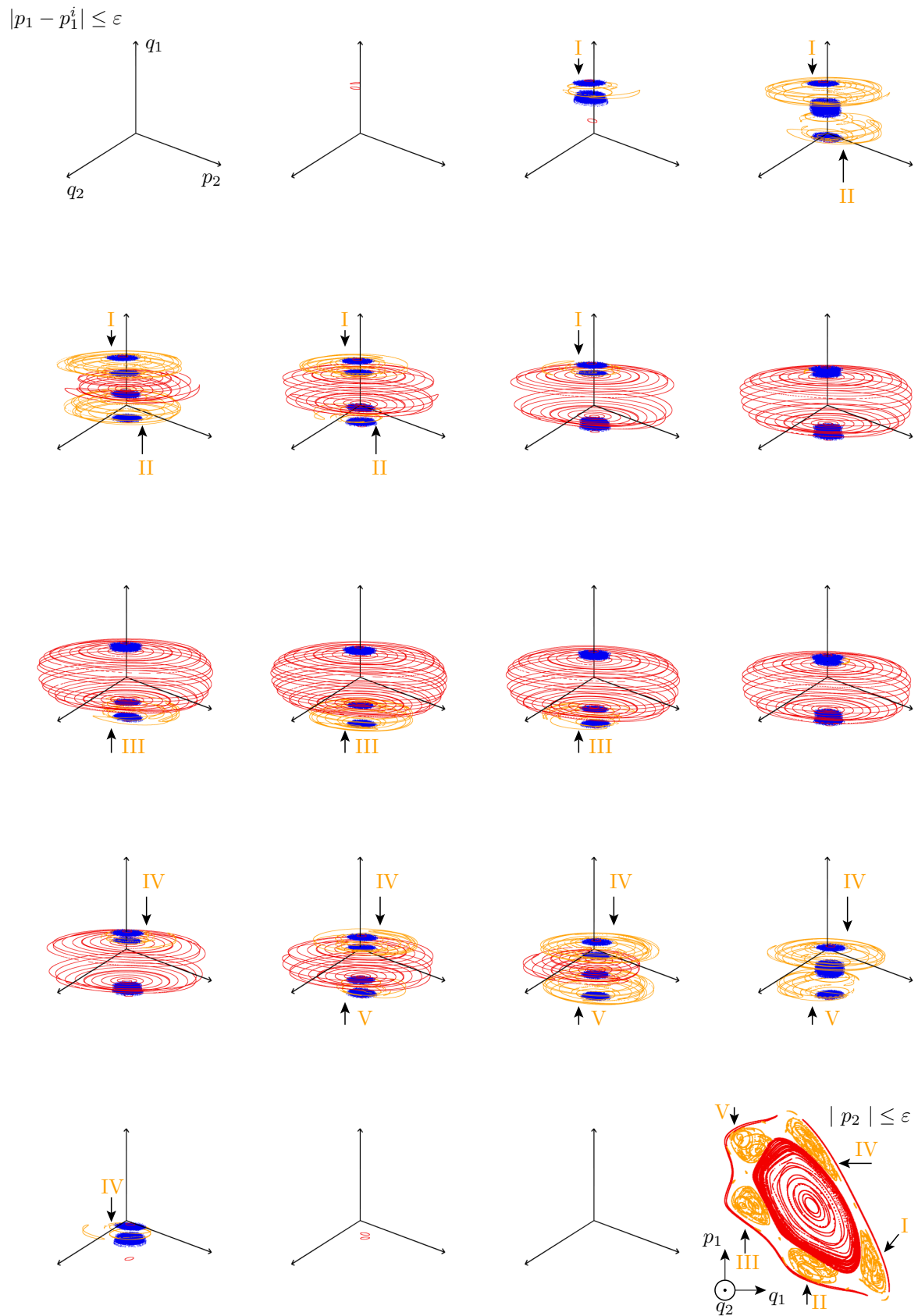


Figure 3.16.: Sections through the 4D phase space of \mathcal{P}_{nnc} at various positions $p_1 = p_1^i$ with $p_1^i = -0.288 + 0.042 \cdot i = -0.288, -0.256, -0.182, \dots, 0.288$ for $i = 0, 1, \dots, 18$. Only up to two resonance zones of the period-5 orbit are visible at the same time as the section shifts through them while changing p_1^i . The labels I to V denote the five resonance-zones around the period-5 EE-type orbit. For comparison the resonances are labeled the same way in the inset on the lower right which is identical to figure 3.11.

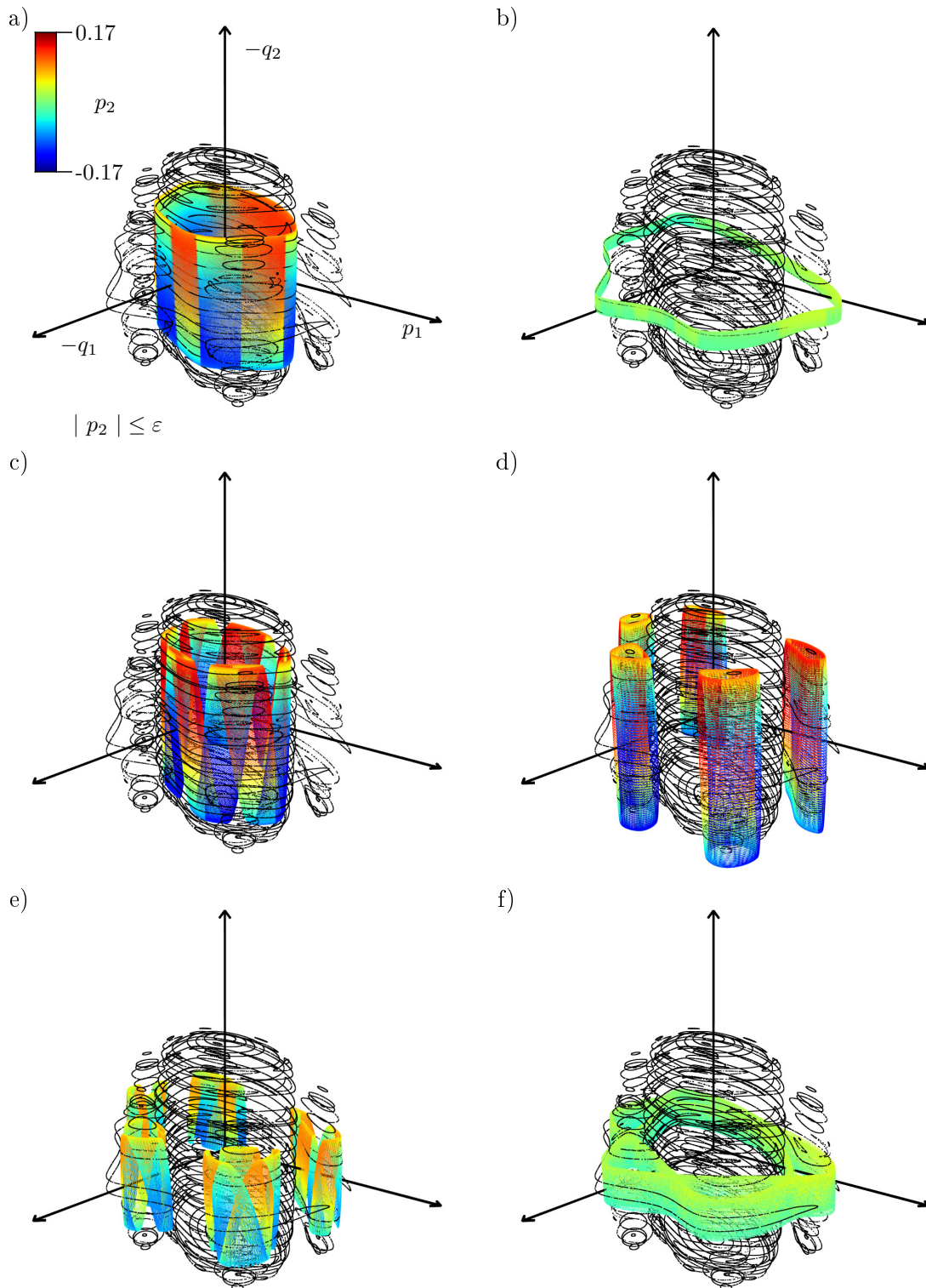


Figure 3.17.: Projection of different 4D orbits of \mathcal{P}_{nnc} using color to visualize the fourth coordinate p_2 . Shown in black are orbits inside the section given by $|p_2| < \varepsilon$. Figures (a) and (b) show orbits belonging to the main regular island inside and outside the resonance, respectively. Figures (c) and (d) show a rank-1 and rank-2 resonance inside the main island, respectively. Figure (e) shows an orbit inside a rank-1 resonance embedded in the rank-2 resonance of figure (d). Figure (f) shows an orbit in the stochastic layer around the rank-2 resonance of figure (d).

orbit within the elliptic part of the rank-1 $6 : -1 : 1$ resonance around the central fixed point. This resonance is already addressed in figure 3.10(d). Within this resonance zone there exists a 1D line being invariant under the dynamics, cf. column (iii) in figure 3.2. Therefore, the resonantly broken tori of this resonance are still given by one connected component in phase space, as is visible in the projection of figure 3.17(c). Figure 3.17(d) shows an orbit in the EE-type vicinity of the rank-2 resonance given by the period-5 periodic orbit. It is clearly visible from the projected orbit that this phase-space structure is decomposed into five disjoint regions. In each of them the topology of the object is the same as the one of the orbits in the main island. As seen in figure 3.14 the vicinity of the EE-type period-5 orbit yields a near-integrable system. This system includes resonances with respect to the 5-fold map. An orbit inside such a sub-resonance is depicted in figure 3.17(e). It belongs to the rank-1 $3 : 1 : 3$ resonance of this subsystem seen in figure 3.14. Figure 3.17(f) shows a chaotic orbit in the stochastic layer of the system. The absence of red and blue colors emphasizes that the stochastic region is indeed a very narrow object in the 4D phase space. The shown orbit only covers a range of $|p_2| < 0.052$.

Skew phase-space sections containing invariant eigenspaces

The skew section introduced in section 3.3.3 can be used to visualize the phase-space structure in the vicinity of one of the elliptic–elliptic resonance zones, namely the period-5 orbit at

$$\mathbf{u}_p := (p_1, p_2, q_1, q_2) = (0.17113955, 0.00258983, -0.17379745, -0.00650123). \quad (3.98)$$

This is shown in figures 3.18 to 3.21. All contain a comparison of perpendicular and skew sections by means of orbits shown in gray. However, in each figure another set of orbits and thereby another aspect of the phase space is highlighted. The perpendicular sections are at $p_2 = 0.00258983$ in figure (c) and at $p_1 = 0.17113955$ in figure (d). The skew sections defined by the linearization $D\mathcal{P}_{\text{nnc}}$, see equation (3.63), contain either the first (a) or the second degree of freedom (b) completely. The sections are all shifted to contain \mathbf{u}_p . In all figures 3.18 to 3.21 the 2D planes tangential to the central manifold of the first and second degree of freedom are shown in blue and green, respectively. Figure (a) contains the blue plane completely while the green one is completely contained in (b) only. In the respective other plots the planes are given by lines.

In figure 3.18 the orbits started on the tangential planes are shown in orange and red. If the orbits were started on the respective center manifold instead of on its tangential, then these orbits would lie on 1D tori. This remarkable difference allows to find the center manifold numerically [109]. As the highlighted orbits in figure 3.18 are started only on the tangential plane to the center manifold they are not exactly 1D but very thin. Hence, the orange and red orbit shown in figure 3.18 stay close to the plane they started on and lie almost completely inside the skew sections (a) and (b), respectively. If the system would be perfectly linear in the vicinity of the periodic point \mathbf{u}_p , then the orbits would lie on these planes exactly. Due to the nonlinearity the orbits bend away from the 2D plane as the initial conditions move further away from \mathbf{u}_p in the middle. The perpendicular sections (c) and (d)

cannot reproduce this clear picture. However, these sections look still similar to the skew ones due to the weak coupling of both degrees of freedom.

In figure 3.19 the orbits are started on a surface parallel to the blue plane of the first degree of freedom. Their initial conditions are placed with increasing distance from the green plane of the second degree of freedom. The corresponding colors are red, orange, and yellow. They highlight the same orbits in all figures (a) to (d). Especially the fact that the initial conditions are chosen parallel to the blue plane with increasing distance to the green plane is clearly visible in (a), where the orbits are concentric, and (b), where the orbits are stacked on top of each other along the blue line.

Figure 3.20 is similar to figure 3.19. This time the orbits are started parallel to the green plane of the second degree of freedom with increasing distance from the plane of the first degree of freedom shown in blue. Again the colors are red, orange, and yellow, respectively.

Finally figure 3.21 shows a chaotic orbit in the stochastic layer in between the EE-type surrounding of \mathbf{u}_p . This layer also contains the EH-type period-5 orbits (not shown) mentioned on page 18.

The orbits shown in figures 3.18 to 3.21 match the observation from the linear case in figure 3.7. There the uncoupled system \mathcal{P}_{llu} was depicted in a skew section $|\cos(\alpha)p_2 - \sin(\alpha)p_1| = 0$. For $\alpha = 0$ and $\alpha = \pi/2$ the sections of \mathcal{P}_{llu} look simple. For intermediate values of α they resemble the structures of the nonlinear map \mathcal{P}_{nnc} viewed in perpendicular sections, $|p_2| = 0$ or $|p_1| = 0$. We can deduce that a part of the effects seen in the nonlinear map \mathcal{P}_{nnc} is due to an inappropriate choice of the section. However, contrary to the uncoupled case it is impossible to globally define an appropriate plane section. Only the vicinity of the periodic point is clarified by the choice from equation (3.63).

Arnold diffusion

In section 3.2.4 the Arnold web is introduced. It describes the chaotic region surrounding the thin resonance zones in near-integrable systems. The system \mathcal{P}_{nnc} we consider here, however, is not near-integrable in a global sense. It is given by a predominantly regular region embedded in a large chaotic sea. In order to discuss Arnold diffusion and the existence of an Arnold web, it is necessary to restrict ourselves to the regular region. As mentioned in section 3.4.2, the cubic terms in the potential transform the regular region of \mathcal{P}_{llu} into the nonlinear and near-integrable one of \mathcal{P}_{nnc} . Therefore, this system is suitable to perform the above mentioned frequency analysis on page 46 and yields an Arnold web. This web is connected to the outside chaotic sea.

In order to analyze this connection it is possible to search for orbits which, for example, start in the stochastic domain deep inside the regular region and very slowly wander outside into the large chaotic sea. Besides calculating such orbits it is also of interest to determine the velocity of this transport towards the chaotic sea, especially under the premise that it is a normal diffusion process. We thereby neglect the possibility that it might also be possible that the transport within the Arnold web might be sub-diffusive due to trapping mechanisms.

The velocity of the diffusion is relevant to understand how quantum mechanical eigenstates are able to penetrate into the region of stochastic motion surrounding the regular islands. The very small rate of diffusion along the resonance layers might be linked to how eigenfunctions decay into the Arnold

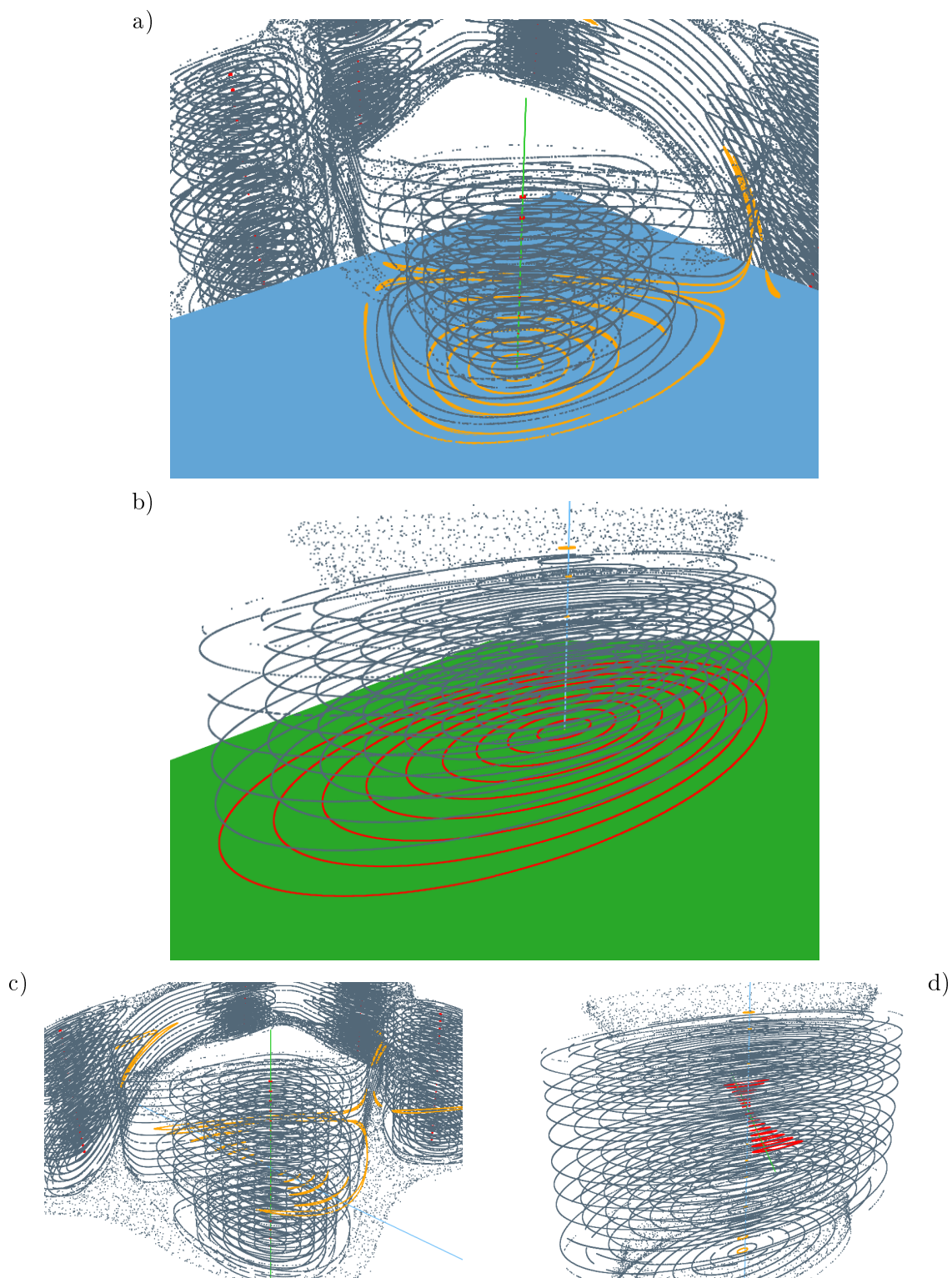


Figure 3.18.: Shown in gray are several regular orbits in the vicinity of \mathbf{u}_p . Shown in blue and green are the tangential planes to the center manifold of \mathbf{u}_p . Shown in orange and red are orbits started on the blue or green surface, respectively.

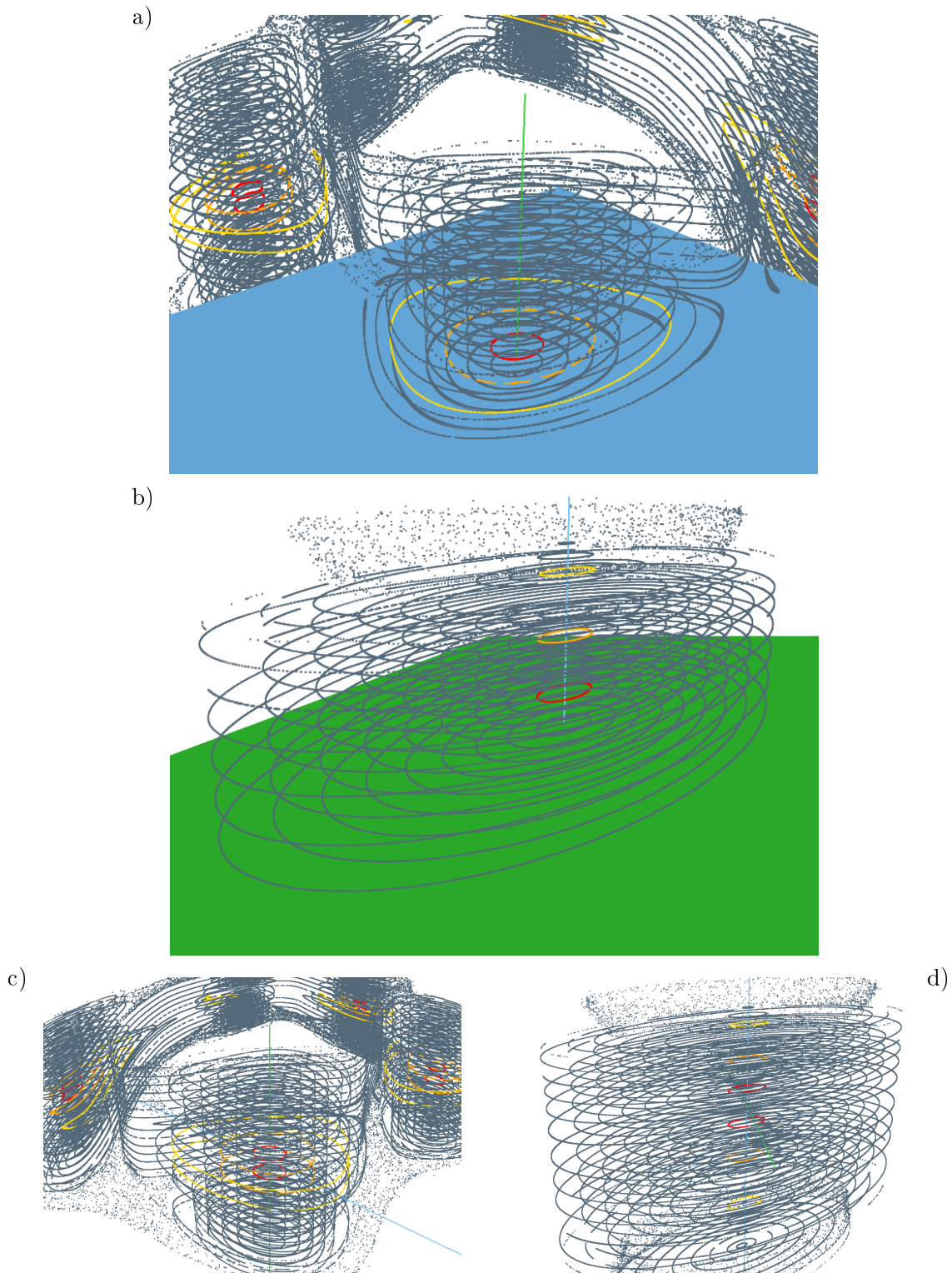


Figure 3.19.: Plot like in figure 3.18. The initial conditions are placed with increasing distance (red to yellow) from the tangential plane of the second degree of freedom (green) parallel to the plane of the first degree of freedom (blue).

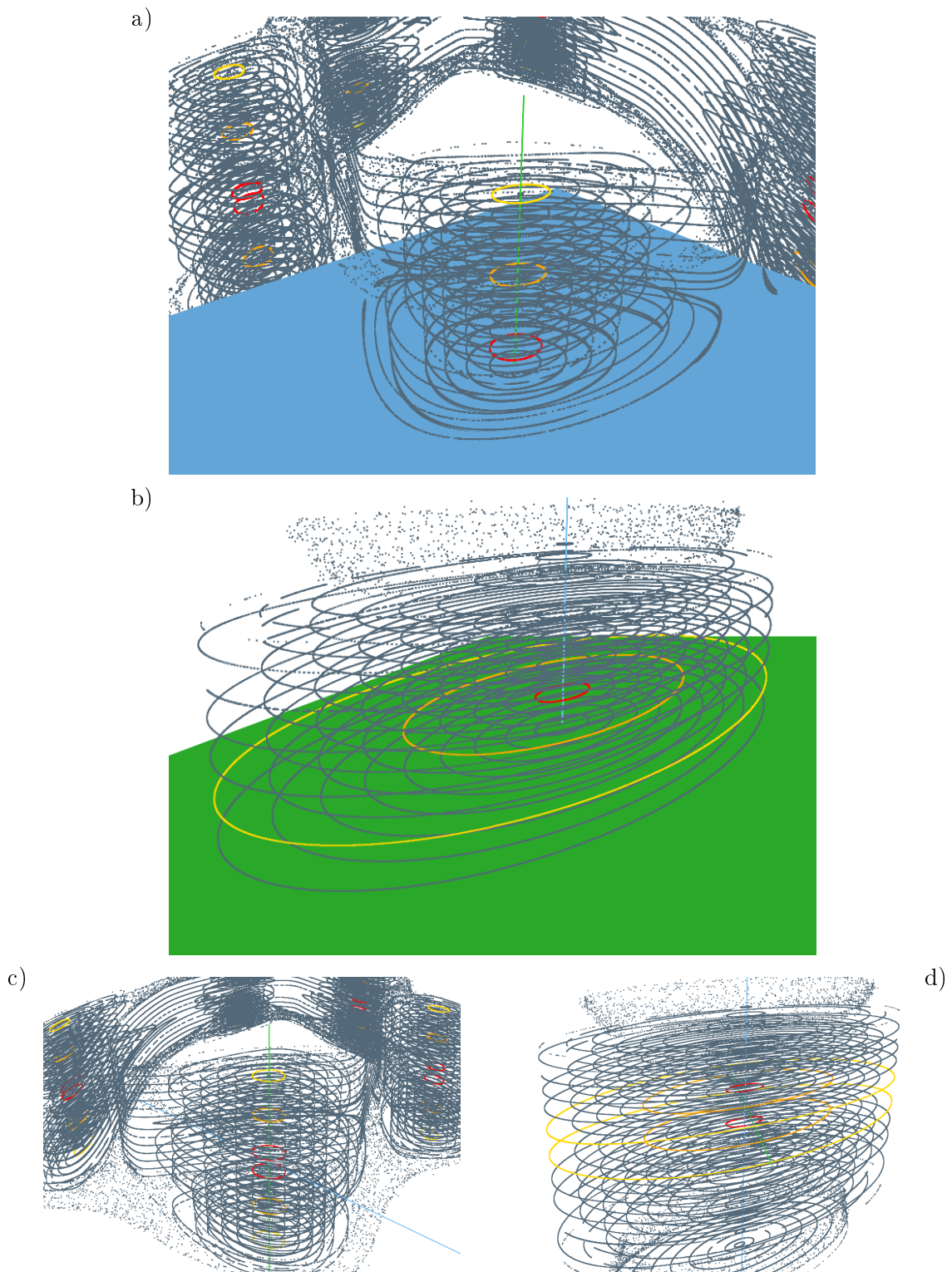


Figure 3.20.: Plot like in figure 3.19. The initial conditions are now placed with increasing distance (red to yellow) from the tangential plane of the first degree of freedom (blue) parallel to the plane of the second degree of freedom (green).

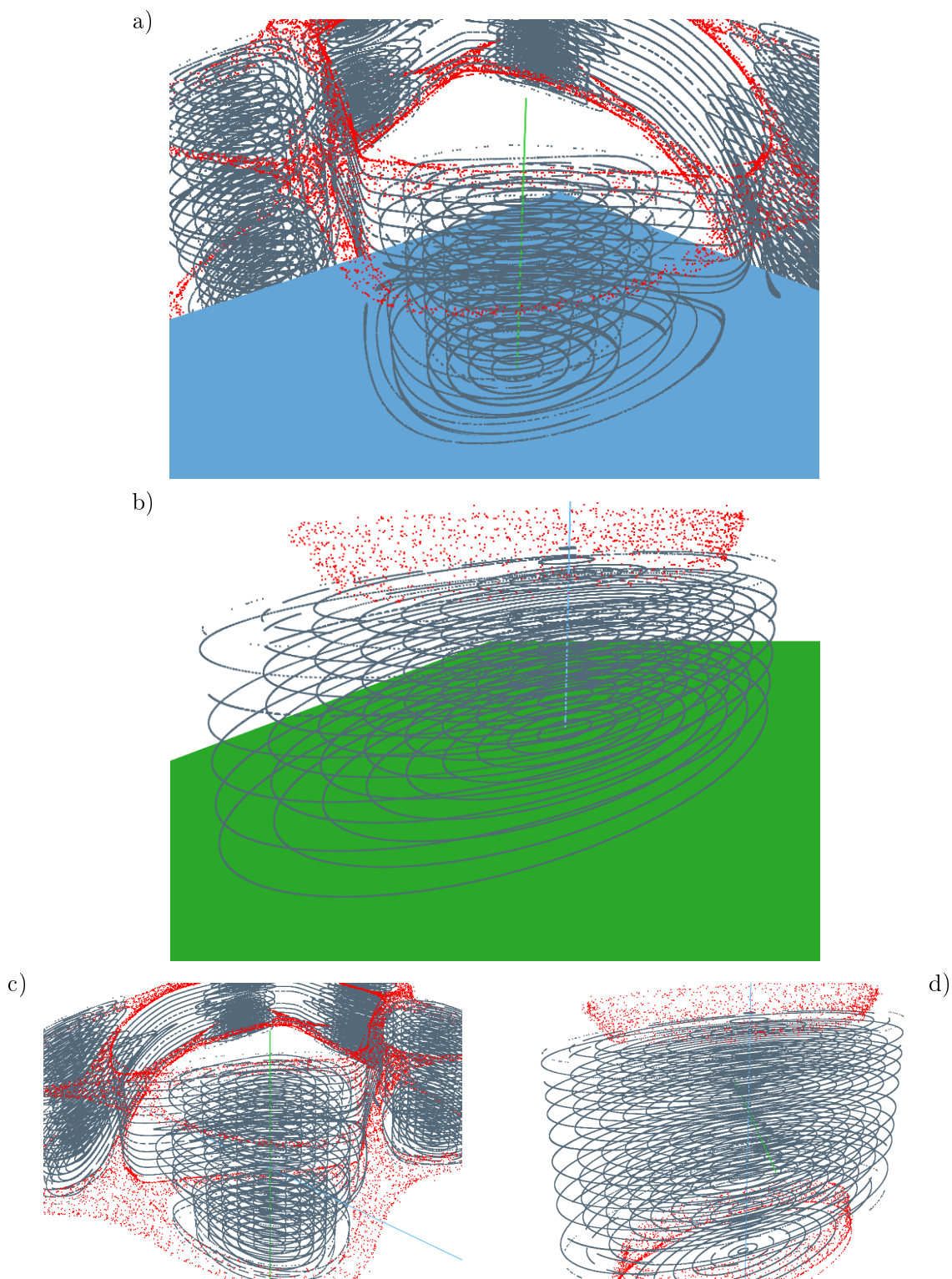


Figure 3.21.: Plot like in figure 3.18. Highlighted is an orbit in the stochastic layer.

web [51–53] just as it is known from dynamical localization [155].

In near-integrable systems as described in section 3.2.4 it is possible to give the direction of Arnold diffusion by means of approximately conserved quantities. This direction can then be used to calculate the rate of the slow diffusion along the resonance layers [37, 43]. This however is not viable in our case of a regular island embedded in a large chaotic sea. Although we might interpret the given system as being the outcome of a small perturbation of some regular system H_{reg} , it is unknown how to build such a fictitious system. Possible ways could be the methods already used for 2D maps [125, 138], namely the analysis of fundamental frequencies, normal form analysis, or Lie-transformation methods. In the case of 4D maps, however, they do not necessarily yield regular systems. For example a normal form might not yield a fully integrable system [107]. Furthermore, these approximations might not be precise enough to determine the direction of the slow diffusion accurately. This is due to the fact that this direction is calculated in the stochastic layers, where the approximations are of less accuracy than in the regular center. Apart from these problems the pure knowledge of H_{reg} is not sufficient as it is also necessary to know the corresponding action–angle variables. We do not address such constructions here and omit the calculation of diffusion coefficients.

3.4.3. Generic maps: Coupled standard maps, \mathcal{P}_{csm}

Although the designed map \mathcal{P}_{nnc} provides a regular island with nonlinear resonances, the transition into the chaotic sea is still very sharp. We can use the coupled standard maps introduced in section 3.1 in order to overcome this non-generic feature. The mapping is given by

$$\begin{aligned} p'_1 &= p_1 + \frac{K_1}{2\pi} \sin(2\pi q'_1) + \frac{\xi_{12}}{2\pi} \sin(2\pi(q'_1 + q'_2)) + 1/2 \pmod{1 - 1/2} \\ p'_2 &= p_2 + \frac{K_2}{2\pi} \sin(2\pi q'_2) + \frac{\xi_{12}}{2\pi} \sin(2\pi(q'_1 + q'_2)) + 1/2 \pmod{1 - 1/2} \\ q'_1 &= q_1 + p_1 \pmod{1} \\ q'_2 &= q_2 + p_2 \pmod{1}. \end{aligned} \tag{3.1}$$

and yields three parameters K_1, K_2 and ξ_{12} . In order to get a phase space with a regular region embedded in a larger chaotic domain we choose $K_1 = 2.25, K_2 = 3.0$, and $\xi_{12} = 0.1$. We will call the map using this parameter set \mathcal{P}_{csm} . In order to analyze the phase-space structure of this system we will first calculate the FLI distribution and then show 3D phase-space sections including this FLI values.

FLI values and volume of the regular and stochastic region

Like for the designed map in section 3.4.1 it is possible to calculate the FLI on a grid over the 4D phase space and thereby estimate the volume of the regular region as well as the region of the embedded stochastic layers. The histogram in figure 3.22 presents the distribution of FLI values calculated on a $128 \times 128 \times 128 \times 128$ grid. Contrary to the case of the designed map with linear regular region in figure 3.8 many resonances are present for the coupled standard maps. Therefore the portion of

phase space with FLI values between regular and chaotic motion is much larger. This is shown by the green area of the histogram. Like in the FLI histogram of \mathcal{P}_{nnc} in figure 3.12 three different kind of orbits can be classified. The leftmost peak is regular and marked in red, the rightmost peak chaotic and therefore marked in blue. The FLI values in between originate from the thin stochastic layers in the regular region and are marked in green.

Again the FLI histogram allows to estimate the volume of the regular region as well as the stochastic zone. The volumes are

$$V_{4\text{D}}^{\text{reg, numerical}} = \frac{\#\{\text{initial conditions with FLI} \leq 15\}}{128^4} = \frac{1,739,913}{268,435,456} = 0.00648 \quad (3.99)$$

and

$$V_{4\text{D}}^{\text{stochastic, numerical}} = \frac{\#\{\text{initial conditions with FLI} \in (15, 65]\}}{128^4} = \frac{1,839,004}{268,435,456} = 0.00685. \quad (3.100)$$

It is important to note that the volume of the stochastic layer of \mathcal{P}_{csm} is by a factor of six larger than for \mathcal{P}_{nnc} , cf. equation (3.96).

The colormap defined by this histogram is also used in figure 3.23 to display the FLI values within a phase-space section. They allow for a clear visualization of the regular part of phase space and the stochastic layer in the coupled standard maps \mathcal{P}_{csm} . The FLI is calculated on a 2D plane given by the first degree of freedom (q_1, p_1) and on the whole 3D section. On the 2D plane the values are indicated directly by their color. The 3D values are visualized by a surface of constant FLI value, $\text{FLI} = 65$.

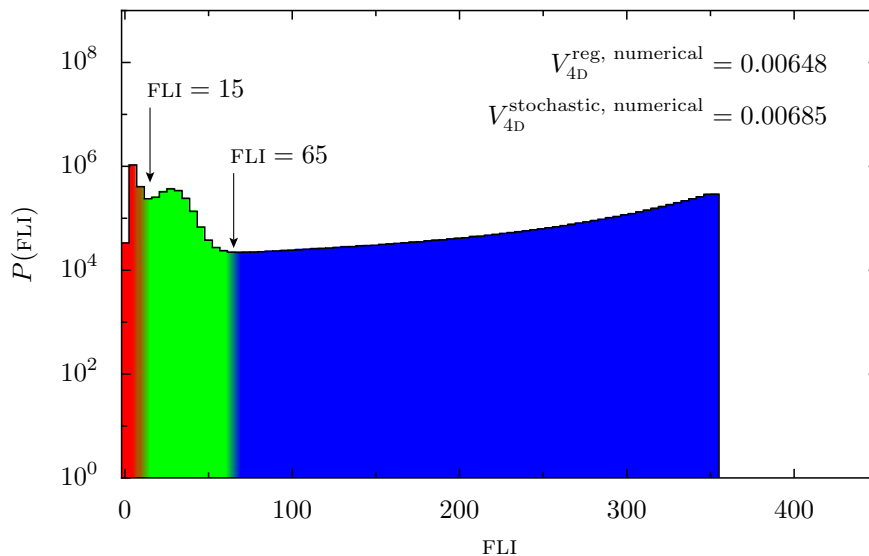


Figure 3.22.: Histogram of FLI values calculated for \mathcal{P}_{csm} . The abscissa shows the FLI values on a linear scale while the ordinate shows the absolute number of FLI values on a logarithmic scale. The colormap in the background is chosen according to the peaks belonging to regular, weakly chaotic, and fully chaotic motion. The FLI-calculation was aborted if the FLI went above 450. The grid of initial conditions is $128 \times 128 \times 128 \times 128$.

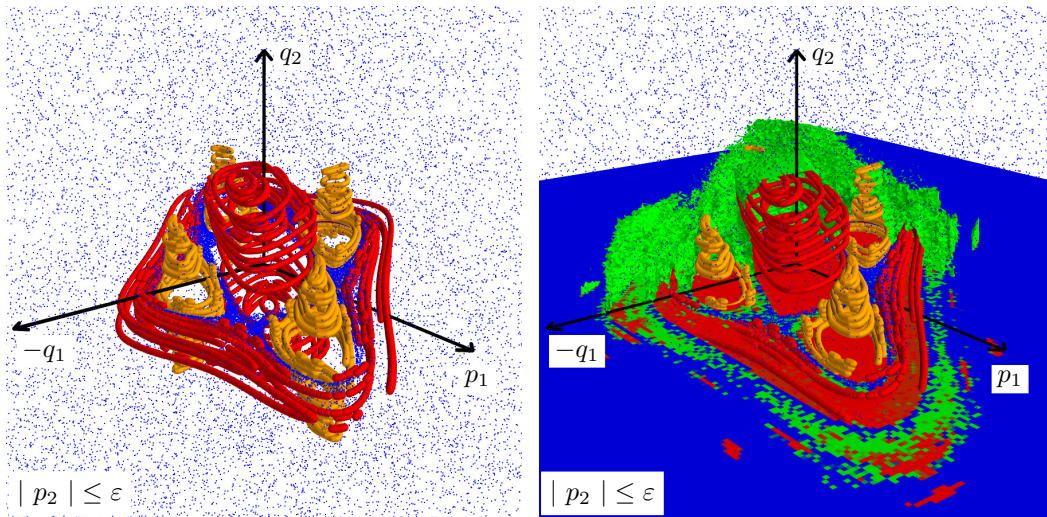


Figure 3.23.: Section of the coupled standard maps \mathcal{P}_{csm} including FLI values. Shown in red are regular orbits of the main island. Resonantly broken tori within the island are marked in orange. Chaotic orbits are shown in blue. The FLI is shown on a 2D (q_1, p_1) plane and by a surface of constant FLI value. This isosurface given by $\text{FLI} = 65$ is cut towards the spectator for better visibility. The orbits in this phase space section are calculated using $\varepsilon = 10^{-5}$.

This isosurface therefore marks the interface between stochastic and fully chaotic motion.

Figure 3.23 features regular orbits around the central fixed point $(p_1, p_2, q_1, q_2) = (0.0, 0.0, 0.5, 0.5)$ shown in red and chaotic orbits shown in blue. The regular region is surrounded by a large chain of resonances shown in orange. This chain is given by a EE-type period-4 orbit. The corresponding EH-type orbit is embedded in the stochastic layer. A chaotic orbit within this layer is also shown in blue. If the FLI values are also visualized, then the extent of the regular region and the interface between stochastic and fully chaotic region gets visible due to the appropriate choice of the colormap according to figure 3.22.

The main difference to 2D maps is that chaotic orbits starting in the outside chaotic component can penetrate the stochastic layer around the resonance chain. This is because neither the broken tori shown in orange nor the outermost regular orbits shown in red are able to separate the central fixed point from the chaotic sea. In figure 3.24 a part of such a chaotic orbit going into the stochastic layer is shown. It was started in the chaotic component and iterated for $N = 3.9 \cdot 10^{12}$ iterations. The majority of the iterates lie in the chaotic component away from the regular center. The plot is restricted to a small cuboid in order to better visualize the penetration of the stochastic layer. The color code of the orbit is given by the iteration count. Early parts of the orbit are shown in blue, intermediate parts in green, and late parts in red. If neighboring points inside this 3D section yield the same color, then this means that the orbit visited the same phase-space region with subsequent iterations. This allows to recognize if and where the orbit gets trapped [109], see the right hand side of figure 3.24. One way of determining at which phase-space structures orbits get trapped is the frequency analysis. Given a chaotic orbit sticking to some small region in phase space a time-dependent frequency analysis may reveal the cause of the trapping [129, 130, 133], see also the wavelet transform

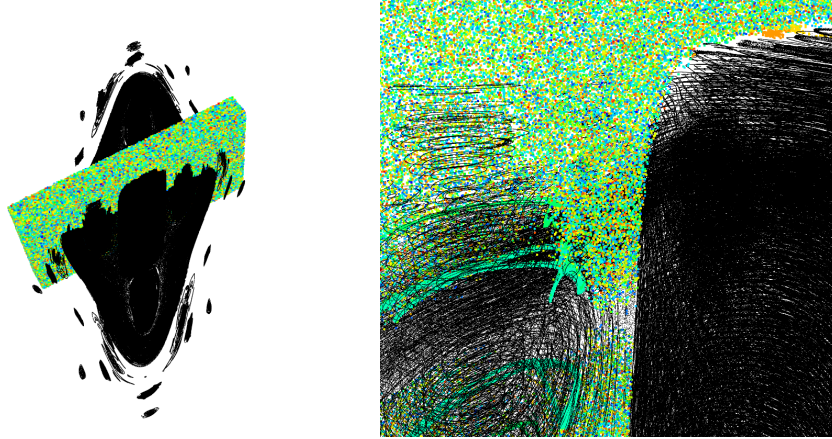


Figure 3.24.: Chaotic orbit penetrating the stochastic layer around the EE-type resonance chain in \mathcal{P}_{csm} . The orbit was started at $(p_1, p_2, q_1, q_2) = (-0.45, -0.45, 0.06, 0.07)$ within the chaotic sea and iterated $N = 3.9 \cdot 10^{12}$ times. Shown in black are the regular and resonantly broken tori from figure 3.23. The color code of the chaotic orbit is given by the iteration count. Early parts of the orbit are shown in blue, intermediate parts in green, late parts in red. The right hand side figure shows regions of stickiness.

in figure 3.4(a) for an example from near-integrable coupled standard maps. Other possibilities cover the analysis of the distribution of Lyapunov exponents [156]. The trapping mechanism is not part of this thesis and discussed elsewhere [109].

Note that the trapping of the chaotic orbit in figure 3.24 happens around a resonance zone of the EE-type subsystem. In order to also analyze the global structure of the system and the EE-type period-4 subsystem, we can perform a frequency calculation of the whole system and of the 4-fold map, as it is done for \mathcal{P}_{nnc} on page 47 and 52.

Analysis of fundamental frequencies

The frequency map analysis has already been applied to coupled standard maps by Laskar [36]. However, he uses a mapping with a slightly different coupling. The result of the frequency analysis of \mathcal{P}_{csm} is shown in figure 3.25. As the initial conditions are placed on a grid with much finer resolution in one direction, the image under the frequency map \mathcal{F} is given by deformed 1D curves. Some resonances are labeled by dashed lines. As the most important ones we can identify the rank-1 resonances $4 : 0 : 1$ and $3 : 1 : 1$. Both are of order five. The two lines intersect at $(\omega_1, \omega_2) = (1/4, 1/4)$. The corresponding rank-2 resonance is of order two, cf. page 48.

In the above frequency map only the most important frequencies are taken into account. These might not always yield enough information. Especially for stickiness phenomena it is necessary to also know higher order frequencies. This is done by taking several frequencies for a given time window of an orbit into account. This leads to several so-called *ridges* in the frequency-time representation of orbits [130]. If a wavelet transform is used to visualize the frequency content of a classical orbit, then the higher order frequencies can be seen directly, see ω_3 later in figure 3.27.

One effect of higher order are sub-resonances being embedded in the regular vicinity of a EE-type

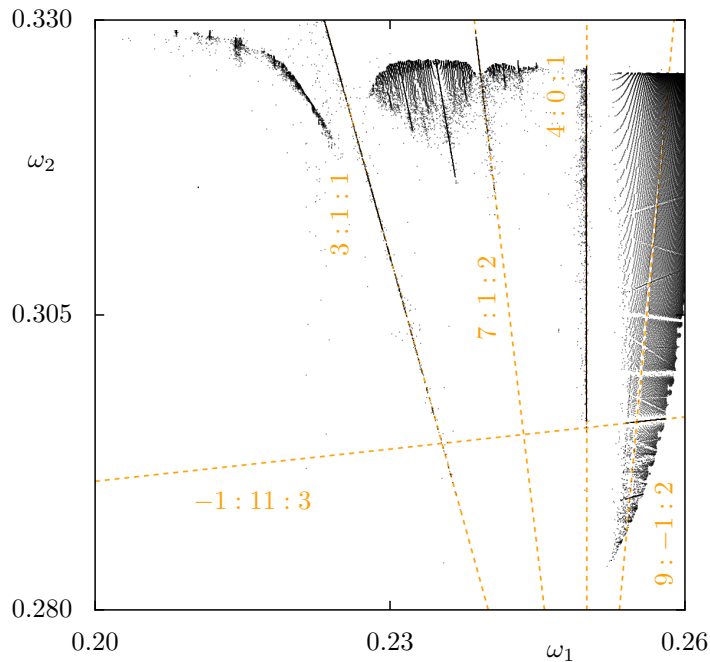


Figure 3.25.: Image of the frequency map \mathcal{F} for \mathcal{P}_{csm} . For each initial condition an orbit was iterated for $N = 4096$ steps and a pair of frequencies (ω_1, ω_2) was calculated using Laskar’s method. In order to reduce the noise on this picture, the FLI was calculated beforehand. If it was too large, then the orbit was discarded from the frequency calculation, cf. figure 3.22. Some resonances are indicated by dashed lines.

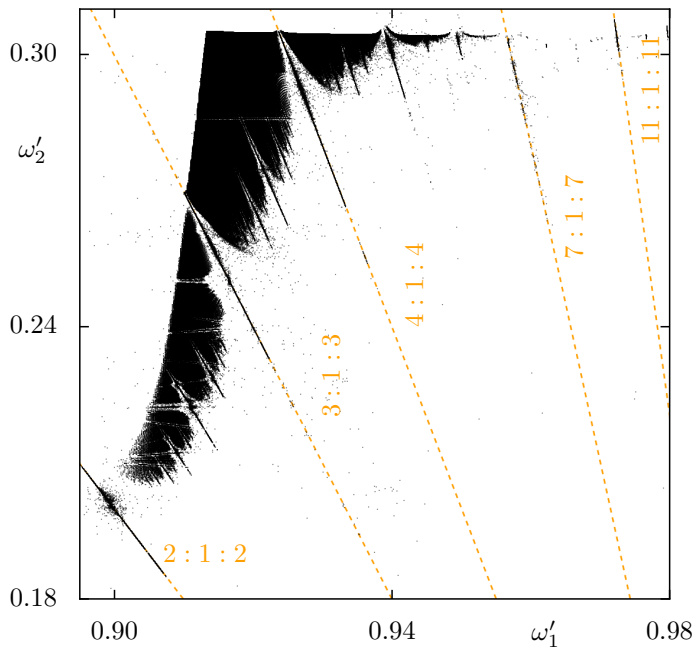


Figure 3.26.: Frequency map analysis around a EE-type rank-2 resonance for \mathcal{P}_{csm} . In order to analyze the subsystem, the 4-fold map is used. The initial conditions are placed close to the period-4 orbit at $(p_1, p_2, q_1, q_2) = (0, 0, 0.60121805, 0.51028145)$. Some resonances are indicated by dashed lines.

periodic orbit. For \mathcal{P}_{csm} we can use the 4-fold iteration in the vicinity of one of the EE-type periodic orbits shown in figure 3.23, just as is done for \mathcal{P}_{nc} on page 52. The frequencies determined for the 4-fold map are labeled with ω'_j in order to distinguish them from the frequencies ω_j calculated from the 1-fold mapping, see figure 3.25. The range spanned by ω'_2 is given by the range of frequencies ω_2 along the 4 : 0 : 1 from figure 3.25 according to $\omega'_2 = 4 \cdot \omega_2 \bmod 1$.

Having determined the resonance structure of the sub-system we can now place an initial condition on one of the rank-1 resonances of figure 3.26, e.g. the 4 : 1 : 4 resonance. A suitable initial condition can be found by using a 2D FLI plane which is calculated over the first degree of freedom at $(q_2, p_2) = (0.52, 0.0)$. In this plane the sub-resonance is well visible such that we can choose an initial condition inside the EE-type vicinity (not shown). Figure 3.27 shows the wavelet calculated from the orbits started at $(q_1, q_2, p_1, p_2) = (0.42, 0.52, 0.16, 0.0)$ and iterated 50000 times. The wavelet has been calculated using the first degree of freedom $z = q_1 - ip_1$ according to section 3.3.1. The left hand side of both figures (a) and (b) show the full wavelet. As the orbit is regular, the wavelet does not change in time significantly. The right hand side of both figures shows the time average of the wavelet which yield prominent maxima. The most important frequencies are calculated using the faster method according to Bartolini, Bazzani, Giovannozzi, Scandale, and Todesco [136] instead of Laskar's method [36]. They are indicated by a blue and a green arrow respectively and are accompanied by higher harmonics up to order 3. The higher harmonics of the first frequency ω_1 must be neglected when searching for the second frequency ω_2 in order to avoid a spurious resonance condition like $\omega_2 = 2\omega_1$, see page 27. The determined frequencies are $\omega_1 = 0.25$ and $\omega_2 = 0.32406436$ in figure 3.27(a) and $\omega_1 = 0.92593564$ and $\omega_2 = 0.29625744$ in figure 3.27(b). While the frequencies from figure 3.27(a)

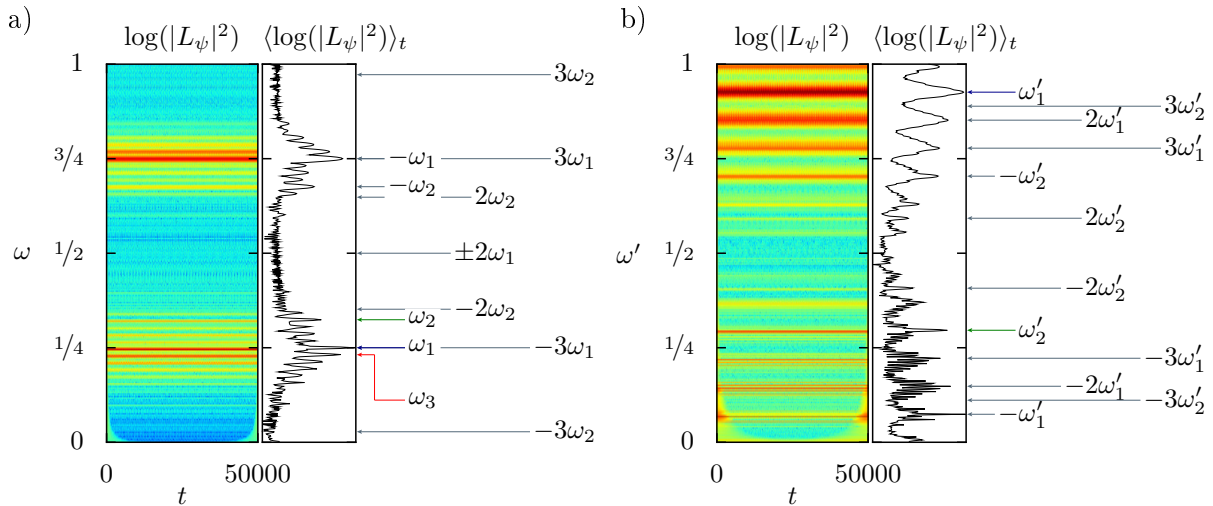


Figure 3.27.: Wavelets L_ψ for \mathcal{P}_{csm} (a) and $\mathcal{P}_{\text{csm}}^4$ (b) for an orbit of the 4 : 1 : 4 sub-resonance of the 4-fold map $\mathcal{P}_{\text{csm}}^4$, see figure 3.26. The figures (a) and (b) are accompanied by a plot of the time-averaged wavelet. The arrows indicate the most important frequencies ω_1 and ω_2 determined by Laskar's method including some higher harmonics. The frequencies are $\omega_1 = 0.25$ and $\omega_2 = 0.32406436$ in figure (a) and $\omega'_1 = 0.92593564$ and $\omega'_2 = 0.29625744$ in figure (b). Figure (a) also contains a higher order frequency given by $\omega_3 = 0.23148391$.

fulfill the $4 : 0 : 1$ resonance from figure 3.25 the ones from figure 3.27(b) fulfill the $4 : 1 : 4$ resonance from figure 3.26. It is important to note that the higher order frequencies given by the analysis of the 4-fold mapping $\mathcal{P}_{\text{csm}}^4$ are also contained in the averaged wavelet and the frequency analysis of the 1-fold map. The corresponding higher order frequency $\omega_3 = 0.23148391$ is linked to the result of the 4-fold map via $\omega'_1 = 4 \cdot \omega_3 \pmod{1}$. Due to being a higher order frequency, ω_3 is not directly visible in the frequency map of figure 3.25 because there only the two most relevant frequencies are plotted. The other frequencies are related by $\omega'_2 = 4 \cdot \omega_2 \pmod{1}$.

Skew phase-space sections containing invariant eigenspaces

Apart from the perpendicular sections given by $p_2 = 0$ in figures 3.23 and 3.24, it is also possible to use skew sections especially in the vicinity of the EE-type period-4 orbit, just as it is done for the designed map \mathcal{P}_{unc} in figures 3.18 to 3.21. Two examples of such a skew section are given in figures 3.28 to 3.30. All figures show the vicinity of the period-4 orbit

$$\mathbf{u}_p := (p_1, p_2, q_1, q_2) = (0.202436103, 0.0205629071, 0.398781948, 0.489718546). \quad (3.101)$$

Figures (a) to (d) visualize the same orbits in gray in different sections but put emphasis on other classes of orbits in each of the figures 3.28 to 3.30 by highlighting the orbits in various colors. The perpendicular sections are placed at $p_2 = 0.0205629071$ in figure (c) and at $p_1 = 0.202436103$ in figure (d). The skew sections defined by the linearization $D\mathcal{P}_{\text{csm}}$, see section 3.3.3 on page 34, contain either the first (a) or the second degree of freedom (b) completely. The sections are all shifted to contain \mathbf{u}_p . In all figures 3.28 to 3.30 the 2D planes tangential to the central manifold of the first and second degree of freedom are shown in blue and green, respectively. Figure (a) contains the blue plane completely while the green one is completely contained in (b) only. In the respective other plots the planes are given by lines.

In figure 3.28 the orbits started on the tangential planes are shown in orange and red similarly to figure 3.18. As mentioned on page 57 the planes are tangential to the center manifolds of \mathbf{u}_p . Therefore, orbits started on them are approximately given by 1D tori. As the center manifolds of \mathbf{u}_p are invariant under the dynamics of the 4-fold map, the map can be restricted to them which then yields 2D maps on these 2D manifolds [104, 105], see also page 13. It is important to note that the center manifolds are broken at resonances of the mapping. As these resonances are distributed densely over the phase space within the EE-type vicinity of \mathbf{u}_p , the center manifolds are highly non-connected objects [109]. However, neglecting this fact and ignoring the resonances the 1D tori on the center manifolds can be said to be a one-parameter family of invariant 1D objects. The same is true for the isolated 1D invariant lines at the center of a rank-1 resonances, see columns (ii) and (iii) in figure 3.2 for details and figure 3.17(c) for an example. Although a single resonant torus breaks up into just one 1D invariant line the rank-1 resonance defines a family of resonant tori in phase space each resulting in a 1D invariant line such that these lines appear in families, again ignoring the resonances.

As the frequency analysis of \mathcal{P}_{csm} in section 3.4.3 points out, there also exist rank-1 resonances

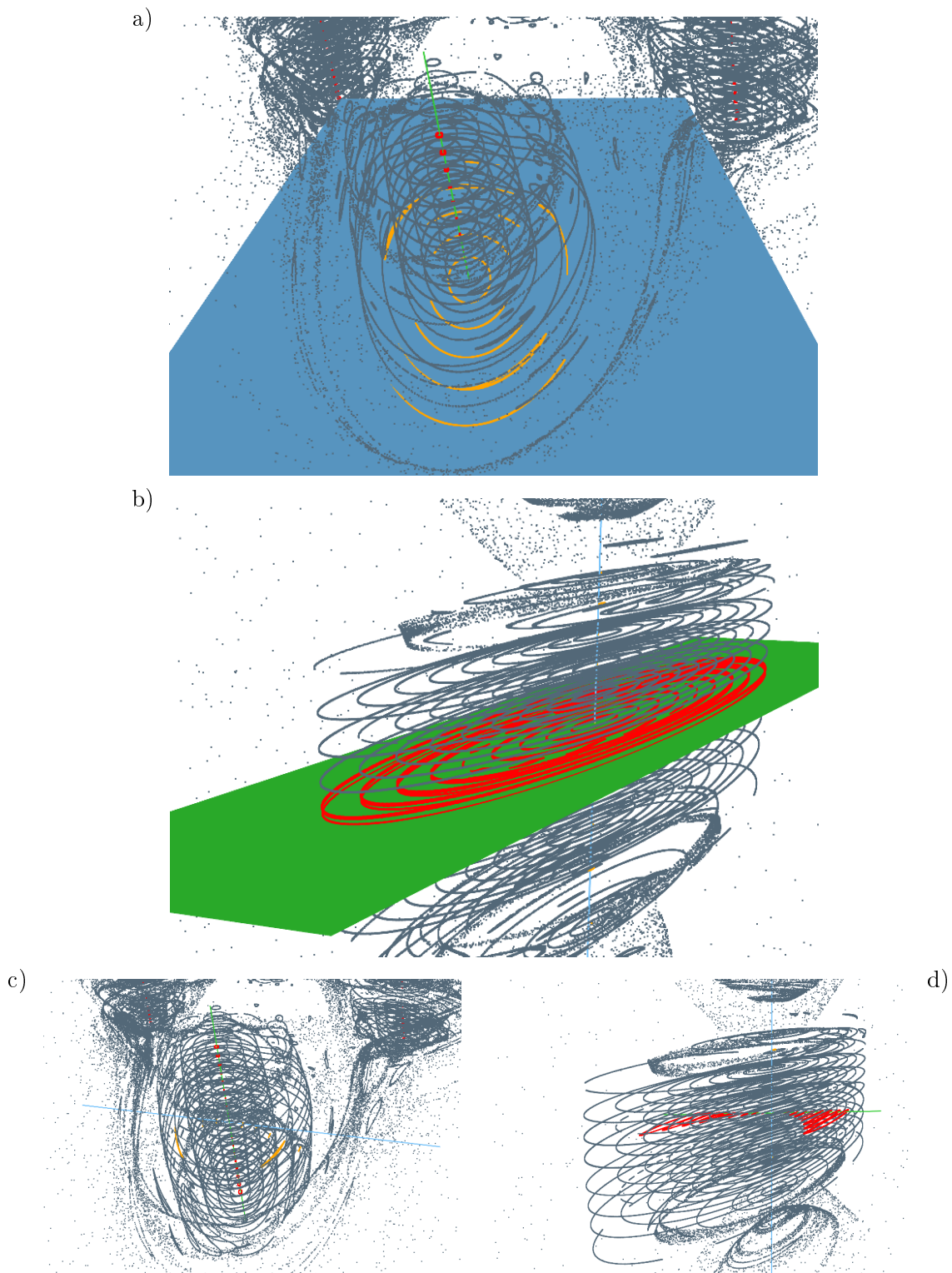


Figure 3.28.: Shown in gray are several regular orbits in the vicinity of \mathbf{u}_p . Shown in blue and green are the tangential planes to the center manifold of \mathbf{u}_p . Shown in orange and red are orbits started on the blue or green surface, respectively.

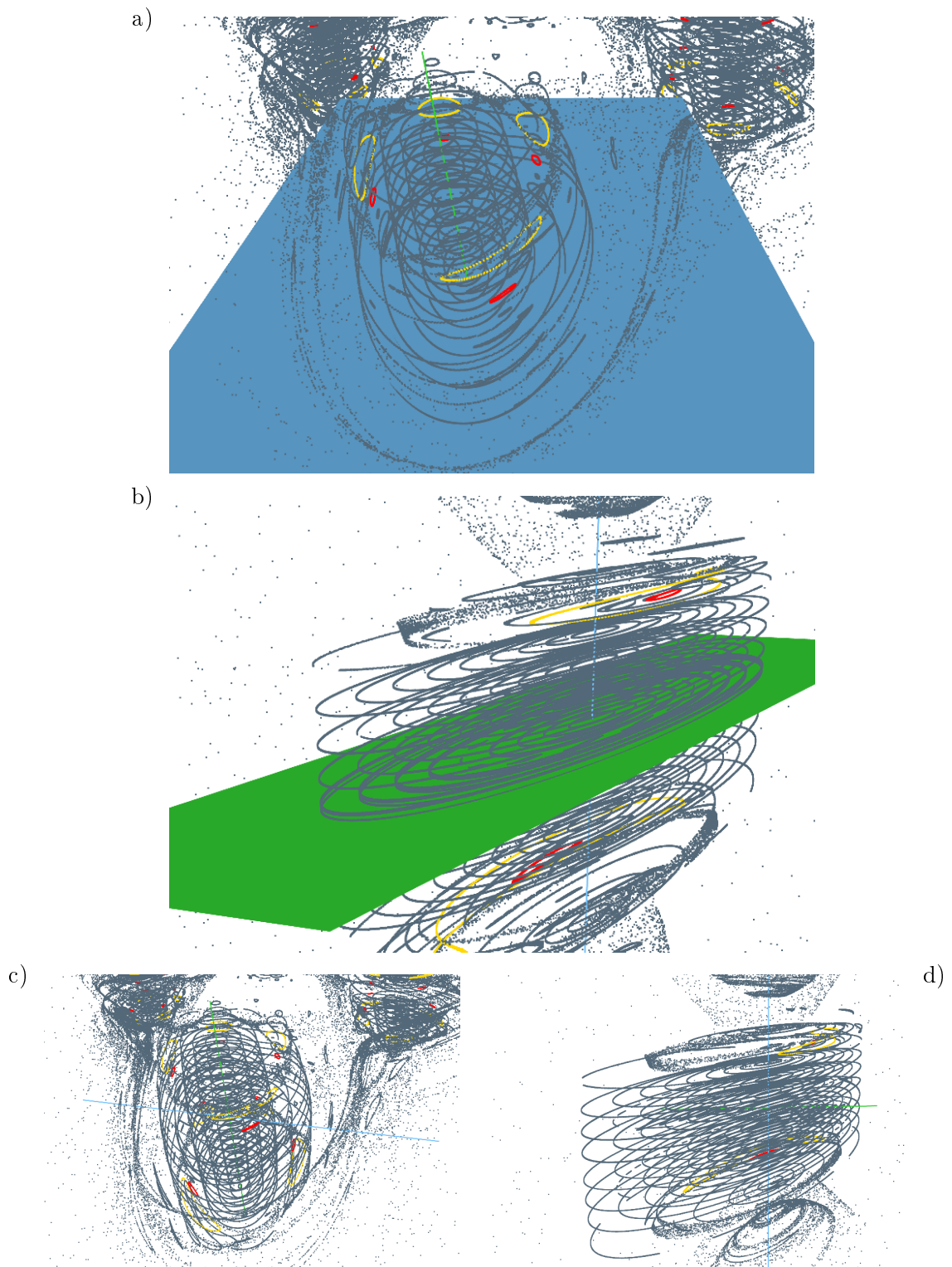


Figure 3.29.: Plot like in figure 3.28. Highlighted are two orbits belonging to a rank-1 resonance around \mathbf{u}_p . In figure 3.27(b) the frequency analysis of an orbit started in this zone is presented. It reveals it to be a $4 : 1 : 4$ resonance of the 4-fold mapping.

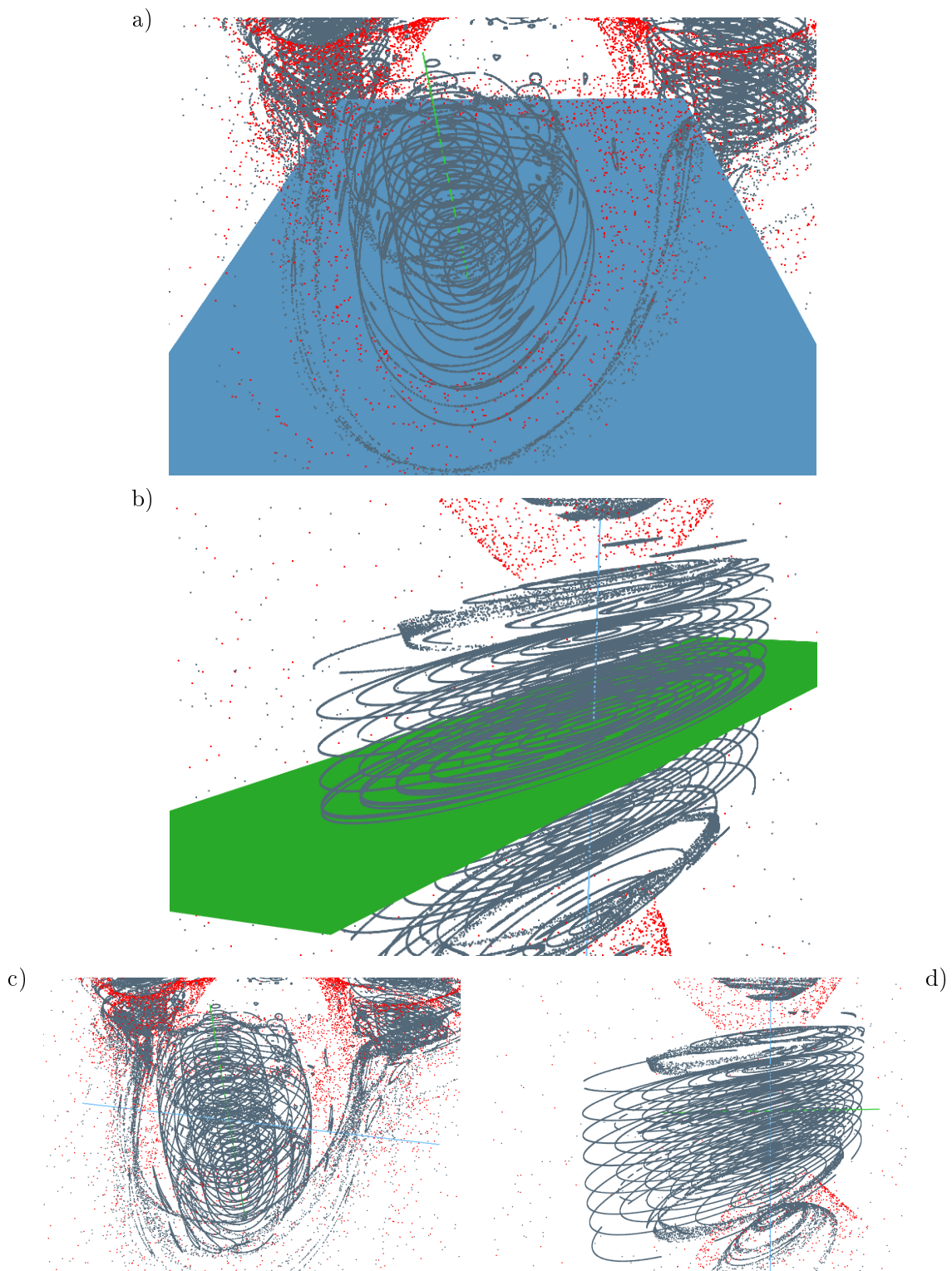


Figure 3.30.: Plot like in figure 3.28. Highlighted is an orbit in the stochastic layer around the resonance. Note that this orbit seems to fill a 2D area only.

in the 4-fold iteration of the coupled standard maps embedded in the EE-type region around \mathbf{u}_p , cf. figure 3.26. One of them is shown in figure 3.29, namely the 4 : 1 : 4 resonance already investigated by the wavelet transform in figure 3.27. At its center resides a 1D line invariant under the 4-fold mapping. This line is given by a family of broken tori fulfilling a rank-1 resonance and breaking up into one 1D invariant line each. It therefore has a completely different origin than the 1D tori on the central manifolds of the EE-type fixed point.

Figure 3.30 shows a chaotic orbit in the stochastic layer in between the EE-type surrounding of \mathbf{u}_p . This layer also contains the EH-type period-4 orbits (not shown) mentioned on page 18. If this chaotic orbit is iterated long enough, it will leave the thin stochastic layer and enter the chaotic sea by taking its itinerary trough the Arnold web. The rate with which this diffusion process takes place is very hard to determine in systems which are far away from near-integrability such as the given \mathcal{P}_{csm} . The reason is that the direction along which the diffusion is slowest is hard to determine. In figure 3.30 the chaotic orbit seems to fill a 2D area. However, it also wanders slowly into a third direction \mathbf{e}_{slow} which will lead the trajectory out into the chaotic sea. Once this direction \mathbf{e}_{slow} is known, the diffusion coefficient of the Arnold diffusion would have to be determined along \mathbf{e}_{slow} . Note that \mathbf{e}_{slow} is position dependent and is in general not given by the normal to the almost 2D area the orbit fills in the 3D section in figure 3.30 (a) to (d). Only the projection of \mathbf{e}_{slow} onto the 3D sections coincides with the normal to the approximately 2D orbit.

The above skew sections are chosen such that they contain the tangential plane to the center manifold. This introduces appropriate phase-space sections for the EE-type vicinities of rank-2 resonances. For rank-1 resonances this cannot be done due to the lack of invariant 2D manifolds connected to them. One possibility is to use a section perpendicular to the tangential at the 1D invariant torus in the center of the EE-zone mentioned in the last row of figure 3.2.

4. Quantum Mechanics

In this chapter we want to focus on the properties of eigenfunctions of systems with a mixed phase space, on quantum mechanical consequences of the Arnold web, and on the quantum mechanical coupling between the regular and the chaotic domain.

Therefore, we will study the 4D maps introduced in chapter 3 quantum mechanically. A main key to the understanding of quantum mechanics is the analysis of the eigenstates of the time evolution operator. For systems with a mixed phase space these eigenstates can typically be divided into *regular* and *chaotic* states as was pointed out by Percival [47]. As regular quantum states predominantly live on the regular phase-space region, their number can be estimated by the volume of this region according to the semiclassical eigenfunction hypothesis [47, 157, 158]. While classically regular and chaotic dynamics exist on separate invariant sets in phase space, both regions are coupled quantum mechanically by the process of *dynamical tunneling* which was introduced by Davis and Heller [56] based on a work by Lawton and Child investigating vibrational modes of the H₂O molecule [159]. Dynamical tunneling is important for a huge range of physical problems such as mesoscopic systems [11, 70], optical or microwave resonators [65–69], the splitting of energy levels and decay rates of excited helium atoms [57–59]. Furthermore, the subject of energy transport in molecules is a field where dynamical tunneling is a topic of intensive recent studies [56, 60–64], experimentally as well as theoretically.

Dynamical tunneling is a purely quantum mechanical phenomenon coupling phase-space regions which are classically disconnected. This covers all kinds of possible couplings between subsystems, e. g. direct couplings or couplings mediated by single intermediate states or entire subsystems. One very prominent example of the latter is the tunneling coupling between two regular regions being mediated and drastically enhanced by chaotic states in between. This process was called *chaos-assisted tunneling* by Bohigas, Tomsovic, and Ullmo [72] in 1993 and intensively investigated thereafter [57, 68, 73–77, 160–162].

The distinction into direct and indirect couplings leads to the nomenclature of *direct tunneling rates* γ^d which solely addresses the direct coupling of phase-space regions. These direct rates can be used to understand the chaos-assisted tunneling as a two-step process given by two direct tunneling contributions, namely a regular-to-chaotic and a chaotic-to-regular tunneling step [79]. In this work we solely focus on tunneling transitions from a regular to a chaotic domain in phase space. They can be predicted if the underlying classical phase space is free of resonances using the fictitious integrable system approach [78]. This approach allowed to predict *direct regular-to-chaotic tunneling rates* for 2D maps [78, 79] and billiard-like systems [81, 82]. Here we apply this approach to higher dimensional systems for the first time.

In generic systems not only the direct processes determines the regular-to-chaotic tunneling phe-

nomena. Especially the presence of nonlinear resonances leads to very effective couplings between the regular and the chaotic domain mediated by excited regular states. This was dubbed *resonance-assisted tunneling* (RAT) by Brodier, Schlagheck, and Ullmo [83, 84] and further investigated in references [163, 164]. Due to the omnipresence of nonlinear resonances this effect is very important, e. g. in molecular systems [62, 165]. An impressive agreement over several orders of magnitude between prediction and numerical experiment was achieved by combining direct tunneling rates with the RAT prediction [166].

In this chapter we will first introduce the quantum mechanical time evolution of classical maps in section 4.1. In order to examine the quantum mechanical properties of the maps from chapter 3, we will present eigenfunctions of the systems \mathcal{P}_{llu} , \mathcal{P}_{nnc} , and \mathcal{P}_{csm} in section 4.2. For this purpose we use Husimi distributions in the 3D phase-space sections introduced in section 3.3.3 and position-space probability-densities. This will allow to determine the difference between regular and chaotic states in 4D maps. As \mathcal{P}_{nnc} and \mathcal{P}_{csm} yield classical nonlinear resonances in the regular region, we can investigate eigenstates living in the elliptical part of the resonance chain as well as in the stochastic layer.

The fundamental difference to 2D maps is the connectivity of the stochastic layers for arbitrary small couplings. We investigate this important subject in section 4.3. This is done by first analyzing the imprint of the Arnold web on eigenstates of the time evolution operator U in section 4.3.1 where we address the issue whether there exist eigenstates inside the web of stochastic layers that reach out into the chaotic sea. We investigate this for the map \mathcal{P}_{csm} by numerically going towards the semiclassical limit. The search for special eigenstates is accompanied by a time evolution of wave packets. This analysis shows in a very clear and convincing way how quantum mechanics can penetrate into the stochastic layers in the semiclassical limit and is presented in section 4.3.2.

The penetration of the stochastic layer by wave packets is a quantum mechanical analogue of a classically allowed process which is unique to systems with more than two degrees of freedom. In contrast to this dynamical tunneling is a purely quantum mechanical coupling of classically disconnected parts of phase space which occurs for arbitrary dimensions. We cover this aspect for 4D maps in section 4.4 in terms of the fundamentally important dynamical tunneling rates γ . For the linear map \mathcal{P}_{llu} we compare numerical data with the first tunneling prediction for 4D mappings using the fictitious integrable system approach and find very good agreement.

If nonlinearities are introduced, we arrive at the system \mathcal{P}_{nnc} for which the effects of resonance-assisted tunneling (RAT) appear drastically in the numerical data, shown in section 4.4.4. Using the theory of RAT, reviewed in section 4.4.5, we present a first approach towards a prediction of the tunneling rates for 4D maps in section 4.4.6. In order to do so, we follow the derivation for 2D maps and thereby gain a qualitative understanding of the underlying coupling mechanisms. However, due to the larger dimension a quantitative prediction is a much harder task than for 2D maps.

4.1. Quantization of Classical Maps

The major advantage of kicked systems is the possibility to express their time evolution operator exactly. The starting point is the Hamiltonian of the form

$$H(\mathbf{p}, \mathbf{q}, t) = T(\mathbf{p}) + V(\mathbf{q}) \sum_{n \in \mathbb{Z}} \delta(t - n). \quad (4.1)$$

The special time dependence $\delta(t - n)$ allows an exact split-operator ansatz [152, 167, 168] for the unitary time evolution operator U ,

$$U = e^{-i/\hbar V(\hat{\mathbf{q}})} e^{-i/\hbar T(\hat{\mathbf{p}})}. \quad (4.2)$$

The quantum mechanical problem is given by solving the eigenvalue equation of U

$$U|\psi\rangle = e^{i\varphi}|\psi\rangle \quad (4.3)$$

leading to the eigenfunctions $|\psi\rangle$ and the eigenphases $\varphi \in [0, 2\pi)$. We evaluate the operator U in position representation, using dimensionless quantities as mentioned on page 12. This also implies that Planck's constant is replaced by a dimensionless effective Planck's constant. It represents the value of the physical constant $\hbar^0 = 6.62606957 \cdot 10^{-34}$ Js divided by the action given by the typical length l^0 and momentum p^0 used to scale the system to the dimensionless coordinates. By means of this quotient $\hbar = \hbar^0/l^0 p^0$ the parameter \hbar expresses how deep into the realm of quantum mechanics the system is. The smaller \hbar the larger is the typical classical action $l^0 p^0$ compared to the physical constant \hbar^0 and the more classical a system will behave. Therefore, the so-called *semiclassical limit* is given by $\hbar \rightarrow 0$ or in other words $1/\hbar \rightarrow \infty$.

If the potential in equation (4.1) is periodic with periodicity lengths $M_{q,i}$ in direction i ,

$$V(\mathbf{q}) = V(\mathbf{q} + \mathbf{M}_{\mathbf{q}}) \quad \text{with} \quad \mathbf{M}_{\mathbf{q}} = \begin{pmatrix} M_{q,1} \\ M_{q,2} \end{pmatrix} \in \mathbb{R}^2, \quad (4.4)$$

then one must use a discrete grid $\mathbf{p}_{\mathbf{j}}$ rather than continuous values \mathbf{p} in the momentum representation of the time evolution operator (4.2) [152, 169]. Given the number of grid points N_i in each direction of momentum space the spacing of the grid in the different directions is given by $\Delta_{q,i} = M_{p,i}/N_i$. In order to ease notation, we introduce the diagonal matrices

$$\underline{\mathbf{M}}_p := \begin{pmatrix} M_{p,1} & 0 \\ 0 & M_{p,2} \end{pmatrix}, \quad \underline{\mathbf{N}} := \begin{pmatrix} N_1 & 0 \\ 0 & N_2 \end{pmatrix} \quad \text{and} \quad \underline{\Delta}_p := \begin{pmatrix} \Delta_{p,1} & 0 \\ 0 & \Delta_{p,2} \end{pmatrix} = \underline{\mathbf{M}}_p \underline{\mathbf{N}}^{-1} \quad (4.5)$$

with which the grid in momentum space reads

$$\mathbf{p}_{\mathbf{k}} = \mathbf{p}_0 + \underline{\Delta}_p \cdot \mathbf{k} \quad \text{with} \quad \mathbf{k} \in \{0, 1, \dots, N_1 - 1\} \times \{0, 1, \dots, N_2 - 1\}. \quad (4.6)$$

The vector \mathbf{p}_0 is the leftmost point with respect to all dimensions. It has to be chosen such that the grid does not leave the allowed momentum space region on which the classical map is defined. This means that for each direction $j = 1, 2$ we have

$$p_{k,j} \in [p_{\min,j}, p_{\min,j} + M_{p,j}) \quad \forall k \in 0, \dots, N_j - 1 \quad \Leftrightarrow \quad p_{0,j} \in [p_{\min,j}, p_{\min,j} + \Delta_{p,j}). \quad (4.7)$$

The vector \mathbf{p}_0 defines the position of the whole grid. By choosing another \mathbf{p}_0 we change the quantum system without altering the resolution \mathbf{N} . This property would make \mathbf{p}_0 a useful parameter in order to generate ensembles of quantum systems. However, restriction (4.7) is a bit cumbersome, especially as it contains the resolution \mathbf{N} of the grid implicitly. It is more convenient to introduce parameters over the domain $[0, 1) \times [0, 1)$ in order to express all possible momentum lattices [169]. This is done according to reference [170, page 22 ff.] by rewriting equation (4.6) to

$$\mathbf{p}_{\mathbf{k}} = \underline{\Delta}_p \left(\boldsymbol{\theta}_q + \mathbf{n}_p^{(0)} + \mathbf{k} \right) \quad \text{with} \quad \mathbf{k} \in \{0, 1, \dots, N_1 - 1\} \times \{0, 1, \dots, N_2 - 1\}. \quad (4.8)$$

Here we introduced the Bloch phases $\boldsymbol{\theta}_q \in [0, 1) \times [0, 1)$ according to the periodic boundary conditions of the potential [169]. In equation (4.8) the integers $\mathbf{n}_p^{(0)}$ are introduced as

$$\mathbf{n}_p^{(0)} = \lceil \underline{\Delta}_p^{-1} \mathbf{p}_{\min} - \boldsymbol{\theta}_q \rceil \quad (4.9)$$

where $\lceil x \rceil$ is the ceiling function, i. e. it is the smallest integer not less than x calculated element wise.

To summarize we can say that for a given momentum space extent $[p_{\min,j}, p_{\min,j} + M_{p,j})$ for $j \in 1, 2$ a grid can be defined using equation (4.8). This definition provides the parameters \mathbf{N} and $\boldsymbol{\theta}_p$. Note that there is a similar grid defined in position space with corresponding parameters $\boldsymbol{\theta}_p$

$$\mathbf{q}_{\mathbf{j}} = \underline{\Delta}_q \left(\boldsymbol{\theta}_p + \mathbf{n}_q^{(0)} + \mathbf{j} \right) \quad \text{with} \quad \mathbf{j} \in \{0, 1, \dots, N_1 - 1\} \times \{0, 1, \dots, N_2 - 1\} \quad (4.10)$$

given the kinetic energy $T(\mathbf{p})$ is periodic. This is the case for the maps we consider here as they are restricted to a 4D phase space with periodic boundary conditions. To be precise the functions in equation (4.2) have to be periodic with respect to the indices \mathbf{j} and \mathbf{k} of the grid, namely

$$e^{-i/\hbar V(\mathbf{q}_{\mathbf{j}})} = e^{-i/\hbar V(\mathbf{q}_{\mathbf{j}} + \underline{\mathbf{M}}_q \mathbf{e})} \quad \forall \mathbf{j}, \mathbf{e} \quad \text{and} \quad e^{-i/\hbar T(\mathbf{p}_{\mathbf{k}})} = e^{-i/\hbar T(\mathbf{p}_{\mathbf{k}} + \underline{\mathbf{M}}_p \mathbf{e})} \quad \forall \mathbf{k}, \mathbf{e}, \quad (4.11)$$

where \mathbf{e} are the vectors of the canonical basis of \mathbb{R}^2 . If necessary, this periodicity can be established by restrictions on the parameters $\boldsymbol{\theta}$ [169]. However, if equation (4.11) is fulfilled, the grid in momentum (4.8) as well as position (4.10) can be used.

As this is the case for the mappings we use, the position grid (4.10) can be inserted into the position-space representation of the time evolution operator (4.2). As there is a total number of $\mathcal{N} := \det \underline{\mathbf{N}} = N_1 N_2$ grid points, this gives rise to a $\mathcal{N} \times \mathcal{N}$ matrix having \mathcal{N} eigenvalues and eigenvectors. This leads to the generalization of the formula used for the time evolution operator for

2D maps

$$U_{\mathbf{n}\mathbf{k}} = \langle \mathbf{q}_{\mathbf{n}} | U | \mathbf{q}_{\mathbf{k}} \rangle = 2\pi\hbar e^{-i/\hbar V(\mathbf{q}_{\mathbf{n}})} \sum_{j_1=0}^{N_1-1} \sum_{j_2=0}^{N_2-1} e^{-i/\hbar T(\mathbf{p}_{\mathbf{j}})} e^{-i/\hbar \mathbf{p}_{\mathbf{j}}(\mathbf{q}_{\mathbf{n}} - \mathbf{q}_{\mathbf{k}})} \quad (4.12)$$

to higher dimensional systems. It requires the specific choice of the effective Planck's constant [152],

$$2\pi\hbar_j = \frac{M_{p,j} \cdot M_{q,j}}{N_j} \quad (4.13)$$

where we introduced Planck's constant of the j -th degree of freedom \hbar_j . It is important to note that the fraction in equation (4.13) is the phase space volume in the j -th degree of freedom divided by the number of grid points in that direction. Assuming that the only physical relevant case is given by the same \hbar_j for every degree of freedom this implies that the left hand side of (4.13) is the same for all j such that we have

$$(2\pi\hbar)^f = \frac{V_{\text{phase space}}}{\mathcal{N}} \quad (4.14)$$

with $\hbar := \hbar_j$ independent of j . Here the exponent f is the number of degrees of freedom of the system, i. e. $f = 2$ in our case. This formula confirms that for f degrees of freedom the total number of quantum states \mathcal{N} is given by the volume in phase space divided by $(2\pi\hbar)^f$. In other words on average every eigenstate will occupy a phase-space volume h^f .

Using the grids from equations (4.10) and (4.8) we can transform equation (4.12) into an expression in which the sums can be carried out by a fast Fourier transform (FFT). Given a set of grid parameters this allows to set up the matrix $\underline{\mathbf{U}}$ very fast. Moreover, it allows to apply $\underline{\mathbf{U}}$ to a vector in position space $\phi_{\mathbf{k}} := \langle \mathbf{q}_{\mathbf{k}} | \phi \rangle$ without the need of building up $\underline{\mathbf{U}}$ completely. This allows to use numerical methods for sparse matrices, see appendix J. This is necessary as the scaling of the matrix size \mathcal{N} with $1/h^2$ leads to large matrix sizes for small h which is required for resolving small classical phase-space regions such as the stochastic layer of \mathcal{P}_{csm} , see equation (3.100). Such computations are performed in section 4.3.1 using the Lanczos algorithm in order to diagonalize systems with $1/h = 1000$ leading to matrices of size $10^6 \times 10^6$.

4.2. Eigenstates of the time evolution operator U

The most direct connection between classical and quantum mechanics can be seen in the properties of the eigenstates. In our case we focus on eigenstates of the time-evolution operator U and present examples for the different classes of eigenstates for the classical systems defined in chapter 3, namely the designed maps without and with nonlinear resonances, \mathcal{P}_{llu} and \mathcal{P}_{nnc} on pages 37 and 48, and the coupled standard maps in the weakly coupled case, \mathcal{P}_{csm} on page 63.

4.2.1. Eigenstates of \mathcal{P}_{llu}

In order to introduce the quantum mechanical viewpoint, we first show some eigenstates of the system. We visualize them in two different ways. One is the position-space probability-density $|\psi(q_1, q_2)|^2$. The other one is a Husimi representation $\mathbf{H}(\mathbf{q}_0, \mathbf{p}_0)$ [171] within a 3D section through the 4D phase space. This representation is given by the overlap of the state $|\psi\rangle$ with coherent states $|\alpha(\mathbf{q}_0, \mathbf{p}_0)\rangle$ placed in phase space at points $(\mathbf{q}_0, \mathbf{p}_0)$,

$$\langle \mathbf{q} | \alpha(\mathbf{q}_0, \mathbf{p}_0) \rangle = \frac{1}{\pi \hbar} \exp \left(-\frac{(\mathbf{q} - \mathbf{q}_0)^2}{4\hbar} + \frac{i}{\hbar} \mathbf{p}_0 \mathbf{q} \right), \quad (4.15)$$

and allows to see connections between classical phase-space structures and quantum states.

As mentioned above the eigenstates can be roughly divided into regular and chaotic states. The number of either class can be estimated by the volume of the corresponding classical region in phase space according to the semiclassical eigenfunction hypothesis [47, 157, 158]. The volume of the regular domain of \mathcal{P}_{llu} is calculated in section 3.4.1 on page 43. As we have $V_{4\text{D}}^{\text{reg}} = 0.01642$, approximately 1.6 percent of the eigenstates are regular. If we choose $1/\hbar = 50$, then there is a total number of 2500 states. Approximately 41 of them are regular states and 2459 are chaotic. It is possible to attribute quantum numbers m_1 and m_2 to regular states. In the case of the linear regular region one can count the nodal lines in position space in order to determine these quantum numbers. Another possibility is to calculate overlaps with eigenstates of the harmonic oscillator, see also appendix B.

A selection of regular eigenstates is shown in figures 4.1 to 4.5. In all these pictures the Husimi distribution is calculated over the 3D phase-space section $p_2 = 0$. The corresponding values are visualized by isosurfaces of the Husimi function. They are plotted using a colormap ranging from opaque-red for large values to translucent-yellow for zero probability. The Husimi distribution is shown in a tilted view and in two straight views along the p_1 and the q_2 axis, shown in (a), (b), and (c), respectively. These plots are accompanied by classical orbits (black) and an inset showing the position-space probability-density $|\psi_{\text{reg}}^{m_1, m_2}|^2$.

For a fully integrable, linear system the ground state is given by a Gaussian coherent state in both degrees of freedom. The ground state $\psi_{\text{reg}}^{0,0}$ in the linear region of \mathcal{P}_{llu} has a very similar shape. However, it also has contributions in the chaotic part of phase space due to dynamical tunneling which are not visible in the plot due to exponential smallness, see section 4.4. The near-Gaussian shape is reflected in the Husimi distribution in the 3D phase-space section of figure 4.1(a) and can also be seen in plot (c) where the first degree of freedom is nicely visible as the view is along the q_2 axis. The view along the p_1 axis in (b) shows that there is only one peak along the q_2 axis for the fixed value $p_2 = 0$ of the section. This is due to the Gaussian shape in the second degree of freedom.

Figure 4.2 shows the eigenstate $\psi_{\text{reg}}^{1,0}$. This is the first excited state with respect to the first degree of freedom. Accordingly the Husimi distribution is concentrated in phase space on a classical torus with a non-zero extent in (q_1, p_1) but residing at $(q_2, p_2) = (0, 0)$. In the second degree of freedom the Husimi distribution is given by a Gaussian function. This can be seen by the fact that there is no nodal line along the q_2 axes. Contrary to that only the second degree of freedom is excited for

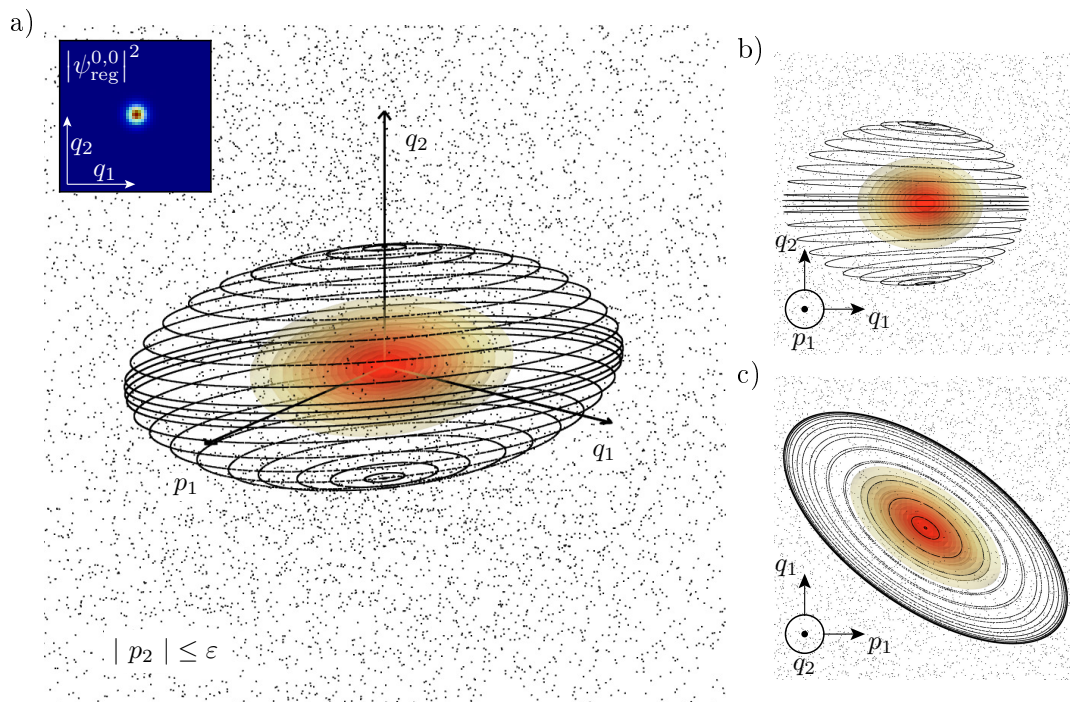


Figure 4.1.: Ground state $\psi_{\text{reg}}^{0,0}$ of \mathcal{P}_{llu} for $1/h = 50$. Figure (a) shows the 3D section also used in figure 3.6. It contains semi-transparent surfaces where the value of the Husimi function is constant. The inset shows the position-space probability-density. Figures (b) and (c) show the same 3D section from two different points of view.

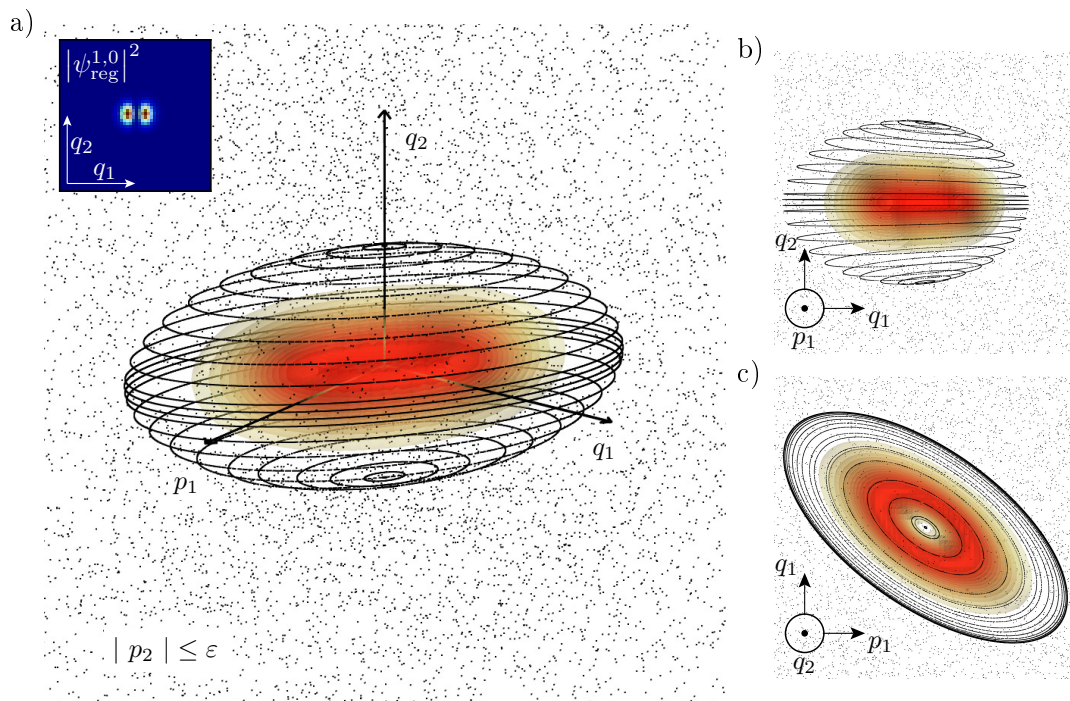


Figure 4.2.: Eigenstate $\psi_{\text{reg}}^{1,0}$ of \mathcal{P}_{llu} for $1/h = 50$. The setup of the plot is the same as in figure 4.1.

the eigenstate $\psi_{\text{reg}}^{0,1}$, shown in figure 4.3. Therefore, the main Husimi weight is concentrated on a 1D torus in the second degree of freedom and on the fixed point of the first degree of freedom at $(q_1, p_1) = (0, 0)$. As the second degree of freedom is cut by the section condition $|p_2| = 0$, the Husimi region with maximum weight is present only at two separate values of q_2 . In the first degree of freedom the Husimi is again given by a Gaussian distribution. If both degrees of freedom are excited with one quantum, we reach state $\psi_{\text{reg}}^{1,1}$, shown in figure 4.4. Here the Husimi distribution is concentrated on a real 2D torus in the 4D phase space. The cut made by the section leads to the Husimi distribution being concentrated on two 1D ellipses inside the 3D section. This ellipses coincide with the respective quantizing classical torus. If both degrees of freedom are higher excited, the quantizing tori are closer to the chaotic sea. An example state with $(m_1, m_2) = (5, 3)$ is shown in figure 4.5 for $1/h = 50$. This state is one of the last states present inside the island at this value of Planck's constant. Due to its vicinity to the chaotic region it shows a remarkable tail into the chaotic sea. This is a consequence of dynamical tunneling which couples the classically disconnected regular and chaotic regions and is the subject of a detailed investigation in section 4.4.

Due to the small volume of the regular island the majority of the eigenstates localize on the chaotic part of phase space. An example is given in figure 4.6. At the edge of the section a box of side length $\sqrt{h} \approx 0.141$ is shown. It is the remnant of a 4D Planck cell of volume h^2 in the 3D section.

The value of the effective Planck's constant is linked to the resolution of the quantum eigenstates. With decreasing h states can explore features of the classical phase space better and a larger number of eigenstates fits into a classical volume of a given size. If we increase $1/h$ from 50 to 90, those states

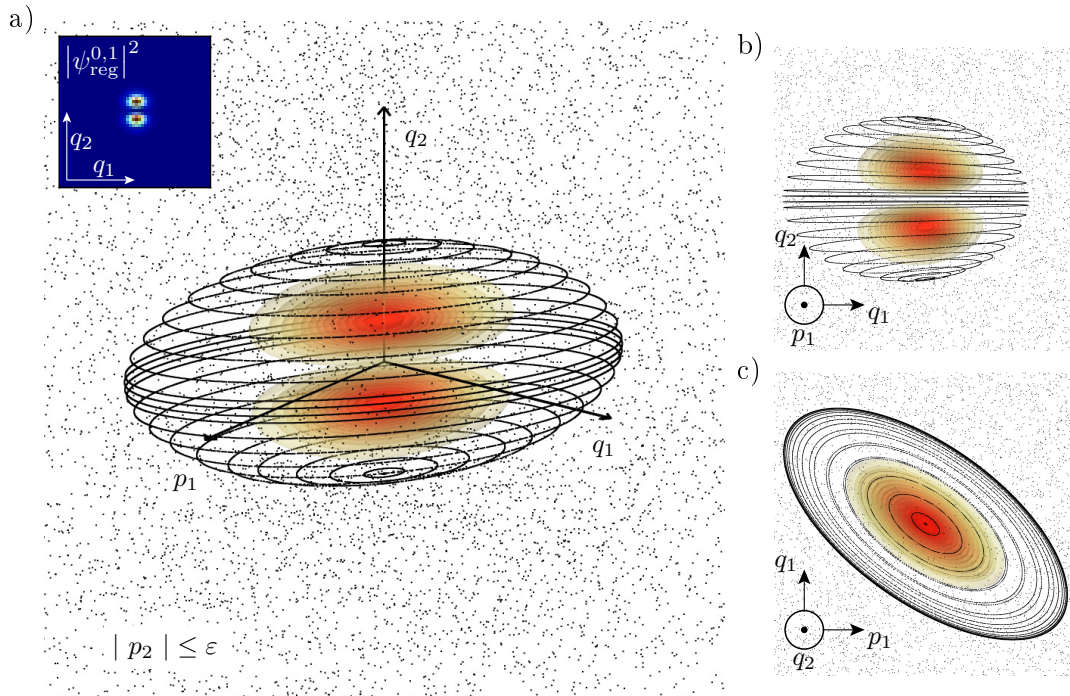


Figure 4.3.: Eigenstate $\psi_{\text{reg}}^{0,1}$ of \mathcal{P}_{llu} for $1/h = 50$. The setup of the plot is the same as in figure 4.1.

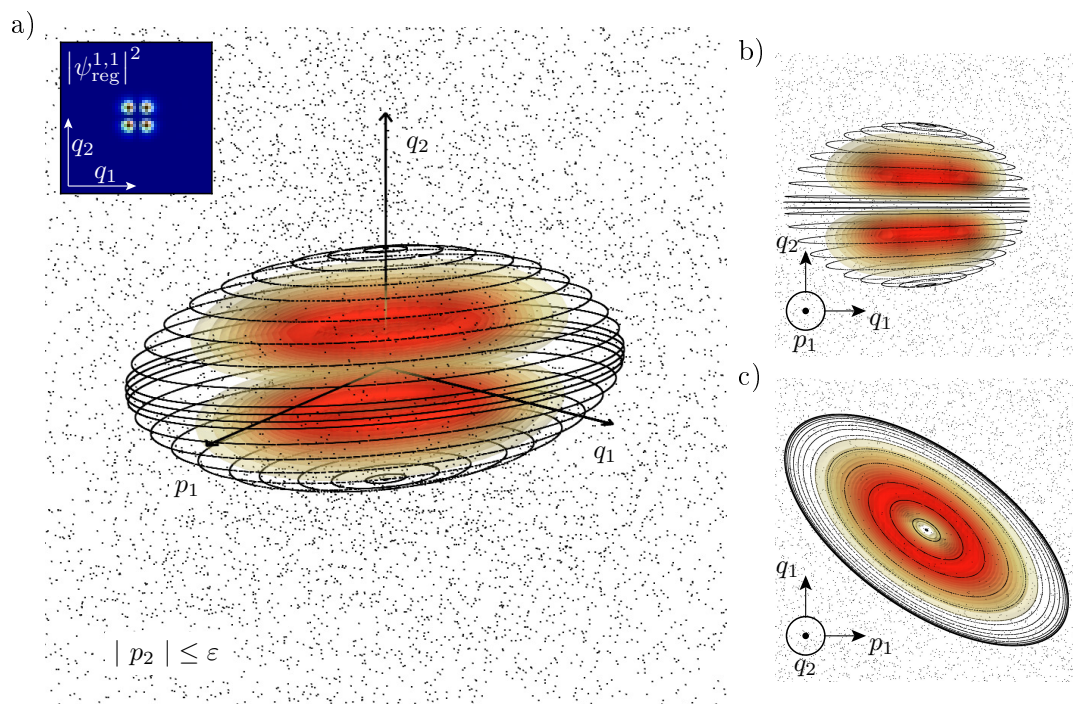


Figure 4.4.: Eigenstate $\psi_{\text{reg}}^{1,1}$ of \mathcal{P}_{llu} for $1/h = 50$. The setup of the plot is the same as in figure 4.1.

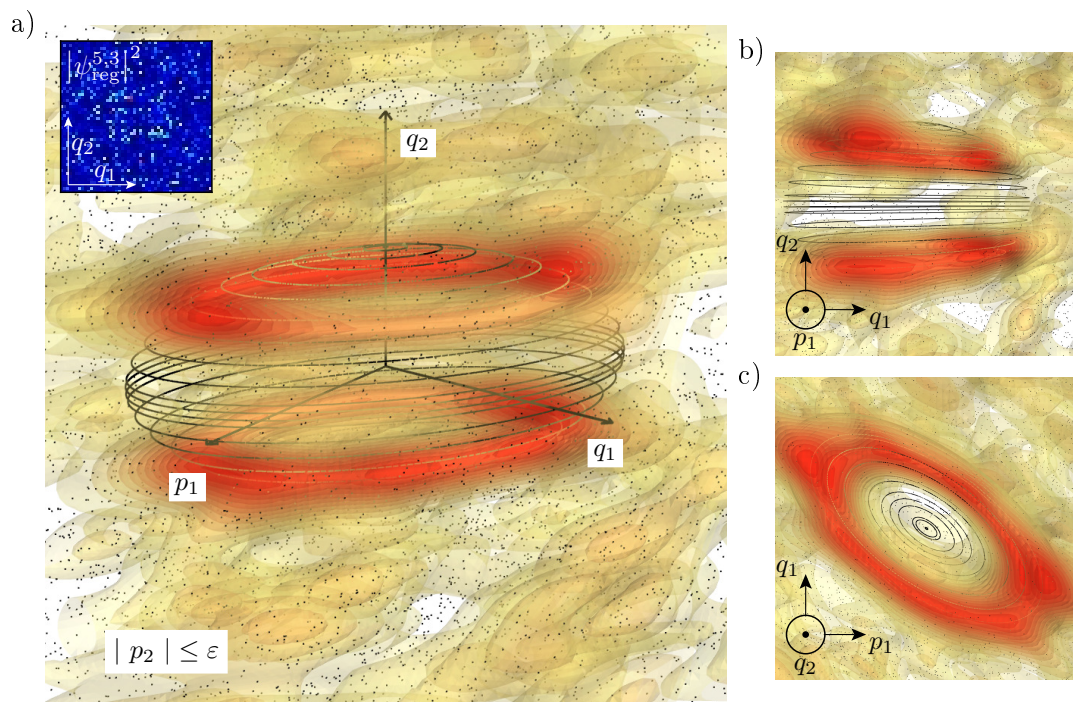


Figure 4.5.: Eigenstate $\psi_{\text{reg}}^{5,3}$ of \mathcal{P}_{llu} for $1/h = 50$. The setup of the plot is the same as in figure 4.1.

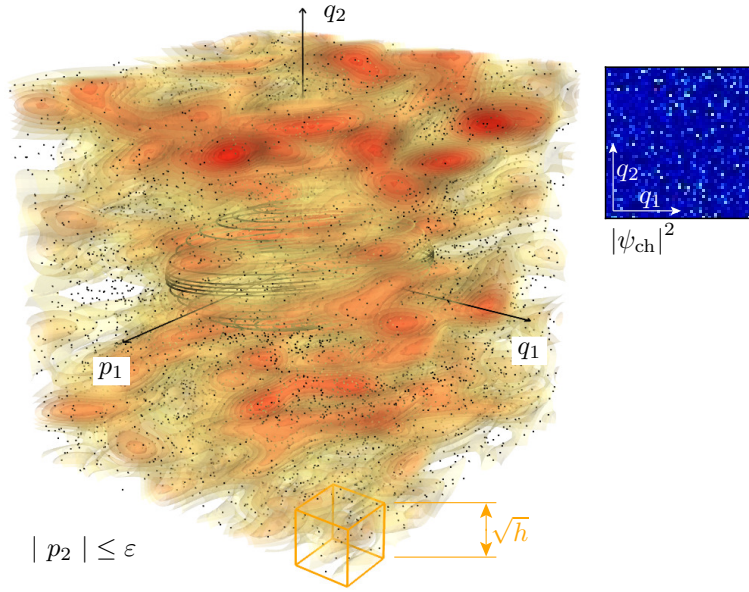


Figure 4.6.: A chaotic eigenstate of \mathcal{P}_{llu} for $1/h = 50$. Due to the small regular phase-space region the majority of the states is looking like this example. The phase-space plot also features a box of side length $\sqrt{\hbar}$ to give a qualitative estimate of the quantum mechanical resolution. The right hand side shows a position-space probability-density plot.

formally living at the interface between regular and chaotic region for $1/h = 50$ move deeper into the regular region and their chaotic admixture decreases. This can be seen in figure 4.7 where the state $\psi_{\text{reg}}^{5,3}$ is depicted for $1/h = 90$. Although it still has an chaotic admixture it is no longer visible in the shown isosurfaces. Due to the higher quantum resolution there are approximately 105 regular states facing 6295 chaotic ones. Figure 4.8 shows a chaotic state at $1/h = 90$. The \hbar -box included in this figure is smaller compared to the one shown for $1/h = 50$ in figure 4.6.

4.2.2. Eigenstates of \mathcal{P}_{nnc}

By introducing nonlinearities to the system its quantum properties change. In order to visualize some eigenfunctions for the map \mathcal{P}_{nnc} we fix $1/h = 50$ such that there are 2500 quantum states in total. As shown in figure 3.12 when calculating the FLI histogram there are three qualitatively different regions in phase space. The regular region should supports approximately 23 eigenstates. The stochastic region would yields enough volume for 2 to 3 states. The majority of the states are chaotic, namely 2475.

Figure 4.9 shows the ground state of the regular subsystem. Similar to the ground state of \mathcal{P}_{llu} it is given by a Gaussian function. The first excited states within the island look also similar to the ones of \mathcal{P}_{llu} such that we omit them here. Figure 4.10 shows $\psi_{\text{reg}}^{5,3}$ which is one of the last regular states supported at $1/h = 50$. The criterion whether a state is regular or not is only fuzzily defined.

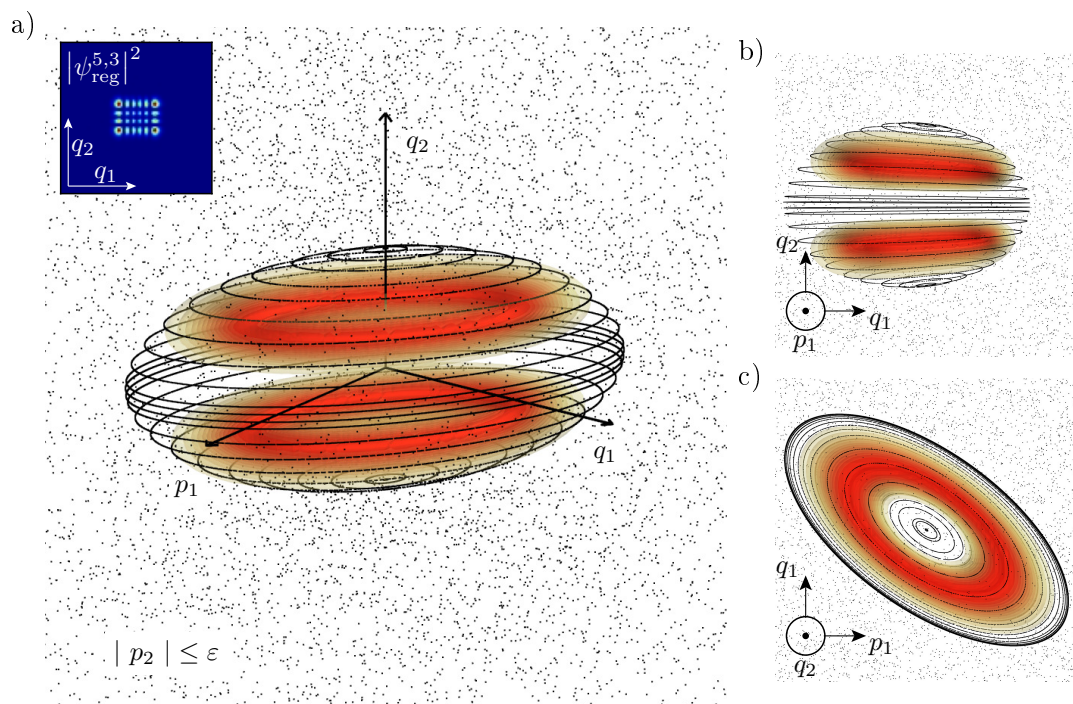


Figure 4.7.: Eigenstate $\psi_{\text{reg}}^{5,3}$ of \mathcal{P}_{lu} for $1/\hbar = 90$. The setup of the plot is the same as in figure 4.1.

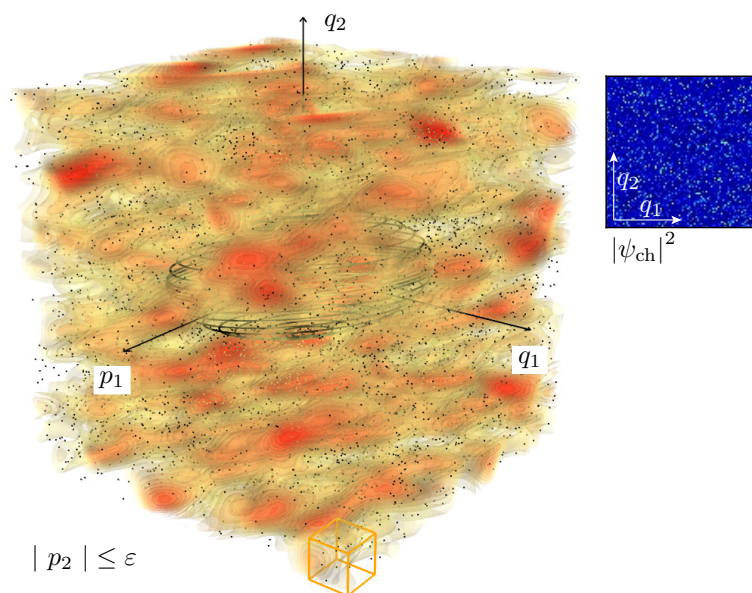


Figure 4.8.: A chaotic eigenstate of \mathcal{P}_{lu} for $1/\hbar = 90$. The phase-space plot also features a box of side length $\sqrt{\hbar}$ to give a qualitative estimate of the quantum mechanical resolution.

It depends on how much weight inside the chaotic domain is tolerated before a state is not called regular any longer. Apart from this fundamental inaccuracy it is hard to tell which eigenstate is the last one. In 2D maps regular eigenstates only have one quantum number and can therefore be ordered according to this number. Therefore, the last state within the regular region can be determined by increasing the quantum number and stopping as soon as the states have too much weight inside the chaotic domain. For 4D maps there are two quantum numbers and the last existing states for $1/h = 50$ are given approximately by $m_1 + m_2 = 8$. Therefore, state $\psi_{\text{reg}}^{5,3}$ is only one of the last regular states. We will come back to this on page 114 when discussing resonance-assisted tunneling phenomena for \mathcal{P}_{nnc} .

Contrary to the linear case, \mathcal{P}_{nnc} yields nonlinear resonances in phase space. They are also able to support eigenstates. However, to see this we have to decrease h considerably. If we choose $1/h = 300$, then there are also eigenstates on the EE-type resonance chain and on the stochastic layer. Two such example states are given in figure 4.11 and figure 4.12. It is an interesting but numerically very challenging question to also find eigenstates living on the rank-1 $6 : -1 : 1$ resonance highlighted by the orbit in figure 3.17(c). We comment on this briefly in section 4.3.1 but will not investigate quantum mechanical consequences of rank-1 resonances in this thesis.

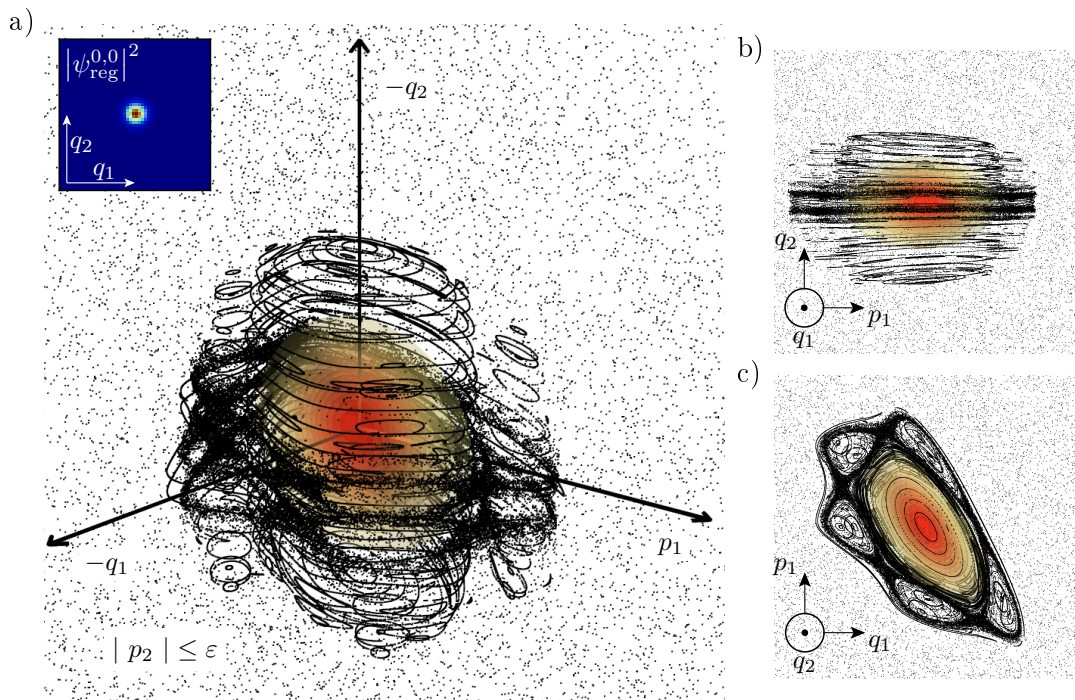


Figure 4.9.: Ground state $\psi_{\text{reg}}^{0,0}$ of the regular region of \mathcal{P}_{nnc} for $1/h = 50$. Figure (a) shows the Husimi function in the 3D section used in the classical picture from figure 3.11. Figures (b) and (c) show views along the q_1 and q_2 axis, respectively.

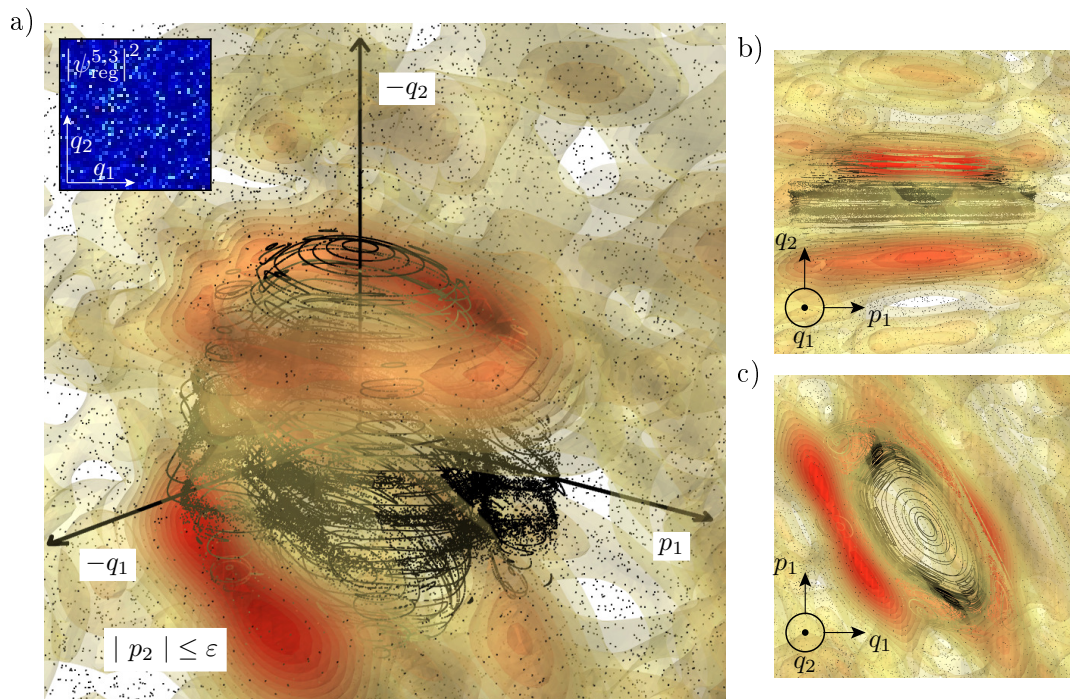


Figure 4.10.: Eigenstate $\psi_{\text{reg}}^{5,3}$ of the regular region of \mathcal{P}_{nnc} for $1/h = 50$. It is one of the last states to exist together with all states whose quantum numbers are $m_1 + m_2 = 8$, see also figure C.1 where the border of existing quantum states is shown.

4.2.3. Eigenstates of \mathcal{P}_{csm}

The classical coupled standard maps are introduced in section 3.4.3 and can be quantized according to section 4.1.

Here the assignment of quantum numbers to regular states is not as simple as for the designed maps. Nevertheless, the lowest states of the regular region are easy to identify. The ground state is shown for the choice of $1/h = 50$ in figure 4.13. At this value of $1/h$ the ground state $\psi_{\text{reg}}^{0,0}$ undergoes an avoided crossing in the eigenphase φ with another state. This can be seen in the position-space probability-density plot of figure 4.13 where a significant admixture of another state can be seen. An analysis of the eigenphases reveals that it is interfering with $\psi_{\text{reg}}^{4,1}$. In the Husimi representation this coupling is less visible. It still resembles a Gaussian state as in figure 4.1. Excited states inside the regular region and chaotic states supported in the chaotic sea look similar to the ones shown for \mathcal{P}_{lu} and \mathcal{P}_{nnc} and we omit them here.

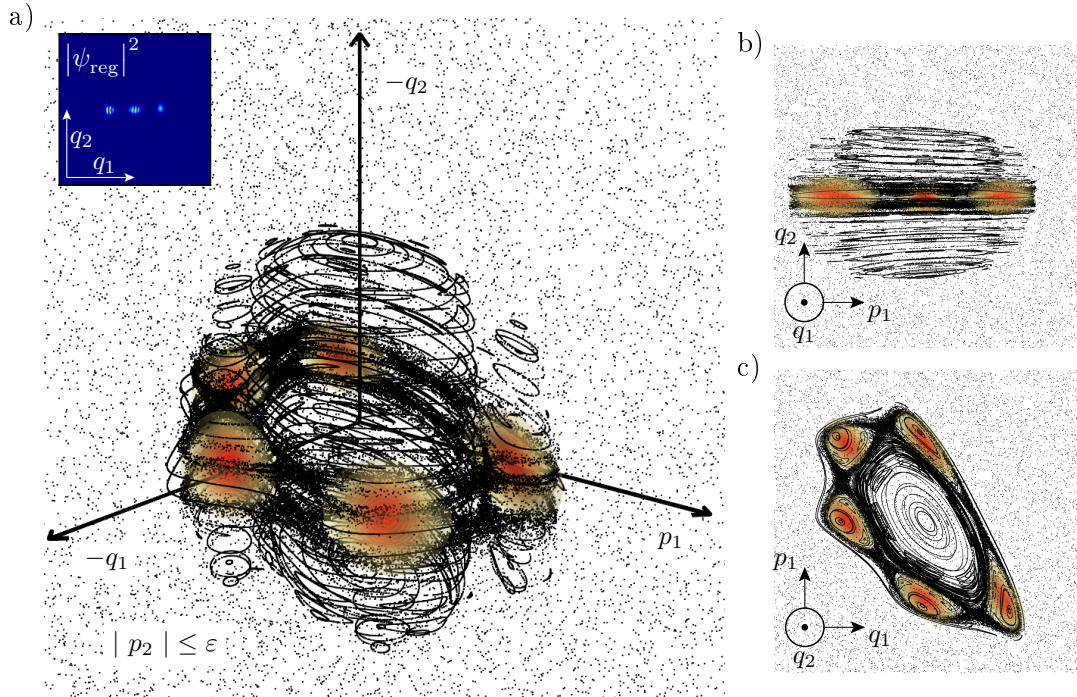


Figure 4.11.: Eigenstate ψ_{reg} of \mathcal{P}_{nnc} for $1/h = 300$ localized on the resonance chain. For this chain the quantum numbers related to the first degree of freedom do not apply. However, it can be said to be the ground state with respect to the second degree of freedom. Also excited states inside this resonance exist at this $1/h$.

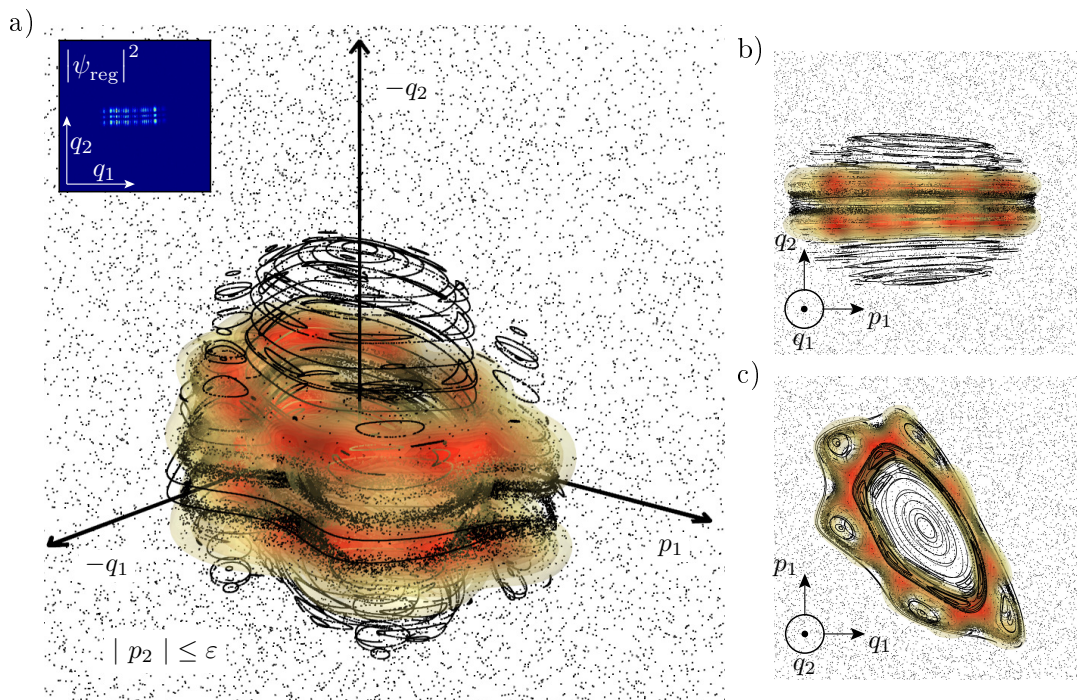


Figure 4.12.: Eigenstate ψ_{reg} of \mathcal{P}_{nnc} for $1/h = 300$ localized on the stochastic part of the resonance chain. For this chain the quantum numbers related to the first degree of freedom do not apply. However, it can be said to have a quantum number of two in the second degree of freedom.

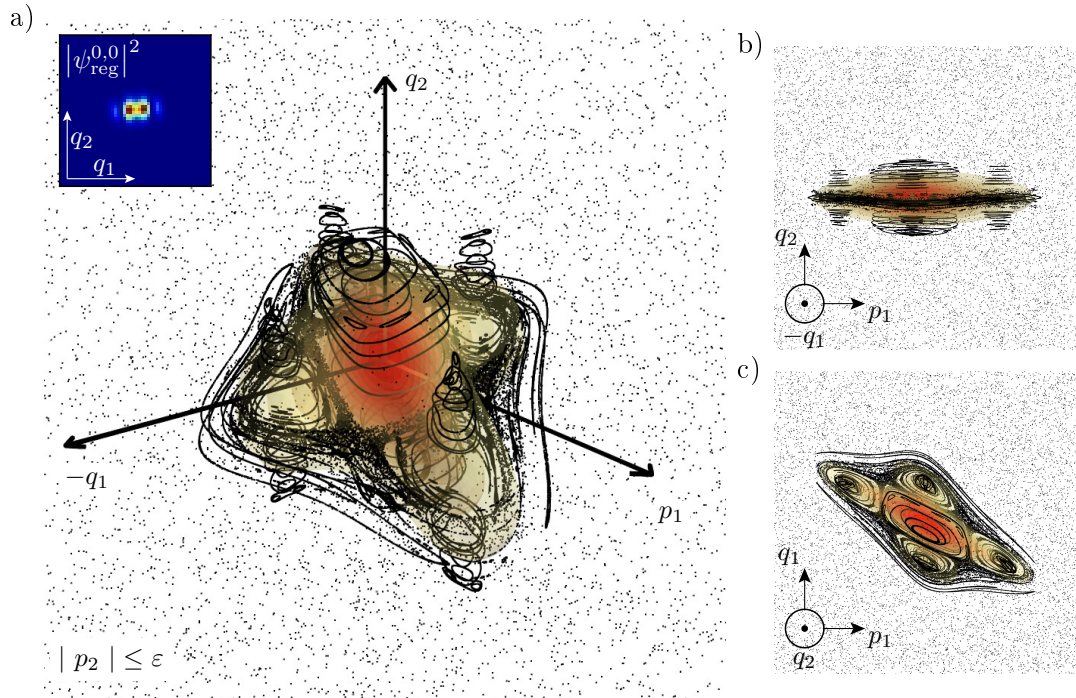


Figure 4.13.: Ground state $\psi_{\text{reg}}^{0,0}$ of \mathcal{P}_{csm} for $1/h = 50$. Figure (a) shows the Husimi function in the 3D section used in the classical picture from figure 3.23. It contains semi-transparent surfaces of constant value of the Husimi and an inset showing the position-space probability-density. Figures (b) and (c) show views along the q_1 and q_2 axis, respectively.

4.3. Quantum signatures of the stochastic layer

The reason why systems with more than two degrees of freedom are so important is not just given by the fact that they match the vast majority of relevant physical systems. It is also the fundamental difference given by the existence of the so-called Arnold web. While there are many works covering the classical aspects of the interconnected web of stochastic layers not much is known about quantum mechanical consequences. Examples are given by the work of Leitner and Wolynes [48] focusing on energy flow in weakly chaotic systems, the investigations of Demikhovskii, Izrailev, and Malyshev addressing Arnold diffusion in quantum systems for driven coupled nonlinear oscillators [50, 51] or rippled waveguides [52], and the work by Malyshev and Chizhova covering a Hamiltonian with two and a half degrees of freedom [53]. Also the influences of Arnold diffusion on ballistic transport in 3D billiards [49] and on nonlinear Schrödinger equations [54, 55] are investigated.

In contrast to the works in the literature we would like to concentrate on systems with a mixed phase space like \mathcal{P}_{csm} . Phase spaces like that of \mathcal{P}_{csm} cover very common physical situations like, for example, driven atoms [19]. Usually the phrase Arnold web is used in the literature for near-integrable systems only. In our context it refers to the interconnected web of chaotic layers around the resonances embedded in the regular domain in the center of phase space. However, as these systems are not near-integrable, much less is known about them analytically and the aspect of the connectivity of chaotic zones of such mixed systems is not very often investigated quantum mechanically. Although,

for example, reference [172] investigates mixed systems by means of coupled standard maps with $K_1 = K_2 = 3.0$ and $\xi_{12} = 0.4$, it addresses how higher dimensional quantum systems do not show effects of dynamical localization. A direct investigation of the Arnold web in the vicinity of the regular region is missing.

We want to determine the influence of the Arnold web on quantum mechanics directly. Therefore, we use the knowledge obtained by the phase-space section of \mathcal{P}_{csm} in section 3.4.3 in order to find the physically relevant regions of stochasticity. Apart from determining the relevant regions in phase space the 3D sections will also be used in order to approximate the direction of slow diffusion. This direction is usually known in near-integrable systems but missing in our setup as mentioned in section 3.4.2.

When investigating the role of the Arnold web in quantum mechanics several approaches are possible: In section 4.3.1 we extend the calculation of eigenstates started in section 4.2.3 to much smaller values of \hbar . First we estimate the necessary quantum resolution in order to resolve the stochastic region with eigenstates of U . Equipped with the ability to calculate eigenfunctions with sufficient resolution we then search for eigenstates living in the chaotic domain as well as reaching into the stochastic web surrounding the resonance chain of the main regular region.

Another approach is given by wave-packet dynamics. In order to mimic the classical itinerary from the outside chaotic sea into the Arnold web shown in figure 3.24, we present the time evolution of wave packets running into the stochastic zone in section 4.3.2. Together with a visualization of the wave packet we will analyze how deep they can penetrate the stochastic domain depending on $1/\hbar$.

4.3.1. Eigenstates resolving the stochastic layer

In this section we want to investigate quantum signatures of the stochastic layer. The fundamental difference to 2D maps is that this layer is accessible classically from the outside chaotic sea as is shown in figure 3.24. Our aim is to investigate whether this process has a quantum mechanical counterpart. This would, for example, be given by eigenstates simultaneously living on the chaotic region and penetrating the stochastic region. As the rank-2 resonance given by the period-4 orbit of \mathcal{P}_{csm} is the biggest one in phase space, we will focus on the stochastic layer containing the EH-type periodic orbit winding around the EE-type periodic orbit. An analysis of a rank-1 resonance, e.g. the $6 : -1 : 1$ resonance from figure 3.17(c), is also very interesting. This is due to the fact that the classical description of such a rank-1 resonances is much simpler because the corresponding integrable approximations are known [6, page 278]. However, the quantum mechanical treatment of this resonance is not covered in this thesis. This is mainly because the surrounding chaotic layer is much smaller than for the rank-2 resonance and therefore much harder to investigate numerically.

The volume of the stochastic layer wrapping around the period-4 island chain is estimated in equation (3.100) to be

$$V_{4\text{D}}^{\text{stochastic, numerical}} = 0.00685. \quad (4.16)$$

According to equation (4.14) every eigenstate belongs to a phase-space volume of \hbar^2 . So in order to

resolve the volume of the stochastic layer we need to have

$$1/h \gtrsim \frac{1}{\sqrt{0.00685}} \approx 12. \quad (4.17)$$

This however assumes that the stochastic region can be well resolved in all directions. But from figure 3.17(f) we know that the stochastic region is very thin. It is confined within $|p_2| < 0.052$. Hence, a quantum state at least has to resolve a phase-space volume of approximately 0.1^4 which yields $1/h \gtrsim 100$. However, the bound $|p_2| < 0.052$ is the total extent of the stochastic layer and neglects the very thin structure of the layer. In order to be able to resolve it, h has to be approximately $1/1000$. This is shown in figure 4.14 where a 2D FLI plane is used to visualize the width of the stochastic layer in a (q_1, p_1) plane. The FLI plane is accompanied by a box of side length \sqrt{h} for $h = 1/1000$. It shows that this choice is in principle capable of resolving the stochastic layer.

In order to carry out the quantum calculation at such a large value of $1/h = 1000$, we use the Lanczos algorithm presented in appendix J based on reference [173]. It allows to perform the diagonalization

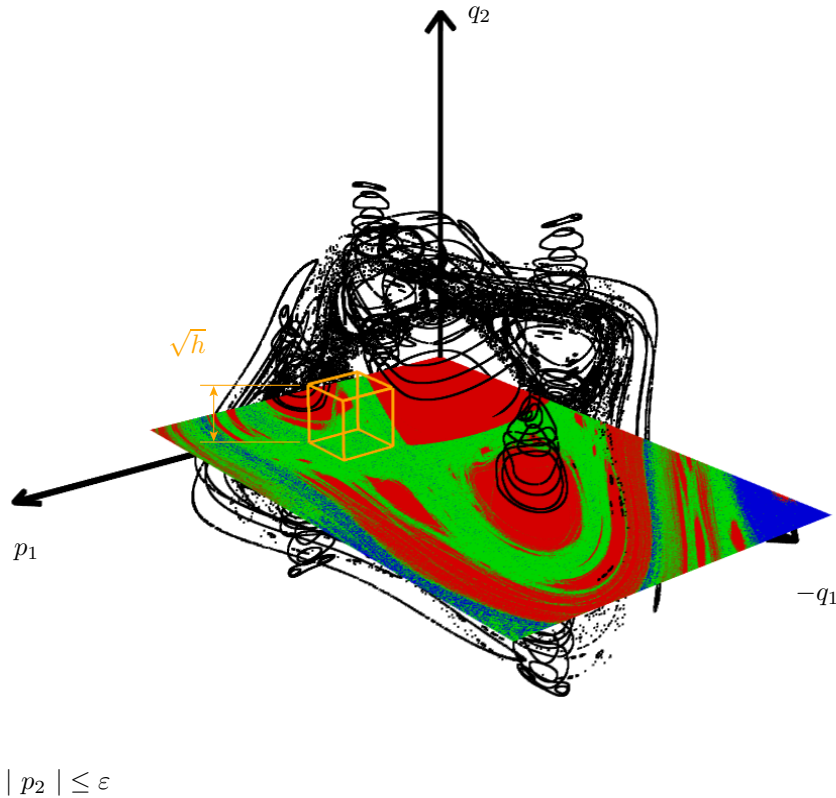


Figure 4.14.: Comparison of the quantum resolution and the size of the stochastic layer of \mathcal{P}_{csm} . The FLI plane is calculated at $(q_2, p_2) = (0.52, 0.0)$ for varying (q_1, p_1) . Red areas belong to regular motion, green orbits represent chaotic motion trapped inside the stochastic layer, and blue regions are part of the chaotic sea. The h -box is shown for $h = 1/1000$ and fits well into the stochastic layer.

of the time evolution operator in an iterative way which is necessary because the storage of the full $10^6 \times 10^6$ matrix U as well as all of its eigenvectors is beyond actual computational resources in terms of memory. The Lanczos algorithm is based on the choice of an initial vector $|\phi_1\rangle$. The final outcome are eigenvectors $|\psi\rangle$ having a maximum overlap with this state, $|\langle\phi_1|\psi\rangle| \rightarrow \max$. This allows to calculate relevant eigenvectors by choosing $|\phi_1\rangle$ appropriately. Here two approaches are possible: Either a coherent state placed at a point of interest in phase space can be used or direct product states of eigenstates of two uncoupled 2D standard maps can be used to create $|\phi_1\rangle$. For the first choice the coherent state would be placed inside the stochastic layer as we are interested in states localizing there. Note that the eigenstates in figures 4.11 and 4.12 have been calculated this way by using the Lanczos algorithm with the initial state placed at the periodic point from equation (3.98) and its EH counterpart, respectively. For the second choice given by eigenstates of uncoupled 2D maps figure 4.15 shows two such eigenvectors for 2D standard maps with parameters similar to \mathcal{P}_{csm} , namely $K_1 = 2.25$ and $K_2 = 3.0$. The eigenstates are chosen such that they concentrate inside the stochastic layer of the first 2D map and inside the chaotic sea of the second 2D map.

One of the resulting eigenvectors from such a calculation is shown in figure 4.16. In figure (a) the Husimi function is visualized over the entire 3D section $|p_2| \leq \varepsilon$ by surfaces of constant value, the colormap ranges from translucent-yellow (low) to opaque-red (high). As the state is chaotic, the regular region is merely visible. The smaller insets in figures (b) and (c) show views along the coordinates p_1 and q_2 , respectively. In these plots the value of the Husimi function is only displayed on the planes $p_1 = 0$ and $q_2 = 0.5$, which corresponds to the planes intersecting the regular island. In the insets the colormap of the Husimi function ranges from yellow (low) to red (high). Especially in (b) one can see that the Husimi has weight in between the resonance and the main island. The corresponding area is marked by a blue arrow.

This example state is one among several being overall chaotic but advancing into the stochastic region. However, the enormously slow classical Arnold diffusion inside this layer might lead to dynamical localization along the web and lead to an exponential decrease of eigenfunctions [51, 52] as

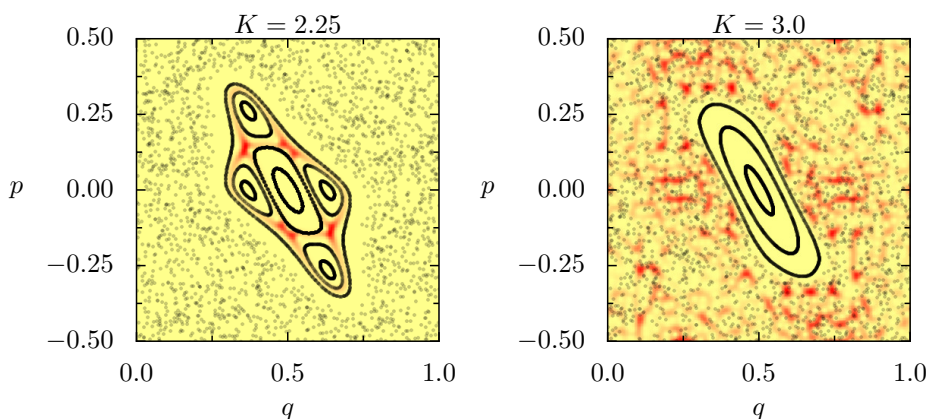


Figure 4.15.: Eigenstates of the 2D standard map for $K = 2.25$ and $K = 3.0$ for $1/\hbar = 1000$. Shown is the Husimi distribution over the 2D phase space. The colormap ranges from yellow (small) to red (large). Superimposed on both is the corresponding classical phase space.

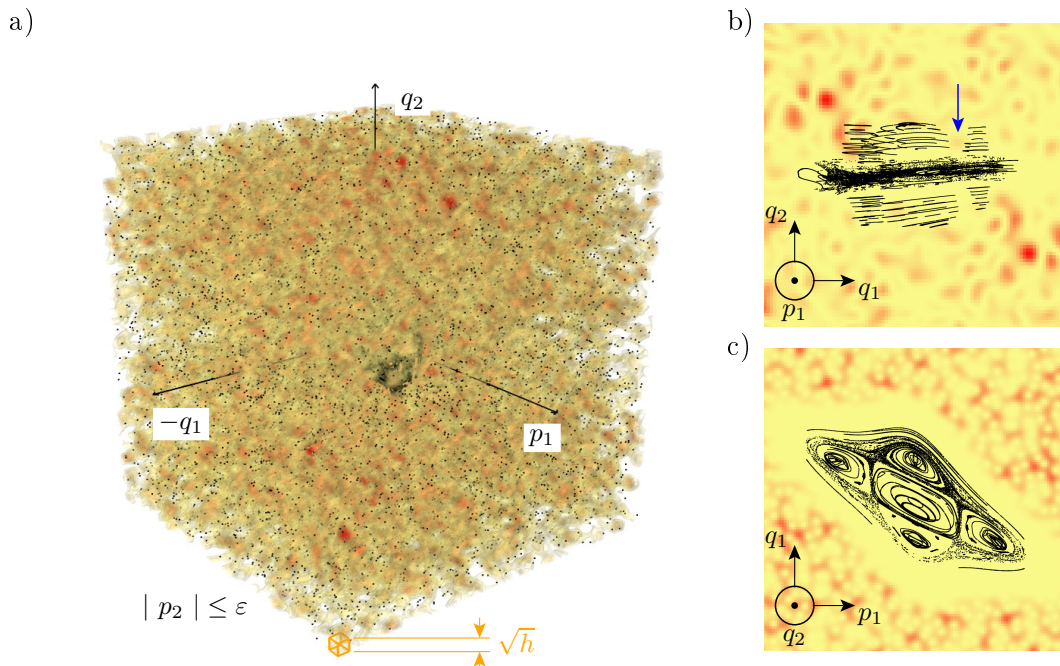


Figure 4.16.: Eigenstate of \mathcal{P}_{csm} for $1/h = 1000$. Figure (a) shows the Husimi function in the 3D section. The small box at the bottom indicates the size of Planck's constant. Figures (b) and (c) visualize the Husimi function on 2D planes at $p_1 = 0$ and $q_2 = 0$, respectively. The blue arrow indicates a region of increased weight of the eigenstate inside the stochastic layer.

known for 2D maps [155]. This does not contradict the observations of Adachi, Toda, and Ikeda [172] of dynamical localization being of less importance in higher dimensions because the slow diffusion process dominating the Arnold diffusion is a 1D process according to section 3.2.4.

In order to find examples of chaotic eigenstates reaching further into the stochastic layers than the state depicted in figure 4.16 one could try to increase the resolution of the quantum calculation by enlarging $1/h$ further. Another approach is to introduce maps which yield a larger stochastic layer region than \mathcal{P}_{csm} . The most promising attempt is to alter the phase space of the coupled standard maps in the following way. As the regular region is placed at the center of phase space, a large portion of the outside chaotic sea can be cut off without changing the island in the middle. This cutting is done by introducing a modulo operation which reduces the effective size of the phase space. While this changes the chaotic region significantly, the regular region stays exactly the same. The shape of the stochastic layer is not affected as it also resides close to the center of phase space. However, every orbit started inside the layer will at some point of its itinerary get into the chaotic sea and thereby sense the change in phase space. As the modulo is applied along the coordinates q_i and p_i the cutting is best done using a symmetrized version of the map allowing to remove a very large part of the chaotic phase space. Although this increased the size of the stochastic layer by a factor of four, we could not find eigenstates reaching significantly further into the stochastic layer than the one shown in figure 4.16.

4.3.2. Wave-packet dynamics into the stochastic layer

The fundamental difference between 4D and 2D maps is the interconnectivity of all chaotic regions. As regular tori do not separate phase-space regions, chaotic orbits are able to penetrate the stochastic region around the resonances, see figure 3.24. In section 4.3.1 quantum signatures of this stochastic layer are analyzed by eigenfunctions of the time evolution operator. In this section we follow the classical process underlying figure 3.24 more directly by considering the time evolution of wave packets initially placed within the chaotic domain. We choose a wave packet placed at $(p_1, p_2, q_1, q_2) = (-0.45, -0.45, 0.05, 0.05)$ which is close to the border of the 4D phase space. We are especially interested in how the time evolved wave packet will penetrate the stochastic region similar to the classical chaotic orbit shown in figure 3.24 and investigate this in dependence on Planck's constant \hbar .

In order to enable the time evolved wave packet to explore all possible details of the phase space it is necessary to propagate the initial state sufficiently long. The time scale for this is given by the so-called Heisenberg time

$$\tau_{\mathcal{H}} = \frac{\hbar}{\Delta\varepsilon} = \frac{\hbar}{\hbar\Delta\varphi} = \mathcal{N} = 1/\hbar^2 \quad (4.18)$$

where $\Delta\varepsilon$ is the mean level spacing of the quasienergies and we used $\varepsilon = -\hbar \cdot \varphi$, the mean eigenphase spacing $\Delta\varphi = 2\pi/\mathcal{N}$, the matrix size \mathcal{N} , and equation (4.14).

Once the time evolution is done for $\tau_{\mathcal{H}}$ steps, the state is propagated for further 1000 steps. At these iterations the Husimi distribution is calculated in the vicinity of the stochastic layer of interest. The values of the Husimi distribution of these 1000 steps are summed up to give a time-averaged Husimi distribution. Figure 4.17(a) shows the time-averaged Husimi distribution for $1/\hbar = 300$ in the vicinity of the stochastic layer around the period-4 orbit. The data is visualized in terms of surfaces of constant value of the Husimi function. The colormap ranges from high (red) to small values (yellow). The position of the spectator is comparable to the one in figure 3.23. In order to visualize the penetration into the stochastic layer, figures 4.17(b) to (f) show a slab of the Husimi values indicated by the green outline in figure 4.17(a) for different values of $1/\hbar$. Figure 4.17(b) shows the averaged Husimi distribution for $1/\hbar = 300$ in this slab. The orange box is of side length $\sqrt{\hbar}$ and denotes the quantum resolution, compare figure 4.14 and 4.16. The Husimi function decays uniformly into the regular domain not noticing the stochastic region at all. This changes significantly for increasing $1/\hbar$. In figure 4.17(f) it is clearly visible how the time evolved wave packet enters into the stochastic domain between the main regular region and the period-4 resonance. In order to quantify the intrusion into the stochastic region, we measure the weight of the Husimi function \mathbf{H} for positions λ along different 1D paths in phase space.

The straight red line in figures 4.17(b) to (f) ranges from the chaotic sea ($\lambda = 0$) directly into the regular region ($\lambda = 1$). The green line starts at the same point inside the chaotic sea ($\lambda = 0$) but points directly into the stochastic layer ($\lambda = 1$). We compare the weight along these lines in figure 4.18. The positional dependence of the averaged Husimi function \mathbf{H} along the line into the regular island is shown by the red curves in figure 4.18(a). The weight of all averaged wave packets

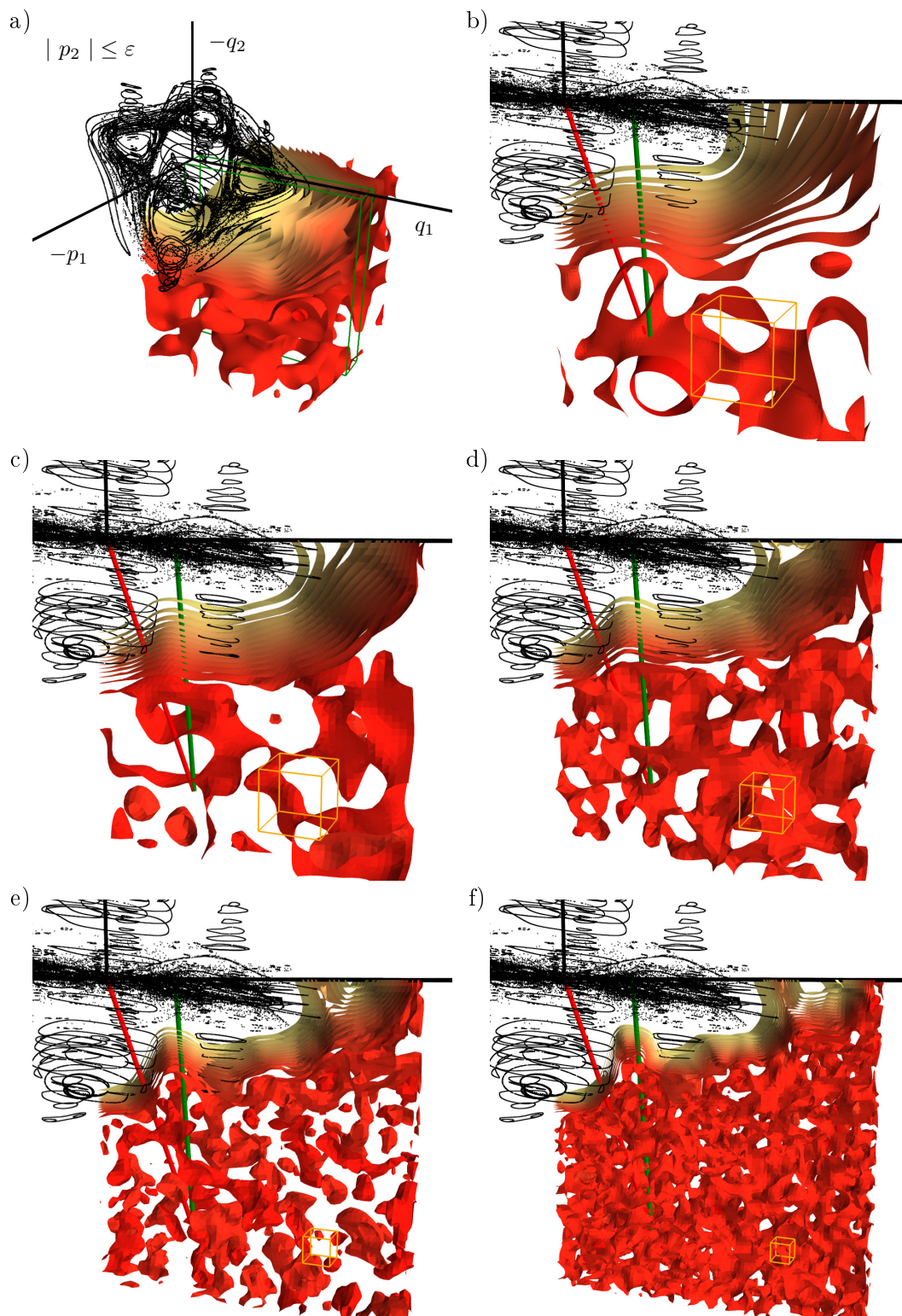


Figure 4.17.: Time evolution of wave packets into the stochastic layer. Figure (a) shows the averaged Husimi function calculated for $1/h = 300$ in the vicinity of the period-4 resonance. The green box indicates the slab shown in figures (b) to (f) which correspond to $1/h = 300, 500, 1000, 2500, 5000$. The orange box is of side length $\sqrt{\hbar}$ and indicates the quantum resolution. The straight lines reach from the chaotic sea into the the regular island (red) and along the stochastic region (green). The position dependent Husimi weight shown in figure 4.18 is calculated along these lines.

decays the same way from the chaotic region ($\lambda = 0$) towards the central EE-type fixed point ($\lambda = 1$) independently of the inverse effective Planck's constant $1/h$. The Husimi-function values $H(\lambda)$ cross the value $1/2$ approximately at the same position $\lambda \approx 0.55$.

The much more striking result is how the wave packet enters the stochastic region in figure 4.18(b) for increasing $1/h$. For $1/h = 300$ the wave packet behaves equivalently when approaching the regular region and the stochastic layer. In both figures (a) and (b) the weight H starts to drop at $\lambda = 0.5$. This reflects the flat shape of the surfaces of constant Husimi-function values in figure 4.17(b). When approaching the semiclassical limit of large $1/h$ the wave packet explores more and more of the stochastic region as can be seen qualitatively from the surfaces of constant Husimi-function values in figure 4.17(f).

We will measure this deeper exploration of the stochastic region using a *quantum mechanical intrusion depth* $\lambda_{1/2}$ defined by

$$H(\lambda_{1/2}) = 1/2, \quad (4.19)$$

i. e. $\lambda_{1/2}$ is the location along the lines at which the time-averaged Husimi function is $1/2$. In order to see the influence of increasing $1/h$ we use $1 - \lambda_{1/2}$, i. e. the distance of the point (4.19) to the endpoint along the green and red paths in figure 4.17. It has the property to go to zero for maximal intrusion. It is shown versus $1/h$ in a double logarithmic plot in figure 4.19. The red points belong to the negative intrusion depth along the line going directly into the regular region. They approximately saturate at $1 - \lambda_{1/2} = 0.45$. Their slight increase towards larger $1/h$ gives a hint that equation (4.19) might not yet be the correct quantity to measure the intrusion depth. The green points belong to the negative intrusion depth along the green line into the stochastic layer. Here the values tend towards zero for

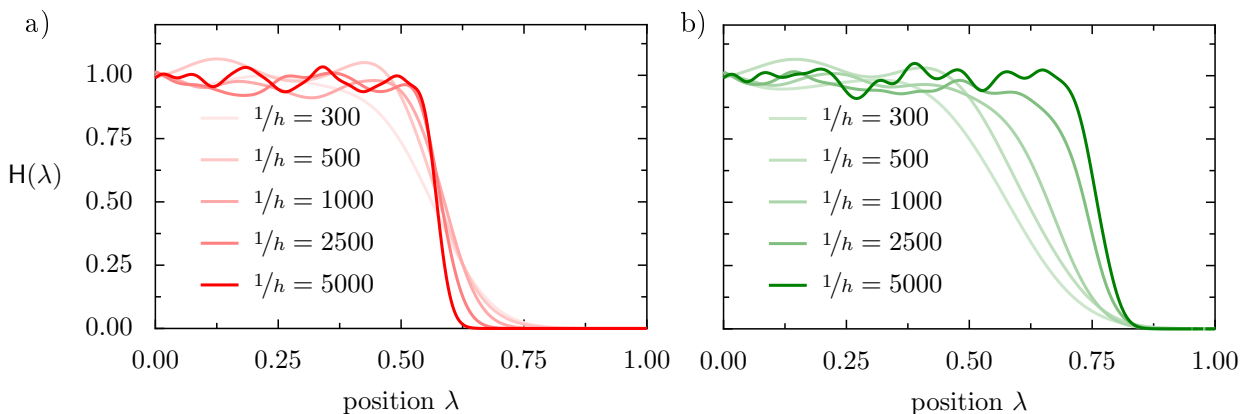


Figure 4.18.: Position dependent Husimi weight along different paths in phase space for different quantum resolutions. Figure (a) shows the weight dependence when going from the chaotic sea ($\lambda = 0$) into the regular domain ($\lambda = 1$, c.f. the red lines in figure 4.17). Figure (b) displays the dependence along the stochastic region (green lines in figure 4.17). All curves are scaled to have the same weight of approximately one in the chaotic sea, $\lambda = 0$.

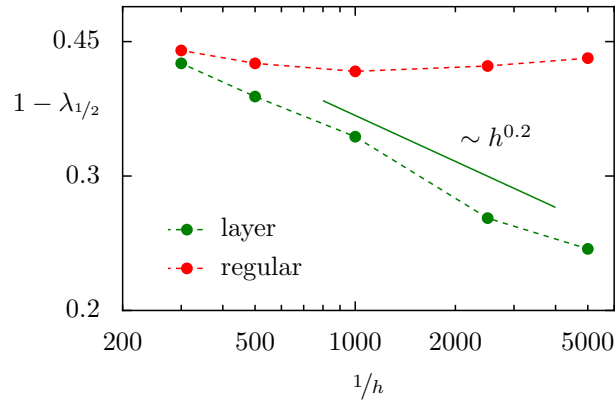


Figure 4.19.: Dependence of the negative quantum mechanical intrusion depth $1 - \lambda_{1/2}$ on $1/h$ for the path into the regular domain (red) and along the stochastic layer (green) in double logarithmic scale. The lines are guides to the eye. A power law with exponent 0.2 (straight line) is obtained from a fit to the data based on the path into the stochastic layer.

increasing $1/h$ and no saturation is visible for the shown $1/h$ range. A fit of the data suggests a scaling

$$1 - \lambda_{1/2} \sim (1/h)^{-0.2} = h^{0.2} \quad (4.20)$$

and is indicated by the straight line in figure 4.19. A comparison of the power law fit from equation (4.20) with a fit to an exponential shows that the residual of the exponential fit is considerably worse. However, as only a very small range of values is covered along the ordinate of figure 4.19, the behavior cannot be significantly distinguished from

$$1 - \lambda_{1/2} = -0.066061 \cdot \log(1/h) + 0.793732. \quad (4.21)$$

It is an open and very interesting question how the functional dependence of the negative intrusion depth $1 - \lambda_{1/2}$ is related to dynamical localization [155] and the classical rate of Arnold diffusion as mentioned in section 3.4.2 on page 63. Due to the fact that the slow Arnold diffusion is a 1D process, eigenstates might undergo the same dynamical localization known from 2D maps although the general setup of dynamical localization was found to be of less significance in higher dimensional systems [172]. This makes the analysis of the intrusion in 6D maps an interesting question because there the classical Arnold diffusion is a 2D phenomenon [6, page 353] and dynamical localization might also be suppressed for the quantum resolution of the Arnold web.

We would like to close with two technical remarks. First, note that the green path along the layer is only roughly equivalent to the direction of slow diffusion inside the layer, \mathbf{e}_{slow} , introduced in section 3.4.3 on page 73. For a more accurate choice of a path into the stochastic layer a careful analysis of the classical properties is necessary. However, we do not expect qualitative difference in the behavior of the curves shown in figure 4.18. Second, equation (4.18) implies that the wave-packet propagation becomes more time consuming for increasing $1/h$. This is because first the propagation time has to be enlarged to \mathcal{N} , and second one step of the time evolution done using the FFT and

various multiplications scales like $\mathcal{N} \log \mathcal{N}$. Therefore, the overall effort scales like $1/h^4 \log 1/h$. Due to this increase of computing effort only the data for $1/h = 300$ to 2500 is based on a wave-packet propagation until the Heisenberg time $\tau_{\mathcal{H}}$ ranging from 90000 iterations to 6250000 iterations. For $1/h = 5000$ we iterated the wave packet only 2145059 times which is approximately $0.086 \cdot \tau_{\mathcal{H}}$ but already took four months of computation on an actual desktop computer.

4.4. Dynamical tunneling rates

Section 4.2 impressively shows that quantum eigenstates of the time evolution operator do not completely live on either the regular or the chaotic domain in phase space. Classically these subsystems are interwoven in a very complicate way but still form disjoint sets each invariant under the dynamics. Quantum mechanically this is no longer the case. If a state is completely localized, for example in the regular island, its weight in the other domain will increase under the time evolution, i. e., the state will tunnel from the regular island into the chaotic sea. This process is called dynamical tunneling after Davis and Heller [56] who introduced it when considering the quantum mechanical connection of classically disconnected regular regions in the phase space of molecules. The key quantity to describe this process is the *tunneling rate* γ . It indicates the speed with which the process takes place and therefore also measures the strength of the coupling between the classically disconnected phase-space regions.

The fact that the majority of physical systems has a mixed phase space makes dynamical tunneling vital for the understanding of these systems in the realms of quantum mechanics. Prominent examples cover classically forbidden processes in atoms and molecules [56–64], optical or microwave resonators [65–69], and mesoscopic systems [11, 70].

Hence, dynamical tunneling rates are very interesting quantities, which however are hard to predict due to the complex underlying classical phase-space structures. In order to find a prediction, several aspects have been investigated in the literature. Tomsovic and Ullmo investigated the level splittings of two symmetry-related regular regions divided by a chaotic domain and found that the chaotic dynamics leads to a large enhancement of the splittings whenever a chaotic state gets close to the two regular states in the quasi-energies [68, 160, 162]. They therefore introduced the notation of *chaos-assisted tunneling*. Here, however, we consider systems with only one regular domain embedded in a chaotic sea. In reference [79] the link between both setups is investigated and they are found to be very similar. For systems with one regular island the tunneling process from the regular to the chaotic region is called *regular-to-chaotic tunneling*. This process appears in two versions. If a regular states couples directly to the ensemble of chaotic states, then it is said to undergo *direct regular-to-chaotic tunneling*. Otherwise the coupling is mediated via intermediate states. The quantum transition into the chaotic sea is called *resonance-assisted tunneling* if the coupling to the intermediate state is caused by a classical nonlinear resonance in phase space.

The direct regular-to-chaotic tunneling might be seen as the most fundamental of these processes because it addresses the most direct coupling between classically disconnected regions. It is investi-

gated intensively for 2D maps [77–79] and systems being reducible to such maps like driven systems with one degree of freedom [71], billiards systems [68, 76], measurements on optical or microwave cavities [67, 78, 80–82], or transport processes in 2D electron systems [11, 70]. Central to this investigation is the possibility of a prediction of this direct tunneling rate. Bäcker, Ketzmerick, Löck, and Schilling [78] introduced a formula based on a fictitious integrable system mimicking the regular phase-space region and with this allowing to derive analytical formulas for the direct tunneling rate γ^d . After presenting numerical data for the map with linear regular region, \mathcal{P}_{llu} , in section 4.4.2 the fictitious-integrable-system approach is applied to 4D maps the first time.

Although the direct regular-to-chaotic tunneling is the more fundamental process it is often overshadowed by the resonance-assisted tunneling (RAT) [83, 84]. The emerging effects are visible for example in highly excited Rydberg states of driven atoms [59] and molecules in general [62, 64]. This theory is especially important in the semiclassical limit $1/\hbar \rightarrow \infty$ where it can predict peaks in the tunneling rates to high accuracy. However, the RAT theory only explains how resonances assist the tunneling process due to an enhancement of the tunneling at certain values of the parameter $1/\hbar$. For a detailed prediction of the dynamical tunneling process it is necessary to incorporate the direct tunneling rates γ^d [166]. We investigate the effects of classical resonances in 4D mappings on the dynamical tunneling rates γ in section 4.4.5 where we present an approach to generalize the RAT approach of 2D maps. The tunneling rates of \mathcal{P}_{nnc} presented in section 4.4.4 are compared to this theory in section 4.4.6. We finish with a numerical investigation of dynamical tunneling rates for the coupled standard maps system \mathcal{P}_{csm} in section 4.4.7.

An important aspect of higher dimensional systems is the smallness of the regular region compared to the chaotic domain. This is not only the case in the mappings introduced in section 3.4 but also for example for highly excited driven helium where the regular region is given by so-called frozen planet configurations [19, 20, 149, 150]. This enormous dominance of the chaotic domain is also investigated for 2D maps where it leads to a *flooding of regular phase-space structures* by chaotic eigenstates [174–176]. The flooding phenomenon is related to the fact that for an increasing number of degrees of freedom more and more phase-space volume of the regular domain is concentrated at the interface to the chaotic region. A link to higher dimensional systems is presented in reference [177] where the high dimensionality of the system is emulated by a quasi-periodically driven 2D standard map.

4.4.1. Numerical calculation of dynamical tunneling rates

In this thesis numerically determined tunneling rates are obtained by introducing an opening into the quantum system. This opening is modeled by changing the time evolution operator U such that the weight of any state in a certain opening region in phase space is set to zero. Furthermore, we choose this opening region such that it does not intersect with the regular domain. Whenever the potential $V(\mathbf{q})$ is evaluated at the points of the opening while constructing U according to equation (4.12) the corresponding values of U are set to zero. This corresponds to the introduction of an additional infinite imaginary potential in the opening region. As a result we obtain a non-unitary quantum map U^{open} .

By introducing the opening the eigenvalue equation (4.3) of U changes to

$$U^{\text{open}}|\psi\rangle = e^{i(\varphi+i\gamma_{\text{decay}}/2)}|\psi\rangle \quad \text{such that} \quad \|U^{\text{open}}|\psi\rangle\|^2 = e^{-\gamma_{\text{decay}}} \|\psi\|^2. \quad (4.22)$$

In this equation the eigenphase of U^{open} is given by $\varphi + i\gamma_{\text{decay}}/2$. Here φ corresponds to the real part of the eigenphase of the unitary operator U plus a possible shift. The imaginary part $\gamma_{\text{decay}}/2$ defines the decay rate of the states. As shown on the right hand side of equation (4.22) it describes how much weight an eigenstate of U^{open} loses per unit time.

In order to use this formalism to calculate regular-to-chaotic tunneling rates we can place the opening in the phase space such that it covers only parts of the chaotic domain. Assuming a fast transport inside the chaotic sea the decay rates γ_{decay} of the regular states can be regarded as being the regular-to-chaotic tunneling rates γ of these regular states. This is because typically the tunneling rate is a very small quantity especially for states far away from the chaotic domain. The slow tunneling process is therefore only minimally perturbed by the very fast transport from the chaotic sea out of the system.

This method of using an open quantum system has a big advantage: As the operator U^{open} is sub-unitary all its eigenvalues lie within the unit circle of the complex plane \mathbb{C} , cf. equation (4.22). This allows to use iterative diagonalization schemes which aim to return the largest eigenvalues. The gain from this is twofold. First, it reduces the memory demand of the computation as it is not necessary to build up the $\mathcal{N} \times \mathcal{N}$ matrix U^{open} . It suffices to apply the linear operator from equation (4.22) on a vector $|\phi\rangle$ of length $\mathcal{N} \propto 1/h^2$. Second, this calculation is much faster as we can stop the diagonalization as soon as all long-lived eigenstates are calculated.

In this thesis the ARPACK-package [178] is used to calculate the wanted eigenvalues and eigenvectors of large sub-unitary matrices U^{open} . The number of states which is calculated for a given value of $1/h$ can be estimated from the phase-space volume of the regular region $V_{4\text{D}}^{\text{reg}}$, see section 3.4 on pages 43, 50, and 63. The number of calculated eigenstates N_{ev} out of all eigenvectors $\mathcal{N} = h^{-2}V_{\text{phase space}}$ is set to $2.5 \cdot V_{4\text{D}}^{\text{reg}}/V_{\text{phase space}} \cdot \mathcal{N}$. The factor 2.5 is chosen to assure that all regular states are found. The opening is specified in position space such that it removes arbitrary points in momentum space. The FLI is used to ensure that the opening does not change the regular part of phase space.

Note that the above method based on projecting weight out of the system is one among several possibilities to calculate dynamical tunneling rates [79, 125, 152]. Other methods are for example based on wave-packet propagation. The advantage of this propagation method is that it is not necessary to set up a $\mathcal{N} \times \mathcal{N}$ matrix U^{open} . However, the algorithm is very slow [152] and only yields one decay rate at a time. Another possibility which has been successfully applied to 2D maps is the determination of avoided crossings [125]. Contrary to the wave-packet based method this requires the diagonalization of the time evolution operator matrix under parameter variation in order to determine all avoided crossings between the regular state of interest and the chaotic states. From the width of the avoided crossings the dynamical tunneling rates can be determined by Fermi's golden rule [79]. As in our case the size of the matrix U^{open} increases with $\mathcal{N} \propto 1/h^2$ this approach does not allow to calculate the tunneling rates in the semiclassical limit of large $1/h$.

4.4.2. Direct regular-to-chaotic tunneling rates γ^d of \mathcal{P}_{llu}

Our aim is to calculate, predict, and understand dynamical tunneling rates for 4D maps with a mixed phase space. In order to predict tunneling rates, it is more promising to use the designed maps of section 3.4.1 as a first subject of investigation rather than the generic system of the coupled standard maps \mathcal{P}_{csm} . This approach already served as a good starting point for the investigation of dynamical tunneling in 2D maps [78, 152]. The advantage is that one can first look at the system without nonlinear resonances and focus solely on the direct-regular-to-chaotic tunneling-rates γ^d . Among the presented maps the system \mathcal{P}_{llu} is the most simple possible setup in terms of well separated regular and chaotic phase-space regions.

Before we present numerically determined data for \mathcal{P}_{llu} we want to comment on the potential V of the mapping. While \mathcal{P}_{llu} was designed to have a continuous potential V its first derivatives yield jumps at the border of the ellipsis separating the different potential definitions in equation (3.70). This can lead to diffraction-like processes [179] in quantum mechanics which play a role if the Hamiltonian is not sufficiently smooth [180, 181]. However, as also diffraction processes describe classically forbidden quantum transitions, we will include them to the processes described as tunneling and not take them into account separately.

In order to calculate the tunneling rates numerically, we open the quantum system by adding absorbing boundary conditions as explained in section 4.4.1. The opening of the system is introduced such that it does not intersect with the regular region. In position space the ellipse defined by the choice of Q^2 in equation (3.70) gives an extent of the regular island in q_1 and q_2 of $q_{1,\text{max}} = \sqrt{2/r_1}Q = 0.2532$ and $q_{2,\text{max}} = \sqrt{2/r_1}Q = 0.2319$, respectively. The FLI values can be used to confirm that the regular domain is included in this region. If the FLI is calculated on a 4D grid in phase space and then averaged over both p -axes then the resulting FLI plot vs. q_1 and q_2

$$q_1, q_2 \mapsto \frac{1}{N^2} \sum_{p_1, p_2} \text{FLI}(p_1, p_2, q_1, q_2) \quad (4.23)$$

shows where the regular region ends projected onto the position space. This is shown in figure 4.20. The projected FLI values will be helpful if the edge of the regular domain cannot be determined analytically.

In figure 4.21 we show the numerically determined tunneling rates γ^d vs. the inverse effective Planck's constant $1/h$. We consider the lowest excited states $\tilde{\psi}_{\text{reg}}^{0,0}$, $\tilde{\psi}_{\text{reg}}^{1,0}$, $\tilde{\psi}_{\text{reg}}^{0,1}$, and $\tilde{\psi}_{\text{reg}}^{1,1}$ of the regular region. Their position-space probability-density is shown in the inset of figure 4.21. For all states we find an exponential decrease of γ^d with increasing $1/h$. Especially for small values of $1/h$ fluctuations are visible in the data due to the coarse grid on which the wave functions are given. The obtained numerical data resembles the data presented for 2D maps [78].

Note that in order to calculate the dynamical tunneling rates from the data obtained by the diagonalization of U^{open} a post-processing of the data is necessary in order to determine the eigenstates of interest for all values of $1/h$. This is described in appendix B.

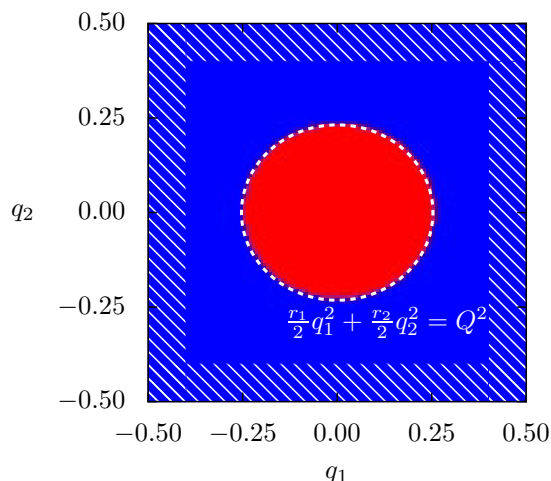


Figure 4.20.: Projected FLI values onto position space for \mathcal{P}_{llu} . At each point (q_1, q_2) the mean value of the FLI (4.23) is calculated. If the value is smaller than 0.999 times the maximum value of $\text{FLI} = 450$ then the corresponding point is shown in red. These points have at least one point in p_1 or p_2 where there is regular dynamics yielding a non-maximum FLI. All other points are marked in blue as they yield chaotic motion for all values of the momenta. The hatched white area denotes the opening of the quantum system which does not intersect with the regular region at any value of the momenta. The white line is given by the designed potential (3.70) and matches the numerical projection of the regular region.

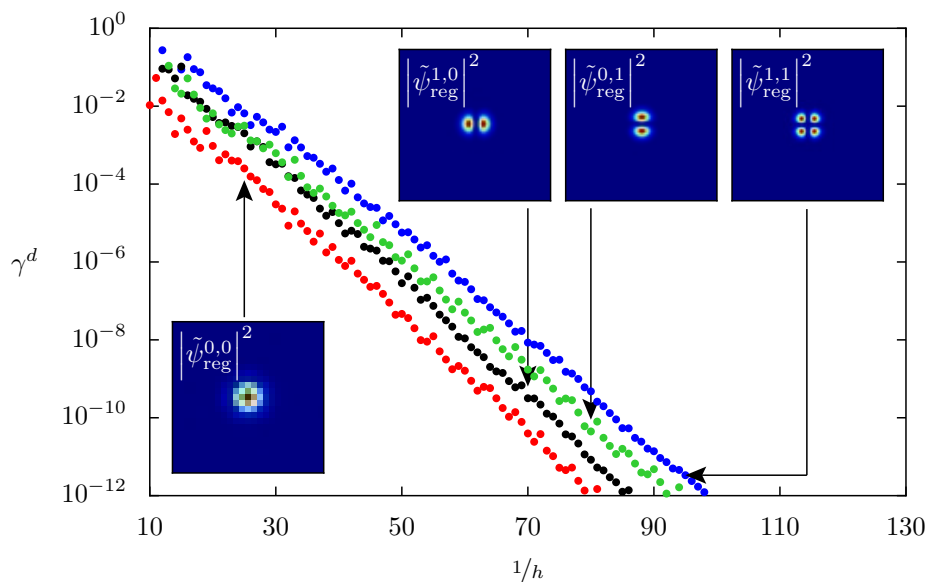


Figure 4.21.: Numerically determined direct regular-to-chaotic tunneling rates γ^d for vs. $1/h$ for \mathcal{P}_{llu} determined by opening the system, equation (4.22). The corresponding eigenstates are shown in insets at fixed values of $1/h$. The quantum numbers for the states are given by the number of nodal lines in q_1 and q_2 direction.

4.4.3. Prediction of γ^d using the fictitious integrable system approach

The fictitious integrable system approach was very successfully applied to 2D maps and 2D billiards [78, 79, 81, 82]. In this section we want to apply this approach the first time to 4D mappings in order to predict direct regular-to-chaotic tunneling rates γ^d and we will find very good agreement. However, first we want to introduce the approach.

The eigenstates of U intrinsically bear the coupling between regular and chaotic domain within them. Especially as shown in figure 4.5 highly excited states in the regular region have a large contribution also in the classically disconnected chaotic domain. However, while the whole quantum system underlies the coupling between regular and chaotic domain, it can be interpreted being the result of a coupling introduced to two previously uncoupled regular and chaotic subsystems. The fictitious integrable system approach aims for creating these subspaces.

Due to dynamical tunneling the eigenstates $\psi_{\text{reg}}^{m,n}$ of the time evolution operator U_{reg} of the quantum system belonging to the purely regular dynamics are not eigenstates of the full system U . Therefore, they are called *quasi-modes*. This notation goes back to Arnold [182] and originally means solutions to the eigenvalue equation for U which are only correct up to a certain order in Planck's constant \hbar . Depending on the relative size of the regular phase-space region in comparison with Planck's constant only a finite number of quasimodes $\psi_{\text{reg}}^{m,n}$ are used to create a projection operator P_{reg} onto the regular subsystem. An arbitrary basis in the orthogonal complement of the subspace defined by P_{reg} can be used to define the decomposition into regular and chaotic subspaces of the full Hilbert space.

If we assume that the basis states of regular and chaotic subsystem, $\psi_{\text{reg}}^{m,n}$ and ψ_{ch} , are known, then it is possible to obtain the coupling v between both subsystems. If a particular regular and chaotic state are considered, then this coupling is given by

$$v_{\text{ch}}^{m,n} = \langle \psi_{\text{ch}} | U | \psi_{\text{reg}}^{m,n} \rangle. \quad (4.24)$$

As v is a consequence of the dynamical tunneling, it is possible to determine the tunneling rates γ^d from the couplings, e. g. via Fermi's golden rule [79]. In these terms equation (4.24) leads to the tunneling rate of $\psi_{\text{reg}}^{m,n}$ into the single chaotic state ψ_{ch} . In order to obtain the overall tunneling rate of $\psi_{\text{reg}}^{m,n}$ into the whole chaotic subsystem, we have to average over all chaotic states. The result in terms of the direct tunneling rate is [79]

$$\gamma_{m,n}^d = \sum_{\text{ch}} |v_{\text{ch}}^{m,n}|^2 \quad (4.25)$$

and can be re-written in terms of a projector $P_{\text{ch}} = \sum_{\text{ch}} |\psi_{\text{ch}}\rangle\langle\psi_{\text{ch}}|$ onto the chaotic subsystem

$$\gamma_{m,n}^d = \|P_{\text{ch}} U \psi_{\text{reg}}^{m,n}\|^2 = \|(1 - P_{\text{reg}}) U \psi_{\text{reg}}^{m,n}\|^2, \quad (4.26)$$

where we further used the projector onto the regular subsystem, $P_{\text{reg}} = \sum_{k,l} |\psi_{\text{reg}}^{k,l}\rangle\langle\psi_{\text{reg}}^{k,l}|$, and the property that both projectors span the full system $P_{\text{reg}} + P_{\text{ch}} = 1$ [79].

Arrived at equation (4.26) the necessary ingredient to predict direct regular-to-chaotic tunneling rates is the knowledge of the purely regular subsystem U_{reg} . For the mapping \mathcal{P}_{llu} such a purely regular system can be constructed. As the classical dynamics of U_{reg} have to coincide with \mathcal{P}_{llu} on the regular part of the latter, we just have to extend the regular dynamics of \mathcal{P}_{llu} beyond its actual domain into the chaotic region. This is done by choosing the potential $V_{\text{reg}}(\mathbf{q})$ of U_{reg} to be given by equation (3.69). For this choice of $V_{\text{reg}}(\mathbf{q})$ it is possible to derive the eigenstates analytically. They are given by the eigenfunctions of two uncoupled harmonic oscillators, see later.

Note that the described construction of U_{reg} implies that the fictitious integrable system is also a kicked system and therefore decomposable into a kinetic and potential part like U in equation (4.2). This can be used to evaluate equation (4.26) semiclassically [79, 152]. The result was applied successfully to various maps and billiards [78, 79, 81, 82]. For 4D maps it is generalized to

$$\gamma_{m,n}^d = \int_{\Gamma_q} d^2q |\psi_{\text{reg}}^{m,n}(\mathbf{q})|^2 2 \left(1 - \cos \left(\frac{V(\mathbf{q}) - V_{\text{reg}}(\mathbf{q})}{\hbar} \right) \right) \quad (4.27)$$

in which $\Gamma_q = [-0.5, 0.5] \times [-0.5, 0.5]$ denotes the whole position space of \mathcal{P}_{llu} , V is the potential from equation (3.70) and V_{reg} is the potential of the fictitious regular system U_{reg} from equation (3.69).

We now want to compare the numerically obtained data from section 4.4.2 with the prediction (4.27). The comparison is shown in figure 4.22 and displays a very good agreement over more than ten orders of magnitude with deviations smaller than a factor of two. This demonstrates that the fictitious integrable system approach is also valid in higher dimensions. The plot also nicely shows that higher excited regular states have higher tunneling rates. This explains the chaotic admixture of the eigen-

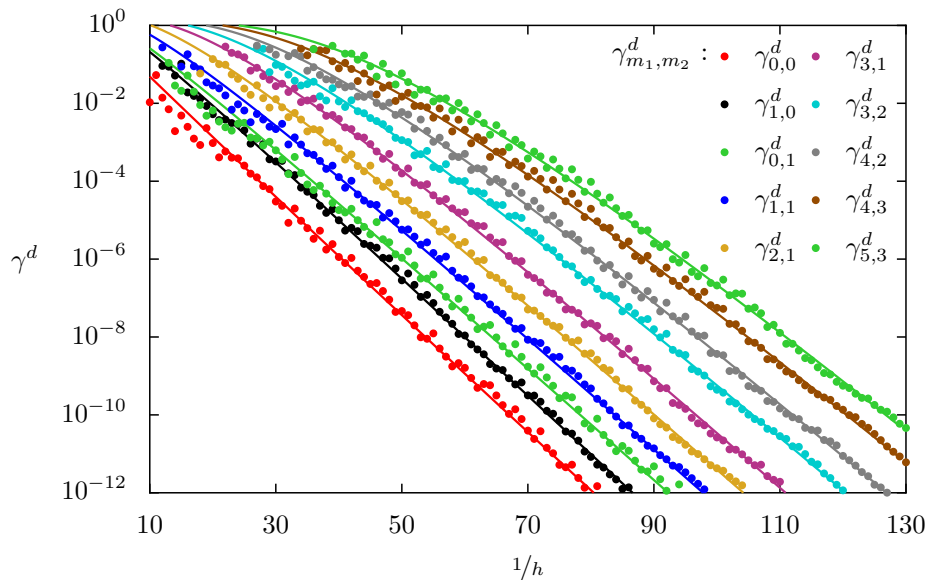


Figure 4.22.: Prediction of direct regular-to-chaotic tunneling rates γ^d for \mathcal{P}_{llu} using the fictitious integrable system approach (4.27) (solid lines) compared to numerically obtained data (dots). For all states a very good agreement is found over up to ten orders of magnitude.

states in section 4.2 especially for $\psi_{\text{reg}}^{5,3}$ at $1/\hbar = 50$ in figure 4.5.

The evaluation of equation (4.27) requires an analytical expression of the quasimodes $\psi_{\text{reg}}^{m,n}$. As mentioned above, they are given by the eigenstates of the harmonic oscillator [79, 152]

$$\psi_{\text{reg}}^{m,n}(\mathbf{q}) = \psi_{\text{reg}}^n(q_1)\psi_{\text{reg}}^m(q_2) \quad \text{with} \quad (4.28)$$

$$\psi_{\text{reg}}^n(q) = \frac{1}{\sqrt{2^n n!}} \sqrt{\frac{\text{Re } \sigma}{\pi \hbar}} H_n \left(\sqrt{\frac{\text{Re } \sigma}{\hbar}} q \right) e^{-\frac{\sigma}{2\hbar} q^2}. \quad (4.29)$$

Here H_n is the n -th order Hermite polynomial orthogonal over \mathbb{R} with weighting function e^{-q^2} . The parameter σ is given according to the entries of the matrix of the linear mapping (3.80) by

$$\sigma = \frac{\sigma' + i(\sigma'^2 - 1) \cos \theta \sin \theta}{\cos^2 \theta + \sigma'^2 \sin^2 \theta} \quad \text{with} \quad (4.30)$$

$$\sigma' = \sqrt{\frac{(M_{21} - M_{12}) \text{sign}(M_{12} + M_{21}) - \sqrt{(M_{12} + M_{21})^2 + (M_{22} - M_{11})^2}}{(M_{21} - M_{12}) \text{sign}(M_{12} + M_{21}) + \sqrt{(M_{12} + M_{21})^2 + (M_{22} - M_{11})^2}}} \quad \text{and} \quad (4.31)$$

$$\tan(2\theta) = \frac{M_{22} - M_{11}}{M_{12} + M_{21}}, \quad (4.32)$$

see again [79] for reference.

4.4.4. Dynamical tunneling rates of \mathcal{P}_{nnc}

To analyze the influence of nonlinear resonances on quantum mechanics in higher dimensions we study the dynamical tunneling rates of the map \mathcal{P}_{nnc} . Numerically, we open the system as described in section 4.4.1. The opening is placed similar to the opening of \mathcal{P}_{lu} . In order to ensure that the

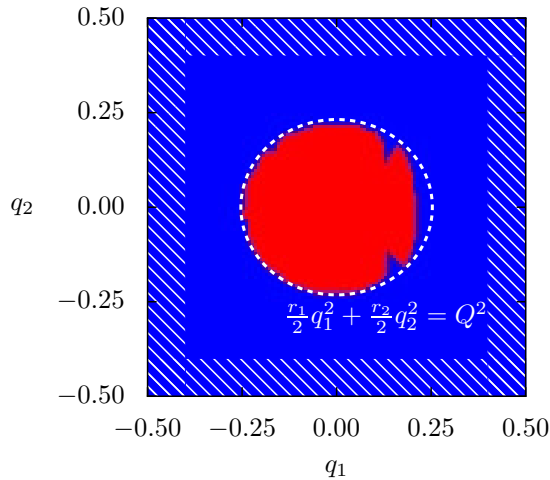


Figure 4.23.: FLI values calculated on the 4D phase space and averaged over the momenta. The values are plotted in the 2D position space in order to reveal the regular region. All points with an average FLI below $0.999 \cdot 450$ are shown in red and all points above in blue. The hatched region denotes the opening used to calculate the tunneling rates γ for \mathcal{P}_{nnc} . The white dashed line is the ellipsis defining the regular region in the designed potential (3.91).

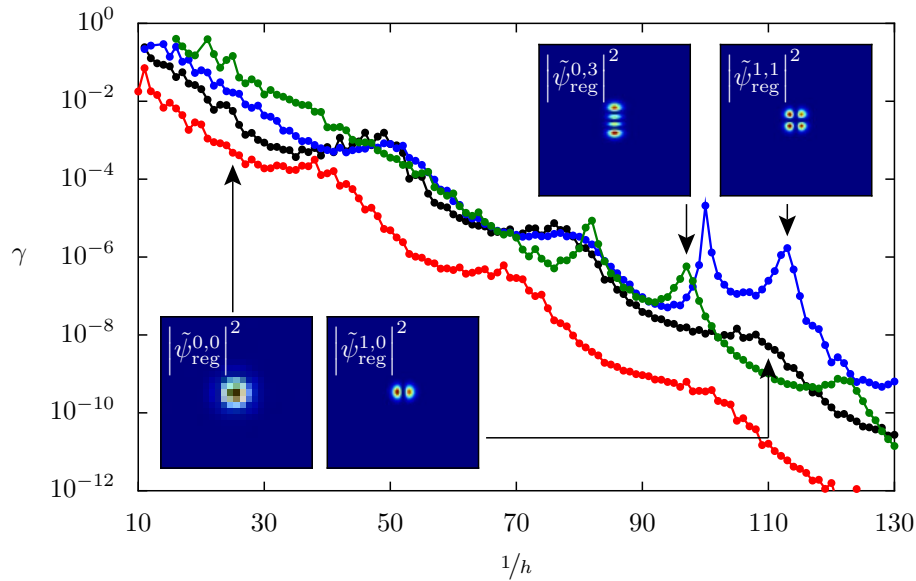


Figure 4.24.: Regular-to-chaotic tunneling rates γ vs. $1/h$ for \mathcal{P}_{nnc} , determined by opening the system, equation (4.22). The corresponding eigenstates are shown in insets at fixed values of $1/h$. Despite an overall exponential trend prominent peaks and plateaus are present.

regular phase-space volume is not affected, the averaged FLI values according to equation (4.23) are shown in figure 4.23 together with the opening used for the quantum calculation.

In figure 4.24 we show numerically determined tunneling rates for the ground state and the first excited states of \mathcal{P}_{nnc} . These rates are strikingly different from the pure exponential decay of the direct rates γ^d for \mathcal{P}_{lu} . Although the data shows an overall exponential trend it also shows rich features given by prominent peaks at single values of $1/h$ and broader plateaus over finite ranges of $1/h$.

In the following we concentrate on the state $\psi_{\text{reg}}^{0,3}$ shown in green. It has two sharp maxima at $1/h = 82$ and 97 as well as a slightly broader one at $1/h = 122$. It is our aim to understand the emergence of these peaks qualitatively and predict them quantitatively. Note that the states $\psi_{\text{reg}}^{0,0}$ and $\psi_{\text{reg}}^{1,0}$ only yield plateaus and no sharp peaks. This phenomenon will also be addressed.

4.4.5. Interlude: Theory of resonance assisted tunneling (RAT)

Nonlinear resonances can introduce drastic changes into quantum properties of classical systems, e. g. for the dynamical tunneling rates. The prediction of these rates in context of classical nonlinearities was done for near-integrable systems [83, 84] and also for mixed systems far from integrability where a regular domain is embedded inside a surrounding chaotic region [163, 164, 166, 183].

The description of tunneling rates in the presence of classical nonlinear resonances is based on a comparison to a system without resonances. The link between these two systems can be described by

the following symbolic representation of the Hamiltonians:

$$\begin{array}{ccc}
 \begin{array}{c} \text{[Symbolic representation of } H_1 \text{]} \\ H_1 \end{array} & \begin{array}{c} \text{perturbation theory} \\ = \end{array} & \begin{array}{c} \text{[Symbolic representation of } H_2 \text{]} \\ H_2 \end{array} + \delta W \\
 & & \end{array} \tag{4.33}$$

$$\begin{array}{ccc}
 & \downarrow & \text{introduce fictitious integrable systems} \\
 \begin{array}{c} \text{[Symbolic representation of } H_3 \text{]} \\ H_3 \end{array} & = & \begin{array}{c} \text{[Symbolic representation of } H_4 \text{]} \\ H_4 \end{array} + \varepsilon V. \\
 & & \end{array} \tag{4.34}$$

Here H_1 is the system we want to analyze. It yields a regular subsystem with nonlinear resonances embedded in a large chaotic sea. It is thought of being the result of a system without nonlinear resonances, called H_2 , under a small perturbation δW . The regular dynamics of H_2 is approximated by a fictitious integrable system H_4 in order to extend the regular phase space into the chaotic domain [78], cf. section 4.4.3. If this fictitious system H_4 is perturbed by εV , the perturbation introduces nonlinear resonances and yields the system H_3 . For simplicity tiny stochastic layers within the regular island are not shown in the symbolic pictures. In order to construct useful quasi-modes whose tunneling rates can be predicted, the eigenstates of H_4 are used.

The main idea behind the fictitious integrable system approach is to describe the tunneling rates of system H_2 by using H_4 as regular subsystem and the eigenstates of H_4 as quasimodes for H_2 , see section 4.4.3. In order to proceed along similar lines for H_1 and H_3 we use the fact that the left hand side and the right hand side of (4.33) and (4.34) are connected only by small perturbations εV and δW , respectively. Using quantum perturbation theory expression, the eigenstates of H_3 can be obtained by means of the eigenstates of H_4 [184]

$$\begin{aligned}
 |\psi_{\text{reg}}^{m,n}\rangle &= |\tilde{\psi}_{\text{reg}}^{m,n}\rangle \\
 &+ \sum_{k,l \neq m,n} \frac{\langle \tilde{\psi}_{\text{reg}}^{k,l} | \varepsilon V | \tilde{\psi}_{\text{reg}}^{m,n} \rangle}{\varepsilon_{m,n} - \varepsilon_{k,l}} |\tilde{\psi}_{\text{reg}}^{k,l}\rangle \\
 &+ 2^{\text{nd}} \text{ order containing } (\varepsilon V)^2 \text{ terms} \\
 &+ 3^{\text{rd}} \text{ order containing } (\varepsilon V)^3 \text{ terms} \\
 &+ \text{higher orders.}
 \end{aligned} \tag{4.35}$$

In this expression $|\tilde{\psi}_{\text{reg}}^{k,l}\rangle$ are the eigenstates of H_4 and thereby suitable quasi-modes of H_2 . Accordingly, the states $|\psi_{\text{reg}}^{m,n}\rangle$ are the eigenstates of H_1 and quasimodes of H_3 . If we now use formula (4.26) and

insert (4.35) we find [79, 166]

$$\gamma_{m,n} = \|P_{\text{ch}} U |\psi_{\text{reg}}^{m,n}\rangle\|^2 \quad (4.36)$$

$$= \|P_{\text{ch}} U |\tilde{\psi}_{\text{reg}}^{m,n}\rangle + \sum_{k,l \neq m,n} \frac{\langle \tilde{\psi}_{\text{reg}}^{m,n} | \varepsilon V | \tilde{\psi}_{\text{reg}}^{k,l} \rangle}{\varepsilon_{m,n} - \varepsilon_{k,l}} P_{\text{ch}} U |\tilde{\psi}_{\text{reg}}^{k,l}\rangle + \text{higher order in } (\varepsilon V)\|^2 \quad (4.37)$$

$$\approx \|P_{\text{ch}} U |\tilde{\psi}_{\text{reg}}^{m,n}\rangle\|^2 + \sum_{k,l \neq m,n} \left| \frac{\langle \tilde{\psi}_{\text{reg}}^{m,n} | \varepsilon V | \tilde{\psi}_{\text{reg}}^{k,l} \rangle}{\varepsilon_{m,n} - \varepsilon_{k,l}} \right|^2 \|P_{\text{ch}} U |\tilde{\psi}_{\text{reg}}^{k,l}\rangle\|^2 \quad (4.38)$$

+ higher order terms in (εV) + interference terms

$$= \gamma_{m,n}^d + \sum_{k,l \neq m,n} \left| \frac{\langle \tilde{\psi}_{\text{reg}}^{m,n} | \varepsilon V | \tilde{\psi}_{\text{reg}}^{k,l} \rangle}{\varepsilon_{m,n} - \varepsilon_{k,l}} \right|^2 \gamma_{k,l}^d \quad (4.39)$$

+ higher order terms in (εV)

+ interference terms omitted by incoherent sum (4.38)

where $\gamma_{k,l}^d$ is again the direct tunneling rate of the state $|\tilde{\psi}_{\text{reg}}^{k,l}\rangle$. In order to see if the incoherent sum is an appropriate simplification, it is possible to compare the different terms in the sum of equation (4.39). As long as one dominates the others it is valid to omit the interference terms. This will be the case for most of the $1/h$ values later.

In equation (4.39) the sum over the states $|\tilde{\psi}_{\text{reg}}^{k,l}\rangle$ represents a coupling of the initial state $|\tilde{\psi}_{\text{reg}}^{m,n}\rangle$ to the states $|\tilde{\psi}_{\text{reg}}^{k,l}\rangle$ whose direct tunneling rate $\gamma_{k,l}^d$ then enter the incoherent sum of equation (4.39). Higher order contributions from equation (4.35) yield further intermediate steps $|\tilde{\psi}_{\text{reg}}^{i,j}\rangle$ in between $|\tilde{\psi}_{\text{reg}}^{m,n}\rangle$ and $|\tilde{\psi}_{\text{reg}}^{k,l}\rangle$ in this tunneling process. This gives rise to tunneling paths Γ connecting the initial state to the final state via intermediate steps

$$\Gamma : \quad |\tilde{\psi}_{\text{reg}}^{m,n}\rangle \rightarrow \cdots \rightarrow |\tilde{\psi}_{\text{reg}}^{i,j}\rangle \rightarrow \cdots \rightarrow |\tilde{\psi}_{\text{reg}}^{k,l}\rangle. \quad (4.40)$$

It is important to note that the dominant contributions to $\gamma_{m,n}$ in equation (4.39) are typically given by the terms of the sum with the largest direct tunneling rates $\gamma_{k,l}^d$. In other words for a given value of Planck's constant $\gamma_{m,n}$ is mostly determined by processes ending in final states $|\tilde{\psi}_{\text{reg}}^{k,l}\rangle$ which are as close to the chaotic sea as possible. We will denote the subset of most relevant paths with \mathcal{G} .

We can now link equation (4.39) to the description of nonlinear resonances using adiabatic perturbation theory, cf. section 3.2.2 on page 18. The resulting Hamiltonian (3.50) of this description tells us that the potential V whose matrix elements $\langle \tilde{\psi}_{\text{reg}}^{m,n} | \varepsilon V | \tilde{\psi}_{\text{reg}}^{k,l} \rangle$ appear in equation (4.39) only consists of a subset of Fourier components. This subset is given by the integer vectors describing the

resonance in whose vicinity the approximation is performed. From equation (3.50) we have

$$H_3(\mathbf{I}, \boldsymbol{\theta}) = H_4(\mathbf{I}) + \varepsilon \sum_{\alpha, \beta \in \mathbb{Z} \setminus 0} V^{\alpha \mathbf{r}^a + \beta \mathbf{r}^b, \alpha s^a + \beta s^b}(\mathbf{I}) e^{i(\alpha \mathbf{r}^a + \beta \mathbf{r}^b) \boldsymbol{\theta}}. \quad (4.41)$$

In this formula the classical resonances enter by $\mathbf{r}^{a,b}, s^{a,b}$ which are given by the resonance conditions imposed on the classical frequencies (3.8) $\mathbf{r}^{a,b} \boldsymbol{\omega}_{\text{res}} = s^{a,b}$.

The fact that only some Fourier modes are present yields selection rules in the possible couplings of the perturbation series (4.35). The simplest approach for determining the quantum system corresponding to the classical Hamiltonian (4.41) is done by a canonical quantization. After the replacement $\mathbf{I} \mapsto \hat{\mathbf{I}}$ and $\boldsymbol{\theta} \mapsto \hat{\boldsymbol{\theta}}$ and choosing the angle-space representation

$$\hat{\mathbf{I}} \mapsto \frac{\hbar}{i} \frac{\partial}{\partial \boldsymbol{\theta}} \quad (4.42)$$

the eigenstates $|\tilde{\psi}_{\text{reg}}^{\mathbf{k}}\rangle \equiv |\tilde{\psi}_{\text{reg}}^{k_1, k_2}\rangle$ of the system H_4 can be written as

$$\langle \boldsymbol{\theta} | \tilde{\psi}_{\text{reg}}^{k_1, k_2} \rangle = \frac{1}{2\pi} e^{i(k_1 + 1/2)\theta_1} e^{i(k_2 + 1/2)\theta_2}, \quad (4.43)$$

where we have used the fact that the coordinates of the adiabatically averaged Hamiltonian have 2π -periodic angles. The exponents $1/2 = \mu/4$ are the Maslov-indices for the two degrees of freedom. As both degrees of freedom yield two turning points per quantizing torus we have $\mu = 2$. The eigenfunctions (4.43) of $\hat{\mathbf{I}}$ with eigenvalues $I_j = \hbar(k_j + 1/2)$ are also eigenfunctions of the unperturbed part of the Hamiltonian (4.41) with eigenvalues

$$H_4(\hbar(k_1 + 1/2), \hbar(k_2 + 1/2)). \quad (4.44)$$

In order to obtain the first order quantum perturbation expression for the perturbed eigenstates we have to calculate the matrix elements of the potential

$$\langle \tilde{\psi}_{\text{reg}}^{k_1, k_2} | \varepsilon \sum_{\alpha, \beta \in \mathbb{Z} \setminus 0} V^{\alpha \mathbf{r}^a + \beta \mathbf{r}^b, \alpha s^a + \beta s^b}(\hat{\mathbf{I}}) e^{i(\alpha \mathbf{r}^a + \beta \mathbf{r}^b) \hat{\boldsymbol{\theta}}} | \tilde{\psi}_{\text{reg}}^{m_1, m_2} \rangle. \quad (4.45)$$

Under the assumption that the Fourier coefficients do not depend on the actions themselves we find

$$\langle \tilde{\psi}_{\text{reg}}^{\mathbf{k}} | \varepsilon V | \tilde{\psi}_{\text{reg}}^{\mathbf{m}} \rangle = \varepsilon \sum_{\alpha, \beta \in \mathbb{Z} \setminus 0} V^{\alpha \mathbf{r}^a + \beta \mathbf{r}^b, \alpha s^a + \beta s^b} \left(\delta_{\mathbf{k}, \mathbf{m} + (\alpha \mathbf{r}^a + \beta \mathbf{r}^b)} + \delta_{\mathbf{k}, \mathbf{m} - (\alpha \mathbf{r}^a + \beta \mathbf{r}^b)} \right). \quad (4.46)$$

The prediction of dynamical tunneling rates according to equation (4.39) in addition requires a prediction of the direct tunneling rates $\gamma_{k,l}^d$. These rates $\gamma_{k,l}^d$ describe the decay of a localized quasi-mode in the absence of nonlinear resonances. Finding these rates, however is a non-trivial task. In 2D maps adiabatic averaging using Lie-transformation techniques, normal form analysis, or recon-

structions from Fourier transformations of classical orbits are used to provide fully regular systems whose eigenvectors are good quasi modes for the regular region [78, 79]. While it is possible to obtain such a system also for the map with linear regular region \mathcal{P}_{lin} , see section 4.4.3, it is not possible to derive such an H_{reg} for maps with nonlinear resonances straightforwardly. The main obstacle is that all forms of interpolations as performed in the 2D case do not necessarily yield integrable systems. The fact that they are time independent is not longer sufficient as is discussed in section 3.2.2 and exemplified in terms of a time independent Hamiltonian with two degrees of freedom in appendix G showing chaotic dynamics.

However, it is possible to give an approximate prediction of the resonance-assisted tunneling rates without the knowledge of the direct tunneling rates from equation (4.39). This approximation is based on neglecting all tunneling paths in equation (4.39) whose endpoint is not sufficiently close to the chaotic sea as mentioned above. There the subset of paths, whose final state cannot couple to another state inside the island having a larger direct tunneling rate, is called \mathcal{G} . For paths Γ in \mathcal{G} the direct tunneling rate $\gamma_{k,l}^d$ is then approximated by the last used Fourier coefficient of the coupling again. This is shown in references [163, 183, equations (7) and (9) or (1.28) and (1.37), respectively] where the mean level splitting is given as

$$\Delta\varphi = \left(\frac{\tau V_{\text{eff}}}{\hbar} \right)^2 \quad (4.47)$$

and the effective potential reads

$$V_{\text{eff}} = V_{r:s} \prod_{l=1}^{k-1} \frac{V_{r:s}}{\varepsilon_0 - \varepsilon_{lr}}, \quad (4.48)$$

where τ is the driving period of the system and k denotes the number of states included in the process. For 2D maps of the Fourier component $V_{r:s}$ in this expression given by the period of the periodic orbit underlying the resonance [163, 183]. The product in equation (4.48) corresponds to the terms of order $k - 1$ in equation (4.39). The prefactor $V_{r:s}$ approximates the direct tunneling rate of the last state along the path of intermediate states.

For 4D maps a reduction to only one Fourier component is only possible if the main resonance in phase space is of rank-1 [6]. However, in \mathcal{P}_{mc} a rank-2 resonance is dominating the phase space as pointed out in 3.4.2. Hence, the resonance-assisted tunneling is based on an approximate Hamiltonian (4.41) which cannot be reduced to just one Fourier term. Such a Hamiltonian system with two degrees of freedom in general yields a mixed phase space as can be seen from the normal form of double resonant Hamiltonians [107]. An example of such a system is shown in appendix G. The presence of chaos highly complicates the determination of the Fourier components from the classical phase space compared to the 2D case. An approach to this determination is presented later in section 4.4.6.

If we assume that the Fourier coefficients of the two basic resonances are known, $V^{\mathbf{r}^a, s^a}$ and $V^{\mathbf{r}^b, s^b}$, then we can generalize formula (4.48) to the multi-resonance case by using the appropriate Fourier coefficient connecting the single intermediate steps $|\tilde{\psi}_{\text{reg}}^{i,j}\rangle$ along the tunneling path Γ . In our case

equation (4.48) therefore translates into

$$V_{\text{eff}}^{\Gamma} = V_{\text{last amplitude}} \prod_{\mathbf{k} \in \{\text{steps along path } \Gamma\}} \frac{|V_{\mathbf{k}}|^2}{\varepsilon_{\mathbf{k},\text{end}} - \varepsilon_{\mathbf{k},\text{begin}}}. \quad (4.49)$$

In this expression the product gathers together all contributions mediated by the single steps along Γ . The energy denominator $\varepsilon_{\mathbf{k},\text{end}} - \varepsilon_{\mathbf{k},\text{begin}}$ is given by the difference in the quasienergy ε of the start and the endpoint of step \mathbf{k} . The coupling matrix element $V_{\mathbf{k}}$ is set to be either $V^{\mathbf{r}^a, s^a}$ or $V^{\mathbf{r}^b, s^b}$ depending on which resonance is responsible for the current step \mathbf{k} .

Finally the tunneling rate from state $\psi_{\text{reg}}^{\mathbf{m}}$ due to the contribution of path Γ is obtained from the effective couplings V_{eff}^{Γ} according to equation (4.47) and the relation between the tunneling splitting and the tunneling rate, $\gamma = \Delta\varphi$ [79, equation 44],

$$\gamma_{\mathbf{m}}^{\Gamma} = \left(\frac{V_{\text{eff}}^{\Gamma}}{\hbar} \right)^2 \quad (4.50)$$

where we used that the period of the driving is $\tau = 1$. The complete prediction of the tunneling rate of state $\psi_{\text{reg}}^{\mathbf{m}}$ based on all paths from \mathcal{G} is then given by the incoherent sum according to equation (4.39)

$$\gamma_{\mathbf{m}} = \sum_{\Gamma \in \mathcal{G}} \gamma_{\mathbf{m}}^{\Gamma}. \quad (4.51)$$

We will use this formula in order to give a prediction to the tunneling rates of \mathcal{P}_{nnc} .

4.4.6. Prediction of tunneling rates for \mathcal{P}_{nnc} , RAT

The prediction of tunneling rates for the system \mathcal{P}_{nnc} based on equation (4.49) depends on three aspects. First, the nonlinear resonance induces selection rules on the possible couplings. Therefore, only certain tunneling paths are present in equation (4.39) from which only the ones in the set of the relevant paths \mathcal{G} are used to calculate effective couplings according to equation (4.49). Second, the energy denominator in the prediction determines which intermediate regular states are responsible for the tunneling enhancement due to avoided crossings in the quasienergy ε . Third, it is necessary to determine the Fourier coefficients of the potential in order to get the coupling matrix elements for a detailed prediction of the tunneling rates. We will concentrate on these three aspects in the following and conclude with a prediction.

Selection rules from nonlinear resonances

In order to understand the emergence of the peaks in the tunneling rates of figure 4.24, we can use the result of the classical analysis of \mathcal{P}_{nnc} from section 3.4.2. The most important feature in phase space is the the period-5 orbit embedded in the regular island given by equation (3.98). It is caused by the rank-2 resonance mentioned on page 48. The analysis of the frequency map in figure 3.10(d)

shows that the two rank-1 resonances

$$5 : 0 : 1 \quad \text{and} \quad 6 : -1 : 1. \quad (3.94)$$

can be used as basis of the resonance module. This fixes this choice of \mathbf{r}^a, s^a and \mathbf{r}^b, s^b in equation (4.41). If we absorb ε into the Fourier modes for brevity and further neglect their action dependence, then the Hamiltonian becomes

$$\begin{aligned} H_3 \quad \text{(I, } \boldsymbol{\theta}) = \quad H_4 \quad \text{(I)} &+ V^{(5,0),1} e^{5i\theta_1} + V^{(6,-1),1} e^{i(6\theta_1 - \theta_2)} \\ &+ V^{(11,-1),2} e^{i(11\theta_1 - \theta_2)} + V^{(1,-1),0} e^{i(\theta_1 - \theta_2)} + \dots + \text{c. c.} \end{aligned} \quad (4.52)$$

where the first line contains the two fundamental Fourier modes according to the choice of \mathbf{r}^a, s^a and \mathbf{r}^b, s^b and the second line contains an example of higher order Fourier modes given by $\alpha = 1, \beta = 1$ and $\alpha = -1, \beta = 1$.

This form of the potential yields selection rules originating from equation (4.46) which read

$$\begin{pmatrix} k \\ l \end{pmatrix} = \begin{pmatrix} m \\ n \end{pmatrix} + \alpha \begin{pmatrix} 5 \\ 0 \end{pmatrix} + \beta \begin{pmatrix} 6 \\ -1 \end{pmatrix}. \quad (4.53)$$

These rules lead to couplings between certain unperturbed states $|\tilde{\psi}_{\text{reg}}^{i,j}\rangle$ such that several tunneling paths Γ emerge. Some examples are shown schematically in figure 4.25 for the initial state $|\tilde{\psi}_{\text{reg}}^{0,1}\rangle$. These paths include processes of different order and therefore the matrix elements (4.46) of these paths contain also higher order Fourier coefficients. In this context higher order means Fourier indices (\mathbf{m}, n) which are multiples of the basic integers given by the resonance conditions, i. e. $|\alpha| > 1$ and/or $|\beta| > 1$ in equations (4.41) and (4.46). The depicted state $|\tilde{\psi}_{\text{reg}}^{0,1}\rangle$ is coupled to $|\tilde{\psi}_{\text{reg}}^{16,0}\rangle$. The coupling is possible given that at least one of the following Fourier components $V^{\mathbf{m},n}$ or product of Fourier components is nonzero:

1st order contributions via Fourier mode $V^{(16,-1),3} \neq 0$ in the sum in (4.35)

2nd order contributions via Fourier modes $V^{(6,-1),1} \times V^{(10,0),2} \neq 0$ in (4.35)

3rd order contributions via Fourier modes $V^{(6,-1),1} \times V^{(5,0),1} \times V^{(5,0),1} \neq 0$ in (4.35).

In this diagram loops are omitted. This is appropriate because we are only interested in tunneling paths Γ which go directly out of the island. All other paths can be neglected as they yield much smaller contributions in equation (4.39) and equation (4.49) due to a larger number of small factors. With the same reasoning also tunneling paths intermediately increasing the second quantum number m_2 are omitted. This might change if the basis of the resonance module is chosen differently as addressed in appendix C. Due to neglecting loop contributions a fourth order term does not exist, as

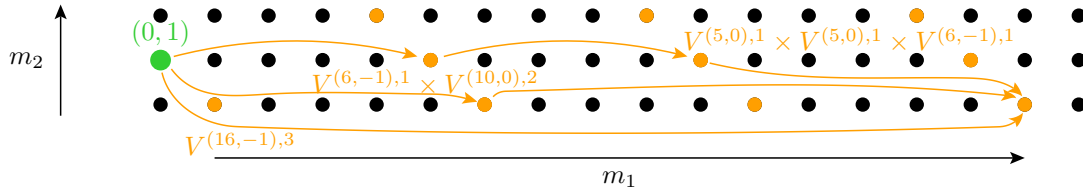


Figure 4.25.: Possible connections between two regular quantum states via RAT for \mathcal{P}_{nnc} based on the choice of equation (3.94). Shown in black are points denoting quantum number pairs (m_1, m_2) . Shown in orange are all points reachable from the initial state $|\tilde{\psi}_{\text{reg}}^{0,1}\rangle$. Given this initial state the arrows indicate via which paths Γ a coupling to $|\tilde{\psi}_{\text{reg}}^{16,0}\rangle$ is possible and which Fourier components are included.

the difference between the two states does not allow a connection based on four single steps with the two given resonances (3.94). Also not all processes of order up to three are shown. For example the second order process is not only possible via $|\tilde{\psi}_{\text{reg}}^{6,0}\rangle$ but also via $|\tilde{\psi}_{\text{reg}}^{10,1}\rangle$. For the first order process there are even 3 possibilities in total.

Which of the processes is dominating depends on the way the Fourier components of the potential decay with increasing order. Usually for an analytic V one assumes [6, page 304]

$$V^{\mathbf{m},n} \propto e^{-\sigma(\|\mathbf{m}\|_1 + |n|)} \quad (4.54)$$

with some coefficient σ which is not relevant here. If σ is small, then the potential contains many harmonics. The dominating process is given by a comparison of equation (4.54) with the relation between different order of the potential, namely εV versus $(\varepsilon V)^2$ and $(\varepsilon V)^3$. In the following we will proceed like for 2D maps and restrict the Fourier series to the first order terms [79], i. e.

$$|\alpha| = 1 \quad \text{and/or} \quad |\beta| = 1. \quad (4.55)$$

However, as mentioned on page 110 this does not guarantee the pendulum approximation (4.52) to be integrable. This is also shown in appendix G where the phase space of the Hamiltonian in equation (4.52) is investigated.

As mentioned on page 106 we want to focus on $|\tilde{\psi}_{\text{reg}}^{0,3}\rangle$ and explain the peaks of $\gamma_{0,3}$ from figure 4.24. For a given value of $1/h$ only a certain number of regular states exist. Therefore only certain coupling paths are possible. They are given exemplarily for $1/h = 90$ in figure 4.26 where the extent of the regular island is visualized by a red dashed line. This line is the border between the existing and the non-existing regular states. Therefore, it is an expression for the interface between the regular and the chaotic domain in phase space transferred to the quantum-number quarter-plane. On the left hand side of this line black dots mark existing regular quantum states. However, the plot is cut off along the m_2 axis. At the right hand side of the line no regular states exist. This is expressed by random blue points symbolizing the chaotic sea. Due to the restriction on the first order Fourier coefficients only two types of arrows are displayed in contrast to the example case of figure 4.25. This reduction onto

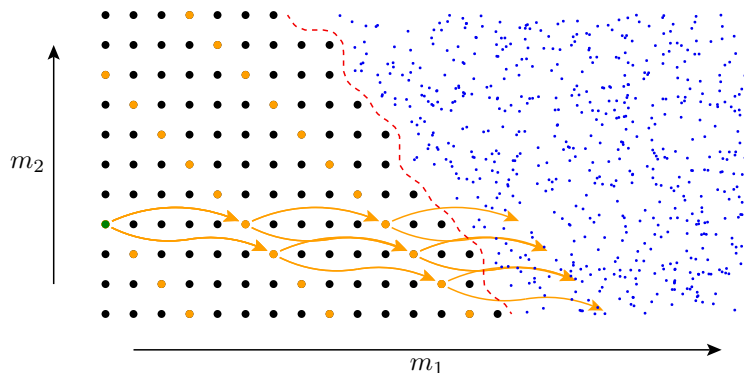


Figure 4.26.: Possible tunneling paths at $1/h = 90$. The black and orange points indicate existing regular states with quantum numbers (m_1, m_2) . The numerically determined border of the regular island of \mathcal{P}_{nnc} is drawn as a dashed red curve in the quantum-number quarter-plane. On the right hand side of this line no regular states exist. This is illustrated by the random blue points, symbolizing the chaotic sea. The arrows indicate possible tunneling paths for the given initial state show in green, $\psi_{\text{reg}}^{0,3}$. The paths depend on the choice of the resonances $5 : 0 : 1$ and $6 : -1 : 1$.

the smallest Fourier mode is an important simplification for which it is very important to note that it highly depends on the choice of the classical resonances used to describe the phase-space structure, here the $5 : 0 : 1$ and the $6 : -1 : 1$ resonance. We comment on an alternative choice in appendix C.

All the paths in figure 4.26 end beyond the dashed line in the chaotic sea. It is important to note that this border cannot be defined in a strict sense as mentioned already on page 86 when discussing the eigenstates of \mathcal{P}_{nnc} . This is because the question when a regular state ceases to exist for decreasing $1/h$ or comes into existence for increasing $1/h$ cannot be defined precisely. Apart from this impreciseness an estimated form of the border is given by a diagonal line $m_2 = N - m_1$ with some offset N depending on $1/h$. This shows that the last states inside the regular zone for a given $1/h$ are approximately given by the states of constant $m_1 + m_2$ and that by increasing $1/h$ new regular states start to exist in groups.

Energy denominators

The question arises which of the potentially important intermediate steps in figure 4.26 are responsible for the enhanced tunneling rates. Therefore, it is necessary to check the prefactor $V^{\alpha\mathbf{r}^a + \beta\mathbf{r}^b, \alpha s^a + \beta s^b}$ of the Fourier mode and the energy denominator $(\varepsilon_{\mathbf{m}} - \varepsilon_{\mathbf{k}})^{-1}$ in equation (4.39). The denominator can be obtained numerically using equation (4.22) and

$$\varepsilon = -\hbar \cdot \varphi. \quad (4.56)$$

If $|\varepsilon_{\mathbf{m}} - \varepsilon_{\mathbf{n}}|$ is very small, the corresponding eigenstates couple to each other and the tunneling rates increase according to equation (4.39). The comparison between γ and small quasienergy differences is shown in figure 4.27. From this picture the main outcome of this investigation can be deduced. It tells which quantum states are responsible for the enhancement of the tunneling rates. In the case of

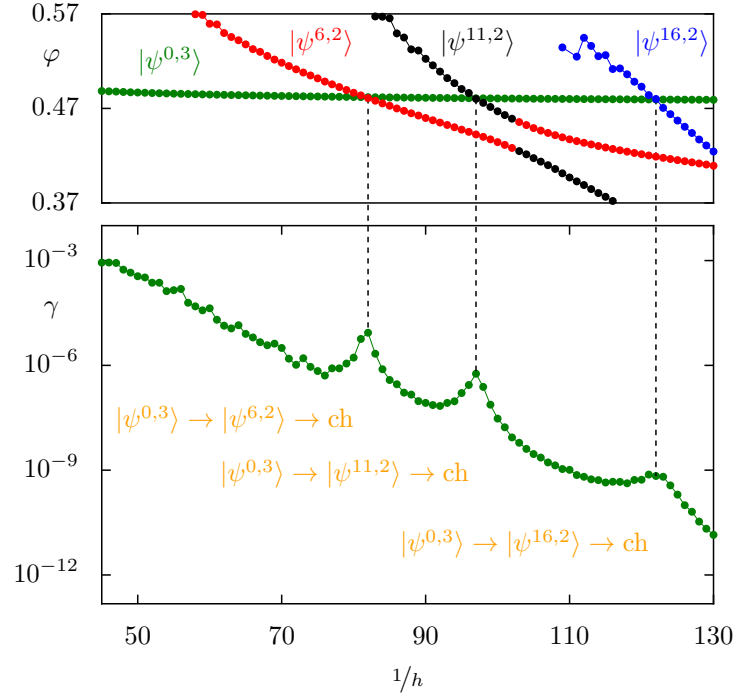


Figure 4.27.: Tunneling rate γ (bottom) and spectrum φ (top) vs. $1/h$ for the state $|\tilde{\psi}_{\text{reg}}^{0,3}\rangle$ of \mathcal{P}_{nnc} . Positions where $\gamma_{0,3}$ shows peaks ($1/h = 82, 97$, and 122) coincide with tiny avoided crossings between $|\tilde{\psi}_{\text{reg}}^{0,3}\rangle$ and three other states which are allowed to couple according to figure 4.26.

the data shown in figure 4.27 the three peaks originate from a coupling of $|\tilde{\psi}_{\text{reg}}^{0,3}\rangle$ to $|\tilde{\psi}_{\text{reg}}^{6,2}\rangle$, $|\tilde{\psi}_{\text{reg}}^{11,2}\rangle$, and $|\tilde{\psi}_{\text{reg}}^{16,2}\rangle$, respectively.

While there exist predictions for the quasienergy for resonance-free islands of 2D maps [152], we would like to use a fit

$$\varepsilon \longrightarrow \text{polynomial fit of the data} \quad (4.57)$$

of the numerical data in order to describe the quasienergies for the prediction of tunneling rates. As the $\varepsilon_{\mathbf{m}}$ highly fluctuate at the smallest values of $1/h$ these fits omit the first part of the $\varepsilon_{\mathbf{m}}(1/h)$ curve. It is further necessary to smoothly fit trough the avoided crossings with other regular states. These avoided level crossings are not necessarily small like the ones of $|\tilde{\psi}_{\text{reg}}^{0,3}\rangle$ in figure 4.27 but can be rather large as the one between $|\tilde{\psi}_{\text{reg}}^{6,2}\rangle$ and $|\tilde{\psi}_{\text{reg}}^{11,2}\rangle$ visible in the same figure. The detailed procedure of the fitting is discussed in appendix F. As the peak positions of the tunneling-rate predictions are given by the zeros of the quasienergy differences, these positions depend highly on the accuracy of the performed smooth interpolation.

Estimating the parameters of the pendulum approximation from phase-space properties

A prediction or interpolation of the quasienergies ε is necessary in order to apply equation (4.49) for a single given path Γ . Furthermore, we need to determine the remaining parameters of the resonance Hamiltonian H_3 from equation (4.52). These are the Fourier coefficients $V^{\mathbf{m},n}$ and the integrable part H_4 in equation (4.41). The system H_4 is usually expanded up to second order [6]

$$H_4(\mathbf{I}) = \frac{1}{2} \mathbf{I}^T \underline{\mathcal{H}} \mathbf{I} \quad (4.58)$$

where a constant term has been dropped. Therefore, the missing parameters are given by the Fourier coefficients and the coefficients of the symmetric matrix $\underline{\mathcal{H}}$ with matrix elements \mathcal{H}_{ij} .

In 2D maps the Hamiltonian approximating the vicinity of the resonance (4.41) gives an autonomous system with one degree of freedom and hence is integrable. If all Fourier coefficients of the one-degree-of-freedom Hamiltonian of order two or higher are neglected as discussed with equation (4.54), then this model reduces significantly. As long as there is just one resonance dominating the phase space of a 2D map, this reduction to only one Fourier term is always uniquely possible. The Fourier coefficient to which the potential is reduced to is given by the period of the resonance. For example for a $r : s$ resonance it is the first term $\cos(r\theta)$ of the sum from equation (4.41). This uniqueness is based on the fact that resonances in 2D maps are always given by periodic orbits of some period r . Therefore there always exists an integer r which gives rise to the lowest order potential term $\cos(r\theta)$. The resulting system is a mathematical pendulum and hence very much is known about it, e. g. the equation of the separatrix and the enclosed area. This can be used in order to obtain the Fourier coefficients from the given classical phase space [125, 163, 166]. Due to the importance of this pendulum model we will also call the adiabatically averaged approximation of the higher dimensional system in the vicinity of the nonlinear resonance a *pendulum approximation* although it is a higher dimensional pendulum now.

We now want to determine the parameters of H_3 in order to predict dynamical tunneling rates for \mathcal{P}_{nnc} . As we know how the pendulum approximation H_3 emerged from the full system \mathcal{P}_{nnc} , namely by the adiabatic averaging described in section 3.2.2, the straight forward way of determining the missing parameters could be following the derivation of H_3 . However, this is not possible as the very starting point in equation (3.5) is not known. In terms of \mathcal{P}_{nnc} this would mean knowing the integrable system without the resonance and furthermore the action–angle variables of it. Generally speaking the basic idea behind the prediction of the missing parameters is to circumvent the necessity of knowing the integrable Hamiltonian [163]. The way this works for 2D maps is outlined by the following three aspects which are written here in more general words such that we can try to apply them also to 4D maps:

1. We have to determine dynamical invariants of the pendulum Hamiltonian H_3 which can be identified geometrically in the phase spaces of \mathcal{P}_{nnc} . In 2D maps this is the periodic point and the separatrix enclosing the resonance chain. In higher dimensional systems a further possibility are paths connecting heteroclinic orbits.

2. Furthermore we have to derive numerical quantities from these geometrical objects which are invariant under canonical transformation. In 2D maps this is achieved by using the area enclosed by the separatrices and by using the trace of the linearization around the periodic orbit. For 4D maps there are more invariants possible, namely enclosed areas and 4D volumes [185, page 286].
3. The relations between the quantities from point 2 and the parameters of H_3 , \mathcal{H}_{ij} and $V^{m,n}$, have to be determined. In 2D maps this is possible as the pendulum model itself is integrable.

If we want to predict the parameters of H_3 for \mathcal{P}_{nnc} in the same way as for 2D maps, we face two fundamental differences. First, it is not as obvious as for 2D maps which Fourier modes to keep in order to match the physical situation while simultaneously gaining a truncated H_3 which is analytically manageable. The overall expected decay behavior of the Fourier modes from equation (4.54) is not helpful here. Second, and probably the more important, the pendulum approximation H_3 is in general not integrable. For 4D maps this can for example be investigated using a Poincaré section reducing H_3 to a 2D mapping. We demonstrate this for the example choice of Fourier modes of equation (4.52) in appendix G where this 2D Poincaré map is introduced.

In the following we demonstrate how to obtain an estimate on the coefficients by making rather crude assumptions. First, the integrable part of equation (4.52) is replaced by its quadratic approximation as done in equation (4.58). If we neglect any coupling in this quadratic term by assuming the matrix \mathcal{H} to be diagonal

$$\mathcal{H}_{11} = \frac{1}{m_1}, \quad \mathcal{H}_{22} = \frac{1}{m_2}, \quad \text{and} \quad \mathcal{H}_{12} = \mathcal{H}_{21} = 0, \quad (4.59)$$

then it is possible to derive a relation between the parameters and the trace of the linearization of \mathcal{P}_{nnc} around the periodic orbit from equation (3.98) if we further restrict the Fourier coefficients V^{α_1, α_2} of the potential in equation (4.52) to be

$$V^{k_1, 0} \neq 0 \quad V^{0, k_2} \neq 0 \quad \text{and} \quad V^{\alpha_1, \alpha_2} = 0 \quad \text{else} \quad (4.60)$$

for a fixed choice of two integers k_1, k_2 . This relation is derived in appendix I and reads

$$\begin{aligned} \frac{(-1)^{k_1} k_1^2 V^{k_1, 0}}{m_1} &= - \left\{ \arccos \left(\frac{\text{tr} D\mathcal{P}_{\text{nnc}}}{4} + \frac{1}{4} \sqrt{8 + 2\text{tr}(D\mathcal{P}_{\text{nnc}}^2) - (\text{tr} D\mathcal{P}_{\text{nnc}})^2} \right) \right\}^2 \text{ and} \\ \frac{(-1)^{k_2} k_2^2 V^{0, k_2}}{m_2} &= - \left\{ \arccos \left(\frac{\text{tr} D\mathcal{P}_{\text{nnc}}}{4} - \frac{1}{4} \sqrt{8 + 2\text{tr}(D\mathcal{P}_{\text{nnc}}^2) - (\text{tr} D\mathcal{P}_{\text{nnc}})^2} \right) \right\}^2. \end{aligned} \quad (4.61)$$

However, note that the restriction to equation (4.60) is not deducible from the rank-2 resonance. If we want to use a resonance approximation suitable for the resonance around a periodic orbit then we must not drop Fourier coefficients coupling the degrees of freedom in equation (4.41). This complicates the equations significantly as shown in equation (I.17). Only if the dominating resonance structure in phase space would be a rank-1 resonance, then the above decoupling of degrees of freedom would

be fully reasonable. An example system where only rank-1 resonances occur is the uncoupled map described in the frequency map analysis of figure 3.10(c). However, there the tunneling rates are completely different from the ones of \mathcal{P}_{nnc} shown in figure 4.24. The tunneling rates of the system with the uncoupled regular region from figure 3.10(c) are shown for comparison in appendix E. They lack the prominent peaks of the data for \mathcal{P}_{nnc} . This emphasizes that the tunneling processes in \mathcal{P}_{nnc} really rely on the coupling of the degrees of freedom and on the rank-2 resonance.

For 2D maps it is possible to relate the size of a single resonance zone to the parameters of the pendulum. If we measure the size of the period-5 resonance zone in both degrees of freedom, namely in (p_1, q_1) at $(p_2, q_2) = (0, 1/2)$ and in (p_2, q_2) at $(p_1, q_1) = (0, 1/2)$, then we get the areas $S_1 = 0.009395$ and $S_2 = 0.075353$. This estimate is calculated using a polygon placed according to the outline of the regular region of the resonance. As this outline is no longer given by an orbit as in 2D maps we use FLI planes to estimate this size. Using the formula from 2D maps from reference [163, equation (3)] with

$$V^{1,2} \cdot m_{1,2} = \left(\frac{S_{1,2}}{16} \right)^2 \quad (4.62)$$

we can solve equation (4.61) and equation (4.62) for V^i . These two numbers are then used as replacement of $V_{r:s}$ in (4.48). If the tunneling path Γ takes a step along the first resonance \mathbf{r}^a then V_1 is used, if it uses a link based on the second resonance \mathbf{r}^b then V_2 is put into the product of equation (4.49).

If the prediction using RAT is compared to the numerical data from figure 4.24, one finds that the above approximation gives one-step couplings V_1 and V_2 which are approximately an order of magnitude too large. Therefore, we choose more appropriate values for the one-step couplings and get

$$V_1 = 2.5 \cdot 10^{-5} \quad \text{and} \quad V_2 = 1.5 \cdot 10^{-5} \quad (4.63)$$

which yield a better agreement. It is an open and challenging question whether it is possible to derive analytical expressions for the matrix elements of the perturbation potential V . It might be that the possibility of reducing the two degree of freedom pendulum Hamiltonian equation (4.41) to a 2D map is helpful, see appendix G. A further possibility is that investigating the 2D center manifolds of the EE-type periodic orbit could yield insight. Also on these manifolds the system is reducible to a 2D map. It might be possible to achieve the three steps mentioned on page 112 for orbits on the center manifolds of \mathcal{P}_{nnc} and on the center manifolds of the pendulum Hamiltonian.

Prediction

If the tunneling paths Γ are all determined according to the selection rules from equation (4.53), then their separate tunneling rates $\gamma_{\mathbf{m}}^{\Gamma}$ can be calculated via equation (4.49) using the energy denominators from the interpolation in appendix F and Fourier coefficients from equation (4.63). These contributions enter the incoherent sum in the first term of equation (4.39). We can compare this prediction with the numerical data obtained from the open system in figure 4.24. This is shown in figure 4.28 for

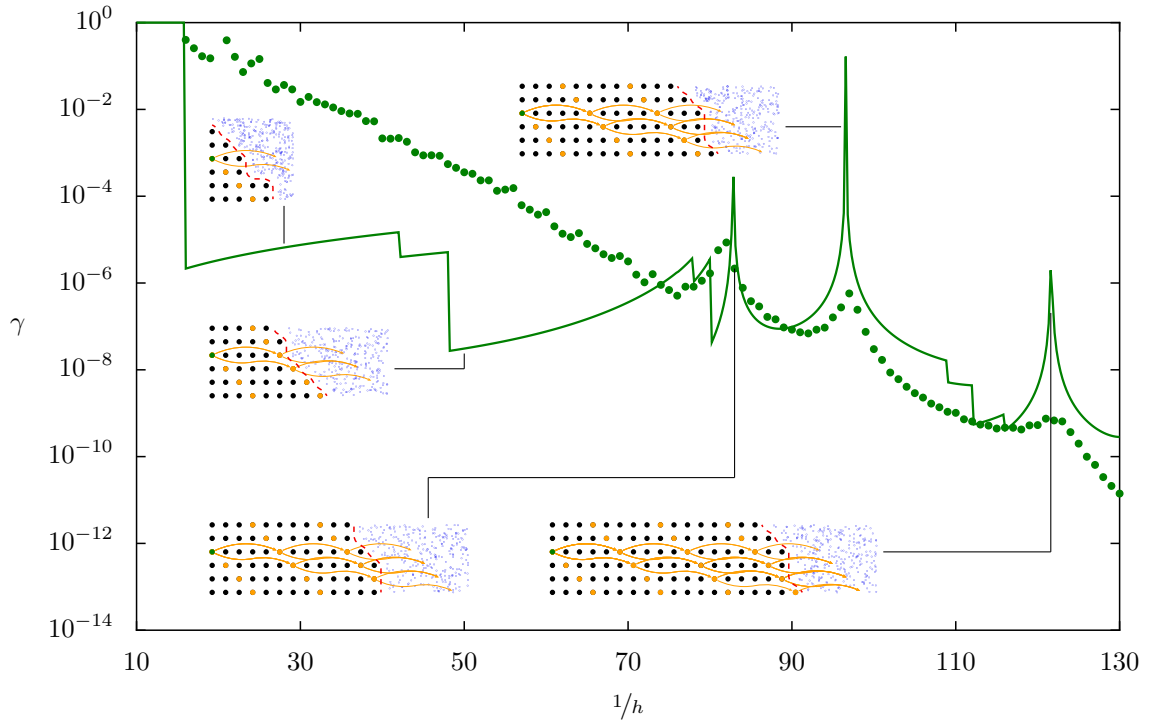


Figure 4.28.: Prediction of tunneling rates for the state $|\tilde{\psi}_{\text{reg}}^{0,3}\rangle$ of \mathcal{P}_{nnc} vs. $1/h$ using RAT. The insets are similar to figure 4.26 and symbolize the possible tunneling paths. The prediction (solid line) is the incoherent sum of all paths.

the state $\psi_{\text{reg}}^{0,3}$. The drops in the predictions stem from the increase of the quantum resolution with increasing $1/h$. Whenever a new regular state is supported inside the island the product in figure 4.49 gains an extra small factor. As the regular states tend to come into existence in groups, these drops appear in an avalanche-like fashion, cf. page 114. This is also shown in the insets. They denote which paths are present at which intervals of the $1/h$ -axis.

Although all of these tunneling paths are possible, only some of them pass the states found to be responsible for the peaks in figure 4.27. The most important path for a given interval of the $1/h$ -axis is given by the largest contribution according to equation (4.49) in the incoherent sum of the direct rates γ^d from equation (4.39). A comparison of the relevance of the paths based on the energy denominators is given in appendix H.

Note that the RAT prediction formula depends on the calculation of the coupling matrix elements (4.45) which themselves are based on the canonical quantization rules in equation (4.42) introduced to quantize the pendulum Hamiltonian (3.50). The drawback of this approach is that the results may deviate from numerical data by orders of magnitude. This was investigated and improved for 2D maps by introducing more appropriate matrix elements [166]. The basic idea is a more appropriate version of quantizing the resonance Hamiltonian (4.41). This is done by first writing the variables of the classical Hamiltonian as harmonic oscillator-like variables and then introduce bosonic ladder operators [110]. In combination with the direct regular-to-chaotic tunneling rates this leads to a much better prediction in 2D maps. [125, 166].

4.4.7. Dynamical tunneling rates of \mathcal{P}_{csm}

We now consider the system \mathcal{P}_{csm} . In order to open the system we use projected FLI values in order to determine a valid opening which does not change the regular region, cf. page 4.4.2. The corresponding FLI plot together with the opening is depicted in figure 4.29. It also shows that the phase space of \mathcal{P}_{csm} does not contain further regular structures besides the main regular island at other positions \mathbf{q} . However, due to being a projection along the momenta the plot does not exclude the possibility of further regular islets in the classical phase space at $\mathbf{q} \approx (1/2, 1/2)$.

After the diagonalizations the relevant eigenstates have to be extracted from the data and connected along the $1/h$ axis as described in appendix B. For the coupled standard maps one faces the severe problem of avoided crossings and a quantum-number assignment is only possible for the lowest states. Higher excited states do not yield such a clear separation of the degrees of freedom and the two quantum numbers cannot just be read off easily.

The tunneling rates of this very generic system are shown in figure 4.30. In contrast to the data of the designed maps \mathcal{P}_{llu} and \mathcal{P}_{nnc} the regular-to-chaotic tunneling rates fluctuate extensively with varying $1/h$. Due to the complicated classical phase-space structure much more resonances are present in the classical system and the tunneling rates are much more complicated than for the designed maps. The fact that \mathcal{P}_{csm} shows much more avoided crossings in the quasienergy spectrum makes it very hard to even identify the important coupling states qualitatively as done for \mathcal{P}_{nnc} in figure 4.27. Therefore, a complete prediction of the tunneling rates is much harder and stays an interesting and challenging problem for future investigations.

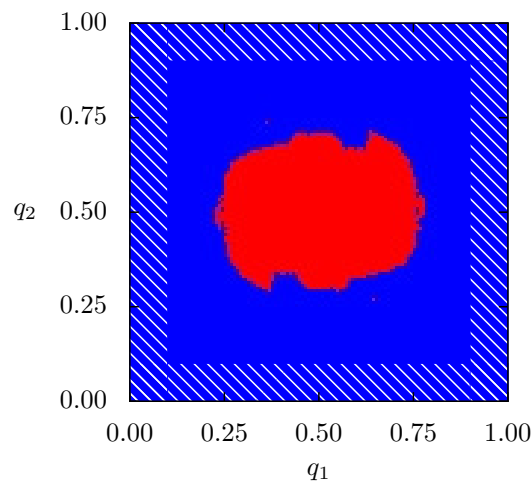


Figure 4.29.: Average FLI values plotted over position space for the coupled standard maps \mathcal{P}_{csm} according to equation (4.23). If the value is smaller than 0.999 times the maximum value of $\text{FLI} = 450$, then the corresponding point is shown in red. These points have at least one point in p_1 or p_2 where there is regular dynamics yielding a FLI not in the rightmost peak of figure 3.22. All other points are marked in blue as they yield chaotic motion for all values of the momenta. The hatched white area denotes the opening of the quantum system which must not intersect with the regular region at any value of the momenta.

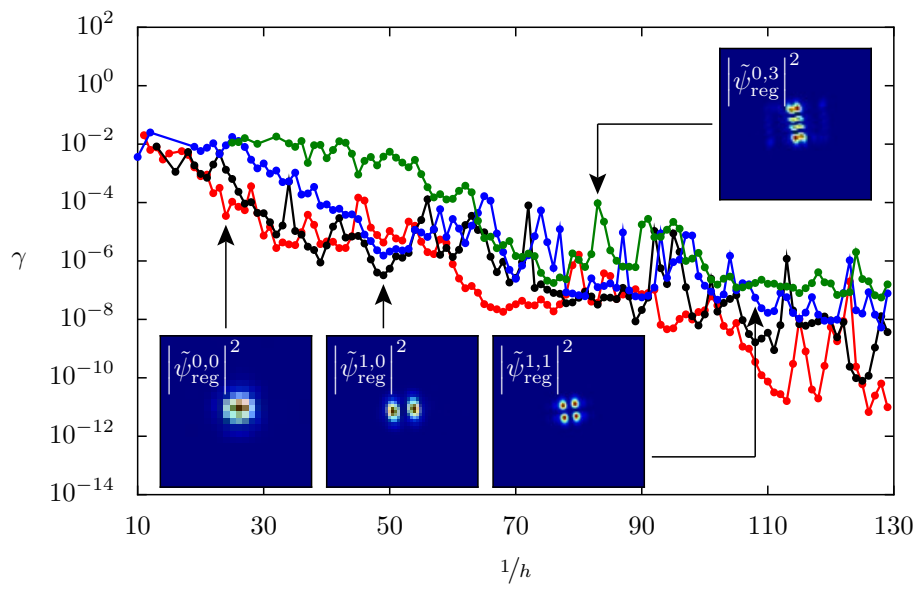


Figure 4.30.: Tunneling rates of \mathcal{P}_{csm} vs. $1/h$ for the states $|\tilde{\psi}_{\text{reg}}^{0,0}\rangle$, $|\tilde{\psi}_{\text{reg}}^{1,0}\rangle$, $|\tilde{\psi}_{\text{reg}}^{1,1}\rangle$, and $|\tilde{\psi}_{\text{reg}}^{0,3}\rangle$ given in the insets. Due to the very complicated classical phase-space structures a lot of resonances introduce various avoided crossings leading to enhanced tunneling rates at several values of $1/h$.

5. Summary and outlook

In order to understand the dynamical properties of physical systems ranging from molecules to solar systems, it is of vital importance to extend the knowledge available for systems with two or fewer degrees of freedom to higher dimensional ones. This thesis is a step towards this direction. Its first main goal is to extend notions and insights from 2D to 4D maps classically as well as quantum mechanically. The second goal is to investigate new phenomena not present in systems with $f \leq 2$, like quantum consequences of the Arnold web.

In chapter 3 the classical dynamics is investigated. Central to this is the introduction of 3D phase-space sections. They allow to recognize structures known from 2D phase spaces in 4D maps. This is exemplified by means of three different mappings of increasing complexity in phase-space. First, we introduce a mapping specifically designed to yield a simple phase-space structure whose regular part is given by completely linear dynamics (section 3.4.1). In order to approach more physically relevant systems, we introduce nonlinearities to this system (section 3.4.2). The final step is an investigation of the generic case of a system of coupled standard maps (section 3.4.3). In order to explore the 4D phase space, in section 3.4.2 we introduce shifted sections as well as skew sections which completely reveal the phase-space structure. They lead to the important result that some of the complicated structures visible in the 3D phase-space sections occur just because of an inappropriate choice of the section. We show how an appropriate section can be obtained based on the linearization around elliptic-elliptic periodic orbits.

Although 3D sections of the classical phase space give important insights, they cannot give the full representation of the dynamics. Therefore, we additionally use projections of orbits from 4D onto 3D, where the missing coordinate is indicated by color. These clearly reveal the difference between resonances of rank one and two in section 3.4.2. This is an aspect which cannot be solely deduced from a picture of the classical phase space, in contrast to 2D maps. Also the overall resonance structure has to be determined by investigating the image of the frequency map. Besides the nonlinear resonances the classical volumes of the regular region in phase space are important quantities. While for 2D maps these volumes are given by the encircled area of the outermost torus, we use the FLI to estimate the 4D volumes.

Quantum mechanically, the 3D phase-space sections are an important companion as well. Using Husimi distributions in chapter 4 they allow to determine if eigenstates localize on the main regular region, on nonlinear resonances, or on the stochastic layer. Furthermore, the sections are an indispensable help when investigating the quantum mechanical consequences of the Arnold web. As this thesis focuses on systems with a mixed phase space, only these sections allow to estimate the location of the Arnold web in phase space. We study the impact of the Arnold web on quantum mechanics by

the propagation of wave packets for which the intrusion depth into the Arnold web is investigated. In section 4.3 we observe how the depth of intrusion changes when going deeper into the semiclassical limit. It is a very important but yet unsolved question whether and how this penetration into the Arnold web is linked to the phenomenon of dynamical localization.

While the Arnold web is present classically and has quantum mechanical consequences, there exist other features only present in quantum mechanics. The most prominent one is the coupling between classically disconnected phase-space regions given by dynamical tunneling. In order to understand the quantum mechanical coupling between the regular and the chaotic region, we analyze dynamical tunneling rates. We therefore extend the fictitious integrable system approach [78] to a 4D mapping and find very good agreement to numerically obtained regular-to-chaotic tunneling rates.

In addition to this direct coupling between the regular and the chaotic region we also investigate resonance-assisted tunneling (RAT) effects for a map with nonlinear resonances. Here the results of the classical frequency map analysis are used to obtain the resonances and intermediate states which are relevant for the tunneling enhancement. This allows to obtain qualitative insights into the resonance-assisted tunneling mechanisms. However, due to the much more complicated resonance structures in phase space a quantitative description is very complicated. Although we give some steps towards a full determination of all necessary ingredients, an understanding as complete as for 2D maps is still an open question.

For the future the main open questions concern how the 3D phase-space sections studied in this thesis can be further optimized to understand strongly coupled systems. This is important classically for investigating trapping mechanism of chaotic orbits and quantum mechanically for analyzing the role of the Arnold web quantitatively. Furthermore, the results of this thesis give insights towards the understanding of dynamical tunneling rates for systems with a higher dimensional mixed phase space. It is an open and challenging task to determine quantitative predictions of the tunneling rates in the setup of resonance-assisted tunneling.

Appendix

A. Potential of the designed map

Section 3.4.1 introduces a map whose potential gives rise to a regular region clearly and cleanly separated from the surrounding chaotic domain. The kinetic energy of this mapping simply reads

$$T(\mathbf{p}) = \frac{1}{2} \mathbf{p}^2. \quad (3.68)$$

As written in section 3.4.1, the potential in position space is also quadratic close to the center of the (q_1, q_2) space. The linear regular region is achieved by setting the potential

$$V_{\text{quadratic}}(\mathbf{q}) = \frac{r_1}{2} q_1^2 + \frac{r_2}{2} q_2^2 \quad (3.69)$$

where r_1 and r_2 are real parameters. This potential has to be truncated at some point in order to get the chaotic part properly. Therefore, we introduce a further parameter Q . As soon as the values of the potential $V_{\text{quadratic}}$ are above a threshold Q^2 , the definition of the potential changes. The first ansatz is

$$V(q_1, q_2) = \begin{cases} V_{\text{quadratic}}(q_1, q_2), & V_{\text{quadratic}}(q_1, q_2) \leq Q^2 \\ Q^2 + \text{const} \cdot f(q_1, q_2), & \text{else} \end{cases} \quad (A.1)$$

where the function f is such that it is zero on the ellipsis defined by $V_{\text{quadratic}}(q_1, q_2) = Q^2$ and increases linearly in radial direction towards the border of the position-space region $[-0.5, 0.5] \times [-0.5, 0.5]$ where it reaches the value 1. This f is given by

$$f(q_1, q_2) = \frac{r(q_1, q_2) - r_{\text{elli}}(q_1, q_2)}{r_{\text{rect}}(q_1, q_2) - r_{\text{elli}}(q_1, q_2)} \quad (A.2)$$

where $r(q_1, q_2) = \sqrt{q_1^2 + q_2^2}$ is the radial distance from the center and the two functions

$$r_{\text{rect}}(\varphi) = \frac{1}{2 \max\{|\sin \varphi|, |\cos \varphi|\}} = \begin{cases} \frac{1}{2|\cos \varphi|}, & \varphi \in [-\pi/4, \pi/4] \cup [3\pi/4, 5\pi/4] \\ \frac{1}{2|\sin \varphi|}, & \varphi \in [\pi/4, 3\pi/4] \cup [5\pi/4, 7\pi/4] \end{cases} \quad (A.3)$$

$$r_{\text{elli}}(\varphi) = \frac{\sqrt{2/r_2} Q}{\sqrt{1 - (1 - \frac{r_1}{r_2}) \cos^2(\varphi)}} \quad (A.4)$$

are the radius in polar coordinates of ellipsis and rectangle respectively. The angle φ is the angle of the polar coordinates in the (q_1, q_2) plane and can be defined using

$$\varphi(q_1, q_2) = \arctan 2(q_2, q_1) = \begin{cases} \arctan(q_2/q_1) & q_1 > 0, q_2 > 0 \\ \arctan(q_2/q_1) + \pi & q_1 < 0, q_2 > 0 \\ \arctan(q_2/q_1) + \pi & q_1 < 0, q_2 < 0 \\ \arctan(q_2/q_1) + 2\pi & q_1 > 0, q_2 < 0 \end{cases} \in [0, 2\pi]. \quad (\text{A.5})$$

For sake of later improvement it is useful to write the potential even more general. Therefore, the function f in (A.1) is replaced by $g \circ f$ which also allows a nonlinear interpolation onto the border of phase space using another function g . It also allows to incorporate an interpolation to a value on the border which depends on the angle φ , see later. The final form of the function is given by the general ansatz mentioned on page 37

$$V(q_1, q_2) = \begin{cases} V_{\text{quadratic}}(q_1, q_2), & V_{\text{quadratic}}(q_1, q_2) \leq Q^2 \\ Q^2 + g(f(q_1, q_2)), & \text{else.} \end{cases} \quad (\text{3.70})$$

In the following we choose a parabola for g

$$g(\tilde{r}) = \tilde{r}(a - (a - b + Q^2)\tilde{r}) + Q^2 \quad (\text{A.6})$$

where \tilde{r} takes values in $[0, 1]$ and a and b are real parameters. To ensure that the dynamics in the chaotic region is really chaotic the second derivative of g at zero must be negative. These points $\tilde{r} = 0$ correspond to the ellipsis defined by $f = 0$. They therefore represent the points at the interface of both domains of definition in (3.70). If the second derivative would be positive, then g would have a local minimum in the (q_1, q_2) plane. In this minimum regular motion would be possible. To avoid this the parameters have to fulfill $b < a + Q^2$.

The derivative in the outside region has to be calculated using polar coordinates (r, φ) . We get

$$\frac{\partial g \circ f}{\partial q_i}(q_1, q_2) = g'(f(q_1, q_2)) \cdot \left(\frac{\partial f}{\partial r}(q_1, q_2) \cdot \frac{\partial r}{\partial q_i}(q_1, q_2) + \frac{\partial f}{\partial \varphi}(q_1, q_2) \cdot \frac{\partial \varphi}{\partial q_i}(q_1, q_2) \right) \quad (\text{A.7})$$

in which $g'(\tilde{r}) = a - 2 \cdot (a - b + Q^2)\tilde{r}$ and

$$\frac{\partial f}{\partial r} \cdot \frac{\partial r}{\partial q_i}(q_1, q_2) = \frac{1}{r_{\text{rect}} - r_{\text{elli}}} \frac{q_i}{r}. \quad (\text{A.8})$$

The φ -part reads

$$\frac{\partial f}{\partial \varphi}(q_1, q_2) = \frac{r - r_{\text{rect}}}{(r_{\text{rect}} - r_{\text{elli}})^2} \frac{\partial r_{\text{elli}}}{\partial \varphi} - \frac{r - r_{\text{elli}}}{(r_{\text{rect}} - r_{\text{elli}})^2} \frac{\partial r_{\text{rect}}}{\partial \varphi} \quad (\text{A.9})$$

and

$$\frac{\partial \varphi}{\partial q_i}(q_1, q_2) = \bar{q}_i / r^2 \quad (\text{A.10})$$

where we have used the abbreviation $\bar{q}_i = q_1 \delta_{2i} - q_2 \delta_{1i}$. The remaining expressions are

$$\frac{\partial r_{\text{rect}}}{\partial \varphi} = \begin{cases} \tan(\varphi) r_{\text{rect}} & \varphi \in [-\pi/4, \pi/4) \cup [3\pi/4, 5\pi/4) \\ -\cot(\varphi) r_{\text{rect}} & \varphi \in [\pi/4, 3\pi/4) \cup [5\pi/4, 7\pi/4) \end{cases} \quad (\text{A.11})$$

and

$$\frac{\partial r_{\text{elli}}}{\partial \varphi} = -\sqrt{\frac{2}{r_2}} Q \frac{(1 - \frac{r_1}{r_2}) \sin(\varphi) \cos(\varphi)}{\left[1 - (1 - \frac{r_1}{r_2}) \cos^2(\varphi)\right]^{-3/2}}. \quad (\text{A.12})$$

With the abbreviations $R = r_{\text{rect}} - r_{\text{elli}}$, $\Delta = \frac{1}{rR} \left[\frac{\partial r_{\text{elli}}}{\partial \varphi} (r - r_{\text{rect}}) - \frac{\partial r_{\text{rect}}}{\partial \varphi} (r - r_{\text{elli}}) \right]$, and $\Xi = \frac{\partial r_{\text{rect}}}{\partial \varphi} - \frac{\partial r_{\text{elli}}}{\partial \varphi}$ we arrive at the following expression for the coupled region

$$\frac{\partial V}{\partial q_i} = g'(f(q_1, q_2)) \cdot \frac{\partial f}{\partial q_i} = g'(f(q_1, q_2)) \cdot \frac{q_i + \bar{q}_i \Delta}{rR}. \quad (\text{A.13})$$

The second derivative can be calculated likewise. Using the expressions

$$\frac{\partial^2 r_{\text{elli}}}{\partial \varphi^2} = \sqrt{\frac{2}{r_2}} Q \frac{\left(3(1 - \frac{r_1}{r_2}) \sin^2(\varphi) \cos^2(\varphi) - (1 - (1 - \frac{r_1}{r_2}) \cos^2(\varphi))(\cos^2(\varphi) - \sin^2(\varphi))\right)}{\left(1 - (1 - \frac{r_1}{r_2}) \cos^2(\varphi)\right)^{-5/2}}, \quad (\text{A.14})$$

$$\frac{\partial^2 r_{\text{rect}}}{\partial \varphi^2} = \begin{cases} r_{\text{rect}} (1 + 2 \tan^2(\varphi)) & \varphi \in [-\pi/4, \pi/4) \cup [3\pi/4, 5\pi/4) \\ r_{\text{rect}} (1 + 2 \cot^2(\varphi)) & \varphi \in [\pi/4, 3\pi/4) \cup [5\pi/4, 7\pi/4) \end{cases}, \quad (\text{A.15})$$

and

$$\frac{\partial^2 \varphi}{\partial q_i \partial q_j} = \frac{\delta_{1i} \delta_{2j} - \delta_{2i} \delta_{1j}}{r^2} - \frac{2}{r^4} \bar{q}_j q_i = \frac{\varepsilon_{ij3}}{r^2} - \frac{2}{r^4} \bar{q}_j q_i \quad (\text{A.16})$$

we can introduce $\Sigma = \frac{\partial^2 r_{\text{elli}}}{\partial \varphi^2} (r - r_{\text{rect}}) - \frac{\partial^2 r_{\text{rect}}}{\partial \varphi^2} (r - r_{\text{elli}})$ and write

$$\frac{\partial^2 f}{\partial q_i \partial q_j} = \frac{1}{rR} \left\{ \delta_{ij} - \frac{q_i q_j}{r^2} - \frac{q_i \bar{q}_j \Xi}{r^2 R} \left(\delta_{i2} \delta_{j1} - \delta_{i1} \delta_{j2} - \frac{2 \bar{q}_i}{r^2} \left(q_j + \frac{\bar{q}_j \Xi}{R} \right) \right) \Delta + \frac{\bar{q}_i}{r^2 R} \left(\frac{\bar{q}_j}{r} \Sigma - q_j \Xi \right) \right\} \quad (\text{A.17})$$

and arrive at

$$\frac{\partial^2 V}{\partial q_i \partial q_j} = g''(f) \frac{\partial f}{\partial q_i} \frac{\partial f}{\partial q_j} + g'(f) \frac{\partial^2 f}{\partial q_i \partial q_j}. \quad (\text{A.18})$$

If b in equation (A.6) is not a constant but varies along the border of phase space, we have to account for the additional φ -dependence. The general expressions in the chaotic region then reads

$$V(q_1, q_2) = Q^2 + g(f(q_1, q_2), \varphi(q_1, q_2)) \quad (\text{A.19})$$

and the corresponding first derivatives are

$$\frac{\partial V}{\partial q_i} = \frac{\partial g}{\partial f} \frac{\partial f}{\partial q_i} + \frac{\partial g}{\partial \varphi} \frac{\partial \varphi}{\partial q_i}. \quad (\text{A.20})$$

Choosing a common shorthand notation for the derivative then the second derivative reads

$$\frac{\partial^2 V}{\partial q_i \partial q_j} = g_{|ff} f_{|j} f_{|i} + g_{|f\varphi} (f_{|j} \varphi_{|i} + f_{|i} \varphi_{|j}) + g_{\varphi\varphi} \varphi_{|i} \varphi_{|j} + g_{|f} f_{|ij} + g_{|\varphi} \varphi_{|ij}.$$

We choose the function g to be a parabola going from the ellipsis to the border. This parabola ends at a value given by a sine along the rectangular border. This sine is of the form

$$V|_{\mathbf{q} \in \text{border}}(q_1, q_2) = \frac{K}{2\pi} \sin(2\pi(m \cdot q_1 + n \cdot q_2)) \quad (\text{A.21})$$

where $n, m \in \mathbb{Z}$ and K is a real parameter. This constraint on the parabola can be met by adding a function depending on φ to the above b

$$b \longrightarrow b(\varphi) = b + \begin{cases} \frac{K}{2\pi} \sin(\pi(n \tan(\varphi) + m)) & \varphi \in [-\frac{\pi}{4}, \frac{\pi}{4}] \\ \frac{K}{2\pi} \sin(\pi(n + m \cot(\varphi))) & \varphi \in [\frac{\pi}{4}, \frac{3\pi}{4}] \\ \frac{K}{2\pi} \sin(\pi(-n \tan(\varphi) + m)) & \varphi \in [\frac{3\pi}{4}, \frac{5\pi}{4}] \\ \frac{K}{2\pi} \sin(\pi(n - m \cot(\varphi))) & \varphi \in [\frac{5\pi}{4}, \frac{7\pi}{4}]. \end{cases} \quad (\text{A.22})$$

The resulting potential is shown in terms of a contour plot in figure 3.5 together with a colormap in the background. Section 3.4.1 addressed the resulting phase-space structures.

The definition of the potential is complicated. This is only necessary in order to ensure that there are no regular regions embedded in the chaotic domain and that there is a sharp transition from regular to chaotic behavior as demanded in section 3.4.1. The most important ingredient of this potential however is its harmonic interior which gives rise to the linear and hence regular dynamics.

B. Quantum-number assignment-algorithm

In this appendix we discuss how the eigenstates from the diagonalization of the open system U^{open} , equation (4.22), are sorted and how quantum numbers are assigned in order to predict the tunneling rate for a given state $\tilde{\psi}_{\text{reg}}^{m,n}$ under variation of $1/\hbar$. This can be done in various ways, e.g. by calculating

overlaps with harmonic oscillator eigenstates or by numerically counting the number of nodes in both q directions, see the $\|\psi\|^2$ -insets in figures 4.1 to 4.5. For generic systems such as the coupled standard maps, it is a non-trivial task to assign quantum numbers to states due to the intense coupling between all eigenstates caused by dynamical tunneling, see for example references [72, 186–188]. In such generic cases it can be helpful to also consider the slope of the eigenphases φ with respect to $1/h$ in order to assign quantum numbers to given states.

In this thesis we proceed as follows in order to extract the regular states from the data. First, we start with the smallest value of h at the rightmost data points of the $1/h$ axis. For every eigenstate calculated for this $1/h$ the eigenstate with the next smaller $1/h$ is determined. The one which looks the most similar to the actual state is said to be the same state. This is performed by an overlap of the two states. As this overlap has to be calculated between two states with different h and therefore different grid sizes and offset, the eigenstate on the finer grid is interpolated down to the coarser grid using a 2D spline-interpolation of SCIPY [189]. In order to leave out chaotic states, the overlap has to be above a certain threshold. This algorithm yields a series of numerical eigenstates for decreasing $1/h$ and thereby tracks quantum states across different diagonalizations. In order to minimize the time of computation, the search for the best matching eigenvector can be reduced to the ones lying close in the eigenphase spectrum with $\varphi(1/h) = -\varepsilon(1/h)/\hbar$. This is due to the fact that the regular states are expected to have a continuous dependency of the eigenphases on h and that their level velocity, i. e. the slope of $\varphi(1/h)$, is not too big. The quantum state tracking algorithm therefore fails at small $1/h$ where the regular states quantize close to the border of the regular region.

While decreasing $1/h$ and following the initial eigenstate through the calculated data the overlap between adjacent states drop below the threshold at a certain value of $1/h_{\max}$, and the tracking is stopped. This occurs for two reasons. First, all regular states have a minimal $1/h_{\max}$ value below which h is too large to resolve the classical phase space sufficiently and therefore the eigenstate ceases to exist. Second, the above algorithm is applied to all calculated eigenstates. If the initial state at the largest $1/h$ is non-regular, the algorithm will already stop at the first step as for a chaotic state there will be no eigenstate at the next smaller $1/h$ with a very large overlap. Thereby it is possible to remove all chaotic eigenstates. For all other states it is possible to assign quantum numbers according to the number of nodal lines of $\|\psi\|^2$ in q_1 and q_2 direction.

The main drawback of the above quantum-number assignment-algorithm is that it will follow avoided crossings along the adiabatic basis instead of the diabatic basis which connects branches of similar looking eigenstates. In order to swap the two branches of each avoided crossing in the eigenphase spectrum, it is necessary to manually reconnect them. The last step is then to attribute quantum numbers to the calculated states. This can again be done semi-automatically for the designed map as there the two degrees of freedom decouple along the coordinate axes q_1 and q_2 in the regular region. Figure B.1 shows an example of an avoided crossing. Here the assignment is changed by hand to the one shown in the figure. The automatic search does not yield the correct swapping of the quantum state at the avoided crossing. In order to finally assign the correct quantum numbers, it is necessary to use a value of $1/h$ where the number of nodal lines of $\|\psi\|^2$ in q_1 and q_2 direction

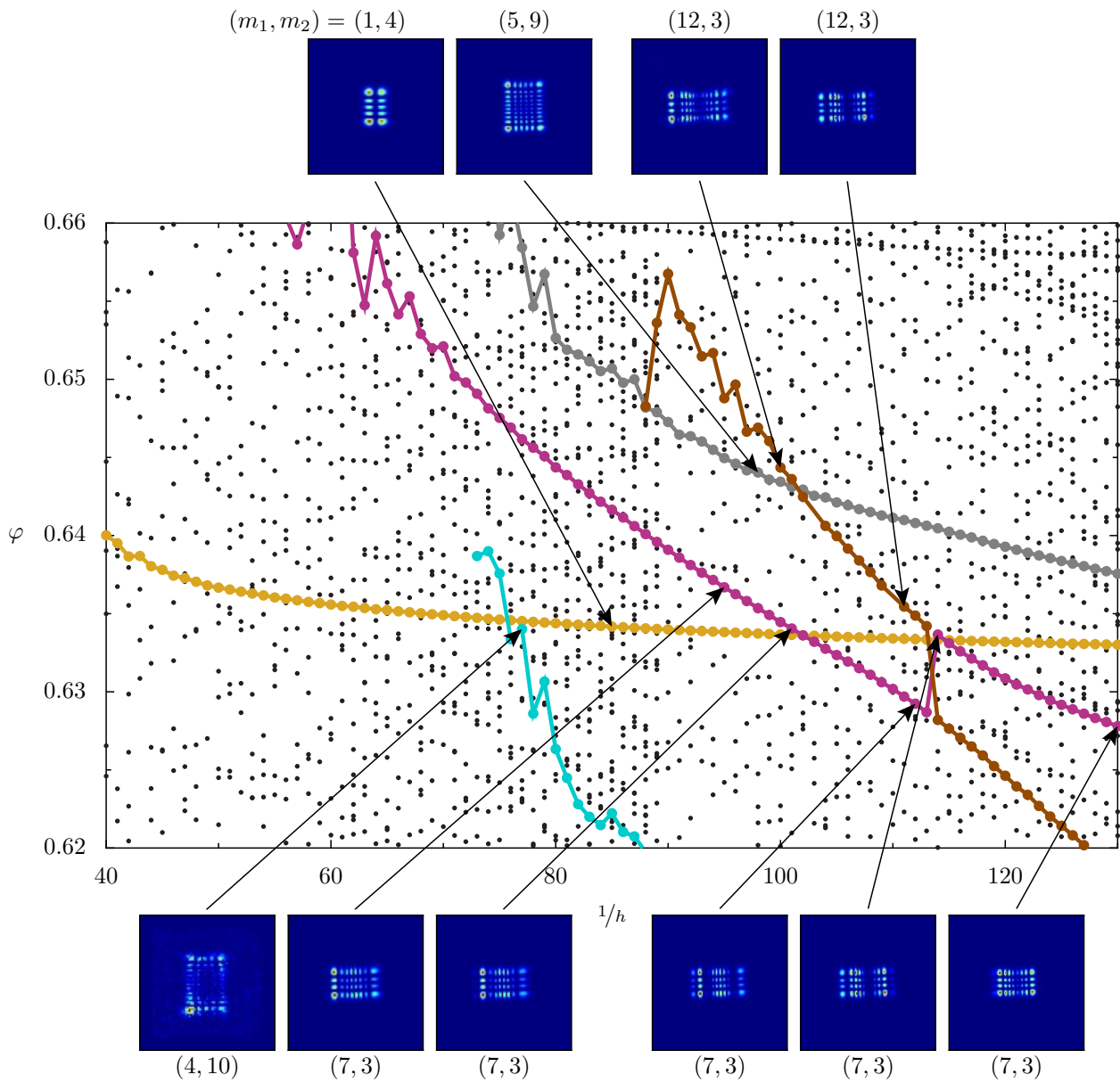


Figure B.1.: Assignment of quantum numbers in the spectrum of the designed map \mathcal{P}_{nnc} . The black dots are the numerical data. As the number of calculated states at each $1/h$ is higher than $V_{4\text{D}}^{\text{reg}}/h^2$, there are also chaotic states in this data. The algorithm filters the regular states and connects them to each other. At avoided crossings the assignment has to be done manually, e.g. between $\tilde{\psi}_{\text{reg}}^{7,3}$ and $\tilde{\psi}_{\text{reg}}^{12,3}$ at $1/h \approx 115$. The result is shown by colored points connected by lines which serve as guide to the eye. The insets show the position-space probability-density $|\tilde{\psi}_{\text{reg}}(\mathbf{q})|^2$ for the states marked by the arrows.

are clearly defined. Apart from these difficulties it is still useful to assign the quantum numbers as automatically as possible as the number of regular states also increases with $1/h^2$ as $1/h$ gets larger. For the right hand side of figure B.1 there are already approximately 180 regular eigenstates which need to be determined and related to the eigenstates at smaller $1/h$.

C. Alternate paths due to alternate resonances in the description of RAT

In figure 4.26 possible resonance-induced tunneling paths Γ for the initial quantum state $|\tilde{\psi}_{\text{reg}}^{0,3}\rangle$ are shown. They symbolize the couplings to higher excited states which potentially lead to an increase of the tunneling rate as discussed in section 4.4.6 on page 112. They are based on the choice that the dominating resonances are $5 : 0 : 1$ and $6 : -1 : 1$. Figure C.1 shows tunneling paths for $|\tilde{\psi}_{\text{reg}}^{0,3}\rangle$ of the map \mathcal{P}_{nnc} at other values of Planck's constant. While we present $1/h = 90$ in the main text, here $1/h = 50$ and $1/h = 130$ are shown. Like in the figure on page 114 the border between regular and chaotic domain is shown by a dashed red line in the quantum-number quarter-plane. As this line is not precisely defined, we obtain a non-convex behavior for the case $1/h = 130$.

If other resonances $\mathbf{r}^{a,b}, s^{a,b}$ are chosen to be the basis of the relevant Fourier subset in equation (4.41), we obtain different selection rules (4.53). Although these selection rules lead to the exact same grid of potentially coupling partners in the RAT paths (4.49), shown in orange in figure C.1, we obtain different paths when truncating the potential at the lowest order of the Fourier modes, i. e. $|\alpha| \leq 1$ and/or $|\beta| \leq 1$, see page 112. At this point we have to keep in mind that the truncation is necessary in order to simplify the resonance Hamiltonian to a form where it might be possible to predict the size of the Fourier components $V^{\mathbf{m},n}$, see the discussion on page 116.

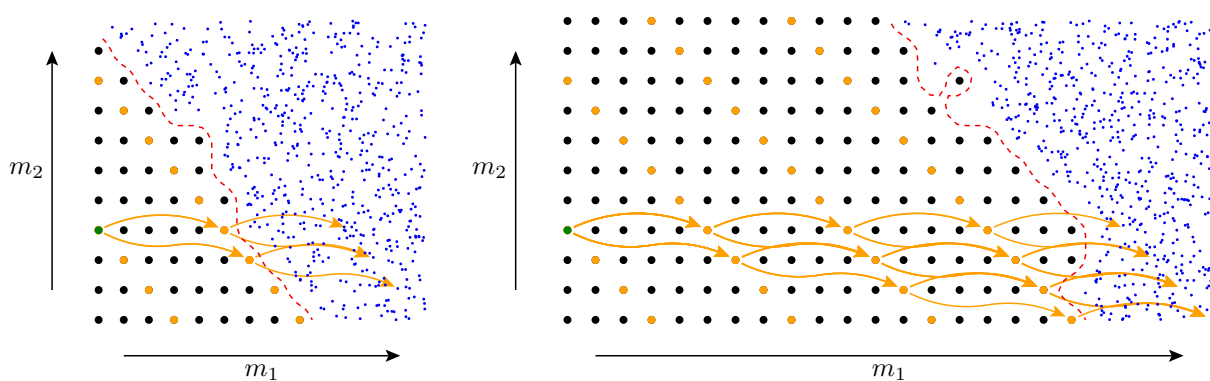


Figure C.1.: Possible tunneling paths Γ at $1/h = 50$ and $1/h = 130$. The black and orange points indicate existing regular states with quantum numbers (m_1, m_2) . The border of the regular island of \mathcal{P}_{nnc} is drawn as a dashed red curve in the quantum-number quarter-plane. At the right hand side of this line no regular states exist. This is illustrated by the random blue points which symbolize the chaotic sea.

Two different choices of resonance vectors as basis of the resonance module $\mathcal{L}(1/5, 1/5)$ are

$$5 : 0 : 1 \quad \text{and} \quad 4 : 1 : 1 \tag{C.1}$$

and

$$6 : -1 : 1 \quad \text{and} \quad 4 : 1 : 1. \tag{C.2}$$

Note that example (C.2) is chosen insufficiently according to the requirement of equation (3.12). The determinant of the matrix given by $\mathbf{r}^{a,b}$ is ten and therefore double the period $p = 5$. We use this to show the consequences of such a wrong choice.

All possible paths emerging for this choices for the state $\psi_{\text{reg}}^{0,3}$ at $1/h = 90$ are shown in figure C.2. Although the grid of reachable states (orange dots) in figure C.2(a) is the same as in figure C.1, the paths Γ leading to states close to the chaotic domain differ. Hence, other quasienergy denominators enter the RAT prediction and might give a different prediction. Note that the state $\psi_{\text{reg}}^{11,2}$ responsible for the peak in the tunneling rate in figure 4.27 is not among the intermediate steps of the tunneling paths Γ . We present a RAT prediction based on this resonance module basis in section D contrary to the choice (3.94) in the main text. Let us again emphasize that this difference comes from the truncation simplification of the resonance Hamiltonian (4.41) and hence is not a direct but an indirect result of changing the basis of the resonance module. Especially the choice of the resonance basis (C.1) allows an increase of the second quantum number with the lowest order transitions $|\alpha| \leq 1$ and/or $|\beta| \leq 1$.

In contrast to equation (C.1) the choice of equation (C.2) is insufficient. This can be seen in figure C.2(b). There the set of reachable states differ from the ones in figure (a). Here the state $\psi_{\text{reg}}^{11,2}$ is really missing and not just unaddressed due to a truncation of the Fourier series.

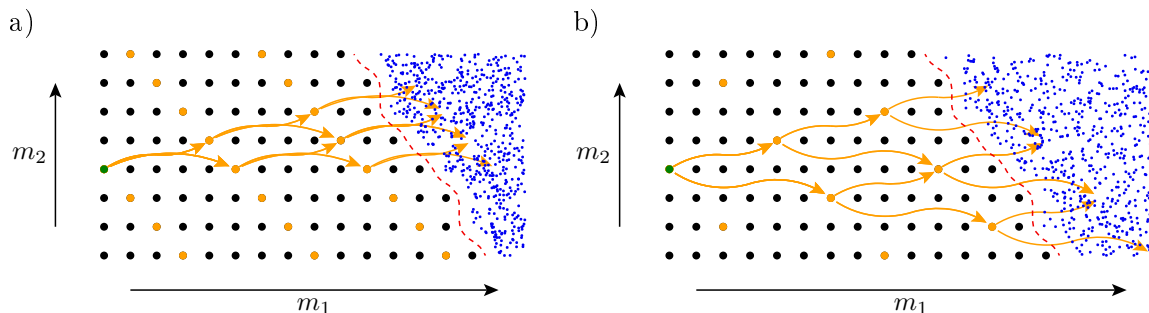


Figure C.2.: Alternative paths Γ for $\psi_{\text{reg}}^{0,3}$ based on different choices of $\mathbf{r}^{a,b}, s^{a,b}$. Figure (a) is based on equation (C.1), figure (b) is based on equation (C.2).

D. Alternate resonances in the description of RAT leading to different tunneling rates

Appendix C shows that a different choice of the basis of the resonance module of the rank-2 resonance of \mathcal{P}_{nnc} gives rise to other sets \mathcal{G} of tunneling paths Γ . From this we might deduce that the RAT prediction based on this choice also differs because different quasienergy denominators appear in equation (4.49).

However, a different choice of the basis also leads to different formulas from which the parameters of the resonance approximation equation (4.52) are determined, see for example appendix I where the linearization of the mapping and the monodromy matrix of the resonance Hamiltonian are discussed. Although we cannot give an analytical expression for the Fourier modes of the potential V and \mathcal{H}_{ij} in terms of quantities determined from the classical phase space, see the discussion on page 116, it is very likely that the coupling matrix elements for different bases of the resonance module are different. This change in the coupling matrix elements of V would compensate the effect of different paths if we would not truncate the paths at lowest order. The truncation can completely remove states from the set of all relevant tunneling paths \mathcal{G} which are vital to the explanation of the peak structure of the tunneling rates. One such example is the state $\psi_{\text{reg}}^{11,2}$ from figure 4.27 which is missing in figure C.2(a) completely. This flaw has serious consequences in the prediction of the dynamical tunneling rates as can be seen in figure D.1. Because of the fact that the state $\psi_{\text{reg}}^{11,2}$, responsible for the peak at $1/h = 97$, is missing in the tunneling paths the RAT prediction misses this peak. The corresponding small quasienergy denominator of equation (4.49) is not present in any of the paths in equation (4.51). The coupling matrix elements V_1, V_2 (4.63) for the resonances have been set to $5.5 \cdot 10^{-5}$ for both resonances.

E. Tunneling rates of map with nonlinear resonances but uncoupled regular region

When introducing nonlinearities to the purely linear and uncoupled regular region of \mathcal{P}_{lu} the transition to \mathcal{P}_{nnc} was done in several steps. While more and more terms were enabled in the potential of equation (3.91) the according change was observed by calculating the image of the frequency map \mathcal{F} in figure 3.10. One of the systems introduced during this transition from \mathcal{P}_{lu} to \mathcal{P}_{nnc} was the system with nonlinearities in both degrees of freedom but no coupling term inside the regular island, see figure 3.10(c).

While the tunneling rates of \mathcal{P}_{nnc} in figure 4.24 require a rank-2 resonance Hamiltonian in order to obtain the responsible tunneling steps in figures 4.26 and 4.27, this is not the case for the nonlinear but uncoupled regular region. As the second degree of freedom does not yield resonances at all, there are just rank-1 resonances in the first degree of freedom as shown in figure 3.10(c) and the tunneling rates of this system shown in figure E.1 look very different from the ones of \mathcal{P}_{nnc} . In particular they lack the prominent RAT peaks for $|\tilde{\psi}_{\text{reg}}^{0,3}\rangle$ at $1/h = 82, 97$, and 122. This emphasizes the necessity of

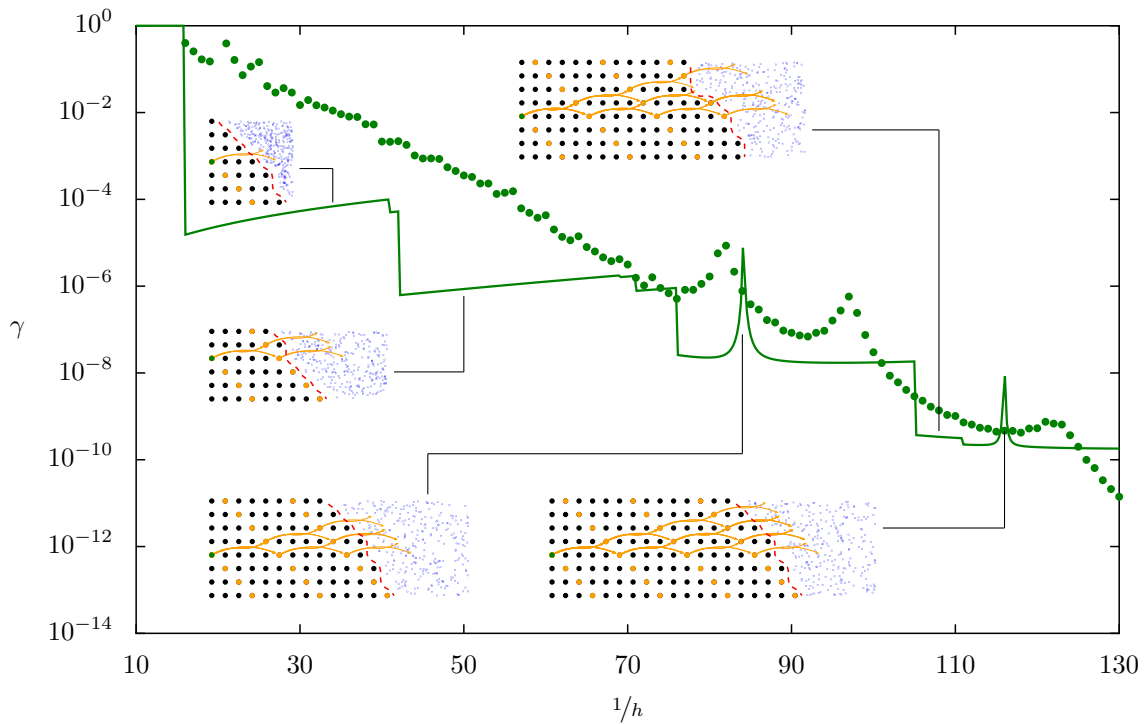


Figure D.1.: RAT prediction of the tunneling rate γ for $\psi_{\text{reg}}^{0,3}$ based on choice (C.1) for the basis of the resonance module \mathcal{L} . The RAT prediction misses the peak at $1/h = 97$ as the state responsible for the coupling, $\psi_{\text{reg}}^{11,2}$, is not covered by the tunneling paths Γ . The insets show the contributing paths at the given values of $1/h$.

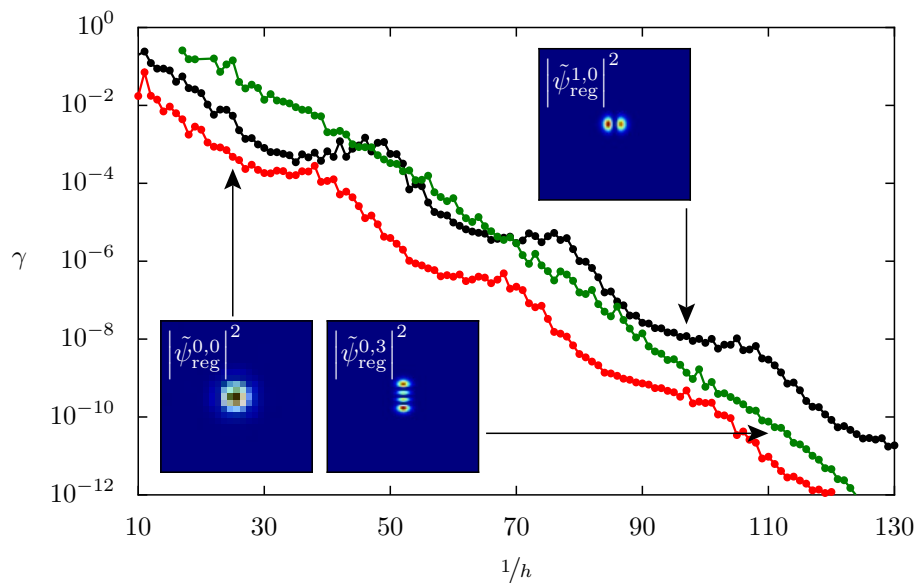


Figure E.1.: Tunneling rates γ of the map with nonlinear resonances but uncoupled regular region, figure 3.10(c). Due to the missing second resonance condition of \mathcal{P}_{nnc} the state $|\tilde{\psi}_{\text{reg}}^{0,3}\rangle$ cannot couple to higher excited ones as in figure 4.27. Hence, it lacks the peaks at $1/h = 82, 97,$ and 122 .

the rank-2 resonance when describing the resonance-assisted tunneling of \mathcal{P}_{nnc} in section 4.4.6.

The plateaus in γ are also present in \mathcal{P}_{nnc} , for example for the ground state $\psi_{\text{reg}}^{0,0}$ in figure 4.24. They emerge from couplings to states which are not supported inside the regular region yet but already start to manifest at the interface between regular and chaotic domains. Such states can be seen in the eigenphase spectrum E.2 of the ground state $\psi_{\text{reg}}^{0,0}$. Although $\psi_{\text{reg}}^{0,0}$ is allowed to couple to $\psi_{\text{reg}}^{5,0}$, $\psi_{\text{reg}}^{10,0}$, and $\psi_{\text{reg}}^{15,0}$ these states do not yet exist at the $1/h$ values where there eigenphases are degenerate. Such states give rise to broad plateaus in the tunneling rate rather than pronounced peaks. This is known for 2D maps. There one can show that states lying symmetrically with respect to the resonance chain will couple very efficiently [84, page 102]. By shifting the resonance closer to the center of the regular island plateaus in γ can be transformed into sharp peaks by creating more accessible volume behind the resonance. As resonance chains are not able to separate regions in the phase space in 4D maps, it is an open question how to generalize this notion of “phase-space volume behind the resonance”.

F. Interpolation of quasienergies

As mentioned in section 4.4.6 it is necessary to predict the quasienergies $\varepsilon_{m,n}$ of regular states $\tilde{\psi}_{\text{reg}}^{m,n}$ in order to calculate the tunneling rates in the case of resonance-assisted tunneling. We do this by fitting the data numerically obtained by diagonalizing the discretized time-evolution operator of the open system U^{open} . For the system \mathcal{P}_{nnc} the eigenphases φ from equation (4.22) converge to a constant value for each state for increasing $1/h$. Therefore, we consider them rather than the quasienergies ε from equation (4.56).

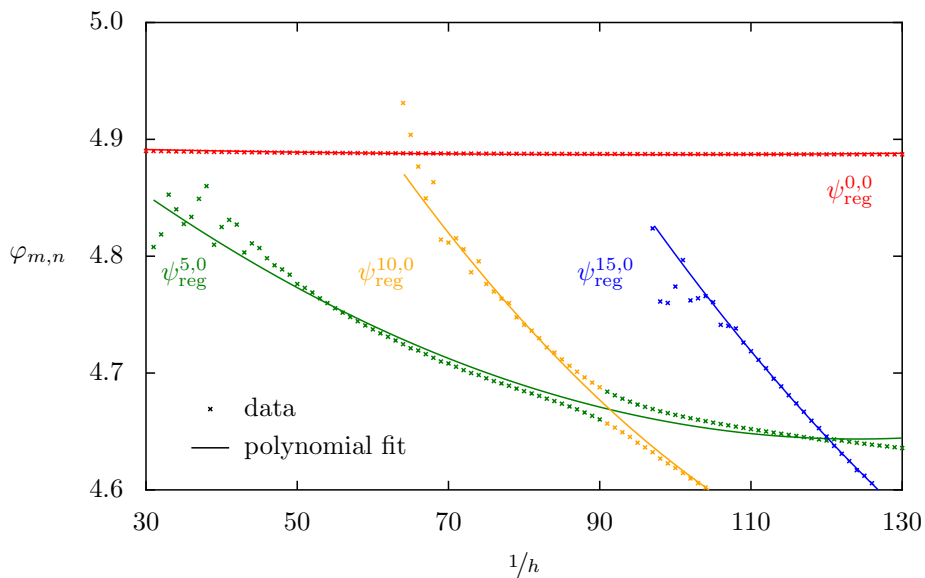


Figure E.2.: Eigenphase φ and polynomial fit of the eigenphase for the ground state $\psi_{\text{reg}}^{0,0}$ and states allowed to couple to it, $\psi_{\text{reg}}^{5,0}$, $\psi_{\text{reg}}^{10,0}$, and $\psi_{\text{reg}}^{15,0}$. All potential coupling partners are not supported inside the regular domain when their phases and hence quasienergies are close to that one of the ground state.

When performing a fit of the quasienergies we have to overcome two problems. First, we do not want to have the highly fluctuating part of the eigenphase data at small values of $1/h$ to have too much influence on the fit. Second, the fit should pass smoothly through the avoided crossings connecting the diabatic bases. In order to solve these issues, the fit of the data is done as follows: First, the numerical data is interpolated by a spline of third order using the `ndimage` library of `SCIPY` [189]. This interpolation is then used to calculate an estimate for the second derivative $\partial^2\varphi/\partial(1/h)^2$ to each numerical data point $(1/h, \varphi)$. If this second derivative is above a certain threshold, the corresponding data point is discarded. The remaining points are used as input for fitting a polynomial of order three. The polynomials for the eigenphases φ enter the RAT prediction (4.49) via the quasienergies ε leading to figure 4.28. The intermediate steps of the interpolation and fitting procedure are shown in figure F.1. It contains the available data from the diagonalization of the open quantum system denoted by small crosses and full circles. This raw data is interpolated by using a cubic spline giving the dashed line. The points where the second derivative of the spline interpolation is sufficiently small are indicated by the full circles while the regions of high oscillation are indicated by the small crosses. The data shown by full circles are used as input for the polynomial fit of order three. This fit is shown by the solid line. The crossings of the solid line of $\psi_{\text{reg}}^{0,3}$ with the ones of $\psi_{\text{reg}}^{6,2}$, $\psi_{\text{reg}}^{11,2}$, and $\psi_{\text{reg}}^{16,2}$ give rise to the peaks of the prediction in figure 4.28.

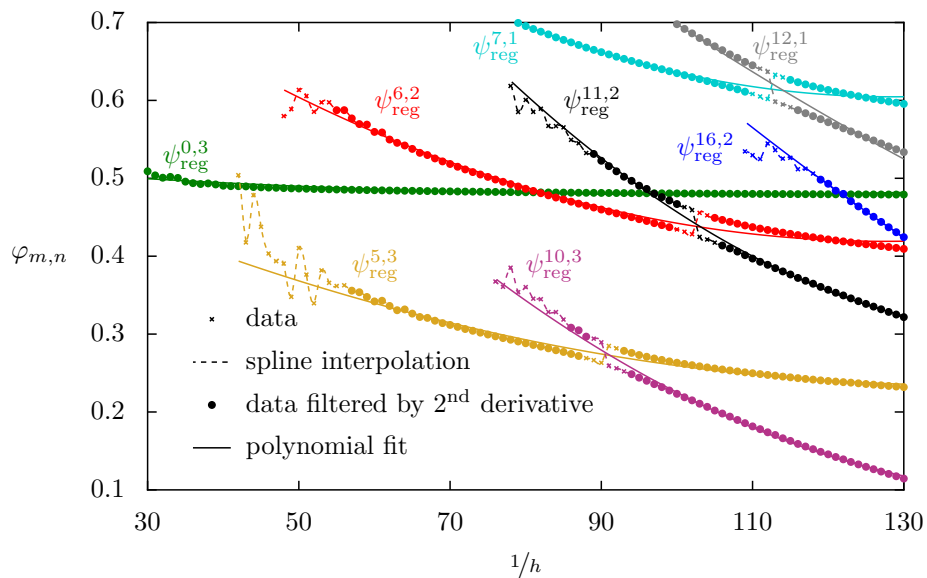


Figure F.1.: Fit of the numerically determined eigenphases φ for some example states. Full dots and small crosses denote the numerical data. The dashed line shows a cubic spline interpolating the data. Points where the interpolation is sufficiently smooth are marked by dots. These dots are used in order to obtain the polynomial fit shown by the solid line.

G. 2D Poincaré map for the pendulum approximation

Systems with less than two and a half degree of freedom are very special compared to the majority of higher dimensional systems mainly because regular tori separate phase space regions. Apart from this there are further, slightly more subtle differences from higher dimensional systems such as the fact that nonlinear resonances always lead to periodic orbits and that the pendulum approximation for the vicinity of resonances – just as every adiabatic approximation – is integrable due to a lack of explicit time dependence. For the 4D mappings considered in this thesis these special properties do not occur.

However, the 4D mappings still have some special properties compared to systems with even more degrees of freedom. One of them is that the Arnold Diffusion of near-integrable systems only proceeds along a 1D line as mentioned on page 25. Another aspect is that the pendulum approximation is given by a time independent Hamiltonian with two degrees of freedom which itself does not yield Arnold diffusion. Furthermore, the dynamics of this approximation can be reduced to a 2D Poincaré section using the fact that the energy of this pendulum Hamiltonian is conserved. Starting point is the Hamiltonian

$$H_3(\mathbf{I}, \boldsymbol{\theta}) = \frac{1}{2} \mathbf{I}^T \underline{\mathcal{H}} \mathbf{I} + V^{(5,0),1} \cos(5\theta_1) + V^{(6,-1),1} \cos(6\theta_1 - \theta_2) + V^{(11,-1),2} \cos(11\theta_1 - \theta_2) \quad (\text{G.1})$$

inspired by equation (4.52). In this Hamiltonian the regular part $H_4(\mathbf{I})$ has been approximated by its quadratic term according to equation (4.58). It is given by the symmetric but in general not necessarily diagonal matrix $\underline{\mathcal{H}}$. The potential terms are chosen to mimic the phase space of \mathcal{P}_{unc} . Note, however, that it is not known which potential terms enter the pendulum approximation of the rank-2 resonance of \mathcal{P}_{unc} . If the off-diagonal element of the matrix are zero, $\mathcal{H}_{12} = 0$, none of the potential terms must be zero too. Otherwise the system would be given by two uncoupled degrees of freedom which could be obtained by introducing an appropriate choice of center of mass coordinates. However, as mentioned on page 143, the center of mass transformation must be done using a unimodular matrix in order to keep the periodicity of the angles $\boldsymbol{\theta}$.

The Poincaré surface of section is placed in the phase space as follows. First, it is defined in the $\boldsymbol{\theta}$ -space only using the restriction

$$\theta_2 = \pi/2. \quad (\text{G.2})$$

To obtain a valid 3D surface of section inside the 4D phase space we further need to restrict it onto the energy shell. This is done by only using one of the actions, namely I_1 , for the mapping and determining I_2 by solving equation (G.1) for it. In order to do this uniquely it is necessary to further restrict the section condition from equation (G.2) to

$$I_2 > 0. \quad (\text{G.3})$$

If an initial point is placed on the (θ_1, I_1) plane, then equations (G.1) to (G.3) allow to solve the

Hamiltonian for the remaining two coordinates (θ_2, I_2) provided the total energy E is fixed beforehand and that the initial condition is compatible with this energy. For this initial condition Hamilton's equations of motion can be integrated numerically. If the trajectory again crosses the section condition, i. e. by fulfilling equations (G.2) and (G.3) at the same time, then the new values of (θ_1, I_1) at this intersection point define the next pair of iterates of the mapping.

The resulting Poincaré mapping is shown in figure G.1. The main figure shows iterates of the 2D mapping defined in the positional coordinate along the green line, i. e. θ_1 , and the action projected onto the green line, i. e. I_1 . The insets show example orbits in position space atop a contour plot of the potential from equation (G.1). They also include the Poincaré surface of section in angle space given by equation (G.2) as a green line.

The integration is performed using the GNU Scientific Library [190] employing the Bulirsch–Stoer method of Bader and Deuffhard. Whenever the orbit crossed the section condition in the correct

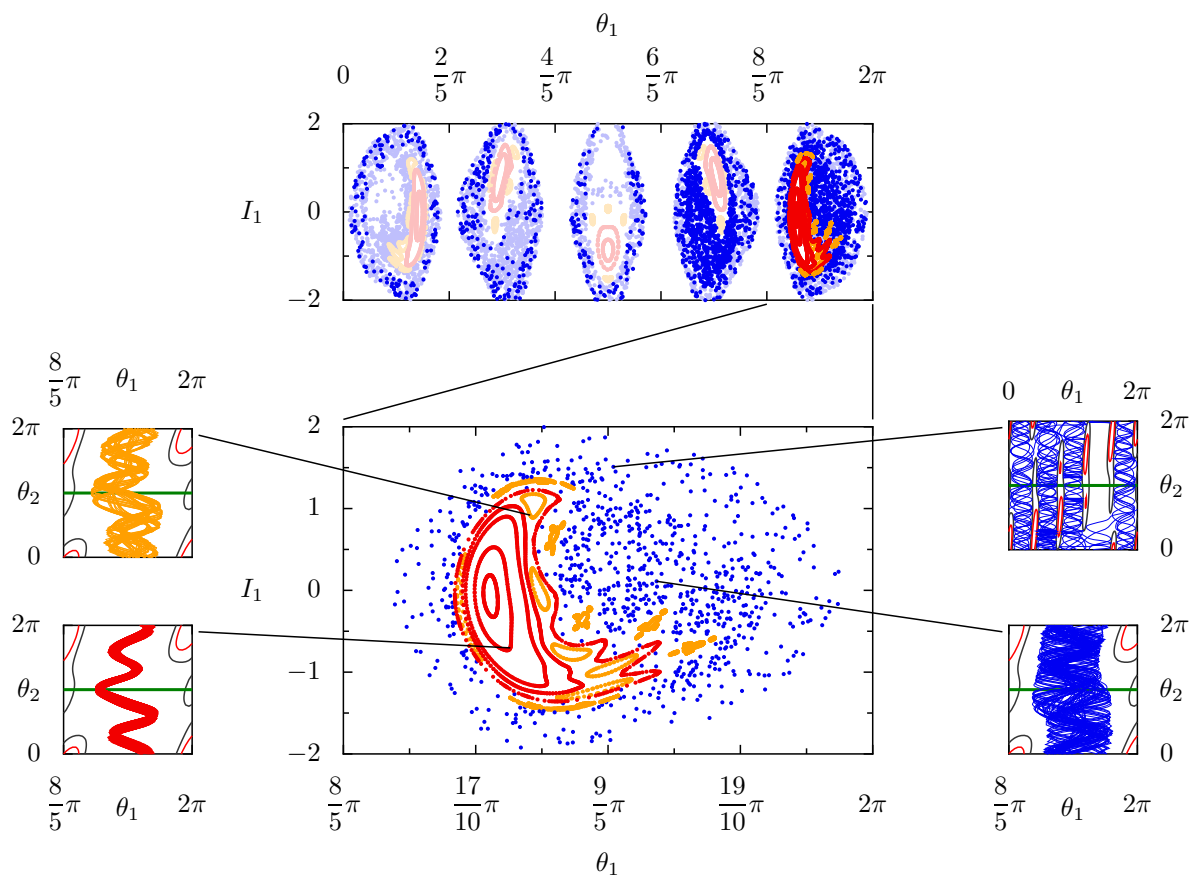


Figure G.1.: Plot of the 2D Poincaré section of the pendulum approximation of a 4D map. The parameters are $\mathcal{H}_1 = \mathcal{H}_2 = 1$, $\mathcal{H}_{12} = 0$, $V^{(5,0),1} = 1.2$, $V^{(6,-1),1} = 0.3$, and $V^{(11,-1),2} = 0.2$. The total energy is set to $E = 1.0$. The upper plot shows the whole θ_1 axis. The lower plot is a magnification of the rightmost island. Initial condition started in or close to the other islands in the upper plot are shown in pale colors. The white areas correspond to invalid initial condition due to the fixed total energy. The insets to the lower plot show example trajectories in position space (θ_1, θ_2) together with a contour plot of the potential V and the Poincaré surface of section shown as a green line.

direction the orbit was integrated onto the section condition using a method proposed by Henon [191].

The presented 2D mapping for the resonance Hamiltonian can provide an insight into how complicated the vicinity of a resonance in the 4D phase space of \mathcal{P}_{nnc} is. For a concrete link between the approximation and the physical system \mathcal{P}_{nnc} it would be necessary to know the parameters of the resonance approximation. In order to get a full impression of the pendulum approximation it would be furthermore necessary to investigate this 2D mapping for other values of the total energy E .

H. RAT prediction broken down to single paths

The incoherent sum (4.39) includes tunneling paths Γ to all possible states in the regular island which are connected to the initial state via the selection rules (4.46). As mentioned on page 108, only a subset \mathcal{G} of them is important, namely these paths Γ which end in states being close to the classical interface of regular and chaotic dynamics. In our prediction only these paths are considered and their single contribution is calculated via equation (4.49).

In order to see which of the paths in \mathcal{G} considered in the incoherent sum of equation (4.49) is the dominant one, it is possible to plot the single contributions of the incoherent sum. This is done in figure H.1. There all paths in \mathcal{G} are shown in gray. The path yielding the largest contribution is marked by color. The dashed line is the incoherent sum of all paths at a given $1/h$. With this the plot

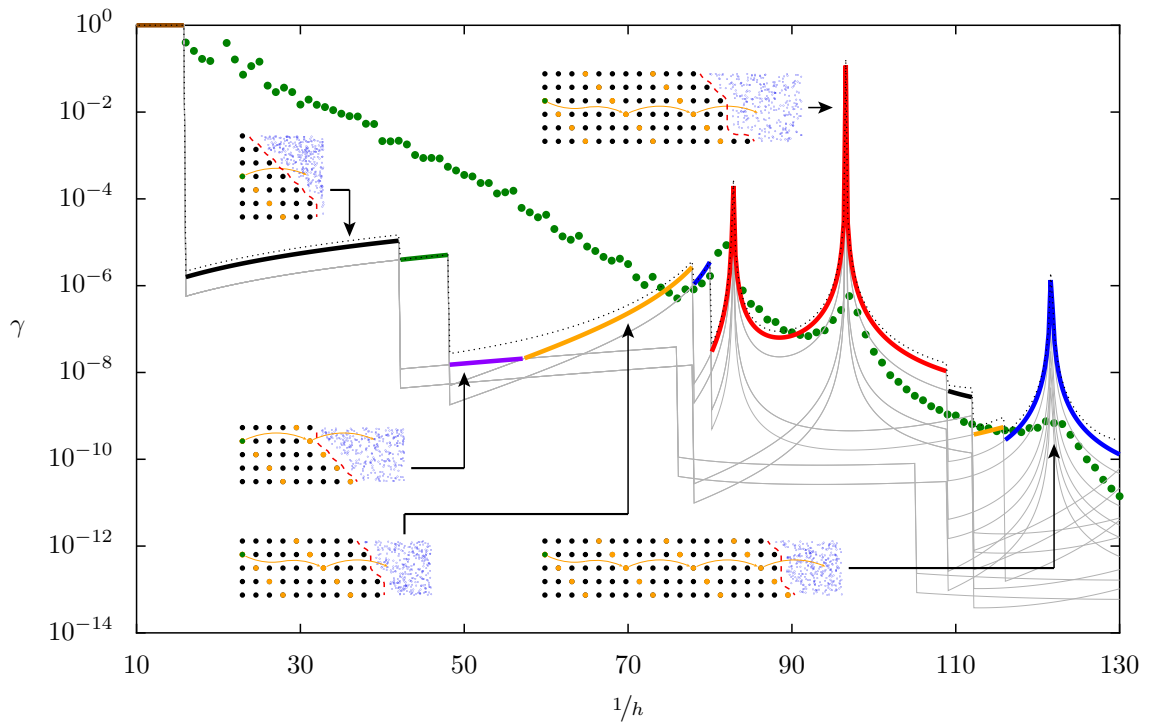


Figure H.1.: RAT prediction of $\gamma_{0,3}$ for \mathcal{P}_{nnc} showing the contributions by single paths Γ . The dashed line is the incoherent sum in equation (4.39) only including paths Γ in \mathcal{G} . The single contribution of these paths is displayed by gray curves. The dominant contribution is highlighted by color. The insets show the dominant path at the values of $1/h$ marked by the arrows.

also allows to check that neglecting the interference terms in equation (4.38) is valid.

I. Linearization of the pendulum approximation

One of the canonical invariants for the link between the Hamiltonian (4.52) approximating the vicinity of the resonance and the real map \mathcal{P}_{nnc} is given by the trace of the linearization around the periodic orbit in the center of the rank-2 resonance. In order to find this trace, we first write the Hamiltonian in a more general form to simplify the notation. The Hamiltonian reads

$$H_3(\boldsymbol{\theta}, \mathbf{I}) = \frac{1}{2} \mathbf{I} \mathcal{H} \mathbf{I} + \sum_{\boldsymbol{\alpha} \in \mathbb{Z}^2 \setminus \{0\}} V^\alpha \cos(\boldsymbol{\alpha} \boldsymbol{\theta}) \quad (\text{I.1})$$

and can be linearized around the stable fixed point $\mathbf{I} = 0$ and $\boldsymbol{\theta} = \boldsymbol{\theta}_0$. The position of this stable fixed point depends on the sign and strength of the Fourier modes. If all of them are positive, then there is a stable equilibrium at $\boldsymbol{\theta}_0 = (\pi, \pi)$. The linearization of the dynamics around this point reads

$$H(\boldsymbol{\theta}, \boldsymbol{\theta}) = \frac{1}{2} \mathbf{I} \mathcal{H} \mathbf{I} + \sum_{\boldsymbol{\alpha} \in \mathbb{Z}^2 \setminus \{0\}} V^\alpha \left(1 - \frac{1}{2} [(\boldsymbol{\theta} - \boldsymbol{\theta}_0) \boldsymbol{\alpha}]^2 \right) \cos(\boldsymbol{\alpha} \boldsymbol{\theta}_0). \quad (\text{I.2})$$

As this system is linear, Hamilton's equation of motion can be solved in general [85]. Using the deviation from the equilibrium $\boldsymbol{\delta} \boldsymbol{\theta} = \boldsymbol{\theta} - \boldsymbol{\theta}_0$ the solution is given by the exponential function

$$\begin{pmatrix} \boldsymbol{\delta} \boldsymbol{\theta}(t) \\ I(t) \end{pmatrix} = \exp(t \underline{\mathcal{A}}) \begin{pmatrix} \boldsymbol{\delta} \boldsymbol{\theta}(0) \\ I(0) \end{pmatrix} \quad (\text{I.3})$$

which contains the matrix

$$\underline{\mathcal{A}} := \begin{pmatrix} 0 & \underline{\mathcal{H}} \\ \underline{\mathbf{V}} & 0 \end{pmatrix} \quad (\text{I.4})$$

where we defined the matrix of second derivatives of the Hamiltonian with respect to the angles evaluated at $\boldsymbol{\theta}_0$

$$\underline{\mathbf{V}} = \frac{\partial^2 H}{\partial \theta_i \partial \theta_j}(\boldsymbol{\theta}_0) = - \sum_{\boldsymbol{\alpha} \in \mathbb{Z}^2 \setminus \{0\}} V^\alpha \cos(\boldsymbol{\alpha} \boldsymbol{\theta}_0) \alpha_i \alpha_j. \quad (\text{I.5})$$

The exponential matrix $\exp(t \underline{\mathcal{A}})$ is the monodromy matrix of the system. Its eigenvalues for $t = 1, 2, \dots$ have to be compared to the eigenvalues of the linearized mapping $D\mathcal{P}_{\text{nnc}}$ and the powers thereof. The eigenvalues of $\exp(\underline{\mathcal{A}})$ are given by the zeros of the characteristic polynomial of $\underline{\mathcal{A}}$ which can be expressed by the characteristic polynomial of the matrix $\underline{\mathcal{H}} \underline{\mathbf{V}}$

$$P_{\underline{\mathcal{A}}}(\lambda) = P_{\underline{\mathcal{H}} \underline{\mathbf{V}}}(\lambda^2). \quad (\text{I.6})$$

For two degrees of freedom the eigenvalues of the 2×2 matrix $\underline{\mathcal{H}\mathcal{V}}$ are given by

$$\rho_{\pm} = \frac{\text{tr}(\underline{\mathcal{H}\mathcal{V}})}{2} \pm \frac{1}{2} \sqrt{\text{tr}(\underline{\mathcal{H}\mathcal{V}})^2 - 4 \det(\underline{\mathcal{H}\mathcal{V}})}. \quad (\text{I.7})$$

Whether the eigenvalues of \mathcal{A} are real or imaginary depends on the choice of θ_0 being the stable or unstable equilibrium. In fact we can encounter all four cases introduced in chapter 3 on page 12, namely EE, EH, HH, or CU-type behavior. It will be of EE-type or HH-type if the eigenvalues of $\underline{\mathcal{H}\mathcal{V}}$ are all negative or all positive real numbers, respectively. If both are real but their sign differs, then it is the EH-case. If the eigenvalues of $\underline{\mathcal{H}\mathcal{V}}$ are conjugate complex numbers, then the equilibrium of the Hamiltonian will be of CU-type.

As mentioned in section 4.4.6, the spectrum of the linearization is an invariant under canonical transformations. Hence, the trace of the monodromy matrix of the time evolution, $\text{tr}\{\exp(\mathcal{A})\}$, is the same as the one for the linearization $D\mathcal{P}_{\text{nnc}}$ of \mathcal{P}_{nnc}

$$\text{tr}\{\exp(\mathcal{A})\} = \text{tr}\{D\mathcal{P}_{\text{nnc}}\}. \quad (\text{I.8})$$

For the different cases of stability the trace for the pendulum model reads

$$\text{tr}(\exp \mathcal{A})^n = \sum_{\lambda \in \mathbb{C}: \lambda^2 \in \sigma(\underline{\mathcal{H}\mathcal{V}})} e^{n\lambda} + e^{-n\lambda} = \begin{cases} 2 \cos(n\omega_1) + 2 \cos(n\omega_2), & \text{EE} \\ 2 \cosh(n\beta_1) + 2 \cos(n\omega_2), & \text{EH} \\ 2 \cosh(n\beta_1) + 2 \cosh(n\beta_2), & \text{HH} \\ 2 \cosh(n(\beta_1 + \omega_1)) + 2 \cosh(n(\beta_2 + \omega_2)), & \text{CU} \end{cases} \quad (\text{I.9})$$

which is expressed in terms of the roots of the eigenvalues of the spectrum σ of $\underline{\mathcal{H}\mathcal{V}}$, $\lambda^2 = \beta + i\omega$. In particular we are interested in 4D maps where the relevant parameters are given by $\text{tr}\{D\mathcal{P}_{\text{nnc}}\}$ and $\text{tr}\{D\mathcal{P}_{\text{nnc}}^2\}$, see figure 3.1. According to equation (I.8) this corresponds to $n = 1$ and $n = 2$ in equation (I.9). These two cases can be combined in order to solve equation (I.9) for ω_1 and ω_2 and we get for the EE case

$$0 = \cos^2(\omega_{1,2}) - \frac{\text{tr}\{D\mathcal{P}_{\text{nnc}}\}}{2} \cos(\omega_{1,2}) + \frac{1}{8} (\text{tr}\{D\mathcal{P}_{\text{nnc}}\})^2 - \frac{1}{8} \text{tr}\{D\mathcal{P}_{\text{nnc}}^2\} - \frac{1}{2}. \quad (\text{I.10})$$

and therefore

$$\omega_{1,2} = \arccos \left(\frac{\text{tr}\{D\mathcal{P}_{\text{nnc}}\}}{4} \pm \frac{1}{4} \sqrt{8 + 2 \cdot \text{tr}\{D\mathcal{P}_{\text{nnc}}^2\} - (\text{tr}\{D\mathcal{P}_{\text{nnc}}\})^2} \right). \quad (\text{I.11})$$

In order to link the parameters of the Hamiltonian equation (I.1) to equation (I.11), we have to express the eigenvalues $\omega_{1,2}$ of $\exp(\mathcal{A})$ by \mathcal{H}_{ij} and the Fourier coefficients of the potential V explicitly. This is not possible in general. Therefore, we have to choose which parts of the full approximation

we neglect, see section 4.4.6 on page 113. For the uncoupled case with no off-diagonal terms in \mathcal{H} ,

$$\mathcal{H}_{11} = \frac{1}{m_1}, \quad \mathcal{H}_{22} = \frac{1}{m_2}, \quad \text{and} \quad \mathcal{H}_{12} = \mathcal{H}_{21} = 0, \quad (4.59)$$

and only one Fourier mode per degree of freedom,

$$V^{k_1,0} \neq 0 \quad V^{0,k_2} \neq 0 \quad \text{and} \quad V^{\alpha_1,\alpha_2} = 0 \quad \text{else} \quad (4.60)$$

for fixed k_1, k_2 , the matrix $\underline{\mathcal{H}\mathcal{V}}$ reads

$$\underline{\mathcal{H}\mathcal{V}} = \begin{pmatrix} -k_1^2 \frac{V^{k_1,0}}{m_1} \cos(k_1\theta_{0,1}) & 0 \\ 0 & -k_2^2 \frac{V^{0,k_2}}{m_2} \cos(k_2\theta_{0,2}) \end{pmatrix}. \quad (I.12)$$

With the abbreviations

$$\tilde{V}^1 := -k_1^2 V^{k_1,0} \cos(k_1\theta_{0,1}) \quad \tilde{V}^2 := -k_2^2 V^{0,k_2} \cos(k_2\theta_{0,2}) \quad (I.13)$$

and equation (I.7) the eigenvalues of $\underline{\mathcal{H}\mathcal{V}}$ are

$$\rho_{\pm} = \frac{1}{2} \left(\frac{\tilde{V}^1}{m_1} + \frac{\tilde{V}^2}{m_2} \right) \pm \frac{1}{2} \left| \frac{\tilde{V}^1}{m_1} - \frac{\tilde{V}^2}{m_2} \right| = \begin{cases} \tilde{V}^1/m_1 \\ \tilde{V}^2/m_2. \end{cases} \quad (I.14)$$

If θ is placed at an EE-type equilibrium, then the eigenvalues from equation (I.14) are all negative. Hence, using equation (I.6) the eigenvalues of the monodromy matrix are

$$\omega_1^{\pm} = \pm i \sqrt{|\rho_+|} = \pm i \sqrt{|\tilde{V}^1/m_1|} \quad \text{and} \quad \omega_2^{\pm} = \pm i \sqrt{|\rho_-|} = \pm i \sqrt{|\tilde{V}^2/m_2|}. \quad (I.15)$$

Therefore we finally have with equation (I.11)

$$\frac{\tilde{V}^{1,2}}{m_{1,2}} = - \left\{ \arccos \left(\frac{\text{tr} D\mathcal{P}_{\text{nnc}}}{4} \pm \frac{1}{4} \sqrt{8 + 2\text{tr}(D\mathcal{P}_{\text{nnc}}^2) - (\text{tr} D\mathcal{P}_{\text{nnc}})^2} \right) \right\}^2. \quad (I.16)$$

Assuming the stable equilibrium at $\theta_0 = (\pi, \pi)$ we have $\cos(k_i\theta_{0,i}) = (-1)^{k_i}$ and therefore obtain

$$\begin{aligned} \frac{(-1)^{k_1} k_1^2 V^{k_1,0}}{m_1} &= - \left\{ \arccos \left(\frac{\text{tr} D\mathcal{P}_{\text{nnc}}}{4} + \frac{1}{4} \sqrt{8 + 2\text{tr}(D\mathcal{P}_{\text{nnc}}^2) - (\text{tr} D\mathcal{P}_{\text{nnc}})^2} \right) \right\}^2 \quad \text{and} \\ \frac{(-1)^{k_2} k_2^2 V^{0,k_2}}{m_2} &= - \left\{ \arccos \left(\frac{\text{tr} D\mathcal{P}_{\text{nnc}}}{4} - \frac{1}{4} \sqrt{8 + 2\text{tr}(D\mathcal{P}_{\text{nnc}}^2) - (\text{tr} D\mathcal{P}_{\text{nnc}})^2} \right) \right\}^2. \end{aligned} \quad (4.61)$$

This is the relation we wanted to obtain in order to relate the parameters of the resonance Hamiltonian (4.52) to properties of the map \mathcal{P}_{nnc} . If more Fourier modes coupling both degrees of freedom are present, it is no longer possible to solve equation (I.7) for the parameters. For example if the

Fourier modes are restricted to

$$V^{k_1,0} \neq 0 \quad V^{k_2,k_3} \neq 0 \quad \text{and} \quad V^{\alpha_1,\alpha_2} = 0 \quad \text{else} \quad (4.60)$$

for fixed k_1, k_2 , and k_3 , then the matrix $\underline{\mathcal{H}\mathbf{V}}$ is given by

$$\underline{\mathcal{H}\mathbf{V}} = \begin{pmatrix} (-1)^{k_1+1} k_1^2 \frac{V^{k_1,0}}{m_1} + (-1)^{k_2+k_3+1} k_2^2 \frac{V^{k_2,k_3}}{m_1} & (-1)^{k_2+k_3+1} k_2 k_3 \frac{V^{k_2,k_3}}{m_1} \\ (-1)^{k_2+k_3+1} k_2 k_3 \frac{V^{k_2,k_3}}{m_2} & (-1)^{k_2+k_3+1} k_3^2 \frac{V^{k_2,k_3}}{m_2} \end{pmatrix} \quad (I.17)$$

and its eigenvalues (I.7) are too convoluted to be solved for, e. g., $\frac{V^{k_1,0}}{m_1}$ and $\frac{V^{k_2,k_3}}{m_2}$. Therefore, these equations have to be solved numerically together with the remaining equations from other phase-space properties like volumes and areas of the resonance mentioned in section 4.4.6.

Note that a canonical transformation with a generating function similar to equation (3.13) – where we set $\mathbf{I}_{\text{res}} = \mathbf{0}$ and the rows of μ to $(k_1, 0)$ and (k_2, k_3) – is not helpful as it simply shifts the coupling to $\underline{\mathcal{H}}$. It is also important to keep in mind the periodicity of θ if the Hamiltonian is further transformed. These transformations should always be done in a way such that the new angles are again 2π -periodic. This is for example possible by using unimodular matrices, i. e. matrices with only integer entries but determinant one. Such transformation yield again the right periodicity. If transformations yield non- 2π -periodic coordinates then the quantum mechanical eigenfunctions of the unperturbed part of equation (I.1) do not have the form given in equation (4.43).

J. Iterative diagonalization schemes for the semiclassical limit

In order to examine quantum mechanical eigenstates in the semiclassical limit, it is necessary to decrease the value of the effective Planck's constant $1/\hbar \rightarrow \infty$. Although our aim is to diagonalize the discretized version of the time evolution operator U , it is not necessary to first create the matrix $\underline{\mathbf{U}}$ and diagonalizing it afterwards. We can circumvent this by exploiting that the action of U on a vector $|\psi\rangle$ can also be expressed by calculating a Fourier transform according to the split-operator like ansatz in equation (4.2). The main drawback is that the algorithms used to determine the eigenstates of U are now iterative algorithms whose convergence is not always guaranteed.

Inverse iteration

Given that we know a good approximation z_0 of an eigenvalue of U then it is possible to calculate the corresponding eigenvector via inverse iteration [192]. Starting from a random initial vector $|\psi_0\rangle$ we have to solve

$$(U - z_i) |\phi_{i+1}\rangle = |\psi_i\rangle \quad (J.1)$$

iteratively for $i = 0, 1, 2, \dots$ by setting the inhomogeneity to $|\psi_{i+1}\rangle = |\phi_{i+1}\rangle / \|\phi_{i+1}\|$ in the next step. The eigenvalue is updated according to $z_{i+1} = z_i + 1.0 / \langle \psi_i | \phi_{i+1} \rangle$. In order to avoid the creation

of the matrix \underline{U} , equation (J.1) has to be solved iteratively. Although U and U^{-1} can be applied to $|\psi\rangle$ very efficiently using FFT algorithms, it is not possible to solve equation (J.1) for $|\phi_{i+1}\rangle$ in the same efficient way. In order to obtain $|\phi_{i+1}\rangle$ we use an iterative solver for sparse linear systems because these methods only need the mapping $|\psi\rangle \mapsto (U - z_i)|\psi\rangle$ in order to solve equation (J.1). The drawback is that the solvers have to apply U very often to determine the solution of equation (J.1) and thereby one step of the inverse iteration. We used the solver BICGSTAB [189]. Therefore, even if only ten steps of the inverse iteration are necessary, we will still have to apply U very often depending on $1/h$. This makes the inverse iteration inappropriate for the maps we consider here. The same reasoning applies for the “shift and invert” method of the Arnoldi method mentioned above because there a linear equation similar to equation (J.1) has to be solved.

Arnoldi method

For open systems we can use the Arnoldi method [178] to calculate the largest eigenvalues and corresponding eigenvectors. This method does not converge for closed systems as there all eigenvalues have a modulus of one and are thereby not well separated from each other. It is also possible to determine eigenvalues close to a given complex number z_0 but this so-called “shift and invert” method requires to solve the linear system $(U - z_0)|\psi\rangle = |\chi\rangle$ with given $|\chi\rangle$. While we are able to perform $U|\psi\rangle$ and $U^{-1}|\psi\rangle$ we cannot simply invert $U - z_0$ as mentioned for the inverse iteration.

Lanczos algorithm

Based on reference [173] we can use the Lanczos algorithm in order to diagonalize the time-evolution operator U . As this algorithm is only applicable to Hermitian matrices we cannot apply it to U directly. We rather use the matrix $H = U + U^\dagger$ which is Hermitian and has the eigenvalues $2\cos(\varphi)$ if the eigenvalues of U are given by $e^{i\varphi}$. As U and H commute they also possess a common set of eigenvectors. We can calculate the eigenvectors of H and later determine if they are also eigenvectors of U , which is the case as long as the eigenvalues are not degenerate.

The Lanczos algorithm for the Hermitian matrix H iteratively creates a $N_{\text{Lanczos}} \times N_{\text{Lanczos}}$ tridiagonal matrix $L_{N_{\text{Lanczos}}}$ which can be diagonalized efficiently by, for example, using LAPACK’s routine for real symmetric tridiagonal matrices `dstvrr`. The creation of the tridiagonal matrix done by choosing an initial vector $|\phi_1\rangle$ together with the definitions $|\omega_0\rangle = |\phi_0\rangle = 0$. Then we perform the following iteration for $j = 1, 2, \dots, N_{\text{Lanczos}}$

$$\begin{aligned}
 |\omega_j\rangle &\leftarrow H|\phi_j\rangle \\
 \alpha_j &\leftarrow \langle \phi_j | \omega_j \rangle \\
 \beta_j &\leftarrow \langle \phi_j | \omega_{j-1} \rangle \\
 |\phi_{j+1}\rangle &\leftarrow |\omega_j\rangle - \alpha_j|\phi_j\rangle - \beta_j|\phi_{j-1}\rangle \\
 |\phi_{j+1}\rangle &\leftarrow |\phi_{j+1}\rangle / \|\phi_{j+1}\rangle
 \end{aligned} \tag{J.2}$$

where the arrow indicates an assignment in the sense of a programming language. Note that due to

H being Hermitian the quantities α_j and β_j are real. They build up the real-symmetric tridiagonal matrix $L_{N_{\text{Lanczos}}}$

$$L_{N_{\text{Lanczos}}} = \begin{pmatrix} \alpha_1 & \beta_2 & & & & \\ \beta_2 & \alpha_2 & \beta_3 & & & \\ & \beta_3 & \alpha_3 & \ddots & & \\ & & \ddots & \ddots & & \\ & & & & \beta_{N_{\text{Lanczos}}} & \\ & & & \beta_{N_{\text{Lanczos}}} & & \alpha_{N_{\text{Lanczos}}} \end{pmatrix}. \quad (\text{J.3})$$

To set up this matrix it is only necessary to apply H repeatedly. The size of the matrix must fulfill $N_{\text{Lanczos}} \geq \mathcal{N}$ with \mathcal{N} being the matrix size of U and H to ensure that the eigenvalues of H are in the spectrum of $L_{N_{\text{Lanczos}}}$ as well. After the creation of $L_{N_{\text{Lanczos}}}$ we diagonalize this matrix to obtain some of the eigenvalues $\cos(\varphi)$ and eigenvectors $|v_{\cos}\rangle$. The fact that we concentrate on a few eigenvectors is necessary because we want to use matrix sizes \mathcal{N} for U which are much too large to fit into the computers memory. Therefore, we are not able to store all eigenvectors at a time.

If we have calculated a couple of eigenvectors $|v_{\cos}\rangle$, we have to transform them back to the position-space representation of the original system H . As the transformation from H to $L_{N_{\text{Lanczos}}}$ is given by the vectors $|\phi_j\rangle$ calculated to obtain $L_{N_{\text{Lanczos}}}$

$$ML_{N_{\text{Lanczos}}}M^\dagger = H \quad \text{with} \quad M = (\phi_1|\phi_2|\dots|\phi_{N_{\text{Lanczos}}}) \quad (\text{J.4})$$

we could have saved all these intermediate vectors and apply the inverse transformation. But as the memory again is not large enough to store these intermediate steps, we have to perform the loop in equation (J.2) again to calculate the columns of M iteratively and calculate the eigenvectors of H from the subset of eigenvectors of $L_{N_{\text{Lanczos}}}$, $\{|v_{\cos}\rangle\}$. Note that the transformation is given by M and M^\dagger as the columns of M are orthogonal vectors which can easily be seen from (J.2) by induction. Hence the transformation on the eigenvectors is given by

$$|\phi\rangle = M|v_{\cos}\rangle \quad \text{and the inverse} \quad |v_{\cos}\rangle = M^\dagger|\phi\rangle. \quad (\text{J.5})$$

Therefore the calculation of eigenvectors of U in the semiclassical limit basically needs two time consuming operations: The creation of $L_{N_{\text{Lanczos}}}$ – which for a given initial vector only has to be done once because we can store it to disk – and the transformation of the eigenvectors of $L_{N_{\text{Lanczos}}}$, $|v_{\cos}\rangle$, to the eigenvectors of H and U , $|\phi\rangle$. If we have the eigenvectors of U we can easily determine the corresponding eigenvalue by the application of U – we just divide the largest entry in $U|\phi\rangle$ by the corresponding value of $|\phi\rangle$.

$$e^{i\varphi} = \langle \mathbf{q}_I | U\phi \rangle / \langle \mathbf{q}_I | \phi \rangle \quad \text{with } I \text{ such that} \quad |\langle \mathbf{q}_I | \phi \rangle| = \max \{ |\langle \mathbf{q}_i | \phi \rangle|, i = 1, \dots, N_{\text{Lanczos}} \}. \quad (\text{J.6})$$

In order to determine eigenstates being supported on regions of interest in phase space we have to select the most relevant eigenvectors of $L_{N_{\text{Lanczos}}}$. This is done by choosing the initial state $|\phi_1\rangle$

close to the state we want to obtain. One possibility is given by coherent states placed at interesting classical structures like inside the stochastic region, see figure 4.12 for an example. Another choice is to set up $|\phi_1\rangle$ as a direct product of eigenstates of 2D maps like in figure 4.16. In the basis where $L_{N_{\text{Lanczos}}}$ is tridiagonal the initial vector is given by the unit vector being zero at every index except for the first entry. Therefore, the first entry of the eigenvectors of $L_{N_{\text{Lanczos}}}$ represent the overlap of the eigenstate with the initial vector. Thus, the eigenstates of U which are of interest are given by the eigenvectors of $L_{N_{\text{Lanczos}}}$ with the largest first component. The tridiagonal matrix can be diagonalized in parallel efficiently. During this calculation all eigenvectors are calculated but only the ones with the largest first component are kept and then transformed back to the position-space representation.

List of Figures

2.1. Phase-space portraits of the 2D standard map for several K	7
3.1. Stability ranges of periodic orbits expressed by the linearization	14
3.2. Overview of resonance structures in 4D maps	16
3.3. Frequency map \mathcal{F} for near-integrable coupled standard maps	29
3.4. Wavelet representations for coupled standard maps	32
3.5. Contour plot of the potential energy of the designed map \mathcal{P}_{llu}	37
3.6. Section of the designed map with linear regular region, \mathcal{P}_{llu}	39
3.7. Skew phase-space section for \mathcal{P}_{llu}	40
3.8. Histogram of FLI values for \mathcal{P}_{llu}	41
3.9. Section of the designed map \mathcal{P}_{llu} including FLI values	42
3.10. Frequency map \mathcal{F} for the transition $\mathcal{P}_{\text{llu}} \rightarrow \mathcal{P}_{\text{nnc}}$	47
3.11. Section of the designed map \mathcal{P}_{nnc}	49
3.12. Histogram of FLI values for \mathcal{P}_{nnc}	50
3.13. Section of the designed map \mathcal{P}_{nnc} including FLI surfaces	51
3.14. Frequency map \mathcal{F} for the main rank-2 period-5 resonance of \mathcal{P}_{nnc}	52
3.15. Sections at various p_2 values for \mathcal{P}_{nnc}	54
3.16. Sections at various p_1 values for \mathcal{P}_{nnc}	55
3.17. Projection of 4D orbits of \mathcal{P}_{nnc} using colors	56
3.18. Skew and perpendicular sections for \mathcal{P}_{nnc} : orbits on tangential planes	59
3.19. Skew and perpendicular sections for \mathcal{P}_{nnc} : initial cond. along 1 st degree of freedom	60
3.20. Skew and perpendicular sections for \mathcal{P}_{nnc} : initial cond. along 2 nd degree of freedom	61
3.21. Skew and perpendicular sections for \mathcal{P}_{nnc} : orbit in the stochastic layer	62
3.22. Histogram of FLI values for \mathcal{P}_{csm}	64
3.23. Phase-space section of \mathcal{P}_{csm} including FLI values	65
3.24. Chaotic orbit penetrating the stochastic layer of \mathcal{P}_{csm}	66
3.25. Frequency map \mathcal{F} for \mathcal{P}_{csm}	67
3.26. Frequency map \mathcal{F} for the main rank-2 period-4 resonance for \mathcal{P}_{csm}	67
3.27. Wavelets L_ψ for \mathcal{P}_{csm} and $\mathcal{P}_{\text{csm}}^4$ for a sub-resonance	68
3.28. Skew and perpendicular sections for \mathcal{P}_{csm} : orbits on tangential planes	70
3.29. Skew and perpendicular sections for \mathcal{P}_{csm} : rank-1 sub-resonance	71
3.30. Skew and perpendicular sections for \mathcal{P}_{csm} : orbit in the stochastic layer	72

4.1. Eigenstate $\psi_{\text{reg}}^{0,0}$ of \mathcal{P}_{llu} for $1/h = 50$	81
4.2. Eigenstate $\psi_{\text{reg}}^{1,0}$ of \mathcal{P}_{llu} for $1/h = 50$	81
4.3. Eigenstate $\psi_{\text{reg}}^{0,1}$ of \mathcal{P}_{llu} for $1/h = 50$	82
4.4. Eigenstate $\psi_{\text{reg}}^{1,1}$ of \mathcal{P}_{llu} for $1/h = 50$	83
4.5. Eigenstate $\psi_{\text{reg}}^{5,3}$ of \mathcal{P}_{llu} for $1/h = 50$	83
4.6. Chaotic eigenstate of \mathcal{P}_{llu} for $1/h = 50$	84
4.7. Eigenstate $\psi_{\text{reg}}^{5,3}$ of \mathcal{P}_{llu} for $1/h = 90$	85
4.8. Chaotic eigenstate of \mathcal{P}_{llu} for $1/h = 90$	85
4.9. Eigenstate $\psi_{\text{reg}}^{0,0}$ of \mathcal{P}_{nnc} for $1/h = 50$	86
4.10. Eigenstate $\psi_{\text{reg}}^{5,3}$ of \mathcal{P}_{nnc} for $1/h = 50$	87
4.11. Eigenstate ψ_{reg} of \mathcal{P}_{nnc} for $1/h = 300$ on resonance chain	88
4.12. Eigenstate ψ_{reg} of \mathcal{P}_{nnc} for $1/h = 300$ on stochastic part	88
4.13. Eigenstate $\psi_{\text{reg}}^{0,0}$ of \mathcal{P}_{csm} for $1/h = 50$	89
4.14. Comparison of quantum resolution and size of the stochastic layer of \mathcal{P}_{csm}	91
4.15. Eigenstates of the 2D standard map: initial states of the Lanczos algorithm	92
4.16. Eigenstate of \mathcal{P}_{csm} for $1/h = 1000$	93
4.17. Time evolution of wave packets into the stochastic layer	95
4.18. Position dependent Husimi weight along paths in phase space.	96
4.19. Scaling of the negative intrusion depth $1 - \lambda_{1/2}$ with $1/h$	97
4.20. Average FLI values on position space for \mathcal{P}_{llu}	102
4.21. Numerically determined direct regular-to-chaotic tunneling rates γ^d for \mathcal{P}_{llu}	102
4.22. Prediction of direct regular-to-chaotic tunneling rates γ^d for \mathcal{P}_{llu}	104
4.23. Average FLI values on position space for \mathcal{P}_{nnc}	105
4.24. Numerically determined regular-to-chaotic tunneling rates γ for \mathcal{P}_{nnc}	106
4.25. Possible connections between two regular quantum states via RAT in \mathcal{P}_{nnc}	113
4.26. Possible tunneling paths at $1/h = 90$	114
4.27. Tunneling rates and spectrum for \mathcal{P}_{nnc}	115
4.28. Prediction of tunneling rates using RAT	119
4.29. Average FLI values in position space for \mathcal{P}_{csm}	120
4.30. Tunneling rates for \mathcal{P}_{csm}	121
B.1. Assignment of quantum numbers in the spectrum of \mathcal{P}_{nnc}	130
C.1. Possible tunneling paths at $1/h = 50$ and $1/h = 130$	131
C.2. Alternative tunneling paths Γ based on different resonance vectors $\mathbf{r}^{a,b}$	132
D.1. RAT prediction based on a different basis of \mathcal{L}	134
E.1. Tunneling rates of the nonlinear map with uncoupled regular region.	134
E.2. Eigenphases φ for the ground state.	135
F.1. Fit of φ based on 2 nd derivative of a spline interpolation.	136
G.1. 2D Poincaré map of the pendulum approximation of a rank-2 resonance	138
H.1. RAT prediction of $\gamma_{0,3}$ for \mathcal{P}_{nnc} showing contributions by single tunneling paths Γ	139

Bibliography

- [1] A. N. Kolmogorov: *Preservation of conditionally periodic movements with small change in the Hamilton function* (in Russian), Dokl. Akad. Nauk. SSSR **98** (1954), 527–530, English translation in [193], 51–56. Cited on pages 1 and 8.
- [2] V. I. Arnold: *Proof of a theorem of A. N. Kolmogorov on the invariance of quasi-periodic motions under small perturbations of the Hamiltonian*, Russ. Math. Surv. **18** (1963), 9–36. Cited on pages 1 and 8.
- [3] J. Moser: *On invariant curves of area-preserving mappings of an annulus*, Nachr. Akad. Wiss. Göttingen **1** (1962), 1–20. Cited on pages 1 and 8.
- [4] E. Ott: *Chaos in Dynamical Systems*, (Cambridge University Press, The Pitt Building, Trumpington Street, Cambridge, United Kingdom), 2nd edn., (2002). Cited on pages 1 and 15.
- [5] L. Markus and K. R. Meyer: *Generic Hamiltonian Dynamical Systems are neither Integrable nor Ergodic*, no. 144 in Mem. Amer. Math. Soc., (American Mathematical Society, Providence, Rhode Island), (1974). Cited on page 1.
- [6] B. V. Chirikov: *A universal instability of many-dimensional oscillator systems*, Phys. Rep. **52** (1979), 263–379. Cited on pages 1, 2, 5, 7, 11, 18, 20, 23, 24, 25, 28, 90, 97, 110, 113, and 116.
- [7] J. M. Greene: *A method for determining a stochastic transition*, J. Math. Phys. **20** (1979), 1183–1201. Cited on pages 1, 8, and 11.
- [8] N. Friedman, A. Kaplan, D. Carasso, and N. Davidson: *Observation of Chaotic and Regular Dynamics in Atom-Optics Billiards*, Phys. Rev. Lett. **86** (2001), 1518–1521. Cited on page 1.
- [9] A. Kaplan, N. Friedman, M. Andersen, and N. Davidson: *Observation of Islands of Stability in Soft Wall Atom-Optics Billiards*, Phys. Rev. Lett. **87** (2001), 274101. Cited on page 1.
- [10] J. Feist, A. Bäcker, R. Ketzmerick, S. Rotter, B. Huckestein, and J. Burgdörfer: *Nanowires with Surface Disorder: Giant Localization Lengths and Quantum-to-Classical Crossover*, Phys. Rev. Lett. **97** (2006), 116804. Cited on pages 1 and 11.
- [11] J. Feist, A. Bäcker, R. Ketzmerick, J. Burgdörfer, and S. Rotter: *Nanowires with surface disorder: Giant localization length and dynamical tunneling in the presence of directed chaos*, Phys. Rev. B **80** (2009), 245322. Cited on pages 1, 3, 75, 98, and 99.

-
- [12] S. Udry and D. Pfenniger: *Stochasticity in elliptical galaxies*, *Astron. Astrophys.* **198** (1988), 135–149. Cited on pages 1, 11, and 33.
- [13] J. Laskar: *The chaotic motion of the solar system: A numerical estimate of the size of the chaotic zones*, *Icarus* **88** (1990), 266–291. Cited on pages 1 and 26.
- [14] D. Merritt and M. Valluri: *Chaos and Mixing in Triaxial Stellar Systems*, *Astrophys. J.* **471** (1996), 82 – 105. Cited on pages 1, 11, and 33.
- [15] D. Merritt and T. Fridman: *Triaxial Galaxies with Cusps*, *Astrophys. J.* **460** (1996), 136–162. Cited on page 1.
- [16] P. M. Cincotta: *Arnold diffusion: an overview through dynamical astronomy*, *New Astron. Rev.* **46** (2002), 13–39. Cited on pages 1 and 2.
- [17] G. Jacucci, M. Toller, G. DeLorenzi, and C. P. Flynn: *Rate Theory, Return Jump Catastrophes, and the Center Manifold*, *Phys. Rev. Lett.* **52** (1984), 295–298. Cited on page 1.
- [18] C. W. J. Beenakker and H. van Houten: *Billiard model of a ballistic multiprobe conductor*, *Phys. Rev. Lett.* **63** (1989), 1857–1860. Cited on page 1.
- [19] K. Richter and D. Wintgen: *Stable planetary atom configurations*, *Phys. Rev. Lett.* **65** (1990), 1965–1965. Cited on pages 1, 35, 89, and 99.
- [20] P. Schlagheck and A. Buchleitner: *Stable classical configurations in strongly driven helium*, *Physica D* **131** (1999), 110–124. Cited on pages 1 and 99.
- [21] H. Waalkens, R. Schubert, and S. Wiggins: *Wigner’s dynamical transition state theory in phase space: classical and quantum*, *Nonlinearity* **21** (2008), R1–R118. Cited on pages 1, 13, and 14.
- [22] V. I. Arnold: *Instability of dynamical systems with several degrees of freedom*, *Sov. Math. Dokl.* **6** (1964), 581–585. Cited on pages 2, 11, and 24.
- [23] V. I. Arnold and A. Avez: *Ergodic Problems of Classical Mechanics*, (Addison-Wesley, Weinheim), (1989). Cited on pages 2 and 24.
- [24] B. Chirikov, E. Keil, and A. Sessler: *Stochasticity in Many-Dimensional Nonlinear Oscillating Systems*, *J. Stat. Phys.* **3** (1971), 307–321. Cited on page 2.
- [25] G. M. Zaslavskii and B. V. Chirikov: *Stochastic Instability of Non-linear Oscillations*, *Sov. Phys. Usp.* **14** (1972), 549–568. Cited on page 2.
- [26] C. Froeschlé and J.-P. Scheidecker: *On the Disappearance of Isolating Integrals in Dynamical Systems with More than Two Degrees of Freedom*, *Astrophysics and Space Science* **25** (1973), 373–386. Cited on pages 2 and 12.

- [27] M. A. Lieberman: *Arnold diffusion in Hamiltonian systems with three degrees of freedom*, Annals of the New York Academy of Sciences **357** (1980), 119–142. Cited on page 2.
- [28] B. V. Chirikov, J. Ford, and F. Vivaldi: *Some numerical studies on arnold diffusion in a simple model*, in: *American Institute of Physics Conference Series*, vol. 57 of *American Institute of Physics Conference Series*, 323–340, (1980). Cited on page 2.
- [29] B. V. Chirikov, M. A. Lieberman, D. L. Shepelyansky, and F. M. Vivaldi: *A theory of modulational diffusion*, Physica D **14** (1985), 289–304. Cited on page 2.
- [30] K. Kaneko and R. J. Bagley: *Arnold Diffusion, Ergodicity, and Intermittency in Coupled Standard Mapping*, Phys. Lett. **110A** (1985), 435–440. Cited on page 2.
- [31] C. Marchal and F. Rannou-Montigny: *A small example of Arnold diffusion*, Celest. Mech. Dyn. Astr. **43** (1987), 177–184. Cited on page 2.
- [32] L. A. Bunimovich: *Many-dimensional nowhere dispersing billiards with chaotic behavior*, Physica D **33** (1988), 58–64. Cited on page 2.
- [33] K. Kaneko and T. Konishi: *Diffusion in Hamiltonian dynamical systems with many degrees of freedom*, Phys. Rev. A **40** (1989), 6130–6133. Cited on page 2.
- [34] H.-t. Kook and J. D. Meiss: *Diffusion in symplectic maps*, Phys. Rev. A **41** (1990), 4143–4150. Cited on page 2.
- [35] B. P. Wood, A. J. Lichtenberg, and M. A. Lieberman: *Arnold diffusion in weakly coupled standard maps*, Phys. Rev. A **42** (1990), 5885–5893. Cited on pages 2, 12, and 25.
- [36] J. Laskar: *Frequency analysis for multi-dimensional systems: global dynamics and diffusion*, Physica D **67** (1993), 257–281. Cited on pages 2, 27, 28, 29, 30, 66, and 68.
- [37] B. P. Wood, A. J. Lichtenberg, and M. A. Lieberman: *Arnold and Arnold-like diffusion in many dimensions*, Physica D **71** (1994), 132–145. Cited on pages 2, 12, 25, and 63.
- [38] L. Bunimovich, G. Casati, and I. Guarneri: *Chaotic Focusing Billiards in Higher Dimensions*, Phys. Rev. Lett. **77** (1996), 2941–2944. Cited on page 2.
- [39] D. M. Leitner and P. G. Wolynes: *Quantization of the Stochastic Pump Model of Arnold Diffusion*, Phys. Rev. Lett. **79** (1997), 55–58. Cited on page 2.
- [40] C. Simó (ed.): *Hamiltonian Systems with Three or More Degrees of Freedom*, vol. 533 of *NATO ASI Series: C - Mathematical and Physical Sciences*. Kluwer Academic Publishers, (1999). Cited on pages 2, 156, and 157.
- [41] E. Fontich and P. Martín: *Arnold diffusion in perturbations of analytic exact symplectic maps*, Nonlinear Analysis **42** (2000), 1397–1412. Cited on pages 2 and 30.

- [42] S. Honjo and K. Kaneko: *Is Arnold diffusion relevant to global diffusion?*, in: *Over the resonance, 35th Symposium on Celestial Mechanics* (Eds. E. Kokubo, H. Arakida and T. Yamamoto), 367–376, (2003). Cited on pages 2 and 30.
- [43] E. Lega, M. Guzzo, and C. Froeschlé: *Detection of Arnold diffusion in Hamiltonian systems*, *Physica D* **182** (2003), 179–187. Cited on pages 2, 31, and 63.
- [44] C. Efthymiopoulos: *On the connection between the Nekhoroshev theorem and Arnold diffusion*, *Celest. Mech. Dyn. Astr.* **102** (2008), 49–68. Cited on page 2.
- [45] M. Guzzo, E. Lega, and C. Froeschlé: *First numerical evidence of global Arnold diffusion in quasi-integrable systems*, arXiv:nlin/0407059 (2004). Cited on pages 2 and 31.
- [46] A. Seibert, S. Denisov, A. V. Ponomarev, and P. Hänggi: *Mapping the Arnold web with a graphic processing unit*, *Chaos* **21** (2011), 043123. Cited on pages 2 and 27.
- [47] I. C. Percival: *Regular and irregular spectra*, *J. Phys. B - At. Mol. Opt.* **6** (1973), L229–L232. Cited on pages 2, 75, and 80.
- [48] D. M. Leitner and P. G. Wolynes: *Intramolecular energy flow in the condensed phase: effects of dephasing on localization in the quantum stochastic pump model*, *Chem. Phys. Lett.* **276** (1997), 289 – 295. Cited on pages 2 and 89.
- [49] J. Ma and K. Nakamura: *Negative Magneto-Resistance Beyond Weak Localization in Three-Dimensional Billiards: Effect of Arnold Diffusion*, arXiv:cond-mat/0108276 (2001). Cited on pages 2 and 89.
- [50] V. Y. Demikhovskii, F. M. Izrailev, and A. I. Malyshev: *Manifestation of Arnol'd Diffusion in Quantum Systems*, *Phys. Rev. Lett.* **88** (2002), 154101. Cited on pages 2 and 89.
- [51] V. Y. Demikhovskii, F. M. Izrailev, and A. I. Malyshev: *Quantum Arnol'd diffusion in a simple nonlinear system*, *Phys. Rev. E* **66** (2002), 036211. Cited on pages 2, 63, 89, and 92.
- [52] V. Y. Demikhovskii, F. M. Izrailev, and A. I. Malyshev: *Quantum Arnol'd diffusion in a rippled waveguide*, *Physics Letters A* **352** (2006), 491 – 495. Cited on pages 2, 63, 89, and 92.
- [53] A. Malyshev and L. Chizhova: *Arnol'd diffusion in a system with 2.5 degrees of freedom: Classical and quantum mechanical approaches*, *J. Exp. Theor. Phys.+* **110** (2010), 837–844. Cited on pages 2, 63, and 89.
- [54] Y. C. Li: *Arnold Diffusion of the Discrete Nonlinear Schrödinger Equation*, arxiv:math/0607443 (2006). Cited on pages 2 and 89.
- [55] D. M. Basko: *Weak chaos in the disordered nonlinear Schrödinger chain: Destruction of Anderson localization by Arnold diffusion*, *Annals of Physics* **326** (2011), 1577 – 1655. Cited on pages 2 and 89.

- [56] M. J. Davis and E. J. Heller: *Quantum dynamical tunnelling in bound states*, J. Chem. Phys. **75** (1981), 246–254. Cited on pages 3, 75, and 98.
- [57] J. Zakrzewski, D. Delande, and A. Buchleitner: *Ionization via chaos assisted tunneling*, Phys. Rev. E **57** (1998), 1458–1474. Cited on pages 3, 75, and 98.
- [58] A. Buchleitner, D. Delande, and J. Zakrzewski: *Non-dispersive wave packets in periodically driven quantum systems*, Phys. Rep. **368** (2002), 409 – 547. Cited on pages 3, 75, and 98.
- [59] S. Wimberger, P. Schlagheck, C. Eltschka, and A. Buchleitner: *Resonance-Assisted Decay of Nondispersive Wave Packets*, Phys. Rev. Lett. **97** (2006), 043001. Cited on pages 3, 75, 98, and 99.
- [60] E. J. Heller: *Dynamical tunneling and molecular spectra*, J. Phys. Chem. **99** (1995), 23625–23634. Cited on pages 3, 75, and 98.
- [61] S. Keshavamurthy, N. R. Cerruti, and S. Tomsovic: *Analyzing intramolecular vibrational energy redistribution via the overlap intensity-level velocity correlator*, J. Chem. Phys. **117** (2002), 4168 – 4177. Cited on pages 3, 75, and 98.
- [62] S. Keshavamurthy: *Dynamical tunneling in molecules: role of the classical resonances and chaos*, J. Chem. Phys. **119** (2003), 161–164. Cited on pages 3, 75, 76, 98, and 99.
- [63] S. Keshavamurthy: *On dynamical tunneling and classical resonances*, J. Chem. Phys. **122** (2005), 114109. Cited on pages 3, 75, and 98.
- [64] S. Keshavamurthy: *Dynamical tunneling in molecules: quantum routes to energy flow*, Int. Rev. Phys. Chem. **26** (2007), 521–584. Cited on pages 3, 75, 98, and 99.
- [65] H.-D. Gräf, H. L. Harney, H. Lengeler, C. H. Lewenkopf, C. Rangacharyulu, A. Richter, P. Schardt, and H. A. Weidenmüller: *Distribution of eigenmodes in a superconducting stadium billiard with chaotic dynamics*, Phys. Rev. Lett. **69** (1992), 1296–1299. Cited on pages 3, 75, and 98.
- [66] J. U. Nöckel and A. D. Stone: *Ray and wave chaos in asymmetric resonant optical cavities*, Nature **385** (1997), 45–47. Cited on pages 3, 75, and 98.
- [67] C. Dembowski, H.-D. Gräf, A. Heine, R. Hofferbert, H. Rehfeld, and A. Richter: *First Experimental Evidence for Chaos-Assisted Tunneling in a Microwave Annular Billiard*, Phys. Rev. Lett. **84** (2000), 867–870. Cited on pages 3, 75, 98, and 99.
- [68] V. A. Podolskiy and E. E. Narimanov: *Chaos-assisted tunneling in dielectric microcavities*, Opt. Lett. **30** (2005), 474–476. Cited on pages 3, 75, 98, and 99.

- [69] G. Vidmar, H.-J. Stöckmann, M. Robnik, U. Kuhl, R. Höhmann, and S. Grossmann: *Beyond the Berry–Robnik regime: a random matrix study of tunneling effects*, J. Phys. A **40** (2007), 13883. Cited on pages 3, 75, and 98.
- [70] B. Huckestein, R. Ketzmerick, and C. H. Lewenkopf: *Quantum Transport through Ballistic Cavities: Soft vs Hard Quantum Chaos*, Phys. Rev. Lett. **84** (2000), 5504–5507. Cited on pages 3, 75, 98, and 99.
- [71] W. A. Lin and L. E. Ballentine: *Quantum tunneling and chaos in a driven anharmonic oscillator*, Phys. Rev. Lett. **65** (1990), 2927–2930. Cited on pages 3 and 99.
- [72] O. Bohigas, S. Tomsovic, and D. Ullmo: *Manifestations of classical phase space structures in quantum mechanics*, Phys. Rep. **223** (1993), 43–133. Cited on pages 3, 75, and 129.
- [73] O. Bohigas, D. Boosé, R. E. de Carvalho, and V. Marvulle: *Quantum tunneling and chaotic dynamics*, Nuclear Physics A **560** (1993), 197 – 210. Cited on pages 3 and 75.
- [74] R. Roncaglia, L. Bonci, F. M. Izrailev, B. J. West, and P. Grigolini: *Tunneling versus Chaos in the Kicked Harper Model*, Phys. Rev. Lett. **73** (1994), 802–805. Cited on pages 3 and 75.
- [75] E. Doron and S. D. Frischat: *Semiclassical description of tunneling in mixed systems: the case of the annular billiard*, Phys. Rev. Lett. **75** (1995), 3661–3664. Cited on pages 3 and 75.
- [76] S. D. Frischat and E. Doron: *Dynamical tunneling in mixed systems*, Phys. Rev. E **57** (1998), 1421–1443. Cited on pages 3, 75, and 99.
- [77] V. A. Podolskiy and E. E. Narimanov: *Semiclassical description of chaos-assisted tunneling*, Phys. Rev. Lett. **91** (2003), 263601 (4 pages). Cited on pages 3, 75, and 99.
- [78] A. Bäcker, R. Ketzmerick, S. Löck, and L. Schilling: *Regular-to-Chaotic Tunneling Rates Using a Fictitious Integrable System*, Phys. Rev. Lett. **100** (2008), 104101. Cited on pages 3, 36, 75, 99, 101, 103, 104, 107, 110, and 124.
- [79] A. Bäcker, R. Ketzmerick, and S. Löck: *Direct regular-to-chaotic tunneling rates using the fictitious-integrable-system approach*, Phys. Rev. E **82** (2010), 056208. Cited on pages 3, 75, 98, 99, 100, 103, 104, 105, 108, 110, 111, and 113.
- [80] R. Hofferbert, H. Alt, C. Dembowski, H.-D. Gräf, H. L. Harney, A. Heine, H. Rehfeld, and A. Richter: *Experimental investigations of chaos-assisted tunneling in a microwave annular billiard*, Phys. Rev. E **71** (2005), 046201. Cited on pages 3 and 99.
- [81] A. Bäcker, R. Ketzmerick, S. Löck, M. Robnik, G. Vidmar, R. Höhmann, U. Kuhl, and H.-J. Stöckmann: *Dynamical Tunneling in Mushroom Billiards*, Phys. Rev. Lett. **100** (2008), 174103. Cited on pages 3, 75, 99, 103, and 104.

- [82] A. Bäcker, R. Ketzmerick, S. Löck, J. Wiersig, and M. Hentschel: *Quality factors and dynamical tunneling in annular microcavities*, Phys. Rev. A **79** (2009), 063804. Cited on pages 3, 11, 75, 99, 103, and 104.
- [83] O. Brodier, P. Schlagheck, and D. Ullmo: *Resonance-Assisted Tunneling in Near-Integrable Systems*, Phys. Rev. Lett. **87** (2001), 64101. Cited on pages 3, 18, 76, 99, and 106.
- [84] O. Brodier, P. Schlagheck, and D. Ullmo: *Resonance-Assisted Tunneling*, Ann. Phys. **300** (2002), 88–136. Cited on pages 3, 21, 76, 99, 106, and 135.
- [85] A. M. Ozorio de Almeida: *Hamiltonian Systems: Chaos and Quantization*, (Cambridge University Press, Cambridge), (1988). Cited on pages 5, 13, 35, and 140.
- [86] B. V. Chirikov: *Research concerning the theory of non-linear resonance and stochasticity*, (CERN, Geneva), (1971), Translated at CERN from the Russian Preprint N 267, Institute of Nuclear Physics, Novosibirsk (1969). Cited on page 7.
- [87] H. G. Schuster: *Deterministic Chaos: An Introduction*, (VCH, Weinheim), (1988). Cited on pages 8, 13, and 16.
- [88] J. Meiss: *Symplectic maps, variational principles, and transport*, Rev. Mod. Phys. **64** (1992), 795–848. Cited on page 8.
- [89] A. J. Lichtenberg and M. A. Liebermann: *Regular and chaotic dynamics*, (Springer-Verlag, New York), 2nd edn., (1992). Cited on pages 11, 13, 15, 21, 25, and 35.
- [90] C. Skokos, G. Contopoulos, and C. Polymilis: *Structures in the Phase Space of a Four Dimensional Symplectic Map*, Celest. Mech. Dyn. Astr. **65** (1997), 223–251. Cited on pages 11 and 33.
- [91] P. A. Patsis and L. Zachilas: *Using color and rotation for visualizing four-dimensional Poincaré cross-sections: With applications to the orbital behavior of a three-dimensional Hamiltonian system*, Int. J. Bifurcat. Chaos **4** (1994), 1399–1424. Cited on pages 11 and 53.
- [92] M. Katsanikas and P. A. Patsis: *The Structure of Invariant Tori in a 3D Galactic Potential*, Int. J. Bifurcat. Chaos **21** (2011), 467–496. Cited on pages 11, 33, and 53.
- [93] C. Froeschlé and J. Scheidecker: *Numerical study of the stochasticity of dynamical systems with more than two degrees of freedom*, J. Comput. Phys. **11** (1973), 423–439. Cited on page 12.
- [94] C. Froeschlé and J. Scheidecker: *Numerical Study of a Four-Dimensional Mapping. II.*, Astron. Astrophys. **22** (1973), 431–436. Cited on page 12.
- [95] G. Contopoulos: *A Classification of the Integrals of Motion.*, Astrophys. J. **138** (1963), 1297–1305. Cited on page 12.

- [96] C. Froeschlé: *On the number of isolating integrals in systems with three degrees of freedom*, *Astrophysics and Space Science* **14** (1971), 110–117. Cited on page 12.
- [97] S. M. Graff: *On the conservation of hyperbolic invariant tori for Hamiltonian systems*, *J. Differ. Equations* **15** (1974), 1–69. Cited on page 12.
- [98] E. Zehnder: *Generalized implicit function theorems with applications to some small divisor problems, II*, *Commun. Pure Appl. Math.* **29** (1976), 49–111. Cited on page 12.
- [99] J. Pöschel: *On elliptic lower dimensional tori in hamiltonian systems*, *Math. Z.* **202** (1989), 559–608. Cited on page 12.
- [100] M. Gemmi and E. Todesco: *Stability and geometry of third-order resonances in four-dimensional symplectic mappings*, *Celest. Mech. Dyn. Astr.* **67** (1997), 181–204. Cited on pages 12, 16, and 24.
- [101] S. Honjo and K. Kaneko: *Structure of Resonances and Transport in Multi-dimensional Hamiltonian Dynamical Systems*, in: *Geometric Structures of Phase Space in Multidimensional Chaos*, 437–463. John Wiley & Sons, Inc., (2005). Cited on pages 12, 27, and 30.
- [102] J. E. Howard and R. S. MacKay: *Linear stability of symplectic maps*, *J. Math. Phys.* **28** (1987), 1036–1051. Cited on pages 13 and 14.
- [103] J. E. Howard and R. S. Mackay: *Calculation of linear stability boundaries for equilibria of Hamiltonian systems*, *Physics Letters A* **122** (1987), 331–334. Cited on page 13.
- [104] D. K. Arrowsmith and C. M. Place: *An introduction to dynamic systems*, (Cambridge University Press, Cambridge), (1990). Cited on pages 14, 34, and 69.
- [105] À. Haro: *Center and center-(un)stable manifolds of elliptic-hyperbolic fixed points of 4D-symplectic maps. An example: The Froeschlé map*, in: Simó [40], 403–407. Cited on pages 14 and 69.
- [106] S. Wiggins: *Normally Hyperbolic Invariant Manifolds in Dynamical Systems*, (Springer-Verlag, New York), (1994). Cited on page 14.
- [107] E. Todesco: *Analysis of resonant structures of four-dimensional symplectic mappings, using normal forms*, *Phys. Rev. E* **50** (1994), R4298–R4301. Cited on pages 16, 18, 24, 53, 63, and 110.
- [108] J. D. Meiss: *The destruction of tori in volume-preserving maps*, *Commun. Nonlinear Sci.* **17** (2012), 2108–2121. Cited on pages 17, 27, 28, 30, and 53.
- [109] S. Lange: *Trapping of chaotic orbits in 4D symplectic maps*, Diplomarbeit, Technische Universität Dresden, Fachrichtung Physik (2012). Cited on pages 18, 27, 57, 65, 66, and 69.

- [110] P. Schlagheck: *Resonance-assisted tunneling in systems with many degrees of freedom*, private communication (MPIPKS: Advanced Study Group 2011: Towards a Semiclassical Theory of Dynamical Tunneling). Cited on pages 21 and 119.
- [111] G. Turchetti and A. Bazzani: *Normal forms for symplectic maps*, in *Advances in Nonlinear dynamics and stochastic processes II*, G. Paladin and A. Vulpiani (eds.), World Scientific, Singapore, New Jersey, Hong Kong (1987), 25–36. Cited on page 24.
- [112] A. Bazzani, M. Giovannozzi, and E. Todesco: *A program to compute Birkhoff normal forms of symplectic maps in \mathbb{R}^4* , Comput. Phys. Commun. **86** (1995), 199–207. Cited on page 24.
- [113] E. Todesco, M. Gemmi, and M. Giovannozzi: *NERO: a code for the Nonlinear Evaluation of Resonances in One-turn mappings*, Comput. Phys. Commun. **106** (1997), 169–180. Cited on page 24.
- [114] P. Lochack: *Arnold diffusion; a compendium of remarks and questions*, in: Simó [40], 168–183. Cited on page 24.
- [115] G. Benettin, L. Galgani, A. Giorgilli, and J.-M. Strelcyn: *Lyapunov Characteristic Exponents for smooth dynamical systems and for hamiltonian systems; a method for computing all of them. Part 1: Theory*, Meccanica **15** (1980), 9–20. Cited on page 26.
- [116] G. Benettin, L. Galgani, A. Giorgilli, and J.-M. Strelcyn: *Lyapunov Characteristic Exponents for smooth dynamical systems and for hamiltonian systems; A method for computing all of them. Part 2: Numerical application*, Meccanica **15** (1980), 21–30. Cited on page 26.
- [117] C. Skokos: *Alignment indices: a new, simple method for determining the ordered or chaotic nature of orbits*, J. Phys. A **34** (2001), 10029. Cited on page 26.
- [118] C. Skokos, C. Antonopoulos, T. C. Bountis, and M. N. Vrahatis: *Detecting order and chaos in Hamiltonian systems by the SALI method*, J. Phys. A **37** (2004), 6269. Cited on page 26.
- [119] T. Manos, C. Skokos, and T. Bountis: *Global dynamics of coupled standard maps*, preprint nlin.CD/08013923 (2008). Cited on page 26.
- [120] G. Contopoulos and N. Voglis: *A fast method for distinguishing between ordered and chaotic orbits.*, Astron. Astrophys. **317** (1997), 73–81. Cited on page 26.
- [121] C. Froeschlé and E. Lega: *Twist angles: a method for distinguishing islands, tori and weak chaotic orbits. Comparison with other methods of analysis*, Astron. Astrophys. **334** (1998), 355–362. Cited on page 26.
- [122] N. Voglis, G. Contopoulos, , and C. Efthymiopoulos: *Method for distinguishing between ordered and chaotic orbits in four-dimensional maps*, Phys. Rev. E **57** (1998), 372–377. Cited on page 26.

- [123] Cincotta, P. M. and Simó, C.: *Simple tools to study global dynamics in non-axisymmetric galactic potentials - I*, *Astron. Astrophys. Sup.* **147** (2000), 205–228. Cited on page 26.
- [124] P. M. Cincotta, C. M. Giordano, and C. Simó: *Phase space structure of multi-dimensional systems by means of the mean exponential growth factor of nearby orbits*, *Physica D* **182** (2003), 151 – 178. Cited on page 26.
- [125] S. Löck: *Dynamical Tunneling in Systems with a Mixed Phase Space*, Dissertation, Technische Universität Dresden, Fachrichtung Physik (2010). Cited on pages 26, 63, 100, 116, and 119.
- [126] E. Lega and C. Froeschlé: *Numerical investigations of the structure around an invariant KAM torus using the frequency map analysis*, *Physica D* **95** (1996), 97–106. Cited on page 26.
- [127] C. Martens, M. Davis, and G. Ezra: *Local frequency analysis of chaotic motion in multidimensional systems: energy transport and bottlenecks in planar OCS*, *Chem. Phys. Lett.* **142** (1987), 519–528. Cited on pages 26 and 27.
- [128] J. Laskar: *Frequency analysis of a dynamical system*, *Celest. Mech. Dyn. Astr.* **56** (1993), 191–196. Cited on pages 26 and 27.
- [129] L. Vela-Arevalo and S. Wiggins: *Time-frequency analysis of classical trajectories of polyatomic molecules*, *Int. J. Bifurcat. Chaos* **11** (2001), 1359–1380. Cited on pages 26, 27, 28, 30, and 65.
- [130] C. Chandre, S. Wiggins, and T. Uzer: *Time-frequency analysis of chaotic systems*, *Physica D* **181** (2003), 171–196. Cited on pages 26, 27, 30, 65, and 66.
- [131] C. Martens, M. Davis, and G. Ezra: *Pathways for Energy Redistribution and Phase Space Bottlenecks in Many-Dimensional Systems*, unpublished, see http://www.chem.cornell.edu/gse1/ocs_2.pdf. Cited on page 26.
- [132] M. Comunian, A. Pisent, A. Bazzani, G. Turchetti, and S. Rambaldi: *Frequency map analysis of a three-dimensional particle in the core model of a high intensity linac*, *Phys. Rev. ST Accel. Beams* **4** (2001), 124201. Cited on page 26.
- [133] C. Chandré and T. Uzer: *Instantaneous frequencies of a chaotic system*, *Pramana* **64** (2005), 371–379. Cited on pages 27, 30, and 65.
- [134] A. Sethi: *Mechanistic insights into the control of driven quantum systems*, Ph.D. thesis, Indian Institute of Technology Kanpur, (2010). Cited on page 27.
- [135] J. Laskar, C. Froeschlé, and A. Celletti: *The measure of chaos by the numerical analysis of the fundamental frequencies. Application to the standard mapping*, *Physica D* **56** (1992), 253–269. Cited on page 27.
- [136] R. Bartolini, A. Bazzani, M. Giovannozzi, W. Scandale, and E. Todesco: *Tune evaluation in simulations and experiments*, *Part. Accel.* **52** (1996), 147–177. Cited on pages 27 and 68.

- [137] A. Bazzani, L. Bongini, and G. Turchetti: *Analysis of resonances in action space for symplectic maps*, Phys. Rev. E **57** (1998), 1178–1180. Cited on page 27.
- [138] S. Löck: *Dynamisches Tunneln im gemischten Phasenraum*, Diplomarbeit, Technische Universität Dresden, Fachrichtung Physik (2006). Cited on pages 30, 36, 46, and 63.
- [139] R. Carmona, W.-L. Hwang, and B. Torrèsani: *Practical Time-Frequency Analysis: Gabor and Wavelet Transforms with an Implementation in S*, (Academic Press), (1998). Cited on page 30.
- [140] C. Froeschlé and E. Lega: *On the Structure of Symplectic Mappings. The Fast Lyapunov Indicator: a Very Sensitive Tool*, Celest. Mech. Dyn. Astr. **78** (2000), 167–195. Cited on pages 31, 33, 38, 50, and 53.
- [141] C. Froeschlé, M. Guzzo, and E. Lega: *Graphical Evolution of the Arnold Web: From Order to Chaos*, Science **289** (2000), 2108–2110. Cited on page 31.
- [142] E. Lega, A. Celletti, G. D. Penna, and C. Froeschlé: *On the computation of lyapunov exponents for discrete time series: applications to two-dimensional symplectic and dissipative mappings*, Int. J. Bifurcat. Chaos **10** (2000), 2791–2805. Cited on page 31.
- [143] C. Froeschlé, M. Guzzo, and E. Lega: *The Fast Lyapunov Indicator. Detection of the Arnold web for Hamiltonian systems and symplectic mappings with 3 degrees of freedom*, in: *The Restless Universe* (Eds. B. A. Steves and A. J. Maciejewski), 327–338, (2001). Cited on page 31.
- [144] M. Guzzo, E. Lega, and C. Froeschlé: *On the numerical detection of the effective stability of chaotic motions in quasi-integrable systems*, Physica D **163** (2002), 1–2. Cited on page 31.
- [145] C. Froeschlé, E. Lega, and M. Guzzo: *Analysis of the Chaotic Behaviour of Orbits Diffusing along the Arnold Web*, Celest. Mech. Dyn. Astr. **95** (2006), 141–153. Cited on page 31.
- [146] M. Katsanikas, P. A. Patsis, and A. D. Pinotsis: *Chains of rotational tori and filamentary structures close to high multiplicity periodic orbits in a 3D galactic potential*, arxiv:nlin.CD/1103.3981 (2011). Cited on pages 33 and 53.
- [147] C. Froeschlé: *Numerical Study of a Four-Dimensional Mapping*, Astron. Astrophys. **16** (1972), 172–189. Cited on pages 33, 38, and 53.
- [148] Wikipedia: *N-sphere* — *Wikipedia, The Free Encyclopedia*, (2011), [Online; accessed 27-September-2011; [#Hyperspherical_coordinates](http://en.wikipedia.org/w/index.php?title=N-sphere&oldid=448493668)]. Cited on page 35.
- [149] U. Eichmann, V. Lange, and W. Sandner: *Positional correlation in laser-excited three-body Coulomb systems*, Phys. Rev. Lett. **64** (1990), 274–277. Cited on pages 35 and 99.

- [150] P. Schlagheck and A. Buchleitner: *Classical support for non-dispersive two-electron wave packets in the driven helium atom*, J. Phys. B - At. Mol. Opt. **31** (1998), 489–495. Cited on pages 35 and 99.
- [151] H. Schanz, M.-F. Otto, R. Ketzmerick, and T. Dittrich: *Classical and Quantum Hamiltonian Ratchets*, Phys. Rev. Lett. **87** (2001), 070601. Cited on page 36.
- [152] L. Schilling: *Direct dynamical tunneling in systems with a mixed phase space*, Dissertation, Institut für Theoretische Physik, Fachrichtung Physik, Fakultät Mathematik und Naturwissenschaften, Technische Universität Dresden (2006). Cited on pages 36, 41, 43, 46, 77, 79, 100, 101, 104, 105, and 115.
- [153] A. Bäcker, R. Ketzmerick, and A. G. Monastra: *Universality in the flooding of regular islands by chaotic states*, Phys. Rev. E **75** (2007), 066204. Cited on page 36.
- [154] J. D. Hunter: *Matplotlib: A 2D graphics environment*, Comput. Sci. Eng. **9** (2007), 90–95. Cited on page 41.
- [155] G. Casati, B. Chirikov, F. Izrailev, and J. Ford: *Stochastic behavior of a quantum pendulum under a periodic perturbation*, in: Casati and Ford [193], 334–352. Cited on pages 63, 93, and 97.
- [156] C. Manchein, M. Beims, and J. Rost: *Footprints of sticky motion in the phase space of higher dimensional nonintegrable conservative systems*, arXiv:nlin/0907.4181 (2009). Cited on page 66.
- [157] M. V. Berry: *Regular and irregular semiclassical wavefunctions*, J. Phys. A **10** (1977), 2083–2091. Cited on pages 75 and 80.
- [158] A. Voros: *Semi-classical approximations*, Ann. I. H. Poincaré A **24** (1976), 31–90. Cited on pages 75 and 80.
- [159] R. Lawton and M. Child: *Local mode vibrations of water*, Mol. Phys. **37** (1979), 1799–1807. Cited on page 75.
- [160] S. Tomsovic and D. Ullmo: *Chaos-assisted tunneling*, Phys. Rev. E **50** (1994), 145–162. Cited on pages 75 and 98.
- [161] F. Leyvraz and D. Ullmo: *The level splitting distribution in chaos-assisted tunnelling*, J. Phys. A **29** (1996), 2529–2551. Cited on page 75.
- [162] S. Tomsovic: *Chaos-assisted tunnelling in the absence of reflexion symmetry*, J. Phys. A - Math. Gen. **31** (1998), 9469. Cited on pages 75 and 98.
- [163] C. Eltschka and P. Schlagheck: *Resonance- and Chaos-Assisted Tunneling in Mixed Regular-Chaotic Systems*, Phys. Rev. Lett. **94** (2005), 14101. Cited on pages 76, 106, 110, 116, and 118.

- [164] P. Schlagheck, C. Eltschka, and D. Ullmo: *Resonance- and Chaos-Assisted Tunneling*, in: *Progress in Ultrafast Intense Laser Science Volume I* (Eds. K. Yamanouchi, S. L. Chin, P. Agostini and G. Ferrante), vol. 84 of *Springer Series in Chemical Physics*, chap. 7, 107–131, (Springer Berlin Heidelberg), (2006). Cited on pages 76 and 106.
- [165] S. Keshavamurthy: *Resonance-assisted tunneling in three degrees of freedom without discrete symmetry*, Phys. Rev. E **72** (2005), 045203. Cited on page 76.
- [166] S. Löck, A. Bäcker, R. Ketzmerick, and P. Schlagheck: *Regular-to-Chaotic Tunneling Rates: From the Quantum to the Semiclassical Regime*, Phys. Rev. Lett. **104** (2010), 114101. Cited on pages 76, 99, 106, 108, 116, and 119.
- [167] M. V. Berry, N. L. Balazs, M. Tabor, and A. Voros: *Quantum maps*, Ann. Phys. **122** (1979), 26–63. Cited on page 77.
- [168] S.-J. Chang and K.-J. Shi: *Evolution and exact eigenstates of a resonant quantum system*, Phys. Rev. A **34** (1986), 7–22. Cited on page 77.
- [169] J. P. Keating, F. Mezzadri, and J. M. Robbins: *Quantum boundary conditions for torus maps*, Nonlinearity **12** (1999), 579–591. Cited on pages 77 and 78.
- [170] M. Michler: *Quantum signatures of partial barriers in phase space*, Dissertation, Technische Universität Dresden, Fachrichtung Physik (2011). Cited on page 78.
- [171] K. Husimi: *Some formal properties of the density matrix*, Proc. Phys. Math. Soc. Jpn. **22** (1940), 264–314. Cited on page 80.
- [172] S. Adachi, M. Toda, and K. Ikeda: *Quantum-Classical Correspondence in Many-Dimensional Quantum Chaos*, Phys. Rev. Lett. **61** (1988), 659–661. Cited on pages 90, 93, and 97.
- [173] R. Ketzmerick, K. Kruse, and T. Geisel: *Efficient diagonalization of kicked quantum systems*, Physica D **131** (1999), 247–253. Cited on pages 91 and 144.
- [174] L. Hufnagel, R. Ketzmerick, M.-F. Otto, and H. Schanz: *Eigenstates ignoring regular and chaotic phase-space structures*, Phys. Rev. Lett. **89** (2002), 154101 (4 pages). Cited on page 99.
- [175] A. Bäcker, R. Ketzmerick, and A. G. Monastra: *Flooding of Chaotic Eigenstates into Regular Phase Space Islands*, Phys. Rev. Lett. **94** (2005), 054102 (4 pages). Cited on page 99.
- [176] L. Bittrich: *Flooding of Regular Phase Space Islands by Chaotic States*, Dissertation, Technische Universität Dresden, Fachrichtung Physik (2010). Cited on page 99.
- [177] A. Ishikawa, A. Tanaka, and A. Shudo: *Dynamical Tunneling in Many-Dimensional Chaotic Systems*, Phys. Rev. Lett. **104** (2010), 224102. Cited on page 99.

- [178] R. B. Lehoucq, D. C. Sorensen, and C. Yang: *Arpack User's Guide: Solution of Large-Scale Eigenvalue Problems With Implicitly Restarted Arnoldi Methods (Software, Environments, Tools)*, (SIAM), (1998). Cited on pages 100 and 144.
- [179] J. B. Keller: *Geometrical theory of diffraction*, J. Opt. Soc. Am. **52** (1962), 116–130. Cited on page 101.
- [180] F. Borgonovi: *Localization in discontinuous quantum systems*, Phys. Rev. Lett. **80** (1998), 4653–4656. Cited on page 101.
- [181] A. Ishikawa, A. Tanaka, and A. Shudo: *Recovery of chaotic tunneling due to destruction of dynamical localization by external noise*, Phys. Rev. E **80** (2009), 046204. Cited on page 101.
- [182] V. I. Arnold: *Modes and quasimodes*, Funct. Anal. Appl. **6** (1972), 94–101. Cited on page 103.
- [183] P. Schlagheck, C. Eltschka, and D. Ullmo: *Resonance- and Chaos-Assisted Tunneling*, arXiv:nlin/0508024v1 [nlin.CD] (2005). Cited on pages 106 and 110.
- [184] L. D. Landau and E. M. Lifschitz: *Lehrbuch der theoretischen Physik: Quantenmechanik*, (Akademie-Verlag Berlin), 9th edn., (1979). Cited on page 107.
- [185] E. T. Whittaker: *Treatise on the Analytical Dynamics*, Cambridge Mathematical Library, (Cambridge University Press, Cambridge), 4th edn., (1988). Cited on page 117.
- [186] S. Keshavamurthy and G. S. Ezra: *Assigning vibrational spectra of highly excited molecules: classical and quantum vibrational dynamics of the H₂O molecule*, Chem. Phys. Lett. **259** (1996), 81 – 90. Cited on page 129.
- [187] S. Keshavamurthy and G. S. Ezra: *Eigenstate assignments and the quantum-classical correspondence for highly-excited vibrational states of the Baggot H₂O Hamiltonian*, J. Chem. Phys. **107** (1997), 156 – 179. Cited on page 129.
- [188] A. Semparathi, V. Charulatha, and S. Keshavamurthy: *Understanding highly excited states via parametric variations*, J. Chem. Phys. **118** (2003), 1146–1157. Cited on page 129.
- [189] E. Jones, T. Oliphant, P. Peterson et al.: *SciPy: Open source scientific tools for Python*, (2001–). Cited on pages 129, 136, and 144.
- [190] M. Galassi, J. Davies, J. Theiler, B. Gough, G. Jungman, M. Booth, and F. Rossi: *Gnu Scientific Library: Reference Manual*, (Network Theory Limited), (2010). Cited on page 138.
- [191] M. Hénon: *On the numerical computation of Poincaré maps*, Physica D **5** (1982), 412–414. Cited on page 139.

-
- [192] W. H. Press, S. A. Teukolsky, W. T. Vetterling, and B. P. Flannery: *Numerical Recipes in C. The Art of Scientific Computing*, (Cambridge University Press, Cambridge), 2nd edn., (1992). Cited on page 143.
- [193] G. Casati and J. Ford (eds.): *Stochastic Behavior in Classical and Quantum Hamiltonian Systems*, no. 93 in Lect. Notes Phys., (Springer-Verlag, Berlin), (1979). Cited on pages 149 and 160.

Danksagung / Acknowledgements

Wissenschaftliche Erkenntnis läßt sich nie allein erlangen. Stets sind wir auf Kritik, Meinungen, Gespräche, Hinweise und vor allem Hilfe anderer angewiesen. Als Wissenschaftler möchte ich meinen Kollegen für Ihre Ausdauer, Freundschaft und Hilfsbereitschaft danken. Allen voran möchte ich meinen Doktorvater, Herrn Prof. Dr. Roland Ketzmerick, und Herrn PD Dr. Arnd Bäcker nennen. Beiden bin ich für ihr stetes Vertrauen in mich, ihre Geduld, ihre Antworten und vor allem ihre Fragen sehr verbunden. Das Thema dieser Arbeit war mir eine Freude und ich bin beiden dafür dankbar.

Dafür, dass auch sie ihr kostbarstes Gut – ihre Zeit – stets mit mir zu teilen bereit waren, mir offene Ohren, Worte der Aufmunterung aber auch Kritik zu Teil werden ließen, danke ich allen Mitgliedern der Arbeitsgruppe Computational Physics. Es kann sich glücklich schätzen, wer sie seine Kollegen nennen kann: Matthias Michler war mir über die Jahre Freund und treuer Begleiter. Mehr als ein Mal half er mir durch seine stets hilfsbereite Art. Steffen Löck danke ich für seine unermüdlich optimistische Art und die gemeinsame Zeit im Büro. Auch Normann Mertig, Clemens Löbner, Lars Bittrich und Waltraut Wustmann danke ich für ihre Aufmunterungen, ihre Aufmerksamkeit und Hilfsbereitschaft. Ebenso möchte ich die angenehmen Gespräche mit Steffen Lange und Martin Körber nicht unerwähnt lassen. Ein spezieller Dank gilt Herrn Prof. Dr. Peter Schlagheck für seine hilfreichen Ratschläge, seine Zeit und die zahlreichen Diskussionen.

Furthermore, I would like to thank Prof. Dr. Srihari Keshavamurthy for his helpful hints and discussions during the Advanced Study Group 2011.

Meiner Familie und meinem Freundeskreis möchte ich für den Halt danken, den sie mir wann immer es nötig war stets in erstaunlichem Ausmaß zukommen ließen. Damit soll es genug sein; ich blicke auf die vier angenehmsten Jahre meines Lebens nicht ganz ohne Wehmut zurück.

Versicherung

Diese Arbeit wurde am Institut für Theoretische Physik der Technischen Universität Dresden unter der wissenschaftlichen Betreuung Prof. Dr. Roland Ketzmericks durchgeführt.

Hiermit versichere ich, dass ich die vorliegende Arbeit ohne unzulässige Hilfe Dritter und ohne Benutzung anderer als der angegebenen Hilfsmittel angefertigt habe; die aus fremden Quellen direkt oder indirekt übernommenen Gedanken sind als solche kenntlich gemacht. Die Arbeit wurde bisher weder im Inland noch im Ausland in gleicher oder ähnlicher Form einer anderen Prüfungsbehörde vorgelegt.

Darüber hinaus erkenne ich die Promotionsordnung der Fakultät Mathematik und Naturwissenschaften der Technischen Universität Dresden vom 23. Februar 2011 an.

Martin Richter

Dresden, April 2012